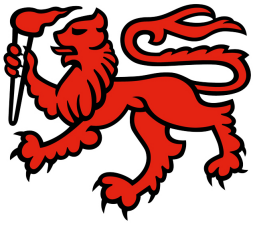

UNIVERSITY*of*
TASMANIA

FINE-SCALE OCEAN PROCESSES DRIVING THE BASAL MELTING OF ANTARCTIC ICE SHELVES

by

Madelaine Gamble Rosevear
B.Sc. Hons
Institute for Marine and Antarctic Studies
College of Sciences and Engineering

Submitted in fulfilment of the requirements
for the Degree of Doctor of Philosophy
University of Tasmania
December 2020

This thesis contains no material which has been accepted for a degree or diploma by the University or any other institution, except by way of background information and duly acknowledged in the thesis, and to the best of my knowledge and belief no material previously published or written by another person except where due acknowledgement is made in the text of the thesis, nor does the thesis contain any material that infringes copyright.

Signed: _____
Madelaine Gamble Rosevear

Date: September 13, 2020

Signed: _____
Madelaine Gamble Rosevear

Date: September 13, 2020

STATEMENT ON CO-AUTHORSHIP

The following people and institutions contributed to the manuscript that forms part of this thesis.

Paper 1 located in Chapter 3: Rosevear, M. G., Gayen, B., and Galton-Fenzi, B. K. (2021) The role of double-diffusive convection in basal melting of Antarctic ice shelves. *Proceedings of the National Academy of Science.* Accepted for publication 2 January 2021.

- Madelaine Meredith Gamble Rosevear, Candidate, University of Tasmania (75%)
- Bishakhdatta Gayen, Advisor, University of Melbourne (12.5%)
- Benjamin Keith Galton-Fenzi, Supervisor, Australian Antarctic Division (12.5%)

Details of authors roles:

Madelaine Gamble Rosevear designed and ran the model experiment, analysed and interpreted the results and led the manuscript preparation.

Bishakhdatta Gayen developed the code for this application and contributed to hypothesis development, interpretation of results and manuscript preparation.

Benjamin Keith Galton-Fenzi contributed to hypothesis development, interpretation of results and manuscript preparation.

We, the undersigned, agree with the above stated "proportion of work undertaken" for the above submitted manuscript contributing to this thesis:

Signed: _____

Ms Madelaine Gamble Rosevear

Candidate

Institute for Marine and Antarctic Studies

University of Tasmania

Signed: _____

Professor Nathaniel Lee Bindoff

Supervisor

Institute for Marine and Antarctic Studies

University of Tasmania

Signed: _____

Professor Neil Holbrook

Head of centre, Oceans & Cryosphere

Institute for Marine and Antarctic Studies

University of Tasmania

Date: January 22, 2021

ABSTRACT

The Antarctic Ice Sheet, which comprises the largest volume of ice on our planet, is losing mass due to ocean-driven melting of its fringing ice shelves. Efforts to represent basal melting in sea level projections are undermined by poor understanding of the turbulent ice shelf-ocean boundary layer (ISOBL), a meters-thick band of ocean that regulates heat, salt and momentum transfer between the far field ocean and the ice. Regional ocean models cannot resolve the ISOBL and instead rely on parameterisations to predict melting. However, observations suggest that these parameterisations only perform well for a subset of relevant ocean conditions, namely in cold, energetic environments. This thesis uses both observational data and turbulence-resolving model simulations to address this shortfall by characterising melting and ISOBL dynamics across a broad range of ocean states.

Chapter 1 of this thesis outlines the motivation and context for the work that follows, highlighting the urgent knowledge gaps that will be addressed. In chapter 2, a unique set of observations from beneath the Amery Ice Shelf, including *in situ* basal melt rate, ocean velocity, temperature and salinity data are analysed and ocean conditions are characterised. The mean basal melt rate at the site (0.5 m yr^1) is a factor of 2–4 lower than predicted from common ice-ocean parameterisations. This result suggests an important role for stratification at this site, either through suppression of heat transport to the ice-ocean interface or a shoaling of the mixed layer depth. These processes cannot be unraveled from the available observational data, further motivating the need for turbulence resolving simulations.

In chapter 3, large-eddy simulation is used to model the ISOBL. The model domain consists of a horizontal ice-ocean interface with a melting boundary condition at the upper surface, underlain by a stratified ocean. The domain is periodic in both horizontal directions, and is forced with a steady flow in geostrophic balance. At relatively warm, low velocity conditions a small-scale mixing process (double-diffusive convection) is shown to determine ice shelf melt rate and the properties of the mixed layer that forms beneath the ice. In double-diffusive regime, melting is found to be inherently unsteady in time and

insensitive to shear from the imposed current. Simulated melt rates and water column structure are consistent with observations made near the grounding line of the Ross Ice Shelf.

In chapter 4, model forcing conditions are expanded to encompass colder and more energetic cavity environments in which current shear controls melting. Two distinct mixing regimes emerge: a stratified regime in which boundary layer turbulence is strongly affected by the surface buoyancy flux due to melting and a well-mixed regime in which buoyancy has little effect. The stratified regime supports strong temperature and salinity gradients near the ice, decoupling the interface and far field conditions. The relative strength of the surface buoyancy flux and shear, characterised by the Obukhov length scale, is shown to be critical to both heat flux and boundary layer depth.

Results from chapters 3 and 4 are used to develop a regime diagram for ISOBL dynamics beneath horizontal, melting ice in discussion chapter 5. This novel diagram provides new insight into the varied and nonlinear responses of basal melting and ISOBL dynamics to local conditions around Antarctica. Comparison to observed sub-ice shelf conditions and melt rates from chapter 2 and other published studies is favorable and demonstrates the relevance of these regimes over a broad range of realistic conditions. Insights from this thesis significantly extend the current understanding of the ISOBL and basal melting. The inclusion of the double-diffusive and stratified regimes in future parameterisations of ice-ocean interactions will significantly improve melt rate estimates, with consequences for predictions of ice sheet stability.

ACKNOWLEDGEMENTS

This thesis was written on the land of the Muwinina people of nipaluna (Hobart). I acknowledge and respect the deep and enduring connection to county and culture held by the Muwinina and palawa peoples, the traditional owners of lutruwita (Tasmania).

They say it takes a village to raise a thesis, and I am so grateful to my village. To my supervisors Ben Galton-Fenzi and Nathan Bindoff, and my external advisor Bishakh Gayen, thank you so much for bringing your expertise to this project. It has been such a pleasure to learn from you and with you. Bishakh, thank you for always bringing such enthusiasm to my project. You never failed to give me back momentum and purpose when it was lacking. To Ben, thank you for your unflinching confidence in my abilities and for the amazing opportunities you've sent my way.

To my parents, Hannah Gamble and Craig Rosevear, thank you for your love and support. I'm so grateful for all the opportunities you've given me. To Felicity McCormack and Anna Cresswell, thank you for blazing the trail, believing in me and always giving me a hand up. To my housemates Claire Butler, Vincent Dodd, Dante Kurth and Maddy Brodie, the home we've made together means so much to me. Thank you so much for all the love, chaos and support. And to my partner, Chris Lang, this would have been so much less fun without you.

In no particular order, I would also like to thank Felicity McCormack, Catherine Vreugdenhil, Anna Cresswell, Chris Lang, Maddy Brodie, Vincent Dodd, Dante Kurth, and Lisa Craw for their editing help; Craig Stevens, Mike Williams, Ben Galton-Fenzi and Paul Winberry for including me in their incredible fieldwork; Ross Griffiths, Andy Hogg, Nerilie Abrams and the GFD group at ANU for early supervision and mentorship; the UTAS ice sheets group and Sue Cook especially for creating a brilliant and supportive research environment; and Ole Richter and Wilma Huneke, my PhD "siblings'', for sharing this journey with me.

TABLE OF CONTENTS

TABLE OF CONTENTS **i**

LIST OF TABLES **v**

LIST OF FIGURES **viii**

1 Introduction **1**

1.1 Sea level, ice sheets and ice shelves 2

1.2 Ice shelf-ocean interactions: large-scale processes and circulation 6

1.3 Ice shelf-ocean interactions: the ice shelf-ocean boundary layer 10

1.3.1 Melting and the ice-ocean interface 10

1.3.2 The frictional ice shelf-ocean boundary layer 11

1.3.3 Convection-driven melting 16

1.4 Observations beneath ice shelves 18

1.5 Thesis objectives and outline 21

2 Observations of basal melting and ocean circulation beneath the Amery Ice Shelf **23**

2.1 Introduction 24

2.1.1 Amery Ice Shelf 25

2.1.2 The ice shelf-ocean boundary layer 26

2.1.3 Modeling ice-ocean interactions 27

2.1.4 Present study 30

2.2 Data and Methodology 31

2.2.1 Instrumentation 31
2.2.2 Melt rate measurements 32
2.3 Observations 33
2.3.1 Oceanographic setting 33
2.3.2 Basal melt rate 40
2.4 Comparison with models 41
2.4.1 Choice of data 41
2.4.2 Ice shelf heat flux 43
2.4.3 Results 44
2.5 Discussion 46
2.5.1 The suitability of shear and convective melting parameterisations at AM06 46
2.5.2 Sampling depth considerations 48
2.5.3 Transfer and drag coefficients 50
2.5.4 Extension to other published studies 51
2.6 Summary and conclusions 52

3 The role of double-diffusive convection in basal melting of Antarctic ice shelves 55

3.1 Introduction 55
3.2 Methods 58
3.2.1 Governing equations 58
3.2.2 Numerical method 60
3.2.3 Domain and initialisation 61
3.3 Results 62
3.3.1 Diffusive convection beneath a melting ice shelf 64
3.3.2 Friction velocity and drag coefficient 72

3.3.3 Melting . . . 73
3.4 Discussion . . . 76
3.5 Supplementary information for chapter 3 . . . 81
3.5.1 Shear mixed layer depth scaling . . . 81
3.5.2 Comparison between simulated melt rates and a common ice-ocean parameterisation . . . 81
3.5.3 Turbulent kinetic energy . . . 82

4 Basal melting of a horizontal ice shelf driven by a steady, geostrophic current 84

4.1 Introduction . . . 85
4.2 Background . . . 86
4.2.1 The ice shelf-ocean boundary layer . . . 86
4.2.2 Models of ice-ocean interaction . . . 89
4.3 Methods . . . 91
4.4 Results . . . 93
4.4.1 Boundary layer evolution and velocity characteristics . . . 93
4.4.2 Mixed layer depth . . . 99
4.4.3 Melting . . . 104
4.5 Discussion . . . 108
4.6 Conclusions . . . 113

5 Discussion 115

5.1 Regimes and transitions in basal melting of Antarctic ice shelves . . . 115
5.1.1 Transitions in the DC regime . . . 115
5.1.2 Boundary layer regimes . . . 118
5.1.3 Heat and salt transfer . . . 120
5.1.4 Revisiting the Amery Ice Shelf . . . 122

6 Conclusions **124**

A Model details **129**

A.1 LES closure 129

A.1.1 Subgrid-scale contributions 129

A.1.2 Closure of the TKE budget 130

A.2 Grid specifications and convergence 131

A.2.1 Aspect ratio testing 131

A.2.2 Horizontal resolution 131

A.3 Forcing considerations: effect of varying Coriolis 132

B Observational data **135**

REFERENCES **137**

LIST OF TABLES

2.1 Type, duration and depth of measurements from the AM06 borehole. Depth given with respect to the ice-ocean interface. 32

2.2 Ellipse parameters for tidal current constituents of the depth-mean flow over the upper 90m of the water column. Presented are velocities of the ellipse major and minor axes, the inclination of the semi-major axis (counter-clockwise from east), and phase of the tidal vector relative to equilibrium tide at Greenwich. 40

2.3 Physical parameters used in melt parameterisation calculations 44

2.4 Melt rates from observations and parameterisations. Columns 2–4 are average values observed over the periods given in column 1, where the period starts on the 7th day of the month. To calculate m_{M87} a drag coefficient of $C_d = 0.0025$ is used. The upper and lower bounds on the observationally constrained transfer coefficient Γ_T are based on using $C_d = 0.0025$ and $C_d = 0.0097$, respectively. The bracketed melt rate estimates show the effect of setting the heat flux into the ice shelf Q_i^T to zero. . . . 46

2.5 Comparison between observed and predicted melt rates for a series of Antarctic ice shelves for which both melt rates and *in situ* oceanographic data are available. Observed variables presented are the time-mean current speed ($\bar{u}$), thermal driving ($\bar{T}^*$) and melt rate (m_{OBS}). Melt rate predictions made from J10 are also presented for each site. Where they are in bold, we have used the estimate from the original study. See Appendix B for further information on the data. $^{\leftrightarrow}$ Sites with a strong tidal component to the flow. 53

3.1 Domain and grid size for the simulations performed. Dimensions of domain (LX, LY, LZ); number of grid points (NX, NY, NZ); grid spacing in wall units $(\Delta X^+, \Delta Y^+, \Delta Z^+)$. 61

LIST OF TABLES

3.2 Free stream velocity (U_0) , reference temperature (T_0), friction velocity ($u^* = (\tau_w/\rho_0)^{1/2}$, where τ_w is the shear stress at the ice-ocean interface), thermal driving ($T^* \equiv T_{ML} - T_f(S_{ML}, p_b)$, the temperature difference between the mixed layer and the freezing temperature at mixed layer salinity and interface pressure), temperature difference between the mixed layer and interface ($\Delta T = T_{ML} - T_b$) and melt rate (m). Overbar denotes quantities that are averaged over 50–100 h. #Observations reported in Begeman et al. (2018), from the period 05 Jan 2015–20 Jan 2015. 64

3.3 Comparison between simulated melt rate (m) and melt rate as predicted by the three-equation parameterisation (m_{pred}). 82

4.1 Grid specifications for different velocity and Coriolis forcing. Free stream velocity U_0; Coriolis frequency f; domain horizontal dimension LX (= LY); domain height LZ; horizontal resolution (in wall units) ΔX^+ (=ΔY^+); vertical resolution at the ice-ocean interface ΔZ^+. 91

4.2 Key parameters and results. Free stream velocity U_0; initial thermal driving T_0^*; friction velocity u^*; drag coefficient C_d; temperature difference between the interface and mixed layer $T_b - T_{ML}$; melt rate m; Obukhov lengthscale L; viscous Obukhov lengthscale L^+; and mixed layer classification as WM (well-mixed), STR (stratified) or DC (diffusive convective). All results are at $t = 3\Delta t$, except runs A3, B3 and C3 which are at $t = 2\Delta t$. 95

4.3 Comparison of transfer coefficients from observational and numerical studies. Thermal Stanton number $C_d^{1/2}\Gamma_T$, drag coefficient C_d, heat transfer coefficient Γ_T, ratio of heat and salt transfer coefficients Γ_T/Γ_S, simulation Lewis number Le, gradient thickness ratio δ_T/δ_S. *Ratio assumed, not measured. #Nominal Le values used to enable comparison with modelling results. 109

5.1 Time to transition from DC-dominated to shear-dominated mixing. Obukhov lengthscale (L); and transition time (t_{DC}). L is evaluated at $t = 10$ h. . 116

LIST OF TABLES

5.2 Key quantities for the Amery Ice Shelf. Column 1–3 are observed quantities from Table 2.4. Columns 4–9 are theoretical estimates based on the choice of drag coefficient C_d. Parameters L, μ, h_μ, L^+ and m_{pred} are calculated using melting Eqs. 4.12 and 4.13 with transfer coefficient Eqs. 4.19 and 4.20. 123

A.1 Grid specifications for supplementary runs varying Coriolis forcing and grid cell aspect ratio. Initial thermal driving T_0^*; Free stream velocity U_0; Coriolis frequency f; viscous lengthscale $\delta_\nu = \nu/u_0^*$; Ekman boundary layer depth δ_{f0}; domain horizontal dimension LX $(= LY)$; domain height LZ; horizontal resolution (in wall units) ΔX^+ $(=\Delta Y^+)$; vertical resolution at the ice-ocean interface ΔZ^+; Aspect ratio $(A = \Delta Z^+/\Delta X^+)$ of grid cells at the edge of the viscous sublayer (Z^+=50). $^{\#}$This run is initialised with a background temperature gradient matching that of run 3 (chapter 3). 134

LIST OF FIGURES

1.1 The connection between Antarctic ice mass loss and ocean forcing from Noble et al. (2020). Gravimetric Mass Balance data for 2002-2016 shows ice mass changes across the continent. Annotations in magenta have been added to show the locations of ice shelves mentioned in this thesis. . . . 4

1.2 The connection between Antarctic ice mass loss and ocean forcing from Noble et al. (2020). Map of the Southern Ocean bottom potential temperature highlights the presences of warmer waters along the West Antarctic margin, based on the WOCE global hydrographic climatology. 5

1.3 Density contours for seawater from Hewitt (2020) at conditions relevant to the polar ocean. The grey lines show liquidus (freezing temperature) curves. The addition of meltwater causes $T-S$ properties to evolve along the purple line, assuming equal eddy diffusivities of heat and salt (e.g. McDougall et al., 2014). 7

1.4 The Antarctic Slope Front. (A–C) Different shelf types via density (black contours) and temperature (shading) along three different sections. This figure is reproduced from Figs. 3d–f from Thompson et al. (2018), annotations were added *a posteriori* for clarity and are based on Figures 3a–c from Thompson et al. (2018). Sections originate from Heywood and King (2002); Thompson and Heywood (2008); Orsi and Whitworth (2005). . . 8

1.5 Idealised schematic of processes operating in an ice shelf cavity at cold or "mode 1" conditions. Fig. adapted from Stern et al. (2014). 9

1.6 Schematic of the ice-ocean system showing the balance of heat and salt at the ice-ocean interface. 10

1.7 A frictional ISOBL consists of a viscous sublayer, surface or "log" layer and a turbulent outer layer. In systems where planetary rotation (Coriolis) is important, the boundary layer depth is expected to scale with the Planetary scale (δ_f). 12

LIST OF FIGURES

1.8 Direct numerical simulation of convective melting of a vertical ice face from Gayen et al. (2016). Panels are (a) vertical velocity w, (b) horizontal velocity u and (c) melt (dissolution) rate and interface temperature (T_i). 17

1.9 Direct numerical simulation of double-diffusive convection (semiconvection) beneath melting ice from Keitzl et al. (2016b). Colour shows normalised buoyancy. 18

1.10 Ice base geometry under Pine Island Glacier ice shelf from Fig. 2 of Dutrieux et al. (2014). (c) Basal elevation (color) of a longitudinal channel. (d) Basal slope angle from horizontal in the area indicated in (c). . . 20

2.1 Ice thickness map of the Amery Ice Shelf in polar stereographic projection with borehole sites AM01–6 labelled. The floating ice shelf is denoted by the bold colours. Map produced with Antarctic Mapping Tools (Greene et al., 2017b) using the Bedmap2 product (Fretwell et al., 2013a) 25

2.2 (A) Conservative Temperature Θ and (B) Absolute Salinity S_A profiles from the two CTD casts at AM06. Individual up- and down-casts are shown (grey lines) as is the four-profile mean (black line). Overlain at the appropriate pressures are the mean ($\pm$ 2σ) microcat Θ and S_A for the month following the CTD data collection. (C) Squared buoyancy frequency N^2, where the grey and black buoyancy frequency curves were obtained using 10 and 40 dbar running window averages, respectively. The shaded grey region shows range in the ice-ocean interface position above the instruments due to the sloping ice base. 33

2.3 Θ-S_A plots for months January, July and October in 2010 at AM06 and AM02 (5 year composite of years 2001, 2003-2006). Freezing temperature curves at surface, AM06 interface (543 dbar; solid blue) and AM02 interface (326 dbar; dashed blue, bottom panel only) pressure are also shown. The dashed grey line is the meltwater mixing line from Fig. 2.4. 35

2.4 Θ-S_A plot of the four-profile mean from Fig. 2.2 coloured by pressure. A meltwater mixing line with gradient $d\Theta/dS_A$=2.38 °Cg^{-1}kg calculated following McDougall et al. (2014) is shown (dashed grey line), as are the local isopycnal slopes (dotted grey lines). The inset shows a line of best fit for the upper 15 m of the water column (red line) which has gradient $d\Theta/dS_A$=4.8 °Ckg g^{-1}. 36

2.5 Time-series of (A) Θ (B) S_A from all three microcats. The freezing temperature (black) at upper microcat salinity and interface pressure is also shown in (A). 38

2.6 (A) Depth-mean current speed $U = \sqrt{u^2 + v^2}$ from the ADCP (grey). Overlaid is the smoothed, depth-mean current speed with tides removed $U_r = \overline{(u - u_T)^2 + (v - v_T)^2}$ (blue). (B) Current direction (grey) and smoothed current direction with tides removed (red). 39

2.7 Depth of the ice shelf base relative to zero depth (defined in Table 2.1), where a more negative depth indicates a thinner ice column above. The area mapped out by the ADCP is determined by the beam angle (20°) and the distance to the ice shelf (92–114 m). Overlain is an outline of the region of the ice base over which melt rates in Fig 2.8 are calculated. . . 41

2.8 Observed melt rates at monthly resolution for (grey) each grid cell ($d\phi$, dr) and (red) the area average, where the area is outlined in Fig. 2.7. 42

2.9 (A) Heat flux into the ice Q_i^T as a function of melt rate m from a one-dimensional advection-diffusion model for a 607 m thick ice shelf with a −20 °C surface and −2.1 °C basal temperature. (B) Ratio of Q_i^T to latent heat flux due to melting Q_{latent}^T as function of melt rate. The vertical dashed lines correspond to the annual average melt rate of 0.51 m yr^{-1}. . 45

2.10 (top) Θ and S_A from the upper microcat 4 m below the ice, (middle) ocean velocity magnitude averaged over 7–19 m below the ice base and (lower) modelled melt rates for the three parameterisations compared in this study. While the J10 and M87 melt rates are strongly modulated by the tidal flow at AM06, MK18 varies only with temperature. 47

2.11 Simplified schematic of the ice base and upper water column showing the position of the upper microcat and ADCP. 49

2.12 Ratio of observed to predicted melt rate for the J10 parameterisation as a function of thermal driving T^* and free stream velocity U for published ice shelf datasets. Map shows the location of the observations. 52

3.1 Schematic of the model domain, which consists of a horizontal ice-ocean interface with cold, salty ocean below. In the interior of the domain the ocean is in geostrophic balance and has velocity $(u, v) = (U_0, 0)$. Near the ice an Ekman boundary layer forms. 59

3.2 Overview of the model domain with flow and melt rate solutions for run 3. The upper $x - y$ surface shows the instantaneous melt rate m, while vertical $y - z$ and $x - z$ planes show the vertical velocity w and temperature T fields respectively. Overlaid are the horizontal velocity profiles (u, v: green solid lines) and buoyancy frequency squared at $t = 0$ h (N_0^2: pink dashed line) and $t = 30$ h (N^2: pink solid line) where $N = (-g/\rho_0(\partial\rho/\partial z))^{1/2}$ is the buoyancy frequency. Unless otherwise stated, all planes and profiles are from $t = 30$ h. 63

3.3 Temporal evolution of the water column for run 3. (a) Plane averaged temperature; (b) salinity; and (c) normalised buoyancy frequency N^2/N_0^2 over the upper water column through time. The mixed layers that emerge over the course of the experiment are annotated as L1, L2 and L3. . . . 65

3.4 Schematic of the proposed mechanism for DC beneath a melting ice shelf, where ρ_T and ρ_S are density contributions from temperature and salinity respectively. The thermal diffusive boundary layer is thicker than its saline counterpart, resulting in a region with a negative density gradient (grey shading) which will overturn. 66

3.5 Profiles of ocean properties through time. Columns from L–R: temperature T; salinity S; stratification expressed as normalised buoyancy frequency squared N^2/N_0^2; Stream-wise u and cross-stream v velocity. Rows are labelled by experiment. Temperature, salinity and stratification for run 2 (not shown) are extremely similar to run 1. 67

3.6 Density ratio R_ρ^* as a function of depth for run 3 at $t = 1$ h (dark blue), $t = 35$ h (medium blue) and $t = 70$ h (light blue). Dashed grey line gives the linear stability criterion $R_\rho^* = 1.07$. The initial temperature and salinity conditions give $R_\rho^* = 8.6$. 68

3.7 Plane-averaged buoyancy flux B as a function of depth and time for (a) run 3* ($U_0 = 1.4$ cm s^{-1}, $T_0^* = 0.375$ °C) and (b) run 3 ($U_0 = 1.4$ cm s^{-1}, $T_0^* = 0.175$ °C). (c) time-series of B at a depth of z=-0.2 m. 70

3.8 The contributions of heat and salt to the buoyancy flux at $t = 50$ h for run 3*. Both diffusive and turbulent contributions are plotted. Horizontal dotted lines show the thermal and saline diffusive sublayer scales given in Eq. 3.12. 72

3.9 Melting and diffusion at the ice-ocean interface. (a) Temporal evolution of melt rate m and (b) scalar diffusive sublayer thicknesses δ_T (solid lines) and δ_S (dashed lines) for all experiments. Also plotted are temperature diffusion lengthscale $h_T = (4\kappa_T t)^{1/2}$ (solid grey line) and salinity diffusion lengthscale $h_S = (4\kappa_S t)^{1/2}$ (dashed grey line). (c) Profiles of near-ice temperature and salinity, scaled as $(T-T_b)/(T_{ML}-T_b)$ and $(S-S_b)/(S_{ML}-S_b)$ for experiments 1 and 3 at $t = 100$ h. In run 1 turbulence is generated by convection only whereas in run 3, shear generated turbulence is also present, resulting in a thinner thermal diffusive sublayer. (d) Diffusive sublayer thickness ratio as a function of friction velocity at $t = 50$ h (pale circles), $t = 100$ h (bold circles) and $t = 200$ h (square, run 1 only). Lines show previous estimates of δ_T/δ_S from Gade (1993) (dashed), Keitzl et al. (2016b) (dot-dashed) and Sirevaag (2009) (dotted). 75

3.10 Melt rate m as a function of thermal driving T^* and friction velocity u^* from this study (circles), where all quantities are averaged over $50 < t <$ 100 h, and from field data collected beneath the Ross Ice Shelf (Begeman et al., 2018) (square). Inset: as for main figure with melt rate (colour) predicted by the three-equation parameterisation with parameters recommended in Jenkins et al. (2010b) (See S1 §3.5.2 for details). Note different scale. For the field observation, u^* is calculated from the free stream velocity as $u^* = C_d^{1/2} U_0$ for $C_d = 0.0025$. Error bars show the range of u^* values obtained from choosing $C_d = 0.01$–0.001. 77

3.11 Plane-integrated buoyancy production B, shear production P, and dissipation ϵ at $t = 50$ h. Positive (negative) values for each term are shown in black (orange). Panels are labelled by run, see Table 1 for details. . . 83

4.1 Schematic of the model domain, which consists of a horizontal ice-ocean interface with cold, salty ocean below. In the interior of the domain the ocean is in geostrophic balance and has velocity $(u, v) = (U_0, 0)$. Near the ice an Ekman boundary layer forms. 92

4.2 Snapshot of output for run A3 at $t = \Delta t$. Horizontal $(x - y)$ plane shows instantaneous melt rate m at the ice-ocean boundary. Vertical planes show vertical velocity w ($z - y$ plane) and temperature T ($x - z$ plane). Only the upper 3.6 m of the domain is shown. 94

4.3 Temporal evolution of key quantities for run A2 over three inertial periods: (A) melt rate m and friction velocity u^*; (B) Turbulent Kinetic Energy k ($\mathrm{m^2\ s^{-2}}$); (C) temperature T (°C); and (D) squared buoyancy frequency N^2 ($\mathrm{s^{-2}}$) with the base of the mixed layer (here defined by the pycnocline depth) highlighted in white. 96

4.4 Temporal evolution of key quantities for run C2 over three inertial periods. Panels as in Fig. 4.3. The base of the mixed layer (here defined by the depth of the strongest pycnocline) is highlighted in white. 97

4.5 Velocity profiles in wall units for (A) experiments A1–3 and (B) experiments C1–3. Over-plotted are the viscous boundary layer scaling $u^+ = z^+$ (solid black line); logarithmic boundary layer scaling (eqn. 4.4; solid grey line) and M-O similarity scaling (eqn. 4.6; dashed lines, colours correspond to labelled experiments). 98

4.6 Normalised geostrophic (u) and ageostophic (v) flow for (A, B) runs A2 and C2 with $U_0 = 1.4$ cm $\mathrm{s^{-1}}$ and (C, D) runs A3 and C3 with $U_0 = 2.8$ cm $\mathrm{s^{-1}}$. In (B) and (D) profiles are plotted as a function of z scaled by the planetary scale δ_f. Velocity components are averaged over $2\Delta t < t < 3\Delta t$ for A2,C2 and $\Delta t < t < 2\Delta t$ for A3, C3. 99

4.7 Schematic showing typical profiles of squared buoyancy frequency (N^2) for the three observed ISOBL "regimes" at $t = \Delta t$ and $t = 2\Delta t$. In each profile the pycnocline depth, which we use as a proxy for mixed layer depth, is shown with an arrow. 100

4.8 Profiles of squared buoyancy frequency (N^2) for all runs (labelled) at $t/\Delta t = 2$. Profiles are offset by $N^2 = 2 \times 10^{-5}$ s^{-2}. 101

4.9 Simulated mixed layer depth h_{obs} scaled by planetary scale δ_f as a function of stratification parameter γ. Dashed line is $h_{obs}/\delta_f = 1.4\gamma^{-1/4}$. Markers show well-mixed (circle) stratified (square) and diffusive-convective (triangle) boundary layers respectively. 102

4.10 (A) Simulated mixed layer depth h_{obs} scaled by planetary scale δ_f as a function of stability parameter μ, the dashed line is $h_{obs}/\delta_f = 0.31\mu^{-1/2}$. (B) Friction velocity u^* normalised by geostrophic velocity U_0 as a function of stability parameter μ, dashed line is $u^*/U_0 = 0.043\mu^{-1/5}$. Markers as for Fig. 4.9. 103

4.11 Simulated mixed layer depth h_{obs} as a function of B^T/N_∞^3, the dashed line is $h_{obs} = 11(B^T/N_\infty^3)^{1/2}$. Markers as for Fig. 4.9. 104

4.12 Melt rate m as a function of friction velocity u^* for (A) $0.0019 \leq T^* \leq 0.0023$, (B) $0.006 \leq T^* \leq 0.007$, (C) $0.04 \leq T^* \leq 0.05$ and (D) $0.14 \leq T^* \leq 0.18$. Markers are are coloured by time $t/\Delta t$. Green lines show the expected dependence of m on u^* from Eqs. 4.12, 4.13 and 4.9 with transfer coefficients $\Gamma_T = 0.011$ and $\Gamma_S = 3.1 \times 10^{-4}$ from Jenkins et al. (2010b). 105

4.13 (A) Gradient thickness in temperature δ_T, (B) gradient thickness in salinity δ_S, (C) heat transfer coefficient Γ_T and (D) salt transfer coefficient Γ_S for runs A3, B3, C2 and C3. Thermal $(4\kappa_T t)^{1/2}$ and saline $(4\kappa_S t)^{1/2}$ diffusion lengthscales are over-plotted (dotted lines) on panels (A) and (B) respectively. 107

4.14 (A) Scatter plot showing ratio of simulated to parameterised melt rates as a function of the viscous Obukhov length L^+, where the predicted melt rates are obtained from the three-equation parameterisation with $\Gamma_T = 0.011$ and $\Gamma_S = 3.8 \times 10^{-4}$. Circles and triangles denote non steady-state and steady-state experiments respectively. For the steady state experiments, (B) Γ_T and (C) Γ_S are plotted as a function of L^+. 108

4.15 (A) Colour contour of heat transfer coefficient $\Gamma_T(L^+)$ for $L^+ > 2500$. Solid black contours show $L^+ = 2500, 25000$ dashed black contours show original $L^+ = 2500, 25000$ that would be obtained from fixed Γ_T, Γ_S. (B) Colour contour of melt rate m (C) L with contours of μ over-plotted in white. Markers denote the well-mixed (circle) stratified (square) and diffusive-convective (triangle) boundary layers respectively. 112

5.1 Evolution of the plane-averaged buoyancy flux due to temperature (B^T) at $z = -0.2$ m (within the mixed layer) in time for runs 1, 2, 3* and C1 compared to the modelled surface buoyancy flux due to temperature (B^T_{mod}) from Eq. 5.2. 118

5.2 Regimes and transitions for the ISOBL. Filled markers show the positions of experiments in T^*, u^* space at $t = 10$ h. Where relevant, markers are coloured by DC transition timescale t_{DC}. Where u^* is measured directly, it is estimated from the free stream flow using $u^* = \sqrt{C_d}U$ with $C_d = 0.0025$ (mid point), $C_d = 0.001$ (lower bound) and $C_d = 0.01$ (upper bound). Observational data are described in Appendix B. Data sources are: WGZ, (Begeman et al., 2018); FRIS, (Jenkins et al., 2010b); RIS, (Stewart, 2018); GVIIS, (Kimura et al., 2015); LCIS, (Davis and Nicholls, 2019); HWD2, (Stevens et al., 2020); and PIIS (Stanton et al., 2013). 119

5.3 Heat transfer coefficient Γ_T (colour) as a function of friction velocity (u^*) and thermal driving (T^*). Observational data as for Fig. 5.2. 121

A.1 Plane-integrated buoyancy production B, shear production P, and dissipation ϵ averaged over $t = 90 - 100$ h. Terms are broken down into resolved (res) and subgrid-scale (sgs) components. The largest subgrid-scale component is the subgrid-scale dissipation, which accounts for 10% of the total dissipation at $U_0 = 0.0$ cm s^{-1} and 35% of the dissipation at $U_0 = 1.4$ cm s^{-1} 130

A.2 Effect of varying Aspect ratio $A = \Delta Z^+/\Delta X^+$ of grid cells at Z^+=50 on Nu for supplementary runs S3–5. Thermal driving and free stream velocity are constant between runs. The vertical dotted line shows $A = 1/8$. 131

A.3 Effect of horizontal resolution on (upper) melt rate; (middle) melt rate normalised by ΔT; (lower) friction velocity u^* for run 3 (main text)and supplementary run S6. Thermal driving and free stream velocity are constant between runs. 132

A.4 Effect of Coriolis parameter f on (upper) melt rate; (middle) melt rate normalised by ΔT; (lower) friction velocity u^* for run A2 (main text) supplementary runs S1 and S2. Thermal driving and free stream velocity are consistent between runs. 133

A.5 Profiles of squared buoyancy frequency N^2 for runs A2, S1 and S2. The depth axis is scaled by $\gamma^{-1/4}$. 134

B.1 Description of the observational data used in chapters 2 and 5 of this thesis. Bold values indicate that the value was not explicitly provided in the original study, and was instead inferred from data plotted or discussed. Values in bold should be considered approximate only. 136

Chapter 1

Introduction

The Antarctic Ice Sheet is losing mass at an accelerating rate, contributing to rising sea level (Paolo et al., 2015; Shepherd et al., 2018; Bamber et al., 2018; Rignot et al., 2019; Smith et al., 2020). In many areas around the Antarctic coast the thick, meteoric ice that makes up the Antarctic Ice Sheet extends beyond the land and floats on the ocean. It is through these floating extensions, known as ice shelves, that the Southern Ocean and the Ice Sheet exchange heat and mass. The processes responsible for this exchange are melting and freezing of the ice shelf base and front (basal melting/freezing) and the loss of large chunks of ice from the leading edge of the ice shelf (ice-berg calving). The processes of basal melting and ice-berg calving each account for roughly half of the mass loss from the continent (Depoorter et al., 2013; Rignot et al., 2013). In a steady state, this mass loss is balanced by mass gain through snow accumulation in the interior of the continent. However, mass loss and mass gain are not balanced at present. Enhanced basal melting of ice shelves is driving thinning of the Antarctic Ice Sheet (Pritchard et al., 2012; Cook et al., 2016; Adusumilli et al., 2018; Meredith et al., 2019). Consequently, the Antarctic contribution to global sea level rise is accelerating, presenting a major threat to coastal regions (Cazenave and Llovel, 2010). Enhanced basal melting of ice shelves also contributes a freshwater flux to the ocean, impacting the production of Antarctic Bottom Water which supplies the lower limb of the global thermohaline circulation (Jacobs and Giulivi, 2010; De Lavergne et al., 2014; Purkey and Johnson, 2013).

Despite the importance of basal melting to sea level and global ocean circulation, many aspects of the interactions between ice shelves and the polar oceans are poorly understood. These interactions involve processes operating on a range of spatial scales, from large-scale ocean processes that transport warm water to the Antarctic coastal seas, to the cavity-scale ocean circulation beneath ice shelves, to the micro-scale boundary layer

processes that regulate the transport of heat and salt to the ice-ocean interface (Dinniman et al., 2016; Noble et al., 2020). Observations beneath and near ice shelves are sparse due to the extreme Antarctic environment and challenging logistics. Consequently, numerical ocean models are heavily relied upon for studies of ice-ocean interactions, and are critical for projections of future ocean circulation, basal melting and ice sheet stability. On the micro-scale, basal melting is regulated by the ice-shelf ocean boundary layer; a narrow band of ocean that controls heat, salt and momentum transfer to the ice (McPhee, 2008). The ice shelf-ocean boundary layer is on the order of metres thick (Davis and Nicholls, 2019) and cannot be resolved in regional- and global-scale ocean models (e.g Naughten et al., 2018b; Gwyther et al., 2020a). The objective of this thesis is to enhance our understanding of the ice shelf-ocean boundary layer, and work towards accurate parameterisation of the fine-scale processes controlling basal melting of Antarctic ice shelves.

This chapter details the motivation and context for the work undertaken in this thesis. The role of ice shelves in ice sheet stability and sea level is outlined in §1.1. The large-scale ocean processes responsible for basal melting are described in §1.2. Ice shelf-ocean boundary layer processes, including the effects of buoyancy and convection, are discussed in §1.3. Observations from beneath ice shelves are reviewed in §1.4, and the structure of this thesis is outlined in §1.5.

1.1 Sea level, ice sheets and ice shelves

Ice sheets have enormous potential to cause large changes in sea level. The Antarctic Ice Sheet alone contains 58 m of sea level equivalent (Fretwell et al., 2013b), while the Greenland Ice Sheet contains 7 m (Dowdeswell, 2006). Both ice sheets are losing mass at an accelerating rate (Bamber et al., 2018; Rignot et al., 2019; Van den Broeke et al., 2016; King et al., 2018). The rate of mass loss from the Antarctic Ice Sheet has accelerated from 51 ± 73 Gt yr^{-1} in the period 1992–2001 to 199 ± 26 Gt yr^{-1} in the period 2012–2016 (Bamber et al., 2018). For Greenland, the rate of loss increased from 8 ± 82 Gt yr^{-1} to 247 ± 15 Gt yr^{-1} over the same time interval (Bamber et al., 2018). The corresponding contribution to sea level rise from both ice sheets combined increased from 0.16 ± 0.3 mm yr^{-1} to 1.24 ± 0.1 mm yr^{-1} (Meredith et al., 2019). In Greenland, mass loss is primarily driven by changes to the surface mass balance (SMB) of the Ice Sheet, dominated by increased surface melt and runoff, and dynamic thinning (acceleration)

of glaciers (Andersen et al., 2015; Van den Broeke et al., 2016; King et al., 2018). In Antarctica, mass changes are also a result of SMB and dynamic thinning. However, unlike in Greenland, Antarctica's SMB is dominated by increased snowfall which partially offsets the mass loss from dynamic thinning (Meredith et al., 2019; Gardner et al., 2018).

The role of ocean forcing in Greenland remains somewhat uncertain (Straneo et al., 2013), however, there is significant evidence that basal melting of ice shelves is playing a key role in Antarctica's mass loss (Khazendar et al., 2013; Meredith et al., 2019; Cook et al., 2016; Adusumilli et al., 2018; Minchew et al., 2018). Increased basal melting thins ice shelves, reducing their ability to buttress (restrain) the glaciers that feed them. Reduced ice shelf buttressing causes dynamic thinning of these glaciers (Meredith et al., 2019; Dupont and Alley, 2005; Fürst et al., 2016), resulting in a net discharge of ice from the Antarctic Ice Sheet into the ocean. The spatial distribution of basal melting is also important, as some regions of the ice shelf are more important to buttressing than others. For example, some ice shelf fronts are "passive" and can be lost with no dynamic effect (Fürst et al., 2016) while other areas, such as grounding zones, are critical to the stability of the ice sheet (Reese et al., 2018).

Dynamic thinning of the ice sheet is concentrated in the areas closest to the warm, salty, subsurface watermass called circumpolar deep water (CDW) (Rignot et al., 2019). Figs. 1.1, 1.2 from Noble et al. (2020) show the spatial distribution of ice sheet thinning in Antarctica and the ocean bottom-temperature, respectively. The highest rates of mass change coincide with the presence of warm CDW on the continental shelf. Variability in melting in these areas, as well as on the Antarctic Peninsula, is controlled by variability in the depth of the thermocline, which modulates the flow of CDW onto the continental shelf (Paolo et al., 2015; Jenkins et al., 2018; Cook et al., 2016; Roberts et al., 2018). The thermocline depth in turn is driven by wind variability (Thoma et al., 2008; Kimura et al., 2017; Dotto et al., 2019) among other processes. Links between wind variability, ice shelf melting and glacier flow response have also been demonstrated for the Totten Glacier in East Antarctica (Roberts et al., 2018; Greene et al., 2017a).

The response of the Ice Sheet to increased basal melting is sensitive to the geometry of the underlying bedrock, and is subject to dynamical instabilities such as the marine ice sheet instability (MISI) [1], which occurs when ice is grounded on bedrock that slopes downwards

[1]MISI: On a retrograde slope, ice shelf thinning causes grounding line retreat, which drives an increase in the flux of ice across the grounding line. In turn, this increased flux thins the ice margin and causes further grounding line retreat (Weertman, 1974).

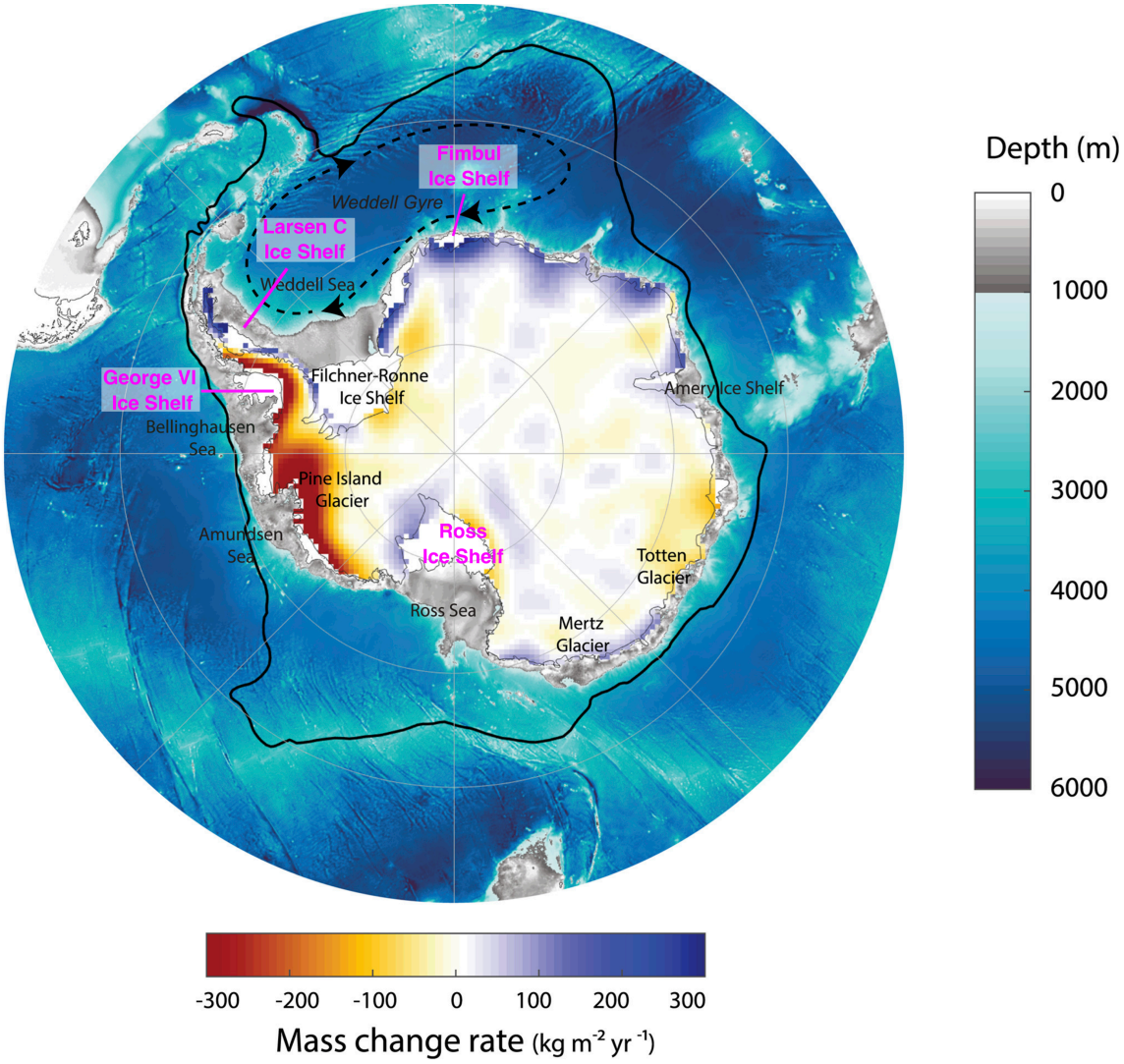

Figure 1.1: The connection between Antarctic ice mass loss and ocean forcing from Noble et al. (2020). Gravimetric Mass Balance data for 2002-2016 shows ice mass changes across the continent. Annotations in magenta have been added to show the locations of ice shelves mentioned in this thesis.

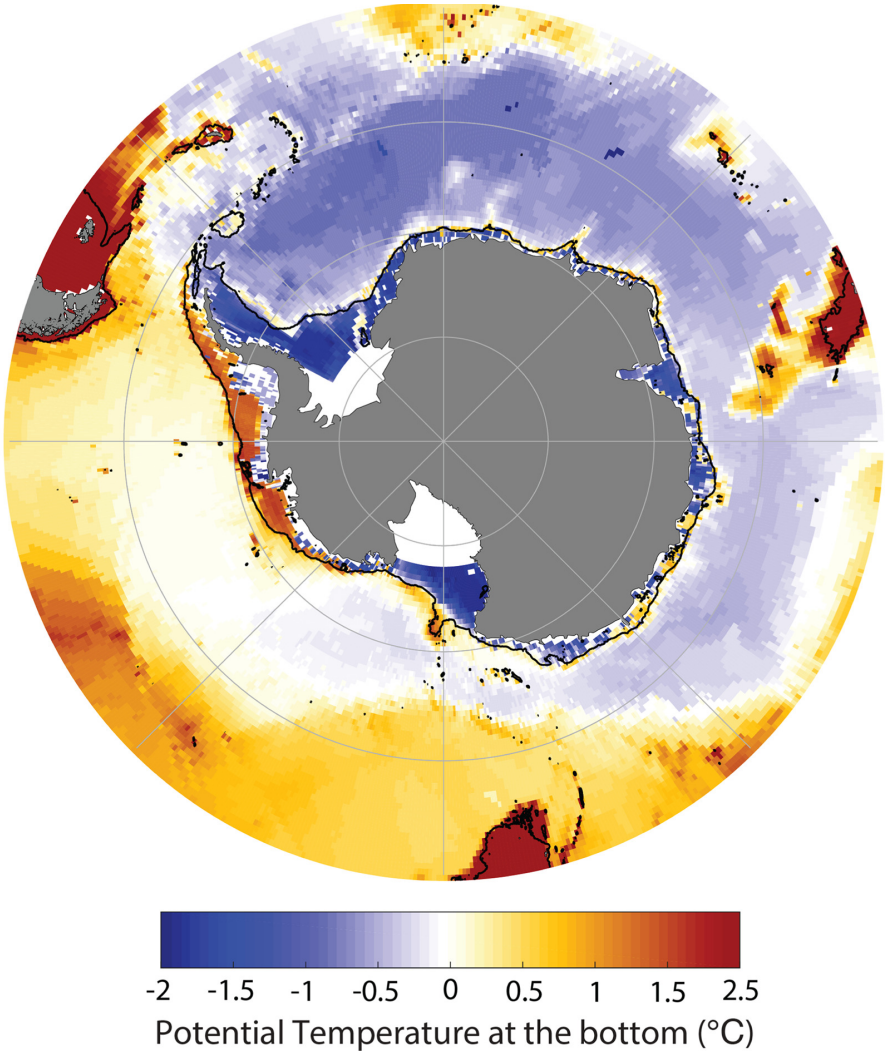

Figure 1.2: The connection between Antarctic ice mass loss and ocean forcing from Noble et al. (2020). Map of the Southern Ocean bottom potential temperature highlights the presences of warmer waters along the West Antarctic margin, based on the WOCE global hydrographic climatology.

moving inland (a "retrograde" slope). Nearly 45% of the Antarctic Ice Sheet is grounded below sea level (Fretwell et al., 2013b), thus many areas are potentially subject to MISI. The timescales for these dynamic ice sheet responses (years–decades) are much longer than the oceanic timescales on which melting varies (months–years). It takes time for thinning signals to propagate inland. Consequently, present day thinning of glaciers may have its origin in past melting events (e.g. Jenkins et al., 2018). Furthermore, the response of individual glaciers to the same forcing depends on their geometry and the stability of their grounding line position (Konrad et al., 2017). In addition, the geometry of the ice shelf cavity affects the ocean circulation (Stern et al., 2014), feeding back into melting. As a consequence of the inter-dependent nature of these processes, coupled ice sheet-ocean models are needed for accurate prediction of the ice sheet response to changes in ocean temperatures, especially over long timescales.

The complex and inter-dependent nature of ice sheet, ice shelf and ocean processes contributes to the deep uncertainty in future sea level contribution from the Antarctic Ice Sheet (van de Wal et al., 2020). Accurate representation of ice shelf-ocean interactions in ocean-climate models is a key challenge for sea level science (Fox-Kemper et al., 2019). Ice-ocean boundary layer processes, including effects of the morphology of the ice, strongly influence heat transport across the ice-ocean interface and the rate of basal melting. Consequently, better understanding and representation of these processes in ocean models is necessary for accurate predictions of the evolution of the Antarctic Ice Sheet (Noble et al., 2020).

1.2 Ice shelf-ocean interactions: large-scale processes and circulation

Basal melting is controlled by ice-ocean interactions on a range of temporal and spatial scales (Dinniman et al., 2016) from large-scale circulation to micro scale ice-ocean boundary layer processes (Gayen et al., 2016; Keitzl et al., 2016b; Vreugdenhil and Taylor, 2019). This section deals with the watermasses, large-scale circulation and shelf processes responsible for basal melting around Antarctica.

The properties of the watermasses that interact with ice shelves are critically important for the magnitude and spatio-temporal variability of basal melting. In the polar ocean, the density of seawater is a strong function of salinity, but only a weak function of tem-

perature due to the smallness of the thermal expansion coefficient at cold temperatures (McDougall and Barker, 2011). Consequently, salinity dominates over temperature in determining the neutral buoyancy depth of a watermass, and it is common to find warmer water at depth. Fig. 1.3 shows the dependence of density on temperature and salinity over a relevant range of ocean conditions.

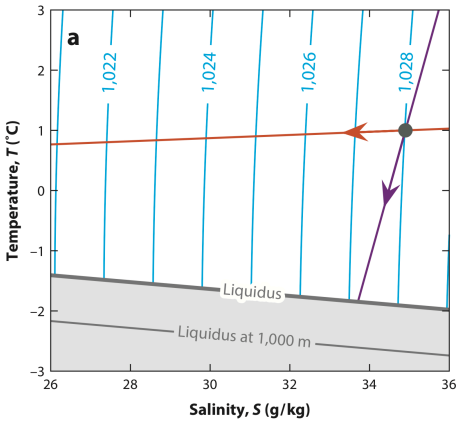

Figure 1.3: Density contours for seawater from Hewitt (2020) at conditions relevant to the polar ocean. The grey lines show liquidus (freezing temperature) curves. The addition of meltwater causes $T - S$ properties to evolve along the purple line, assuming equal eddy diffusivities of heat and salt (e.g. McDougall et al., 2014).

In the Southern Ocean, Ekman divergence upwells a relatively warm, salty watermass known as Circumpolar Deep Water (CDW). In many areas, the ice shelves are shielded from CDW by the Antarctic Slope Front (ASF)[2], which provides a dynamic barrier separating the relatively the cold, fresh water on the continental shelf from the warmer saltier water offshore (eg. Fig 1.4A). However, factors such as deep shelves, a weak ASF (e.g. Fig. 1.4C & D) or bathymetric features such as troughs and canyons cutting across the continental shelf provide routes by which CDW can access ice shelves (e.g. Wählin et al., 2010; Morrison et al., 2020). In coastal areas of Antarctica "Shelf Water", characterised by temperatures close to the surface freezing point, is prevalent. At the sea surface, salt rejection during sea ice formation in wintertime densifies the surface waters and drives deep convective mixing forming "Dense" or "High Salinity" Shelf Water (DSW/HSSW). The lightest watermass on the continental shelf is Antarctic Surface

[2]The ASF is a persistent cross-slope density gradient, with density surfaces (isopyncals) that dip down on the approach to the continental shelf. The ASF is associated with the Antarctic Slope Current (ASC), which flows along the continental shelf.

Water (AASW). A product of sea ice-melt and seasonal solar heating, AASW is relatively warm and fresh. Finally, Ice Shelf Water (ISW) is produced by the interactions between ice shelves and the ocean at depth and is characterised by temperatures lower than the surface freezing point. This is possible due to the depression of the freezing point temperature with pressure; for every km of depth the freezing point lowers by ~ 0.75 K (Fofonoff and Millard, 1983) as shown in Fig. 1.3.

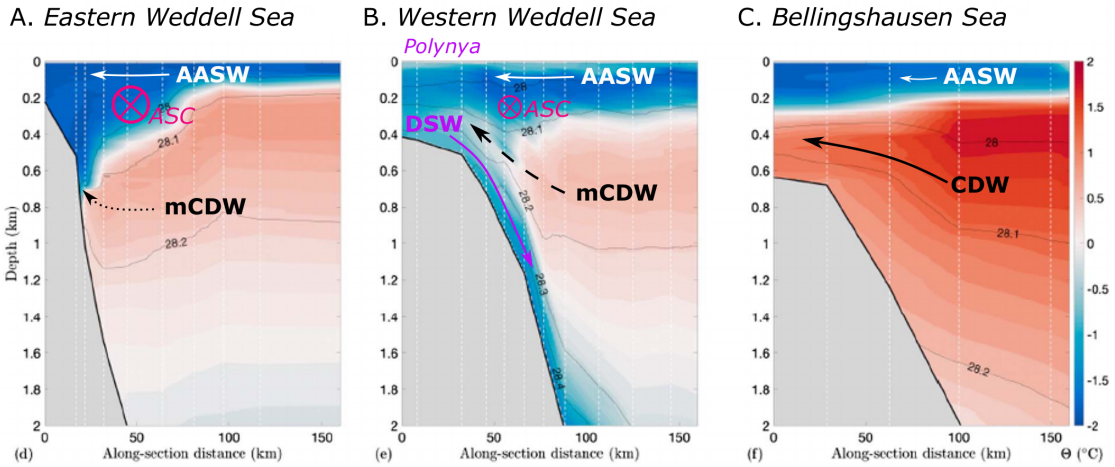

Figure 1.4: The Antarctic Slope Front. (A–C) Different shelf types via density (black contours) and temperature (shading) along three different sections. This figure is reproduced from Figs. 3d–f from Thompson et al. (2018), annotations were added *a posteriori* for clarity and are based on Figures 3a–c from Thompson et al. (2018). Sections originate from Heywood and King (2002); Thompson and Heywood (2008); Orsi and Whitworth (2005).

The presence and geometry of ice shelves exerts a unique influence on the underlying ocean. The ocean beneath an ice shelf is shielded from wind stress, yet subject to strong buoyancy forcing both near the surface and at depth through thermodynamic interaction with the ice shelf (Williams et al., 1985). As the densest watermass on the Antarctic continental shelf, DSW can access the deepest parts of the ice shelf cavity (Fig. 1.5). Ice shelf cavities flooded with DSW are called cold cavity or "mode 1" ice shelves (Jacobs et al., 1992). Many of the largest ice shelves, such as the Ross, Filchner-Ronne and Amery Ice Shelves are cold cavity ice shelves. While melt rates are typically low in these cavities, the pressure dependence of the freezing temperature means that even watermasses at the surface freezing temperature (~ -1.9 °C) can drive high melting at depth. For example, at the 2200 m-deep grounding line of the Amery Ice Shelf the freezing temperature is

depressed by almost 2°C, resulting in melt-rates that exceed 30 m yr^{-1} (Galton-Fenzi et al., 2012). The resulting meltwater mixes with the ambient ocean, forming buoyant Ice Shelf Water which ascends the underside of the ice shelf. The cavity-scale circulation associated with the inflow of DSW, melting at depth and the outflow of ISW is known as the ice-pump (Lewis and Perkin, 1986). At some point, the ascending ISW may become colder than the *in situ* freezing point, allowing frazil ice to form and accumulate on the underside of the ice shelf (Fricker et al., 2001; Craven et al., 2009; Herraiz-Borreguero et al., 2013).

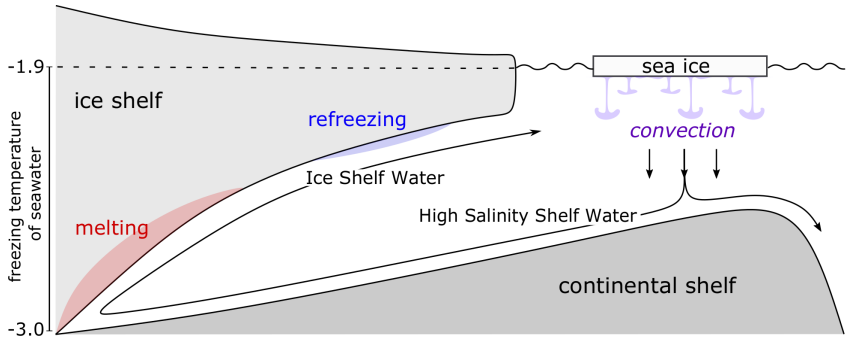

Figure 1.5: Idealised schematic of processes operating in an ice shelf cavity at cold or "mode 1" conditions. Fig. adapted from Stern et al. (2014).

Warm cavity or "mode 2" melting is driven by modified CDW (mCDW). Despite being modified by mixing with colder watermasses as it intrudes onto the continental shelf, mCDW is still warm (~ 0 °C) when it enters the ice shelf cavity. Because CDW resides at depth, the pressure dependence of the freezing temperature gives it even greater melting potential. Consequently, warm cavities exhibit the highest melt rates (Rignot et al., 2019). Mode 2 melting is prevalent in West Antarctica (Cook et al., 2016; Jacobs et al., 2011; Jenkins et al., 2018), however, factors such as wide or shallow continental shelves, or a deep thermocline, tend to protect East Antarctic ice shelves from mCDW, with exceptions such as the Totten Glacier Ice Shelf (Roberts et al., 2018) and Shirase Ice Tongue (Hirano et al., 2020). "Mode 3" or shallow melting is driven by Antarctic Surface Water (AASW), another relatively cold watermass. In wintertime and at depth, AASW is at surface freezing temperature ($T \sim -1.9$ °C) and drives low melt rates much like DSW. However, in summertime, AASW is warmed by interaction with the atmosphere and drives much higher melt rates in the shallower parts of the cavity (Arzeno et al., 2014; Stewart et al., 2019).

1.3 Ice shelf-ocean interactions: the ice shelf-ocean boundary layer

Basal melting is limited by the rate of transport of both heat and salt through the oceanic boundary layer beneath an ice shelf. At the stationary ice-ocean interface, both ocean velocity and turbulent fluctuations go to zero. Thus, the transport of heat and salt must occur by molecular diffusion alone. Outside of this diffusive layer, turbulent transport dominates. The source of this turbulence may be shear instability due to friction between the ocean and ice (e.g. Davis and Nicholls, 2019; Vreugdenhil and Taylor, 2019) or convection due to the buoyancy supplied by meltwater (e.g. Kerr and McConnochie, 2015; Gayen et al., 2016). An extensive review of the roles of current shear and convection in ice-ocean interactions can be found in Malyarenko et al. (2020). For a sloping ice shelf, buoyant meltwater drives a turbulent plume up-slope (McConnochie and Kerr, 2018; Mondal et al., 2019), while for a flat or quasi-flat ice shelf, meltwater tends to stratify the boundary layer and suppress turbulence (McPhee, 1994; Vreugdenhil and Taylor, 2019). In this section we describe the thermodynamic conditions at the ice-ocean interface, outline physical models of the ice shelf-ocean boundary layer, and discuss insights from laboratory and high-resolution modelling studies.

1.3.1 Melting and the ice-ocean interface

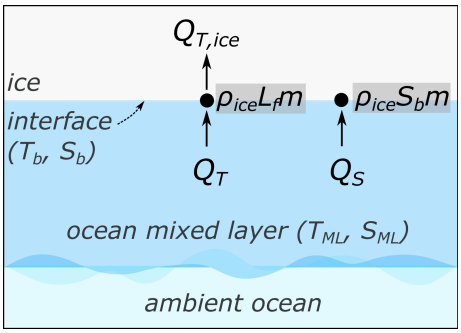

Figure 1.6: Schematic of the ice-ocean system showing the balance of heat and salt at the ice-ocean interface.

At thermodynamic equilibrium, the ice-ocean interface temperature (T_b) and salinity (S_b) satisfy the freezing temperature (liquidus) relationship:

$$T_b = T_f(S_b, p_b), \tag{1.1}$$

where T_f is the freezing temperature and p_b is the interface pressure (see Fig. 1.3). Heat and salt fluxes from the ocean to the interface (Q_T, Q_S) are balanced by latent heat (Q_{latent}) and brine (Q_{brine}) fluxes from melting and, for heat, conductive fluxes away from the interface within the ice $Q_{T,ice}$, as shown in Fig. 1.6. These balances are expressed as:

$$Q_{latent} = Q_T - Q_{T,ice} \tag{1.2}$$

$$Q_{brine} = Q_S \tag{1.3}$$

where $Q_{latent} = L_f m \rho_i$, $Q_{brine} = S_b m \rho_i$, m is the melt rate, L_f is the latent heat of freezing and ρ_i is the ice density. The volume input of water due to ice melt is assumed to be zero, based on the expectation that the melt rate is extremely small with respect to ocean velocities (Holland and Jenkins, 1999). The ice salinity is also assumed to be zero, as is typical for ice shelves (Oerter et al., 1992). These flux balance equations can be solved alongside the liquidus relationship for the interface conditions m, T_b and S_b. Heat conduction into the ice shelf can be incorporated by modelling the steady state temperature profile within the ice (Holland and Jenkins, 1999), however, the oceanic flux terms are poorly constrained. This system of equations, often called the "three-equation parameterisation", was first applied by Hellmer and Olbers (1989) and is still used today. However, the details of the ocean flux parameterisations have evolved from constant rates of heat and salt diffusion (Hellmer and Olbers, 1989; Determann and Gerdes, 1994) to current speed dependent models in which heat and salt transfer are represented by empirical functions (Jenkins, 1991; McPhee et al., 1987) or observationally-constrained coefficients (Jenkins et al., 2010b). Here, we will explore the physical basis of these formulations.

1.3.2 The frictional ice shelf-ocean boundary layer

Typically, the ice shelf-ocean boundary layer (ISOBL) refers to the frictional boundary layer that forms adjacent to the (stationary) ice due to a mean flow or current. The presence of Coriolis gives the boundary layer a natural depth scale which depends on the Coriolis frequency (f) and the strength of the turbulence which is characterised by the friction velocity (u^*), a function of shear stress at the interface ($u^* = \sqrt{\overline{\tau_w/\rho_0}}$). In an unstratified environment this scale, often called the planetary scale, is given by $\delta_f \sim u^*/f$ (e.g. McPhee, 2008). Beneath ice shelves, the planetary scale is on the order of 10 m.

Within the boundary layer there are several distinct regions (Fig. 1.7). Close to the ice

is the viscous sublayer, a region of laminar flow. The thickness of the viscous sublayer is proportional to the viscous scale $\delta_\nu \sim \nu/u^*$ which depends on molecular viscosity ν and friction velocity u^*. Within the viscous sublayer the velocity scales with distance from the ice ($u(z) \sim zu^*/\nu$). Analogous to the viscous sublayer, diffusive sublayers for temperature (T) and salinity (S) form adjacent to the ice-ocean interface. The molecular diffusivities of heat (κ_T) and salt (κ_S) are smaller than molecular viscosity; the Prandtl and Schmidt numbers are $Pr = \nu/\kappa_T \sim 14$ and $Sc = \nu/\kappa_S \sim 2500$ respectively. Consequently the diffusive boundary layers for heat and salt are thinner than than the viscous sublayer.

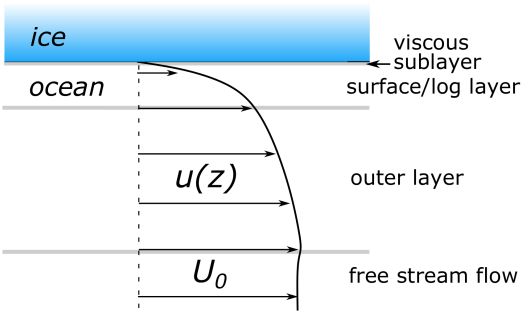

Figure 1.7: A frictional ISOBL consists of a viscous sublayer, surface or "log" layer and a turbulent outer layer. In systems where planetary rotation (Coriolis) is important, the boundary layer depth is expected to scale with the Planetary scale (δ_f).

The surface or log layer occupies the ∼20% of the turbulent Ekman layer nearest the ice. Within the surface layer, the size of the turbulent eddies increases with distance from the solid ice-ocean boundary. Vertical shear is inversely proportional to the distance from the surface (z) and proportional to the friction velocity as:

$$\frac{\partial u}{\partial z} \sim \frac{u^*}{z} \tag{1.4}$$

(e.g. Pope, 2001). Integrating this relationship vertically yields a logarithmic scaling of velocity with height:

$$u(z) = \frac{u^*}{k} \ln \frac{z}{z_0} \tag{1.5}$$

where $k = 0.41$ is the von-Karman's constant and z_0 is the roughness lengthscale.

The assumption of similarity between velocity and scalar profiles follows from Monin-Obukhov (MO) similarity theory, which is commonly applied to wall-bounded stratified shear flows. Based on similarity, expressions for heat and salt transfer coefficients

(Γ_T, Γ_S) are derived based on the dynamics of the surface layer (Kader and Yaglom, 1972). These transfer coefficients relate the total heat and salt transfer across the boundary layer to the mean properties of the flow. Coefficients Γ_T and Γ_S are given by:

$$\Gamma_T = (2.12 \ln(u^* h/\nu) + 12.5 Pr^{2/3} - 9)^{-1} \tag{1.6}$$

$$\Gamma_S = (2.12 \ln(u^* h/\nu) + 12.5 Sc^{2/3} - 9)^{-1}. \tag{1.7}$$

Because of the appearance of Pr and Sc the heat transfer coefficient is larger than that for salt ($Sc > Pr$, therefore $\Gamma_T > \Gamma_S$). These expressions also have a functional dependence on a Reynolds number ($Re = u^* h/\nu$), which compares viscous and inertial forces, using the friction velocity u^* and boundary layer depth h. Using Γ_T and Γ_S, Jenkins (1991) formulated expressions for the oceanic heat and salt fluxes Q_T and Q_S, allowing Eqs. 1.1–1.3 to be solved for interface conditions T_b, S_b and m. Assuming boundary layer turbulence produces a well-mixed layer in temperature and salinity adjacent to the ice, Jenkins (1991) set the heat flux as proportional to the product of the friction velocity u^*, the temperature difference between the interface T_b and the mixed layer T_{ML}, and a thermal exchange coefficient Γ_T, with an equivalent expression for salinity:

$$Q_T = c_p \rho \Gamma_T u^* (T_{ML} - T_b) \tag{1.8}$$

$$Q_S = \rho \Gamma_S u^* (S_{ML} - S_b) \tag{1.9}$$

Under the assumption of hydraulically smooth ice[3] While Eqs. 1.6 and 1.7 have a solid basis in empirical studies, there have been few occasions to test the functional form of these expressions beneath melting sea ice, and none beneath ice shelves. Sea ice- and ice shelf-ocean interactions differ in that ice shelves are stationary while sea ice moves under wind stress, independently of the ocean currents beneath it. Heat flux measurements made beneath smooth melting sea ice do not support the Reynolds number dependence of Eqs. 1.6 and 1.7. Instead, McPhee et al. (1999) found that a constant transfer coefficient was more appropriate[4].

[3]A hydraulically smooth boundary is one for which the interface roughness is thinner than the laminar sublayer of the flow. In this case $z_0 \sim 5\delta_\nu$ in Eq. 1.5.

[4]This work used a reduced "two-equation" formulation which, instead of solving for the interface temperature, considers the temperature difference between the mixed layer and the local freezing temperature at mixed layer salinity and interface pressure.

Buoyancy effects on the frictional ice shelf-ocean boundary layer

Thus far we have not considered the effect of buoyancy on the dynamics of the ISOBL. The addition of meltwater cools and freshens the ocean beneath the ice. With respect to density, meltwater is less dense than the ambient ocean, and will tend to stratify or stabilise the water column. Meltwater therefore constitutes a stabilising flux of buoyancy at the ice-ocean interface. For flow that is strongly affected by stratification, the velocity profile in the surface layer is expected to depart from a simple logarithmic relationship. Monin-Obukhov similarity theory extended for stratified shear flow allows the velocity shear to be expressed as a function of the distance from the ice base, z, divided by the Obukhov lengthscale, L (Monin and Obukhov, 1954), where the Obukhov length is an estimate of the distance away from the ice where stratification starts to dominate the flow (Obukhov, 1946). The velocity gradient is given by:

$$\frac{\partial u}{\partial z} \sim \frac{u^*}{z} f\left(\frac{z}{L}\right) \tag{1.10}$$

where the Obukhov lengthscale is given by $L = u^{*3}/(kB)$ where B ($\mathrm{m^2\ s^{-3}}$) is the surface buoyancy flux (Obukhov, 1971). For a stabilising buoyancy flux, the Obukhov lengthscale compares the roles of shear and buoyancy in the production/suppression of turbulence, where a large, positive L indicates that the flow is unaffected by stabilising buoyancy. This expression (1.10) implies that stratification is affecting the mixing length, or the maximum vertical distance over which eddies can diffuse momentum (McPhee, 1994).

Including the effects of both rotation and stratification, McPhee et al. (1987) developed expressions for heat and salt transfer beneath sea ice, which have since been applied to ice shelves (e.g. Holland and Jenkins, 1999). The effects of rotation and stratification are encapsulated in the stability parameter (η), which is given by:

$$\eta = \left(1 + \frac{\xi u^*}{f L R_c}\right)^{-1/2}, \tag{1.11}$$

where f is the Coriolis parameter and $\xi = 0.052$ and $R_c = 0.2$ are constants. Assuming a hydraulically smooth interface, the transfer coefficients from McPhee et al. (1987) can be expressed as:

$$\Gamma_T = \left(\frac{1}{k}\ln\left(\frac{u^*\xi\eta^2}{f h_\nu}\right) + \frac{1}{2\xi\eta} + 12.5 Pr^{2/3} - 8.5\right)^{-1} \tag{1.12}$$

$$\Gamma_S = \left(\frac{1}{k}\ln\left(\frac{u^*\xi\eta^2}{f h_\nu}\right) + \frac{1}{2\xi\eta} + 12.5 Sc^{2/3} - 8.5\right)^{-1} \tag{1.13}$$

following Holland and Jenkins (1999). In these expressions, $h_\nu \sim 5\delta_\nu$ is the viscous sublayer thickness. Because L is a function of the surface buoyancy flux due to melting, Eqs. 1.1–1.3 must be solved iteratively for the melt rate.

For large L, when the flow is relatively unaffected by buoyancy, the stability parameter $\eta \to 1$ and the transfer coefficient formulations 1.12 and 1.13 are equivalent to 1.6 and 1.7. Despite many ocean models implementing 1.12 and 1.13 to parameterise melting, it is common practise to set $\eta = 1$ (e.g. Galton-Fenzi et al., 2012; Gwyther et al., 2016; Naughten et al., 2018b). Holland and Jenkins (1999) showed that the stability parameter made less than a 10% difference to the predicted melt rate for temperatures less than 0.5 °C above the freezing temperature and friction velocities greater than 0.1 cm s^{-1} (corresponding to a free stream flow of ∼2 cm s^{-1}). However, subsequent work suggests that neglecting the effect of stratification on boundary layer dynamics could cause melt rates to be significantly overestimated. In high resolution numerical simulations, Vreugdenhil and Taylor (2019) showed that stratification is extremely important in determining the transfer across the ISOBL. They found that transfer coefficients Γ_T and Γ_S depend on the frictional Obukhov lengthscale[5] (L^+). At relatively warm, low u^* conditions, which correspond to low L^+, they found that the efficiency of heat and salt transfer decreased, melt rates were suppressed and the boundary layer was overall more stratified. This study considered only the surface layer, and did not include the effects of rotation. Further work is required to understand rotation, buoyancy and the usefulness of the stability parameter η.

Friction velocity and the effects of interfacial roughness

The friction velocity u^* appears in the expressions for the oceanic heat and salt fluxes (Eqs. 1.8 and 1.9). However, in practise, u^* is not carried in an ocean model and must be expressed as a function of the mean flow speed U_0 some distance from the ice base. Assuming a quadratic relationship between the shear stress and the mean flow $\tau = \rho_0 C_d U_0^2$, where C_d is the dimensionless drag coefficient, gives an expression for u^* in terms of the mean flow $u^* = \sqrt{C_d} U_0$. In reality, C_d also depends on the roughness of the ice-ocean interface, which can exert more drag on the ocean current than a hydraulically smooth ice base. However, C_d is extremely poorly constrained beneath

[5]The frictional Obukhov lengthscale (L^+) is the ratio of the Obukbov lengthscale to the viscous scale $L^+ = L/\delta_\nu$ and determines whether any portion of the flow is unaffected by either stratification or viscosity.

ice shelves. In keeping with the assumption of hydraulically smooth ice, relatively low drag coefficients in the range C_d =0.0015–0.003 are typically implemented in ice-ocean models (e.g. MacAyeal, 1984; Gwyther et al., 2015; Naughten et al., 2018b).

There have been extremely few opportunities to investigate this assumption. Beneath the Filchner-Ronne Ice Shelf at melting conditions Davis and Nicholls (2019) reported a value of $C_d = 0.0022$. Observations beneath melting sea ice have yielded values of C_d in the range 0.002–0.009 (e.g. McPhee, 1992). Recent studies of the sea ice-ocean boundary layer have found values up to two orders of magnitude larger than this for regions where platelet ice (the sea ice analogue to marine ice) is present (Robinson et al., 2017), thus we expect that C_d may also be considerably higher beneath marine ice than in melt zones on ice shelves.

1.3.3 Convection-driven melting

The ice-ocean parameterisations outlined thus far have focused on the case where melting is proportional to the intensity of turbulence generated by current shear. One interpretation of this parameterisation is that the width of the laminar sublayer, across which heat and salt must diffuse, is controlled by the shear stress exerted by the flow (Wells and Worster, 2008; McConnochie and Kerr, 2017a). However, this is not the only possible mechanism. In the case of a vertical or sloping ice shelf, buoyant instability of the sublayer itself could instead play this role (Wells and Worster, 2008). In this paradigm, buoyant meltwater drives a plume up the slope and along the ice (Fig. 1.8) as investigated in laboratory and high resolution numerical studies of a melting, vertical or sloping ice shelf (Josberger and Martin, 1981; Kerr and McConnochie, 2015; Gayen et al., 2016; McConnochie and Kerr, 2018; Mondal et al., 2019). Kerr and McConnochie (2015) and Gayen et al. (2016) showed that the melt rate of vertical ice m_v depends upon the thermal driving T^* (the difference between the ambient temperature and the local pressure and salinity dependent freezing temperature) as $m_v \sim T^{*4/3}$ and is independent of the plume velocity. McConnochie and Kerr (2018) and Mondal et al. (2019) extended this result to sloping ice, independently determining that the melt rate for sloping ice (m_s) was proportional to m_v scaled by the basal slope angle from the horizontal (θ) as $m_s \sim m_v \sin^{2/3}\theta$. While the $\sin^{2/3}\theta$ dependence of the melt rate on slope angle was only demonstrated experimentally for $\theta > 50°$, the simulations showed that this relationship holds down to $\theta = 10°$. The effect of ambient stratification on melting has also been investigated

in a laboratory setting. McConnochie and Kerr (2016a) showed that stratification has a strong influence on convectively-driven melting and plume velocity when the ambient stratification is large compared to the plume buoyancy flux.

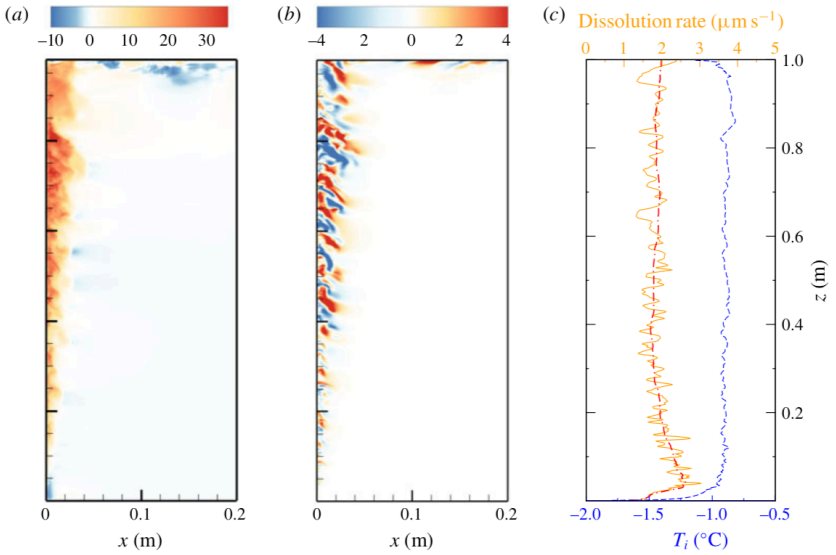

Figure 1.8: Direct numerical simulation of convective melting of a vertical ice face from Gayen et al. (2016). Panels are (a) vertical velocity w, (b) horizontal velocity u and (c) melt (dissolution) rate and interface temperature (T_i).

As the buoyant plume accelerates, it is anticipated that shear will become increasingly important and a transition may occur between convective and shear dominated melting (Wells and Worster, 2008). Because of the small physical scale of the laboratory and numerical experiments conducted thus far, this transition has not yet been observed. However, McConnochie and Kerr (2017a) suggest that a transition from a convectively-controlled to a shear-controlled diffusive sublayer is expected above a critical velocity in the range 2–4 cm s^{-1} for a vertical ice face at $T^* \sim 0.5$ °C, based upon their empirical melting parameterisation and a critical Rayleigh number argument. The effects of slope angle and stratification are not taken into account in this critical speed. A recent review paper by Malyarenko et al. (2020) used observational data to estimate a critical Reynolds number for the transition from convective to shear-controlled melting. Based upon the ability of shear and convective parameterisations to represent observed melt rates beneath the Filchner-Ronne and Ross Ice Shelves, Malyarenko et al. (2020) suggest that this transition occurs at $Re_\delta = W\delta/\nu = 20$, where δ is the molecular sublayer thickness

and W is the velocity at the edge of that sublayer.

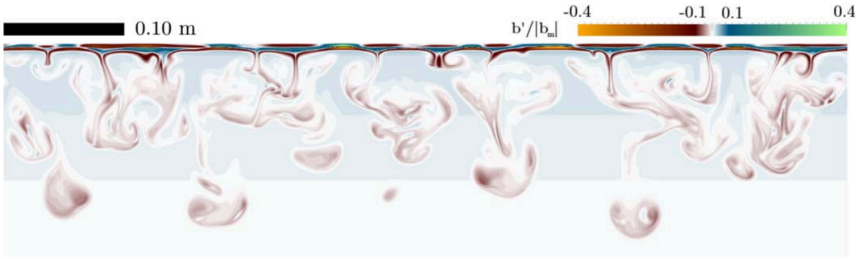

Figure 1.9: Direct numerical simulation of double-diffusive convection (semiconvection) beneath melting ice from Keitzl et al. (2016b). Colour shows normalised buoyancy.

Beneath a flat ice shelf, stabilising buoyancy from melting cannot drive a mean flow. Experimental and direct numerical simulation (DNS) studies have investigated melting of flat ice at quiescent (zero mean flow) conditions. In this case, the boundary layer is characterised by a diffusive sublayer near the ice with a gravitationally unstable boundary layer beneath it and a deeper region of convection below (Martin and Kauffman, 1977; Keitzl et al., 2016b). For a flat ice-ocean interface, the buoyancy supplied by melting at Antarctic conditions is stabilising. However, a type of convection known as double-diffusive or 'semi-' convection can occur. Double-diffusive convection is a consequence of the rapid diffusion of heat (κ_T) compared to salt (κ_S) which allows the thermal diffusive boundary layer to grow more quickly than than its saline counterpart, creating an unstable density boundary layer and driving convection. Both Martin and Kauffman (1977) and Keitzl et al. (2016b) found that the diffusive region near the ice grew in time, resulting in time-dependent fluxes to the ice-ocean interface. Fig. 1.9 shows convective plumes caused by double diffusion beneath melting ice (Keitzl et al., 2016b). Small-scale convective processes such as double-diffusive convection and buoyant plumes are not resolved or well-parameterised in regional ocean models, and thus their effect on melting and cavity-scale circulation is not accounted for.

1.4 Observations beneath ice shelves

Observations from within ice shelf cavities are relatively sparse due to the difficulty of accessing the ocean through hundreds of meters of ice. Available observations show a broad range of environmental conditions. Here, we focus on the observations relevant to

melting and the ISOBL, such as the temperature, salinity and stratification, the strength and drivers of currents near the ice, the roughness and slope of the ice base, and evidence of turbulence intensity and mixing.

Amongst the ice shelves classified as "cold cavity", a wide variety of conditions have been observed. Boreholes drilled through the Filchner-Ronne Ice Shelf show cold conditions, low stratification, strong tidal currents and melt rates on the order of 1 m yr $^{-1}$ (Jenkins et al., 2010b; Nicholls, 2018). Similar conditions have been observed beneath the Larsen C Ice Shelf (Davis and Nicholls, 2019), where turbulence measurements from within the ISOBL show that buoyant meltwater does not play a strong role in the boundary layer turbulence at these conditions. Beneath the Amery Ice Shelf, another cold cavity ice shelf, significant zones of refreezing have been observed. The western flank of the ice shelf is characterised by a thick, well mixed boundary layer, negative thermal driving (i.e. "supercool" water with temperature colder than the *in situ* freezing temperature) and the presence of accreted frazil ice (ice crystals that form within the water column and settle on the underside of the ice shelf; Herraiz-Borreguero et al., 2013).

Cold temperatures are also typical of the interior of the Ross Ice Shelf cavity, where observations show temperatures within ~ 0.01°C of the *in situ* freezing temperature near the ice base (Stevens et al., 2020). Measurements made in the 1970s show a well mixed boundary layer (Foster, 1983) and slow refreezing on the order of 2 cm yr^{-1} (Zotikov et al., 1980). More recent observations found a similar well-mixed boundary layer and marginal intermittent melting/freezing conditions (Stevens et al., 2020). Melting is much stronger at the front of the RIS due to the influence of seasonally warmed surface waters (Arzeno et al., 2014; Stewart, 2018; Stewart et al., 2019). Here, ocean temperatures in the range 0.1–1°C above the *in situ* freezing temperature drive melt rates of several meters per year (Stewart et al., 2019). Seasonal variation in melting is also a feature of the Fimbul Ice Shelf, where temperatures vary seasonally from supercool in winter to above freezing in summer, when fresh surface waters enter the cavity (Hattermann et al., 2012).

Beneath the Pine Island Ice Shelf, CDW is present and consequently thermal driving is high (~ 1.5 °C). Concurrent measurements also showed relatively strong, steady flow (10–15 cm s^{-1}) and high melt rates ($\sim$15 m yr^{-1}) (Stanton et al., 2013). The steady flow is attributed to a buoyant meltwater plume based on the density structure and the basal slope of the ice. Another warm, CDW-flooded cavity is the George VI ice shelf. Despite being subject to even larger thermal driving (~ 2.3 °C) than Pine Island Ice

Shelf, George VI melt rates are an order of magnitude lower. As well as low melt rates, a diffusive convection-favorable thermohaline staircase was observed (Kimura et al., 2015). Thermohaline staircases are the hallmark of double-diffusive convection. The remarkable difference in melt rates between the Pine Island and George VI Ice Shelf cavities may be attributed to the presence of a basal slope and associated turbulent plume at the Pine Island Ice Shelf site, as compared to the flatter, more highly stratified George VI Ice Shelf site. Observations from the grounding line of the Ross Ice Shelf suggest that stratification effects are not limited to CDW-affected, high thermal driving locations. At this grounding zone site, which was characterised by low-moderate thermal driving (~ 0.1 °C) due to the presence of DSW and weak currents (~ 1 cm s^{-1}), the thermohaline structure was suggestive of double-diffusive convection (Begeman et al., 2018).

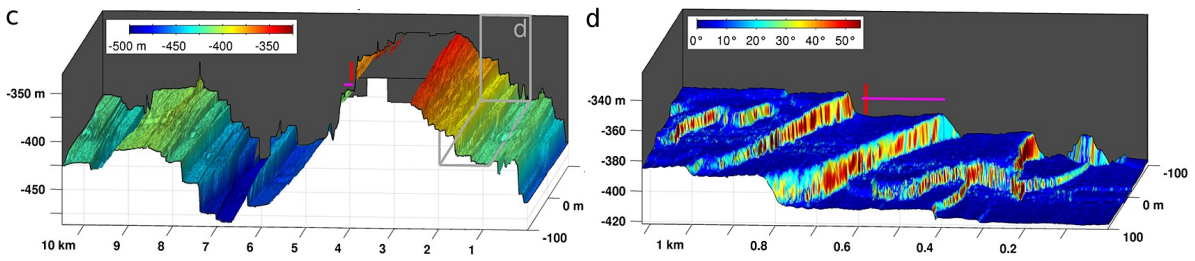

Figure 1.10: Ice base geometry under Pine Island Glacier ice shelf from Fig. 2 of Dutrieux et al. (2014). (c) Basal elevation (color) of a longitudinal channel. (d) Basal slope angle from horizontal in the area indicated in (c).

The morphology of the underside of the ice shelf is also crucial to melting and flow on both large and small scales. With respect to the slope of the ice base, Antarctic ice shelves have small aspect ratios (vertical/horizontal lengthscales of $\sim 2/100$ km) corresponding to a small overall basal slope ($\theta < 1°$). However, on smaller scales, steep slopes have been observed associated with terraces and channels in the ice base (e.g. Jenkins et al., 2010a; Stanton et al., 2013; Dutrieux et al., 2014), as is shown in Fig. 1.10. These features are certain to influence basal melting, and some may be formed or reinforced through melting. Features at even smaller spatial scales may affect melting by increasing the roughness of the ice base, which is expected to increase the heat flux to the ice (Gwyther et al., 2015). However, no observational studies to date have investigated the effect of roughness on basal melting of ice shelves.

Another crucial set of observations for understanding the ISOBL are turbulence quantities such as dissipation (ϵ). However, only a handful of measurements of turbulence

dissipation have been made beneath Antarctic ice shelves. Beneath the Pine Island Ice Shelf a large spatial survey was conducted, finding average and maximum values of $\epsilon = 3 \times 10^{-9}$ W kg^{-1} and 6.2×10^{-8} W kg^{-1} respectively near the ice (Kimura et al., 2016). Within the cold, tidally-dominated boundary layer beneath Larsen C Ice Shelf dissipation values in the range 10^{-9}–10^{-6} W kg^{-1} were measured (Davis and Nicholls, 2019), while Venables et al. (2014) reported much lower dissipation values from beneath George VI Ice Shelf ($\sim 4 \times 10^{-10}$ W kg^{-1}). This latter value is consistent with the observation of a thermohaline staircase beneath the George VI Ice Shelf, as thermohaline staircases are not expected to coexist with strong turbulence (Radko, 2013; Shibley et al., 2017).

These observations have revealed a wide range of cavity environments and phenomena that challenge the assumption, inherent in common ice-ocean parameterisations, of a well-mixed, turbulent boundary layer formed by flow over smooth, melting ice. Crucially, observations of features such as thermohaline staircases (Kimura et al., 2015; Begeman et al., 2018), buoyant plumes and near-ice stratification (Stanton et al., 2013) suggest that the role of buoyancy in melting, mixing and circulation beneath Antarctic ice shelves has thus far been underestimated and requires further study.

1.5 Thesis objectives and outline

The preceding text has shown that ocean-driven melting of ice shelves is a leading cause of mass loss from Antarctica and is crucial to ice sheet stability and global sea level. Furthermore, efforts to predict the melting response of Antarctic ice shelves to a warming ocean are undermined by poor understanding of the small-scale ice-ocean boundary layer processes that control melting. This thesis seeks to address this knowledge gap by characterising melting and ISOBL dynamics across a broad range of ocean states. The aims of this thesis are to:

- Describe and contextualise the processes influencing basal melting of the Amery Ice Shelf
- Evaluate the performance of common ice-ocean parameterisations in reproducing observed melt rates beneath the Amery Ice Shelf using *in situ* ocean data
- Develop an idealised model configuration of the rotationally and buoyancy affected

ISOBL guided by and evaluated against available data from within ice shelf cavities

- Investigate the ISOBL under a variety of conditions, especially warm and/or quiescent conditions for which existing parameterisations perform poorly
- Determine the physical relationships between melting and ocean state in different ISOBL "regimes" and develop the capacity to predict the conditions under which these regimes apply to different Antarctic ice shelves.

The following chapters of this thesis are organised as follows. **Chapter 2** presents a unique set of observations from beneath the Amery Ice Shelf, including *in situ* basal melt rate and ocean conditions, and evaluates existing ice-ocean parameterisations using this dataset. **Chapter 3** introduces the numerical model of the ISOBL, and shows that double-diffusive convection determines ice shelf melt rates and mixed layer properties at relatively warm, low velocity conditions. **Chapter 4** extends the model forcing conditions to encompass colder and more energetic cavity environments in which the current shear controls the melt rate. The transition from well mixed to stratified conditions, where ISOBL turbulence is strongly affected by buoyancy, is investigated and the effect of near-ice stratification on melting is quantified. **Chapter 5** discusses the results from Chapters 2, 3 and 4 and synthesises both simulation and observational data into a regime diagram. Finally, conclusions and future work are presented in **Chapter 6**.

Chapter 2

Observations of basal melting and ocean circulation beneath the Amery Ice Shelf

Abstract

Ocean driven melting of Antarctic ice shelves is causing grounded ice to be lost from the continent at an accelerating rate. However, the ocean processes governing ice shelf melting are not well understood, contributing to uncertainty in projections of Antarctica's contribution to sea level. Here, we analyse oceanographic data and *in situ* measurements of ice shelf melt collected from an instrumented mooring beneath the Amery Ice Shelf. Results show a moderate annually-averaged melt rate of 0.51±0.18 m yr^{-1}, consistent with modelling results and glaciological estimates, driven by temperatures $\sim$ 0.2 °C above the local freezing point and currents with mean and peak tidal speeds of 5.0 cm s^{-1} and 17.0 cm s^{-1}, respectively. There is significant seasonal variation in melting with a maximum in May and a minimum in September. We analyse coincident measurements of ice shelf melt and oceanographic forcing to constrain the oceanic heat transfer through the ice-ocean boundary layer, and evaluate parameterisations of ice-ocean interactions. We find that parameterisations in which there is an explicit dependence of the melt rate on the speed of the currents beneath the ice tend to overestimate the local melt rate by between 200% and 400%, depending on the drag coefficient assumed. A new convective parameterisation, in which the melt rate depends on the slope of the ice base, is also evaluated and is shown to under-predict melting by 20%. We show that the misfit between current speed-dependent parameterisations of melt rate and observed melt rate is widespread across available observations.

2.1 Introduction

The Antarctic Ice Sheet is losing mass, and raising sea level, at an accelerating rate (Bamber et al., 2018; Shepherd et al., 2018; Meredith et al., 2019). This mass loss is caused by the acceleration of the glaciers that make up the Antarctic ice sheet in response to reduced ice shelf buttressing (Meredith et al., 2019), a process whereby floating ice shelves provide resistance to the flow of grounded ice upstream (Dupont and Alley, 2005; Fürst et al., 2016; Reese et al., 2018). The reduction of ice shelf buttressing is driven primarily by increased sub-ice shelf melting (e.g. Khazendar et al., 2013; Cook et al., 2016; Adusumilli et al., 2018; Minchew et al., 2018). Modelling studies have demonstrated the grounded ice response to enhanced melting is more sensitive in some areas, like grounding zones, than others (Reese et al., 2018). Accurate modelling of both the magnitude and distribution of melt rates is therefore critical for accurately predicting the future sea level contribution from the Antarctic Ice Sheet, which is deeply uncertain at present (Meredith et al., 2019).

Sub-ice shelf melt rates are controlled by ice-ocean interactions involving a range of temporal and spatial scales (Dinniman et al., 2016) from large-scale circulation to micro scale ice-ocean boundary layer processes (Gayen et al., 2016; Keitzl et al., 2016b; Vreugdenhil and Taylor, 2019). Of critical importance to the magnitude, spatial pattern and seasonality of the melt rate are the properties of the watermass/es that intrude into the ice shelf cavity. For example, some ice shelves are flooded by Dense Shelf Water (DSW), a cold ($T \sim -1.9$ °C) watermass generated by sea ice formation. As the densest watermass on the Antarctic continental shelf, DSW can access the deepest parts of the ice shelf cavity, where the pressure dependence of the freezing temperature allows it to drive high melt rates. This is known as mode 1 melting, where three modes were described by Jacobs et al. (1992). Mode 2 is driven by relatively warm Circumpolar Deep Water (CDW; $T \sim 1$ °C) which intrudes onto the continental shelf and, after some modification, into ice shelf cavities where is drives rapid melting. Mode 2 melting is particularly prevalent in West Antarctica (e.g. Cook et al., 2016; Jacobs et al., 2011; Jenkins et al., 2018). However, factors such as wide or shallow continental shelves, or a deep thermocline, tend to protect East Antarctic ice shelves from CDW. Mode 3 melting is driven by Antarctic Surface Water (AASW), another relatively cold watermass. In wintertime and at depth, AASW is at surface freezing temperature ($T \sim 1$ °C) and drives low melt rates much like DSW. However, in summertime, AASW is warmed by interaction with the atmosphere

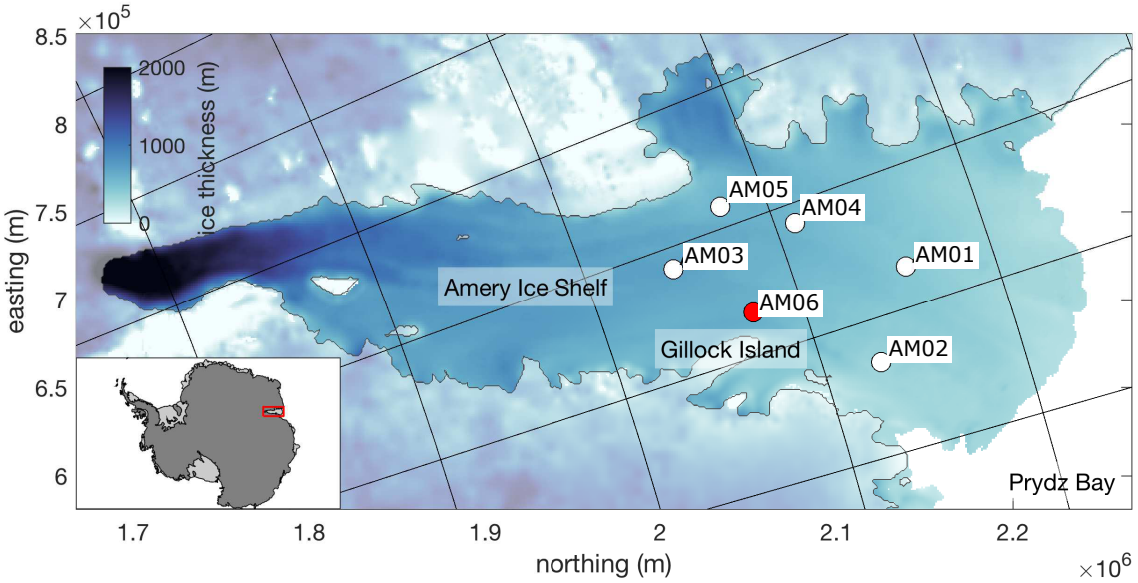

Figure 2.1: Ice thickness map of the Amery Ice Shelf in polar stereographic projection with borehole sites AM01–6 labelled. The floating ice shelf is denoted by the bold colours. Map produced with Antarctic Mapping Tools (Greene et al., 2017b) using the Bedmap2 product (Fretwell et al., 2013a)

and drives much higher melt rates in the shallower parts of the cavity (e.g. Arzeno et al., 2014).

2.1.1 Amery Ice Shelf

The Amery Ice Shelf (AIS) is an embayed ice shelf in East Antarctica which has an area of ∼62,000 km^2 and some of the deepest Antarctic ice (∼2200 m; Fricker et al., 2001) in contact with the ocean. Modelling studies (Williams et al., 2001; Galton-Fenzi et al., 2012) suggest that DSW is present beneath the AIS where it drives moderate melt rates along the eastern flank of the ice shelf cavity. The deep draft of the AIS allows DSW to drive strong melting at the grounding line: a draft of 2,200 m depresses the freezing temperature by almost 2°C, resulting in melt-rates that exceed 30 m yr^{-1} (Galton-Fenzi et al., 2012). These elevated melt rates at the grounding line produce cold, fresh, buoyant melt water called Ice Shelf Water (ISW). The ISW ascends the underside of the ice shelf along the western flank where it becomes colder than the *in situ* freezing temperature, allowing frazil ice to form and accumulate on the underside of the ice shelf (Fricker et al.,

2001; Herraiz-Borreguero et al., 2013). ISW then exits the cavity on the western flank of the AIS at depth (Herraiz-Borreguero et al., 2016; Williams et al., 2016). The inflow of DSW on the eastern flank and the outflow of ISW on the western flank create a cyclonic circulation within the cavity.

A sustained observational campaign has improved our understanding of circulation in Prydz Bay and beneath the AIS. The Amery Ice Shelf-Ocean Research (AMISOR) project has been monitoring the ocean beneath the AIS for nearly two decades (2001-ongoing) (Allison, 2003). The data include oceanographic surveys and moorings from the calving front of the AIS as well as from boreholes in the ice shelf itself. In total, 6 boreholes were drilled through the ice and a variety of data and material was collected including sediments, marine and glacial ice samples and ice temperature measurements. Oceanographic measurements were collected from profiling and the deployment of instrumented moorings for longer-term monitoring (Craven et al., 2004, 2014; Herraiz-Borreguero et al., 2013; Post et al., 2014). These moorings confirmed the presence of both DSW and ISW beneath the ice shelf, but also found that a modified version of CDW was present. Modified CDW (mCDW) was observed entering the cavity at intermediate depths during the austral winter (Herraiz-Borreguero et al., 2015). Coincident observations from under-ice mooring AM02, approximately 70 km southwest of the calving front, shows ISW with a fresher source water mass during this time, suggesting that mCDW drives melting in some areas of the AIS cavity.

Several studies have presented area-averaged melt rate estimates for the AIS, with glaciological studies (Yu et al., 2010; Wen et al., 2010; Rignot et al., 2013; Depoorter et al., 2013) finding values in the range 0.5–0.8 m yr^{-1}, and modeling (Galton-Fenzi et al., 2012) and oceanographic (Herraiz-Borreguero et al., 2016) studies reporting values of 0.74 m yr^{-1} and 1.0 m yr^{-1}, respectively. Galton-Fenzi et al. (2012) showed a seasonal cycle in area-averaged melt with a maximum of 0.8 m yr^{-1} in winter and a minimum of 0.7 m yr^{-1} in summer.

2.1.2 The ice shelf-ocean boundary layer

The ice shelf-ocean boundary layer (ISOBL) regulates heat and salt exchanges between the ice and the far-field ocean, and plays a crucial role in determining the rate at which the ice shelf melts. Close to the ice, where viscosity dominates, these exchanges occur by molecular diffusion (McPhee et al., 1987; Gayen et al., 2016; Keitzl et al., 2016b).

Further from the ice, turbulent fluxes dominate (Keitzl et al., 2016b; Sirevaag, 2009; Vreugdenhil and Taylor, 2019). Often, this turbulence is produced by vertical shear: velocity must transition from zero at the ice-ocean interface to its free stream value some distance away. A steep velocity gradient can become unstable, producing a turbulent boundary layer. Buoyancy fluxes due to melting or freezing can enhance or suppress this turbulence (McPhee et al., 1987; Vreugdenhil and Taylor, 2019).

The ISOBL is subgrid-scale in ocean models. Typically, the resolution of general circulation models (e.g. Naughten et al., 2018a) and regional models (e.g. Gwyther et al., 2016; Galton-Fenzi et al., 2012) is far too coarse to capture the ISOBL processes that regulate melting. Instead, a parameterisation is used to diagnose the interface temperature, salinity and melt rate from far-field ocean properties. Basal melting parameterisations typically assume that melt is controlled by the shear (gradient in velocity) induced by large-scale currents or buoyant plumes and set the melt-rate as a function of current velocity.

2.1.3 Modeling ice-ocean interactions

Shear-controlled melting

Ice shelf melt is calculated by balancing fluxes of heat and salt at the ice-ocean interface (e.g. McPhee et al., 1987; Hellmer and Olbers, 1989; Jenkins, 1991; Holland and Jenkins, 1999), and assuming that the interface temperature T_b is at the freezing temperature at interface salinity and pressure $T_b = T_f(S_b, p_b)$. The interface temperature and salinity are therefore related by the linearised liquidus relationship:

$$T_b = \lambda_1 S_b + \lambda_2 + \lambda_3 p_b. \tag{2.1}$$

The values of empirical constants λ_1, λ_2 and λ_3 are given in Table 2.3. As described in detail in §1.3, the divergence of heat at the interface is balanced by a latent heat flux due to melting, with an equivalent balance for salt (Eqs. 1.2 and 1.3). The melt rate m appears in the latent heat ($Q_{latent} = L_f m \rho_i$) and brine ($Q_{brine} = S_b m \rho_i$) fluxes, respectively, where L_f is the latent heat of freezing and ρ_i is the ice density. The heat balance expression is given by:

$$\rho_i m L_f = \rho_i c_i \kappa_{T,i} \frac{\partial T_i}{\partial z}_{\ b} - \rho c_p \Gamma_T u^* (T_b - T_{ML}) \tag{2.2}$$

where the first term on the right hand side is the diffusive heat flux into the ice shelf, where $(\partial T_i/\partial z)_b$ is the ice shelf vertical temperature gradient evaluated at the ice-ocean interface and c_i and $\kappa_{T,i}$ are the heat capacity and thermal diffusivity of the ice, respectively. The second term on the right hand side is the oceanic heat flux, here parameterised in terms of the bulk temperature difference across the boundary layer ($T_b - T_{ML}$, where T_{ML} denotes the mixed layer temperature), the friction velocity u^* and a transfer coefficient Γ_T. Parameters ρ and c_p are the density and heat capacity of the ocean mixed layer, respectively. An equivalent expression is given for the balance of salt:

$$\rho_i m(S_b - S_i) = \rho \Gamma_S u^* (S_b - S_{ML}), \tag{2.3}$$

where Γ_S is the salt transfer coefficient. In this expression the ice salinity and the diffusive salt flux within the ice are assumed to be zero. The friction velocity u^* is defined as the square root of the kinematic stress at the ice-ocean interface. However, in this instance u^* is estimated as a function of the free-stream current speed U through a simple parameterisation:

$$u^* = C_d^{1/2} U \tag{2.4}$$

where drag coefficient C_d is often taken to be 0.0025 (Gwyther et al., 2015).

Heat and salt flux expressions 2.2 and 2.3, in which m depends upon u^*, are common to many ice-ocean parameterisations (e.g. McPhee et al., 1987; Jenkins, 1991; Jenkins et al., 2010b). However, the form of oceanic heat and salt transfer coefficients Γ_T and Γ_S varies between studies. McPhee et al. (1987) expresses Γ_T, Γ_S as:

$$\Gamma_T = \left[\frac{1}{k} \ln \left(\frac{u^* \xi \eta^2}{f h_\nu} \right) + \frac{1}{2\xi\eta} + 12.5 Pr^{2/3} - 8.5 \right]^{-1} \tag{2.5}$$

$$\Gamma_S = \left[\frac{1}{k} \ln \left(\frac{u^* \xi \eta^2}{f h_\nu} \right) + \frac{1}{2\xi\eta} + 12.5 Sc^{2/3} - 8.5 \right]^{-1} \tag{2.6}$$

where Pr (Sc) is the Prandtl (Schmidt) number, $k = 0.4$ is von-Karman's constant, f is the Coriolis parameter, $\xi = 0.052$ is a dimensionless constant, and $h_\nu = 5\nu/u^*$ the thickness of the viscous sublayer. The stability parameter (η; Eq. 1.11) describes the influence of an interfacial buoyancy flux B, which reduces the ISOBL depth. Buoyancy flux B is itself determined by the melt rate. Holland and Jenkins (1999) showed that for $T' < 0.5$ °C and $u^* > 0.1$ cm s^{-1} (corresponding to $U \sim 20$ cm s^{-1}) the stability parameter makes less than a 10% difference to the estimated melt rate. These conditions are thought to

be applicable to most of Antarctica's largest ice shelves such as the Ross, Filchner-Ronne and Amery, thus many ocean models discount the effect of a stabilising buoyancy flux and set $\eta = 1$ (e.g. Galton-Fenzi et al., 2012; Gwyther et al., 2016; Naughten et al., 2018b). For $\eta = 1$, the parameterisation becomes analogous to that presented in Jenkins (1991) with transfer velocity formulation $\Gamma_{T,S} = (2.12\ln(u^* h/\nu) + 12.5(Pr,\ Sc) - 9)^{-1}$ from Kader and Yaglom (1990). Melting Eqs. 2.2 and 2.3 are functions of friction velocity u^*. To avoid obtaining $m = 0$ for cases where the free stream velocity $U = 0$, a lower bound on u^* is sometimes implemented to represent "diffusive" melting (e.g. Gwyther et al., 2015).

Several studies have compared observed melt rates to predictions made using parameterisations, with varying results (Jenkins et al., 2010b; Kimura et al., 2015; Begeman et al., 2018). When applied to the cold, energetic ocean conditions observed beneath the Filchner-Ronne and Larsen C Ice Shelves, the parameterisation outlined in Jenkins (1991) under-predicted melt-rates by 40% (Jenkins et al., 2010b). However, when applied to warmer, less energetic cavity environments, this parameterisation tended to over-predict melt rates (Kimura et al., 2015; Begeman et al., 2018), by factors of 4–30. Unfortunately, no observational study to date has been able to test the functional form of the parameterisation.

While Eqs. 2.5 and 2.6 are still widely implemented, many studies now set Γ_T and Γ_S to constant values (e.g. Dansereau et al., 2014; Jourdain et al., 2017). This form is supported by observations beneath sea ice (McPhee, 2008). Jenkins et al. (2010b) used ice shelf melting, upper-ocean temperature and current meter measurements to observationally constrain these transfer coefficients. As u^* was not directly measured, they inverted for the products $\sqrt{C_d}\Gamma_T$ and $\sqrt{C_d}\Gamma_S$, which they term thermal and saline Stanton numbers, using the drag relationship (Eq. 2.4) and assuming constant C_d. The best fit to the data was found for $\sqrt{C_d}\Gamma_T$=0.0011, $\sqrt{C_d}\Gamma_S$= 3.1×10^{-5} assuming the ratio $\Gamma_T/\Gamma_S = 35$.

Convection-controlled melting

Recent laboratory (McConnochie and Kerr, 2016a), turbulence-resolving numerical (Gayen et al., 2016; Mondal et al., 2019) and theoretical (Kerr and McConnochie, 2015) studies have found that melting of sloping or vertical ice is controlled by the thermal driving (the difference between the ambient temperature and the local pressure- and salinity-

dependent freezing temperature) and does not depend directly on current speed. In this "convective" regime, buoyant instability controls the near-wall properties and therefore melt rates.

Scaling analysis and laboratory experiments were used to develop a model for the ablation of a vertical (Kerr and McConnochie, 2015) or sloping (McConnochie and Kerr, 2018) ice-ocean interface. This model envisages that the thermal and saline boundary layers adjacent to the ice grow diffusively until some characteristic timescale when they are periodically removed by the eddies associated with turbulent convection. The convection is driven by destabilising buoyancy associated with the fresh meltwater flux. The interface temperature is given by:

$$T_\infty - T_b = \frac{\rho_i L_f + \rho_i c_i (T_b - T_i)}{\rho c_p} \quad \left(\frac{\kappa_S}{\kappa_T}\right)^{1/2} \quad \frac{S_\infty - S_b}{S_\infty - S_i} \quad , \tag{2.7}$$

where κ_T and κ_S are the molecular diffusivities of heat and salt and the subscript ∞ denotes the ambient ocean values. The melt rate is then given by:

$$m = \gamma \sin^{2/3}\theta \quad \left(\frac{g(\rho_\infty - \rho_b)\kappa_s^2}{\rho_\infty \nu}\right)^{1/3} \quad \frac{S_\infty - S_b}{S_\infty - S_i} \quad , \tag{2.8}$$

where γ is a constant of proportionality equal to 0.09 (Kerr and McConnochie, 2015) and θ is the angle of the ice-ocean interface to the horizontal. The liquidus relationship 2.1 allows this system of equations to be solved for interface conditions and melt rate. This model implies that m scales as $\Delta T^{4/3}$, where $\Delta T = T_\infty - T_b$ is the temperature difference between the interface and ambient ocean, and with the basal slope θ as $\sin^{2/3}\theta$. An equivalent expression for melting of a sloping ice face was determined using turbulence-resolving numerical simulations (Mondal et al., 2019). While the $\sin^{2/3}\theta$ dependence of the melt rate on slope angle was only demonstrated experimentally by McConnochie and Kerr (2018) for angles greater than 50°, the simulations of Mondal et al. (2019) showed that this relationship holds for slope angles of 10° and greater.

2.1.4 Present study

This chapter is presented as follows. The data collection and processing are described in §2.2. Ocean and melt rate variability is quantified at seasonal and higher frequencies in §2.3. In §2.4, ocean and melt rate observations are used to evaluate shear and convective parameterisations of ice-ocean interactions. Finally, in §2.5, the comparison between

observed and predicted melt rates is expanded to include other published studies of melt rates and *in situ* ocean observations.

2.2 Data and Methodology

2.2.1 Instrumentation

The borehole at AM06 (70°14.7' S; 71°28.1' E) was hot water drilled during the 2009/2010 summer at a site that was predicted to be melting (Galton-Fenzi et al., 2012). The ice shelf is 607 m thick, with 73±2 m of freeboard, and the water column thickness is 295 m. The ice ocean interface and seafloor are at 523±2 (upper limit) and 837±2 dbar, respectively.

Before the mooring was deployed, several CTD casts were collected over the full depth of the cavity during a two day period using a Falmouth Scientific Instruments (FSI) 3" Micro Conductivity Temperature Depth (CTD) instrument (serial 1610). Pre-season laboratory calibrations of the FSI CTD temperature, pressure and conductivity sensors were done at the Commonwealth Scientific and Industrial Research Organisation Division of Marine Research, however no *in situ* calibrations were performed due to the difficulty of deploying Niskin bottles through the ice shelf, nor was a shipboard calibration check performed. Based upon the largest corrections from previous AMISOR sites (using the same instrument) the error is expected to be less than 0.005°C, 0.3 psu and 3 dbar for temperature, salinity and pressure, respectively. *In situ* temperature (T) and Practical Salinity (S) are converted to Conservative Temperature (Θ) and Absolute Salinity (S_A) using the Gibbs Seawater Matlab package (McDougall and Barker, 2011).

A mooring, comprising three Seabird SBE37IM Microcats and one upward looking RDI 300kHz Workhorse Acoustic Doppler Current Profiler (ADCP), was then deployed through the ice. All instruments sampled at 30 minute intervals. In the vertical, the ADCP sampled 27 bins at 4 m resolution, where 23 of the bins were within the water column. The ADCP uses four beams to calculate velocity, and each beam is at an angle of 20° from the vertical. The locations of the instruments with respect to the ice-ocean interface are outlined in Table 2.1. The duration of the ADCP record is 366 days, thus we restrict the analysis of the Microcat data to the same period for this study.

Table 2.1: Type, duration and depth of measurements from the AM06 borehole. Depth given with respect to the ice-ocean interface.

	start date	duration (days)	pressure (dbar)	depth (m)
interface	∼	∼	547	0
CTD	01/01/10	2	0–837	0–286
mCAT1	07/01/10	366	551	4
ADCP	07/01/10	366	640	92
mCAT2	07/01/10	366	681	132
mCAT3	07/01/10	366	790	286

2.2.2 Melt rate measurements

The rate of melting of the ice shelf base at AM06 is calculated from the rate of change of the range from the upwards facing ADCP to the ice. Range from the ADCP to the ice shelf is obtained by post-processing the echo amplitude (intensity) of the ADCP pings, rather than using the Bottom Tracking functionality. Following the method outlined in Shcherbina et al. (2005), a modified Gaussian is used to approximate the surface reflection peak profile $A(z)$:

$$A(z) = a_0 \exp\left(-\left(\frac{z - h_0}{\delta}\right)^2\right) + a_1 z + a_2 \tag{2.9}$$

where $a_0,\ a_1,\ a_2,\ h_0$ and δ are obtained by a least squares fit of Eq. 2.9 to the echo amplitude data in the vicinity of the surface peak. The fitted value of h_0 is an estimate of the range from the ADCP to the ice shelf.

The fit is found for each of the four ADCP beams independently. Ideally, an average over the four beams would be used to decrease the statistical error (Shcherbina et al., 2005), however this was not possible due to the shape of the ice shelf base. We show that the ice shelf draft changes by 20 m over a horizontal distance of only 40 m. The method of fitting a curve to the echo amplitude relies on having data on both sides of the surface reflection peak. In the case of the ice with shallower draft (longer range), the peak is not resolved and therefore cannot be fitted with Eq. 2.9. Consequently, range is calculated only for headings $-30 \leq \theta \leq 50$ and melt rate estimates are only possible over this area. The heading, pitch, and roll data recorded by the ADCP are used to map the range data onto a plane in polar coordinates. The data are then binned and all four ADCP beams

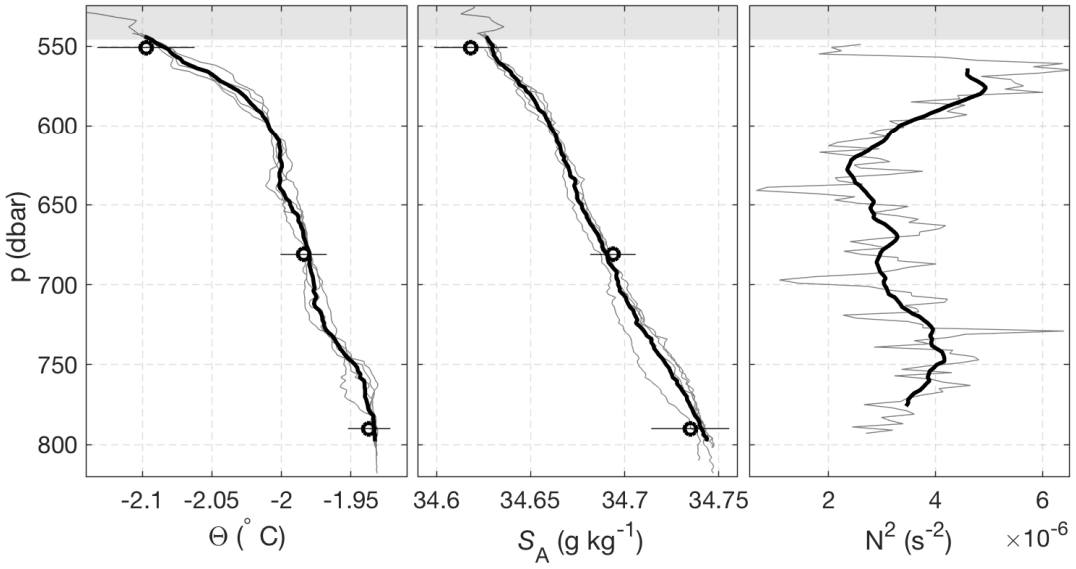

Figure 2.2: (A) Conservative Temperature Θ and (B) Absolute Salinity S_A profiles from the two CTD casts at AM06. Individual up- and down-casts are shown (grey lines) as is the four-profile mean (black line). Overlain at the appropriate pressures are the mean ($\pm$ 2σ) microcat Θ and S_A for the month following the CTD data collection. (C) Squared buoyancy frequency N^2, where the grey and black buoyancy frequency curves were obtained using 10 and 40 dbar running window averages, respectively. The shaded grey region shows range in the ice-ocean interface position above the instruments due to the sloping ice base.

are averaged together over a month-long period to obtain a mean ice-surface position for that month. Differencing these surfaces yields monthly melt rate estimates.

2.3 Observations

2.3.1 Oceanographic setting

CTD casts collected before the deployment of the mooring at AM06 show a water column stratified in both temperature and salinity, with cooler, fresher water overlying warmer, saltier water (Fig. 2.2). There is no discernible difference between the up- and down-casts of the CTD. The water column is stably stratified with depth-mean stratification $N^2 \sim 3.5 \times 10^{-6}$ s^{-2}, where $N = [-(g/\rho_0)(\partial\rho/\partial z)]^{1/2}$ is the buoyancy frequency. There is

no clear mixed layer beneath the ice, in fact temperature gradients are especially strong in the upper 30 m of the water column. There is some evidence for a basal mixed layer below ∼790 dbar, although this was not consistently sampled by the CTD.

Fig. 2.4 shows the four cast-mean $\Theta - S_\mathrm{A}$ properties from the CTD. A defining feature of ocean properties beneath ice shelves is the presence of meltwater from meteoric (fresh) ice, which causes ocean properties to evolve along nearly-straight line in $\Theta - S_\mathrm{A}$ space (e.g., Gade, 1979; Hattermann et al., 2012; Stevens et al., 2020). Under the assumption of equal eddy diffusivities for heat and salt, the gradient ($d\Theta/dS_\mathrm{A}$) of this "meltwater mixing line" can be calculated (Gade, 1979; McDougall et al., 2014). At local conditions Eq. 16 of McDougall et al. (2014) gives $d\Theta/dS_\mathrm{A} = 2.38$ C g^{-1} kg, and explains the $\Theta - S_\mathrm{A}$ properties well over the pressure range 560–650 dbar. Near the interface, the $d\Theta/dS_\mathrm{A}$ gradient steepens, deviating from the meltwater mixing line. A line of best fit over this 15 m thick layer has slope $d\Theta/dS_\mathrm{A} = 4.8$ C g^{-1} kg. This result indicates that the turbulent diffusivities of heat and salt are not equal over this region, which could be explained by a mixing process such as double-diffusive convection (Kimura et al., 2014) or the presence of stratification (Jackson and Rehmann, 2014).

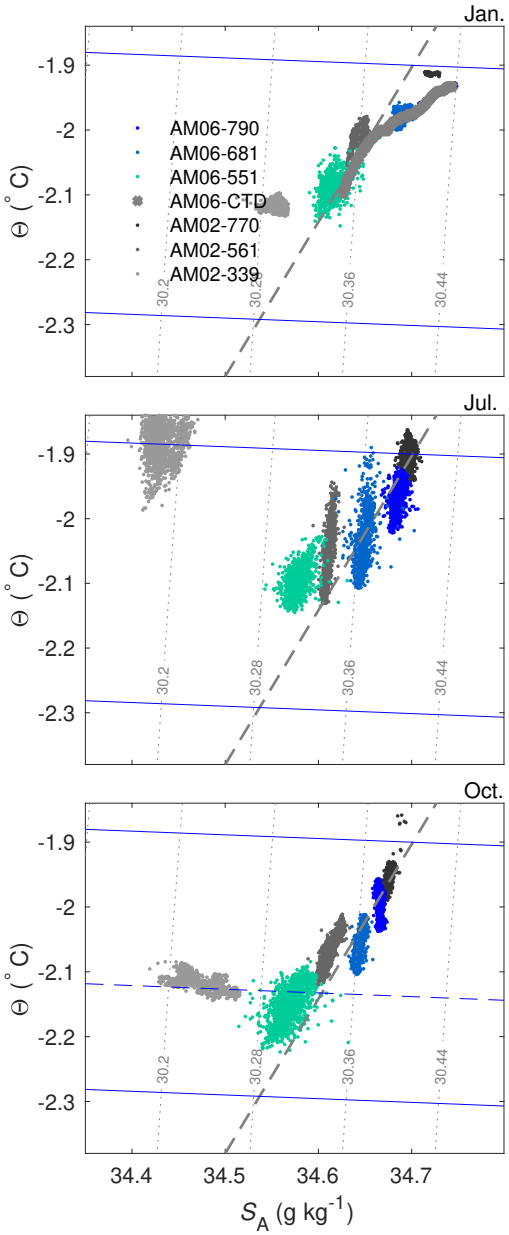

Figure 2.3: Θ-S_A plots for months January, July and October in 2010 at AM06 and AM02 (5 year composite of years 2001, 2003-2006). Freezing temperature curves at surface, AM06 interface (543 dbar; solid blue) and AM02 interface (326 dbar; dashed blue, bottom panel only) pressure are also shown. The dashed grey line is the meltwater mixing line from Fig. 2.4.

The timeseries of temperature and salinity measurements from the upper water column suggest that AM06 is a site of melting year-round. For the whole period sampled, the

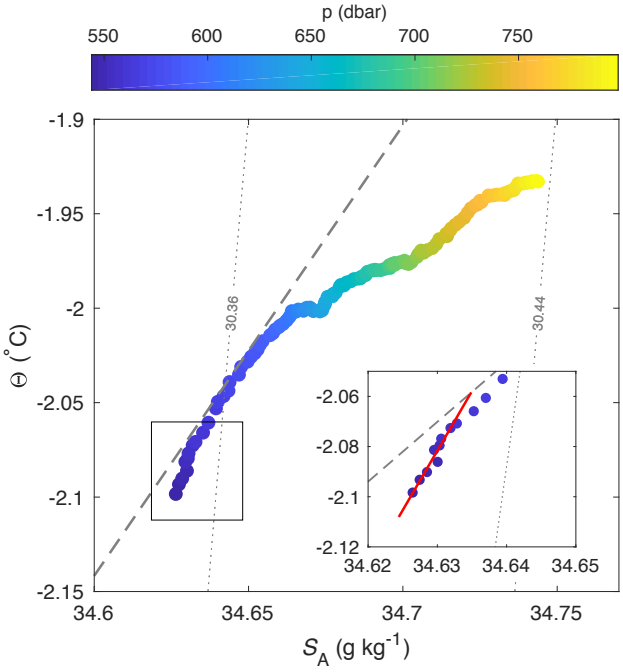

Figure 2.4: Θ-S_A plot of the four-profile mean from Fig. 2.2 coloured by pressure. A meltwater mixing line with gradient $d\Theta/dS_A$=2.38 °Cg^{-1}kg calculated following McDougall et al. (2014) is shown (dashed grey line), as are the local isopycnal slopes (dotted grey lines). The inset shows a line of best fit for the upper 15 m of the water column (red line) which has gradient $d\Theta/dS_A$=4.8 °Ckg g^{-1}.

temperature recorded by the upper microcat is greater than the *in situ* freezing temperature at the interface pressure (543 dbar), by 0.2 °C on average (Fig. 2.5). Temperatures recorded at all depths are colder than the surface freezing temperature (-1.9 °C) indicating the presence of ISW, and show similar seasonality at all depths (Fig. 2.5). The water column, which is warmest in summer and autumn, cools over winter and reaches a minimum temperature in spring. The cooling is coincident with freshening at all depths. In October, the cooling and freshening trend reverses, and temperatures and salinities increase rapidly towards their previous summer values.

Microcat temperatures and salinities fall on a melt-freeze line (McDougall et al., 2014), demonstrating that the water masses arriving at AM06 have been modified by the addition of fresh water due to ice melt, with the highest fraction of melt-water at the microcat nearest the ice base. The ISW present at AM06 follows a single melt-freeze line year round (Fig. 2.3), suggesting a single ISW source water mass with S_A ∼34.68 g kg^{-1}.

Whilst it is not possible to use the melt-freeze relationship to unequivocally identify the source water masses of the ISW, the salinity suggests that it is DSW driving melt at AM06. Figure 2.3 shows that $\Theta - S_A$ minimum in spring is the result of a high degree of modification of DSW by meltwater.

A multi-year composite of $\Theta - S_A$ from mooring AM02 (Herraiz-Borreguero et al., 2015), situated mid-way (∼70 km) from AM06 to the calving front and spanning the years 2001, 2003-2006, is also shown in Fig. 2.3. The data from AM02 microcats at 561 and 770 dbar show similar seasonality and properties to AM06. The $\Theta - S_A$ properties at the two mooring locations follow the same meltwater mixing line, suggesting the same source watermass, however the ocean is typically warmer and saltier at AM02 than at AM06 at an equivalent depth. These observations suggest a pathway for DSW from the calving front along the eastern flank of the AIS, consistent with the modelling results of Galton-Fenzi et al. (2012). The warm, fresh ISW observed by the upper microcat at AM02 in winter (Fig. 2b), which has been identified as ISW with mCDW as its source (Herraiz-Borreguero et al., 2015), is not observed at AM06 in 2010.

Tidal currents are evident in the ADCP velocity measurements beneath AM06 (Fig. 2.6). Harmonic analysis (Pawlowicz et al., 2002), restricted to frequencies higher than semi-annual due to the limited duration of the ADCP record, shows that the tides have mixed semi-diurnal and diurnal properties. The ellipse semi-major velocities of semi-diurnal constituents S_2 and M_2 are 3.3 and 3.0 cm s^{-1}, respectively; larger than than those of diurnal constituents K_1 and O_1, which are 1.9 and 1.8 cm s^{-1} (Table 2.2). Ellipse semi-minor velocities for both diurnal and semi-diurnal constituents are positive, indicating clockwise rotation of the current vector in time. However the semi-minor velocities are also small, as tides are close to rectilinear. Tides are oriented NNE/SSW, roughly normal to the AIS calving front. These findings are consistent with results from a barotropic tidal model which showed mixed semidiurnal and diurnal tidal currents beneath the AIS, with the magnitude of the semi-major axis generally less than 5 cm s^{-1} for the semidiurnal tide and less than 2 cm s^{-1} for the diurnal tide (Hemer et al., 2006). An estimate of the typical tidal current magnitude is given by:

$$U_{typ} = \sum_{i=1}^{4} (u_{e,i}^2 + v_{e,i}^2)^{1/2} \tag{2.10}$$

where u_e and v_e are the magnitude of the semimajor axis and semiminor axis of the tidal ellipse, with subscript i representing the four main tidal constituents. Using the constituents in Table 2.2 yields $U_{typ} = 9.8$ cm s^{-1} at AM06. U_{typ} is roughly the maximum

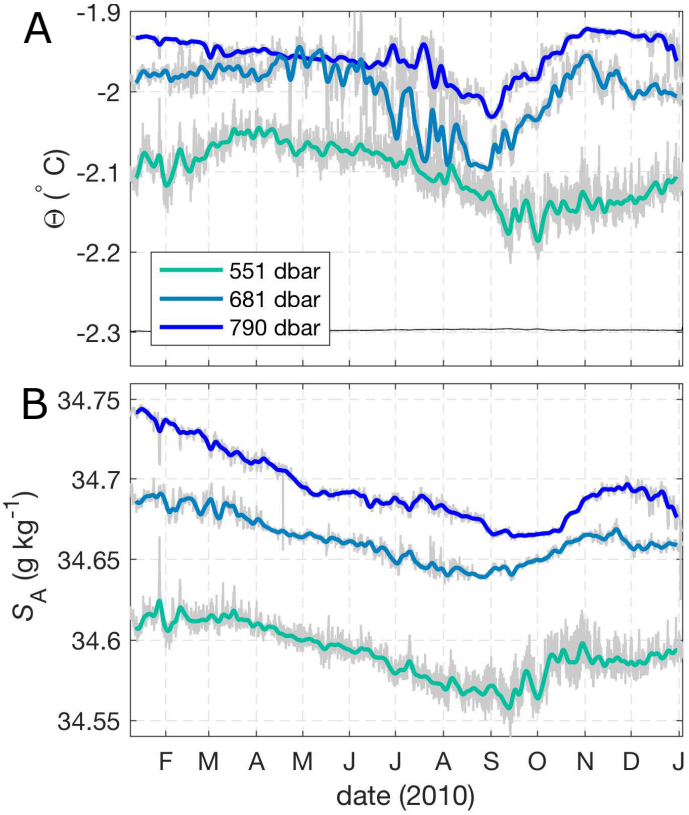

Figure 2.5: Time-series of (A) Θ (B) S_A from all three microcats. The freezing temperature (black) at upper microcat salinity and interface pressure is also shown in (A).

current speed available from these four constituents. Instantaneous current speeds at AM06 in excess of 15 cm s^{-1} (Fig. 2.6) are a consequence of the superposition of mean and tidal currents.

In order to consider the tidal and non-tidal (residual) currents separately, we remove the modelled tidal velocities from the depth-mean velocities. Fig. 2.6 compares the total and residual flow speeds, where the residual flow is smoothed with a Gaussian filter with a half width of one week. The residual flow U_r is oriented into the cavity (220°N) and has an annual mean speed of 3.2 cm s^{-1}. The strength of U_r varies seasonally and at higher frequencies. Notably, in the period August–December, the residual circulation is much weaker ($\sim$2.0 cm s^{-1}). This period of weaker circulation is coincident with a cold, fresh water column (Fig. 2.3), suggesting increased residence time beneath the ice and a higher meltwater fraction.

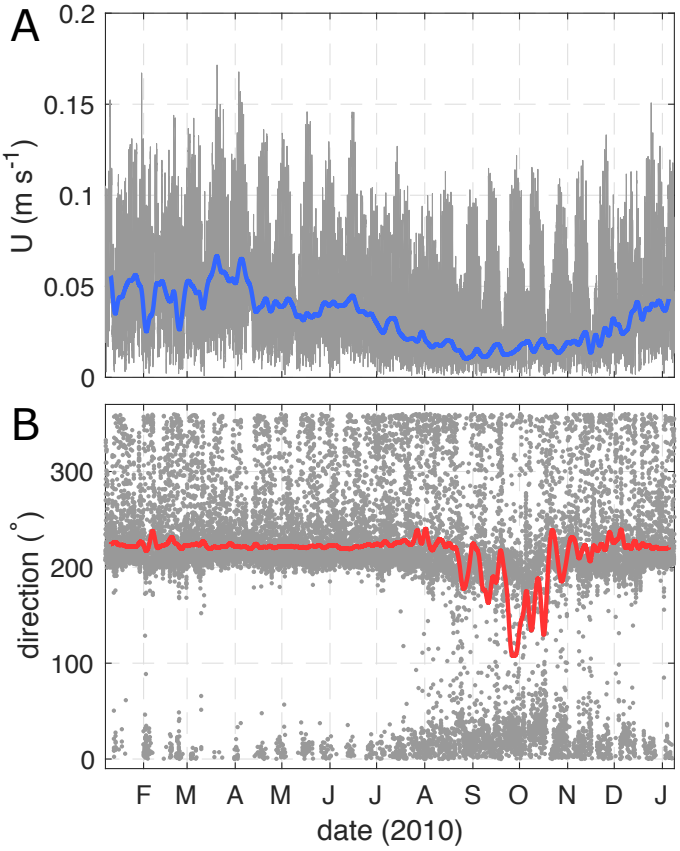

Figure 2.6: (A) Depth-mean current speed $U = \sqrt{u^2 + v^2}$ from the ADCP (grey). Overlaid is the smoothed, depth-mean current speed with tides removed $U_r = \sqrt{(u - u_T)^2 + (v - v_T)^2}$ (blue). (B) Current direction (grey) and smoothed current direction with tides removed (red).

Beyond measuring the water column velocities, the ADCP also reveals a large, step-like feature in the underside of the ice shelf at AM06. The base of the ice is mapped out using the range from the ADCP to the ice as a function of the instrument bearing (heading) and angle (pitch, roll). The bottom tracking function of the ADCP provides four independent estimates of range from four separate beams, each oriented at 20° to the vertical and at 90° to each other. The instrument rotates about the mooring line due to currents, allowing the ADCP beams to map out a circular swath of the underside of the ice (Fig. 2.7) and revealing a significant feature in the ice above. This feature has a vertical extent of $\sim$ 20 m and a maximum slope of 45°. The horizontal extent of the ADCP coverage is $\sim$ 80 m square. The sloped feature is continuous across this distance, but the total extent of the feature cannot be determined using the available data.

Table 2.2: Ellipse parameters for tidal current constituents of the depth-mean flow over the upper 90m of the water column. Presented are velocities of the ellipse major and minor axes, the inclination of the semi-major axis (counter-clockwise from east), and phase of the tidal vector relative to equilibrium tide at Greenwich.

name	frequency cph	major cm s^{-1}	minor cm s^{-1}	inclination ◦	phase ◦
S2	0.0833	3.30	0.37	69	56
M2	0.0805	2.95	0.01	72	313
K1	0.0418	1.79	-0.01	71	23
O1	0.0387	1.75	0.04	72	17

2.3.2 Basal melt rate

The annual mean melt rate at AM06 is 0.51±0.18 m yr^{-1} (Fig. 2.8). Monthly-averaged melt rates range from a maximum of 0.8 m yr^{-1} in late Autumn to a minimum of 0.2 m yr^{-1} in Spring. The seasonality in melting is consistent with the seasonality of upper microcat temperatures. Broadly speaking, when temperatures are warmer, higher melt rates are observed (Fig. 2.5). However, the period of maximum melt in June does not coincide with the warmest ocean temperatures, which are observed in April for the upper microcat. The dominance of tidal currents in the velocity record means that seasonality in the current forcing is less pronounced. The weak residual flow period August–November is coincident with the period of low melt rates (Fig. 2.6).

The melt rate measured here *in situ* is consistent with the modelled melt rate in the vicinity of AM06 (Galton-Fenzi et al., 2012, ∼1 m yr^{-1}), and more broadly with AIS area-averaged melt rates from models (0.74 m yr^{-1}; Galton-Fenzi et al., 2012), oceanographic proxies (1.0 m yr^{-1}; Herraiz-Borreguero et al., 2016) and glaciological studies (0.5–0.8 m yr^{-1}; Yu et al., 2010; Wen et al., 2010; Rignot et al., 2013; Depoorter et al., 2013). However, the seasonal cycle in melting at AM06 is somewhat out of phase with the modelled cavity-average, which has a maximum in July and a minimum in January (Galton-Fenzi et al., 2012). The maximum modelled cavity-average meltrate in July leads the period of cooling and freshening at AM06 in July–October, suggesting that the high degree of meltwater modification at AM06 is the result of strong melting elsewhere in the cavity.

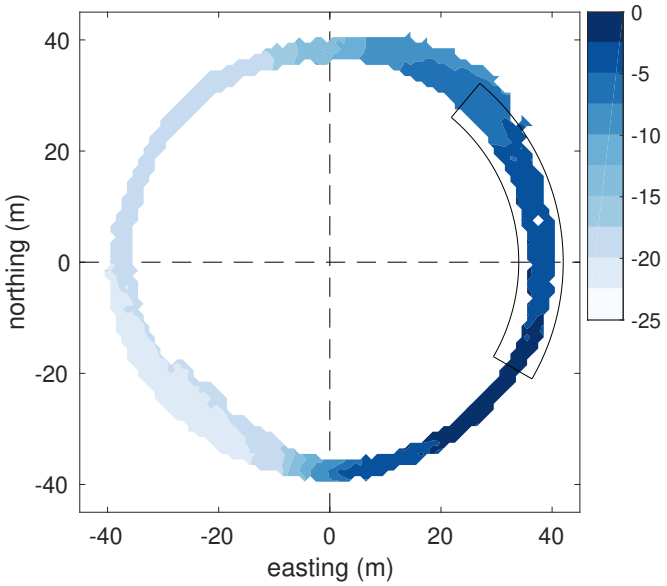

Figure 2.7: Depth of the ice shelf base relative to zero depth (defined in Table 2.1), where a more negative depth indicates a thinner ice column above. The area mapped out by the ADCP is determined by the beam angle (20°) and the distance to the ice shelf (92–114 m). Overlain is an outline of the region of the ice base over which melt rates in Fig 2.8 are calculated.

2.4 Comparison with models

2.4.1 Choice of data

Here we use the concurrent temperature, salinity and velocity measurements from site AM06 to predict the local melt rate using three different melt-rate parameterisations. We test two shear-dependent parameterisations solving 2.1, 2.2 and 2.3, one with the constant transfer coefficients recommended in Jenkins et al. (2010b) (hereafter J10) and the other using 2.5 from McPhee et al. (1987) (hereafter M87). We also test the convective parameterisation solving 2.1, 2.7 and 2.8 from McConnochie and Kerr (2018) (hereafter MK18). The temperature and salinity are taken from the upper microcat. Because of the sloped interface, the positioning of this instrument with respect to the interface is somewhat ambiguous. Here we use the lower bound on the interface position (z=-541 m) as our reference depth. The upper microcat is therefore situated at a depth of 4 m (Table 2.1).

All parameterisations included in this study assume a water column structure where

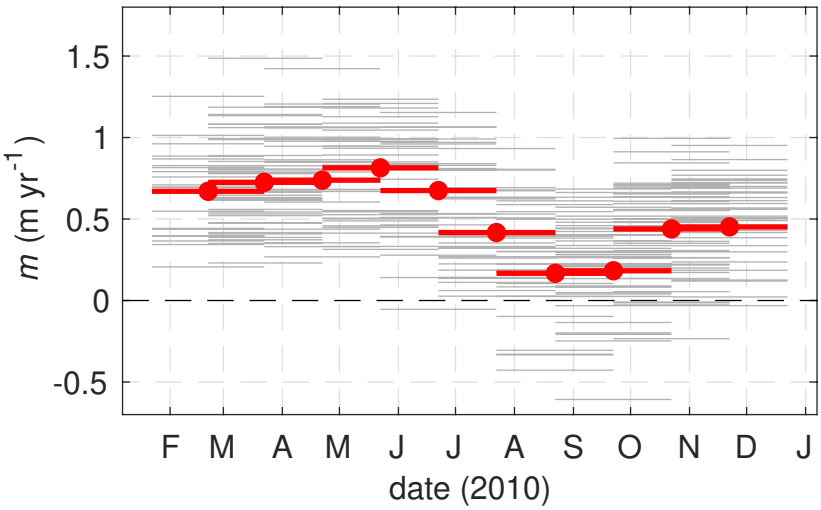

Figure 2.8: Observed melt rates at monthly resolution for (grey) each grid cell ($d\phi$, dr) and (red) the area average, where the area is outlined in Fig. 2.7.

strong mixing in a boundary current or plume produces a well mixed layer of water near the ice such that, so long as they are measured within the layer, temperature and salinity do not vary in depth. However, the CTD profiles collected at the start of the observational period do not convincingly demonstrate the presence of a mixed layer adjacent to the ice (Fig. 2.2). As such, our results will be sensitive to the depth at which T_{ML} and S_{ML} are taken. Over the upper 10 m of the water column the temperature gradient is $d\Theta/dz = 0.0017$ °C m^{-1}. We assess the sensitivity of the predicted melt rate to the depth at which the temperature is taken in §2.5.

The melting (2.2 and 2.3) and transfer coefficient (2.5 and 2.6) equations call for the friction velocity u^*. The assumption that u^* specifies the structure of the flow near the ice results in the logarithmic Law of the Wall (LOW) with the form $u(z) = u^*/k \ln(z/z_0)$, where $k = 0.41$ is Von-Karman's constant and z_0 is the roughness length. The region over which the LOW holds is also called the surface layer. The velocity profiles recorded by the ADCP were analysed for a logarithmic profile, however the vertical resolution proved to be insufficient to capture the surface layer. As such, in Eq. 2.5 we model u^* using 2.4 with $C_d = 0.0025$.

In order to use the quadratic drag relationship 2.4 with fixed C_d we require the flow speed U measured outside the surface layer. Typically, the surface layer occupies ∼10% of the total boundary layer depth, and for the polar oceans is typically in the range 2–4 m deep

(McPhee, 2008). The Ekman layer depth scales as $\delta \sim u^*/|f|$, where f is the Coriolis frequency. For a free stream velocity $U = 5.0$ cm s^{-1} and $f = -1.4 \times 10^{-4}$ s^{-1} we find $\delta \sim 18$ m and therefore a surface layer depth of ∼1.8 m. The uppermost bin sampled by the ADCP is 3 m below the ice, however, this data point is likely to be contaminated as it falls within the upper 6% of the instrument range (Teledyne, 2006). This point has therefore been discarded. As the upper water column velocity structure is relatively homogeneous in depth we use the four-bin mean over 7–19 m. This averaging gives a continuous record of velocity data, and does not bias the speed low or high compared to taking the velocity at 7 m only. There is a significant amount of missing velocity data in the upper water column from January through to early April. As such, the shear-dependent parameterisations are tested using data from April onwards.

To test the constant transfer coefficient parameterisation outlined in J10 we take the recommended values $\sqrt{C_d}\Gamma_T$=0.0011 and $\sqrt{C_d}\Gamma_S$= 3.1×10^{-5}. Inherent in these values is the assumption that Γ_T/Γ_S=35. Various laboratory (Martin and Kauffman, 1977) and modelling (eg. Holland and Jenkins, 1999; Keitzl et al., 2016b) studies have attempted to estimate the ratio Γ_T/Γ_S, however the range of values obtained by these studies is large, from 30 to 100, resulting in a large uncertainty in the calculated fluxes.

Finally, to apply the MK18 model, the basal slope θ is needed. As the melt rate was measured over the section of ice bounded by $-30° \leq \phi \leq 50°$, θ is taken to be the local slope within this region, $\sim 9°$. It is worth noting that this is a large slope with respect to the overall ice shelf slope; the mean slope of this ice shelf will be of the order $\tan^{-1}(H/L) = 0.2°$, where H (∼2 km) is the approximate thickness change and L (∼600 km) is the approximate length of the AIS.

2.4.2 Ice shelf heat flux

Some of the heat supplied to the ice-ocean interface by the ocean is lost to the ice. In order to estimate how much, the heat transport within the ice shelf is approximated as a balance between vertical advection and diffusion. We assume that the vertical velocity is equal to the basal melt rate and constant within the ice shelf and that the ice shelf is in a steady state, meaning all ice added at the base is balanced by surface accumulation (for a thorough discussion around different ice shelf heat transport approximations see

Table 2.3: Physical parameters used in melt parameterisation calculations

name	symbol	unit	value
Thermal diffusivity ocean	κ_T	$m^2\ s^{-1}$	1.4×10^{-7}
Thermal diffusivity ice shelf	$\kappa_{T,i}$	$m^2\ s^{-1}$	1.1×10^{-6}
Salt diffusivity of ocean	κ_S	$m^2\ s^{-1}$	1.3×10^{-9}
Latent heat fusion	L_f	$J\ kg^{-1}$	3.34×10^5
Specific heat capacity ice shelf	c_i	$J\ (kg\ K)^{-1}$	2009
Specific heat capacity ocean	c_p	$J\ (kg\ K)^{-1}$	3974.0
Ocean reference density	ρ	$kg\ m^{-3}$	1030.0
Ice shelf reference density	ρ_i	$kg\ m^{-3}$	920.0
Liquidus slope (salinity)	λ_1	$°C\ kg\ g^{-1}$	-0.069
Liquidus slope (pressure)	λ_2	$°C\ dbar^{-1}$	-7.6×10^{-4}
Liquidus offset	λ_3	°C	0.0826
Von-Karman's constant	k	$\sim$	0.41

Holland and Jenkins, 1999):

$$\frac{\partial^2 T_i}{\partial z^2} + \frac{m_i}{\kappa_{T,i}} \frac{\partial T_i}{\partial z} = 0 \tag{2.11}$$

where $m_i = \rho_m/\rho_i m_b$. We can solve 2.11 over an ice shelf of thickness H with surface temperature T_s and basal temperature T_b. At AM06 H = 607 m, $T_s \sim -20$ °C and $T_b \sim -2.1$ °C. At the annual average melt rate of 0.51 m yr^{-1} this model gives a heat flux into the ice of Q_i^T=-0.5 W m^{-2} (Fig. 2.9A). The ratio of heat lost to the ice Q_i^T to the latent heat flux Q_{latent} as a function of melt rate m is constant and equal to 0.095 for $m > 0.2$ m yr^{-1} (Fig. 2.9B), indicating that $\sim$ 10% of the heat supplied by the ocean is lost to the ice. Based upon this result, Eq. 1.2 may be approximated as $Q_T \sim 1.095 Q_{latent}$ at AM06.

2.4.3 Results

We first investigate the different behaviours of the J10, M87 and MK18 parameterisations by considering the melt rates they predict when applied to a short slice of observational data (Fig. 2.10). On short timescales the shear-dependent parameterisations exhibit large variability in melting, primarily due to the tidal flow at AM06 which varies between 1 and 14 cm s^{-1} over the two week period shown in Fig. 2.10. Variability in melting as predicted by the convective parameterisation is much smaller in magnitude as it driven

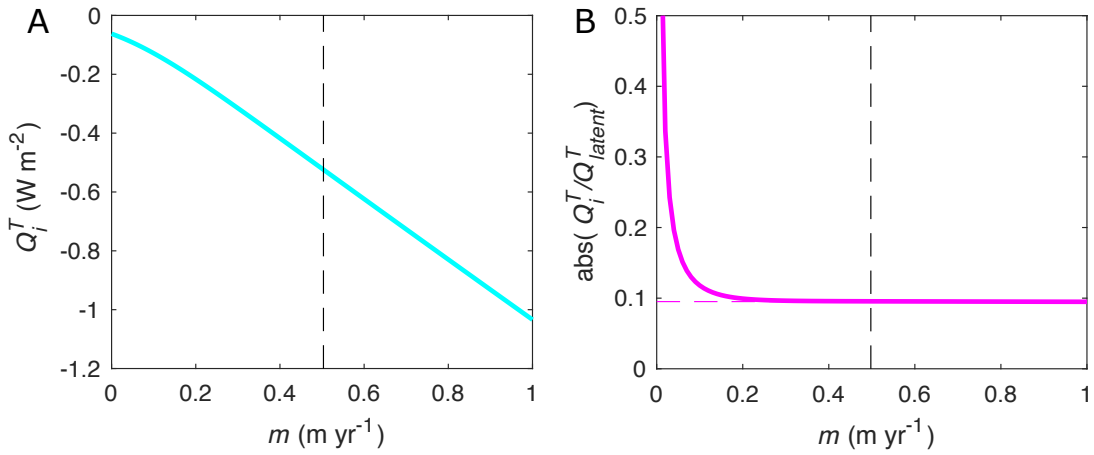

Figure 2.9: (A) Heat flux into the ice Q_i^T as a function of melt rate m from a one-dimensional advection-diffusion model for a 607 m thick ice shelf with a -20 °C surface and -2.1 °C basal temperature. (B) Ratio of Q_i^T to latent heat flux due to melting Q_{latent}^T as function of melt rate. The vertical dashed lines correspond to the annual average melt rate of 0.51 m yr^{-1}.

solely by fluctuations in temperature, which are small in amplitude. Both the J10 and M87 parameterisations predict much higher melt rates than are observed, while the MK18 convective parameterisation prediction is similar to observations.

The parameterisations are evaluated quantitatively by calculating the mean of the predicted melt rate over different averaging periods and comparing to the observed melt rate for the same period. The periods were chosen to minimise the uncertainty in the observed melt rates yet still capture some of the seasonal variability in the record. The observed T^*, U and m are presented in Table 2.4 alongside the predictions. The model that best fits the observations is the convective parameterisation based on the local slope angle, which under-predicts melt by 20% over period February–November. The shear-dependent parameterisations (M87 and J10) are not evaluated over the full period February–November due to missing upper water column velocity data. J10 melt rates are 400% larger than the observed melt rates, while M87 melt rates are roughly 200% the observations. In all cases, the fit worsens by ∼6% if the heat flux into the ice is neglected. CTD profiles taken at the beginning of the observational period (Fig. 2.2) measure a temperature gradient of $d\Theta/dz = 0.0017$ °C m^{-1} over the upper 10 m of the water column. Accordingly, if the melt rate calculated using J10 for $\Theta(d = 4)$ is 2 m yr^{-1}, taking $\Theta(d = 1)$ yields 1.95 m yr^{-1} while $\Theta(d = 10)$ results in 2.1 m yr^{-1}.

Table 2.4: Melt rates from observations and parameterisations. Columns 2–4 are average values observed over the periods given in column 1, where the period starts on the 7th day of the month. To calculate m_{M87} a drag coefficient of $C_d = 0.0025$ is used. The upper and lower bounds on the observationally constrained transfer coefficient Γ_T are based on using $C_d = 0.0025$ and $C_d = 0.0097$, respectively. The bracketed melt rate estimates show the effect of setting the heat flux into the ice shelf Q_i^T to zero.

period	T^* °C	U cm s^{-1}	m_{OBS} m yr^{-1}	m_{MK18} m yr^{-1}	m_{J10} m yr^{-1}	m_{M87} m yr^{-1}	Γ_T $\times 10^{-3}$
Feb–Nov	0.20	$\sim$	0.51	0.41	$\sim$	$\sim$	$\sim$
Apr–Jul	0.23	4.2	0.62	0.46	2.35(2.49)	1.35(1.44)	2.7–5.3
Aug–Nov	0.16	3.9	0.30	0.29	1.44(1.52)	0.83(0.89)	2.1–4.2
Apr–Nov	0.20	4.0	0.46	0.37	1.85(1.96)	1.07(1.13)	2.5–5.0

The final column in Table 2.4 shows the best-fit (constant) transfer coefficient Γ_T obtained by solving Eqs. 2.1, 2.2 and 2.3 given the observed melt rate and assuming $\Gamma_T/\Gamma_S = 35$. For $C_d = 0.0025$ we obtain $\Gamma_T \sim 5.0 \times 10^{-3}$ and for $C_d = 0.0097$ we obtain $\Gamma_T \sim 2.5 \times 10^{-3}$ over the period April—November.

2.5 Discussion

2.5.1 The suitability of shear and convective melting parameterisations at AM06

In the preceding section we evaluated both shear and convective melting parameterisations using melt rate and ocean observations from site AM06, finding that the convective parameterisation performed better. Here, we will briefly address the suitability of both types of parameterisation to the study site, based on the topography of the ice base and the flow conditions. While the local topography at AM06 is steep (above the mooring we observe a sloping feature in the ice base with a maximum slope of 45°), we measure the melt rate on an adjacent section of ice with a mean slope of 9°. Thus, the basal slope angle of 9° is most relevant to this discussion.

The MK18 convective parameterisation is only relevant for sloping ice, where melting is controlled by buoyant instability of the saline sublayer adjacent to the ice. In principle, shear parameterisations such as J10 and M87 may be applied to both flat and sloping

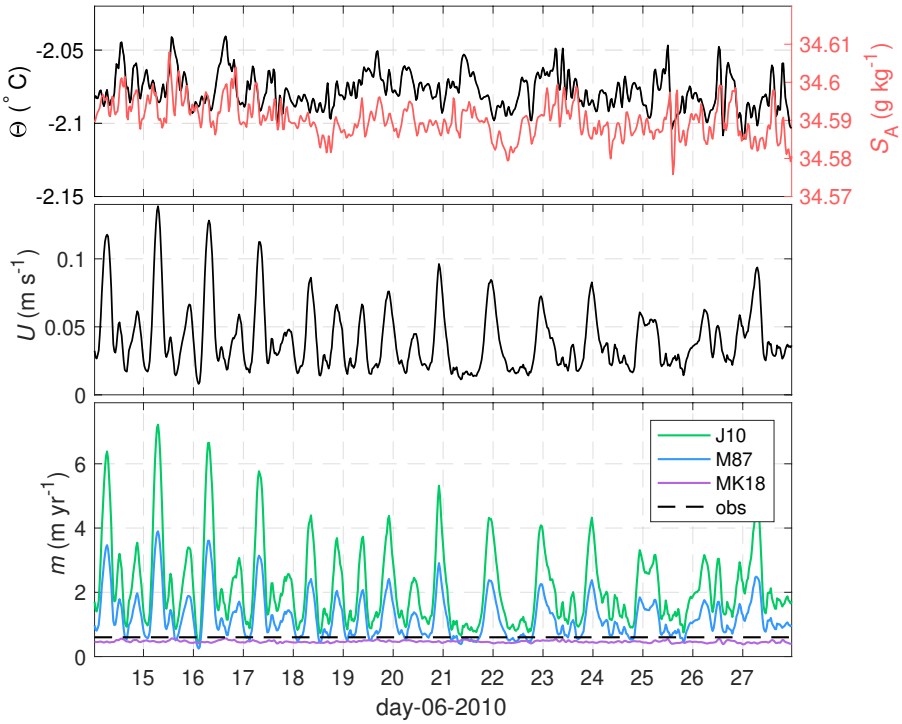

Figure 2.10: (top) Θ and S_A from the upper microcat 4 m below the ice, (middle) ocean velocity magnitude averaged over 7–19 m below the ice base and (lower) modelled melt rates for the three parameterisations compared in this study. While the J10 and M87 melt rates are strongly modulated by the tidal flow at AM06, MK18 varies only with temperature.

ice, providing that the shear is sufficiently strong. However, as mentioned in §1.3.3, the threshold between convection and shear controlled melting is poorly constrained, although may be in the range 2–4 cm s^{-1} for vertical ice at $T^* \sim 0.5$ °C (McConnochie and Kerr, 2017a). The mean speed over the upper 7–19 m of the water column is ~ 4.0 cm s^{-1}, close to the suggested transition value. However, due to the presence of tidal currents, instantaneous speeds can be in excess of 15 cm s^{-1}. Thus, we are in a situation where the basal slope of the ice permits either shear or convective melting, while the magnitude of the tidal current speeds suggests that shear should dominate. However, we find that the convective parameterisation better replicates the observed melt rates at the site. On the basis of these observations, we cannot make a definitive statement about which process is dominant at AM06. Should the melting be convection-dominated, the variation in observed basal slope at the site is expected to affect melting. For example, an increase in basal slope from 9° to 45° (the maximum observed at AM06), would increase

the melt rate by a factor of 3 based on convective melting Eq. 2.8. Consequently, the melt rate presented here may not be representative of a larger area.

An important consideration for the application of slope-dependent convective parameterisations in regional ocean models is the ice shelf basal topography. Here, we apply the MK18 parameterisation to the local slope measured by the ADCP, however, features such as this will be subgrid-scale in the circumpolar or regional-scale ocean models for which ice-ocean parameterisations are needed. These models have resolution beneath ice shelves on the order of kilometers (e.g. Naughten et al., 2018b). Basal topography such as the sloped feature observed at AM06, or the basal terraces beneath Pine Island Glacier (Dutrieux et al., 2014), will either be non-existent or considerably smoothed in the ice shelf thickness products used in regional and circumpolar ocean models. As such, while the convective melt rate parameterisation is a relatively good fit for our observations, there remain significant challenges to the implementation of such a parameterisation in ocean models, where these features are not resolved.

2.5.2 Sampling depth considerations

Poor agreement between the parameterised and observed melt rates may be a result of the depth at which the temperature, salinity and velocity are measured. At AM06 we observe the near-ice region is stratified in both temperature and salinity, contrary to the paradigm of a well mixed ISOBL on which the three-equation parameterisation is based. Other boreholes such as those in the McMurdo (Robinson et al., 2010) and George VI (Kimura et al., 2015) ice shelves also show stratification in temperature and salinity below the ice. Beneath the Ross Ice Shelf, the absence of a well mixed layer beneath the ice was found to reduce the fit between the three-equation parameterisation and the observed melt rates (Stewart, 2018), and result in a sub-linear dependence of melt rate on thermal driving. The importance of measuring the current speed at an appropriate depth has also been demonstrated. Beneath the Larsen C Ice Shelf, Davis and Nicholls (2019) found that at low flow speeds, when their fixed-depth velocity measurements were taken outside of the log layer, the drag relationship (Eq. 2.4) did not estimate the friction velocity accurately, introducing large errors in the predicted melt rate.

In the present study, there are additional uncertainties due to the steep slope in the ice base. Fig. 2.11 shows the position of the upper microcat on the mooring, as well as the location that where basal melt rates are measured. While the upper microcat is

only at 4 m depth, it is laterally displaced from the location where basal melt rates are measured. Thus, while we consider it likely that the upper microcat temperature and salinity measurements are representative of the ice shelf-ocean boundary layer, horizontal gradients in temperature and salinity may be supported by flow dynamics associated with the steep slope.

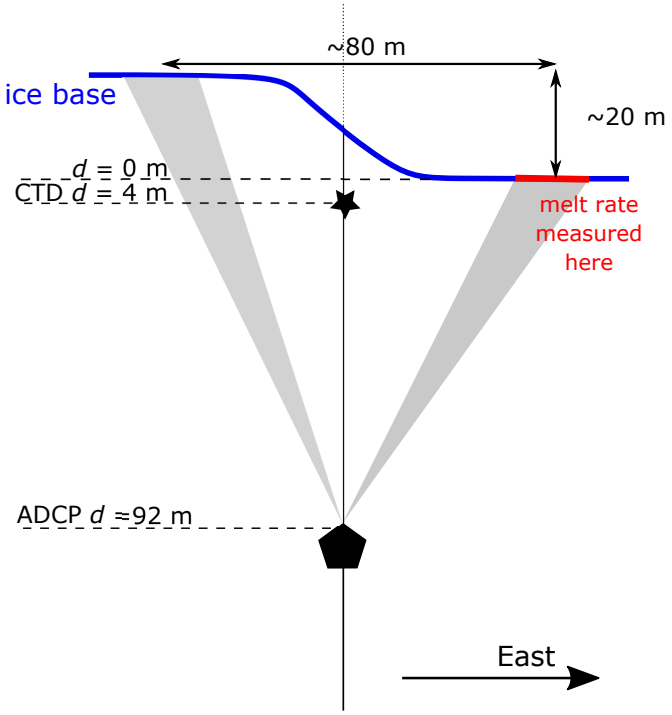

Figure 2.11: Simplified schematic of the ice base and upper water column showing the position of the upper microcat and ADCP.

The problem of correctly identifying the depth at which Θ, S_A and U should be sampled is not limited to observational studies. The numerical models for which these parameterisations were developed are also sensitive to the choice of sampling depth, as well as the way in which the meltwater flux is distributed (Gwyther et al., 2020a). Sampling and distributing meltwater at the upper grid cell introduces a dependence of the melt rate on the grid resolution.

2.5.3 Transfer and drag coefficients

A lack of information about the frictional properties of the ice base at AM06 forces an arbitrary choice of C_d in order to apply the shear-dependent parameterisations to the oceanographic data. This issue is not just specific to our study–in general, C_d is extremely poorly constrained beneath ice shelves (e.g. Gwyther et al., 2015). Furthermore, C_d is often used as a tuning parameter when attempting to reconcile observed and parameterised melt rates (e.g. Jenkins et al., 2010b; Nicholls, 2018). In ice-ocean models, drag coefficients in the range 0.0015–0.003 are typical (e.g. MacAyeal, 1984; Gwyther et al., 2015; Naughten et al., 2018b). Recent turbulence measurements beneath the Larsen C Ice Shelf were used to infer a drag coefficient of $C_d = 0.0022$ at a melting site with a cold, unstratified, tidally forced ISOBL (Davis and Nicholls, 2019). Beneath melting sea ice, values in the range 0.0025–0.01 have been measured (McPhee, 1992), while values in excess of 0.01 have been observed beneath sea ice in the presence of rough platelet ice (Robinson et al., 2017). The drag coefficient $C_d = 0.0097$ recommended by Jenkins et al. (2010b) is within this range of estimates.

In the preceding section, observed melt rates were compared to predictions from the three-equation parameterisation using the constant Stanton number ($\sqrt{C_d}\Gamma_T = 0.0011$) formulation from Jenkins et al. (2010b). This was motivated by the fact that the Stanton number (as opposed to the individual parameters $C_d = 0.0097$ or $\Gamma_T = 0.011$) is the parameter constrained most robustly in their study. However, the turbulence-resolving simulations of Vreugdenhil and Taylor (2019) for melting of smooth, planar ice yielded a remarkably similar transfer coefficient of $\Gamma_T = 0.012$ for their coldest and most energetic (least buoyancy-affected) experiment. They found $\Gamma_T/\Gamma_S = 31$, close to the assumed ratio of 35, while the drag coefficient in the simulation was $C_d = 0.0015$. The similarity between the simulated and observationally-derived transfer coefficients supports the notion of a constant heat transfer coefficient of $\Gamma_T \sim 0.011$ when buoyancy is relatively unimportant. This result suggests that it may be more appropriate to adopt the heat transfer coefficient from Jenkins et al. (2010b), rather than the Stanton number with its implicit drag coefficient.

When surface buoyancy flux due to meltwater is important, heat and salt transfer are reduced. Vreugdenhil and Taylor (2019) showed, for constant friction velocity, that increasing ocean temperatures results in near-ice stratification which decreases the efficiency of heat and salt transfer to the ice. Thus, it is possible that stratification effects

are responsible for the misfit between the parameterised and observed melt rates at AM06. This theme will be further explored in Chapter 5 of this thesis.

2.5.4 Extension to other published studies

In this section the comparison between observed and parameterised melt rates is extended to include other published studies of ice shelf melt rate and *in situ* ocean observations from around Antarctica. Due to limitations in the data available, this comparison is made for the J10 parameterisation only. The observed and parameterised melt rates, mean thermal forcing and current speed at each location are presented in Table 2.5, where the data are sourced from the relevant publications. More detail on the observational data is provided in Appendix B.

The ratio of observed to parameterised melt rates m_{OBS}/m_{J10} is plotted as a function of the local thermal driving and flow speed in Fig. 2.12. The misfit between the J10 parameterisation and observations is widespread. For the majority of sites m_{OBS}/m_{J10} is less than 1/3, indicating that J10 tends to significantly over-predict melt rates. The exceptions to this are beneath the Filchner-Ronne Ice Shelf (FRIS), to which the transfer coefficients were tuned, and the Larsen C Ice Shelf (Davis and Nicholls, 2019). Both the FRIS and Larsen C sites are characterised by low thermal driving ($T^* \sim 0.05$ °C) and strong, tidally-dominated flow.

For large areas of relevant T^*–U parameter space, J10 does a poor job of capturing the observed melt rates. Beneath George VI Ice Shelf, where thermal driving is extremely high, predicted melt rates are ∼50 times larger than observed ($m_{OBS}/m_{J10} = 0.02$). At this site, a thermohaline staircase (which is indicative of double-diffusive convection) was observed (Kimura et al., 2015). Similarly, it was suggested that double-diffusive convection may play a role in melting at the grounding line of the Ross Ice Shelf (Begeman et al., 2018). At this site, current speeds are extremely small ($U \sim 1.0$ cm s^{-1}), while thermal driving is moderate ($T^* \sim 0.1$ °C). Thus, both these sites are characterised by strong thermal forcing relative to the current speed. The misfit between parameterised and observed melt rates may be explained by stratification, which decreases the efficiency of heat transport to the ice (Vreugdenhil and Taylor, 2019). Alternatively, another process such as convection (Kerr and McConnochie, 2015; Mondal et al., 2019) or double-diffusive convection (Kimura et al., 2015; Keitzl et al., 2016b) may dominate over current shear in determining the melt rate for some of the observed conditions.

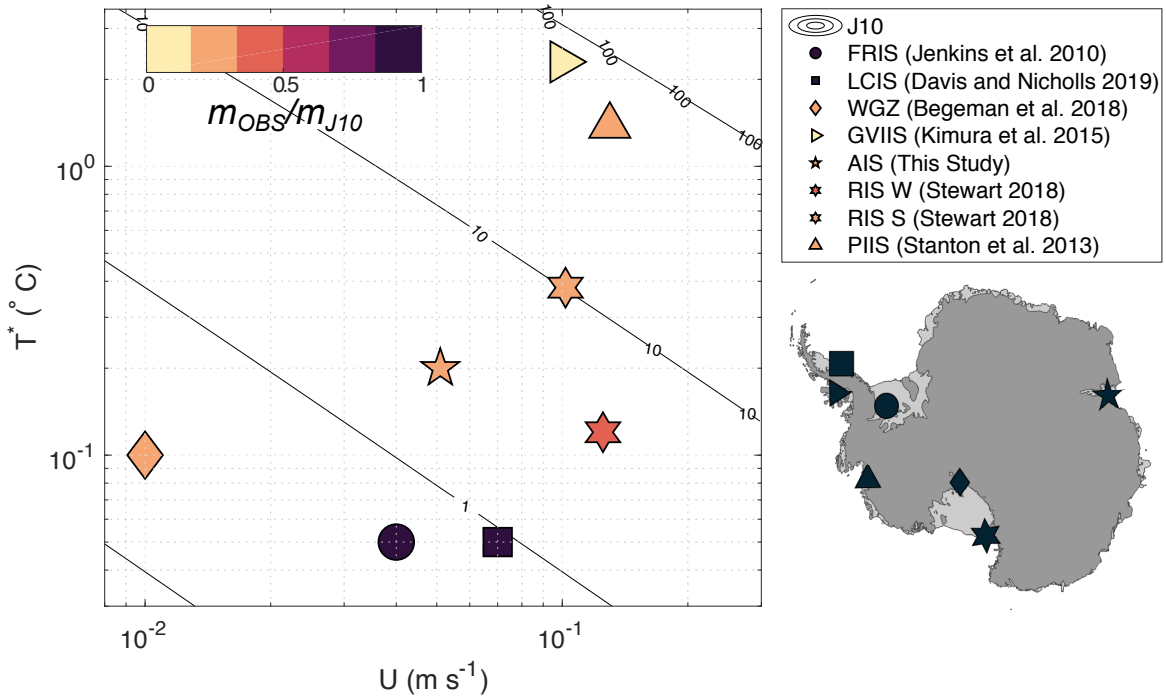

Figure 2.12: Ratio of observed to predicted melt rate for the J10 parameterisation as a function of thermal driving T^* and free stream velocity U for published ice shelf datasets. Map shows the location of the observations.

The Amery (this study) and Ross Ice Shelves (Stewart, 2018) are both "cold" ice shelf cavities characterised by the presence of DSW and, in the case of the Ross Ice Shelf, AASW. As such, the thermal driving is only moderate ($T^* < 0.5$°C). Furthermore, the current speeds are similar to those observed beneath Larsen C and Filchner-Ronne ice shelves. However, the melt rates at these locations are over-predicted by 300% to 400% by the J10 parameterisation.

2.6 Summary and conclusions

We have presented a year-long record of observations of the melting and oceanographic environment beneath the AIS in East Antarctica. Ocean temperatures, which were consistently greater than the *in situ* freezing temperature, resulted in year-round melting with a mean value of 0.51±0.18 m yr^{-1}, consistent with previous glaciological and modelling estimates. The water mass present is ISW with DSW, a product of sea ice formation, as its source water mass. Temperature, salinity and melt rate vary seasonally.

Table 2.5: Comparison between observed and predicted melt rates for a series of Antarctic ice shelves for which both melt rates and *in situ* oceanographic data are available. Observed variables presented are the time-mean current speed ($\bar{u}$), thermal driving ($\bar{T}^*$) and melt rate (m_{OBS}). Melt rate predictions made from J10 are also presented for each site. Where they are in bold, we have used the estimate from the original study. See Appendix B for further information on the data. $^{\leftrightarrow}$ Sites with a strong tidal component to the flow.

location	period	$\bar{U}$ (cm s^{-1})	$\bar{u^*}$ (cm s^{-1})	$\bar{T}^*$ (°C)	m_{OBS} (m yr^{-1})	m_{J10} (m yr^{-1})
AIS (this study)	Apr–Nov 2010	$4.0^{\leftrightarrow}$		0.20	0.46	1.9
FRIS (Jenkins et al., 2010b)	Jan–Dec 2001	$4.0^{\leftrightarrow}$		0.05	0.554±0.006	**0.553**
LCIS (Davis and Nicholls, 2019)	Dec 2011 – Feb 2013	$7.0^{\leftrightarrow}$	0.33^a	0.05	0.7±1.0	$\mathbf{0.69 \pm 0.6}$
George VI (Kimura et al., 2015)	Jan 2012	10.0		2.3	1.4	71
RIS S (Stewart, 2018) I	Dec–Mar 2012–14	$10.2^{\leftrightarrow}$		0.38	2.7	10
RIS W(Stewart, 2018) II	Apr–Nov 2011–14	$12.5^{\leftrightarrow}$		0.12	1.4	3.8
PIIS (Stanton et al., 2013)	Dec 2012	13.0	0.86	1.39	14.6	50
WGZ (RIS) (Begeman et al., 2018)	Jan 2015	1.0		0.1	0.05	0.24^b

[a] Calculated from $\bar{U}$ and observed drag coefficient $C_d = 0.0022$.

[b] This value differs from the reported value of 0.15 in Begeman et al. (2018). The discrepancy may be due to the inclusion of the conductive ice shelf heat flux by Begeman et al. (2018) or the use of a different drag coefficient other than the $C_d = 0.0097$ suggested in Jenkins et al. (2010b).

2.6. SUMMARY AND CONCLUSIONS

The warmest conditions and highest melt rates were observed in the Austral autumn and the coolest, lowest-melt conditions occurred in the Austral spring. The springtime minimum in melt is coincident with the most highly meltwater-modified conditions at AM06, suggesting a link between high melting elsewhere in the cavity and low melting at AM06.

Flow at AM06 is oriented into the AIS cavity, even near the surface, consistent with a "three dimensional" picture of cavity circulation with DSW inflow on the eastern flank of the cavity being balanced by the outflow of ISW in the west. The currents at AM06 have both a tidal and residual component. The annual average residual flow speed is 3.2 cm s^{-1} at 220 °N, roughly normal to the calving front. The tidal currents have mixed semi-diurnal and diurnal properties and are responsible for current speeds of ∼10 cm s^{-1}. The tidal and mean flow combined can result in peak flow speeds of ∼ 15.0 cm s^{-1}. In addition, we mapped a large (∼20 m in height) step-like feature in the base of the ice shelf above the mooring.

In situ oceanographic and melt rate observations were used to evaluate common ice-ocean parameterisations. Despite the presence of tidal currents, we found that the convective, ice shelf-slope dependent parameterisation of McConnochie and Kerr (2018) performed relatively well at AM06, underestimating observed melt rates by ∼20%. We also tested the velocity dependent three-equation parameterisation with two different turbulent transfer expressions. The constant Stanton number parameterisation from Jenkins et al. (2010b) overestimated melting by 400%, while the expression from McPhee et al. (1987) overestimated the melt rate at AM06 by 200% using a drag coefficient of 0.0025. Extension of our analysis to other published studies of *in situ* oceanographic data demonstrated that the misfit between the Jenkins et al. (2010b) parameterisation and observations is widespread in temperature-velocity space: the parameterisation only performs well under the coldest, most energetic conditions. Previous studies have shown that this parameterisation performs poorly for warm and/or quiescent conditions. However, here we have shown that even "cold cavity" ice shelves such as the Ross and Amery Ice Shelves, which have strong currents and only moderate (0.1–0.5 °C) thermal driving, are not well represented by this parameterisation. Further work remains to understand the effects of buoyancy on the ISOBL.

Chapter 3

The role of double-diffusive convection in basal melting of Antarctic ice shelves

Abstract

The Antarctic Ice Sheet loses about half its mass through ocean-driven melting of its fringing ice shelves. However, the ocean processes governing ice shelf melting are not well understood, contributing to uncertainty in projections of Antarctica's contribution to global sea level. We use high resolution large-eddy simulation to examine ocean driven melt in the first geophysical-scale model of the turbulent ice shelf-ocean boundary layer, focusing on the ocean conditions observed beneath the Ross Ice Shelf. We quantify the role of double-diffusive convection in determining ice shelf melt rates and oceanic mixed layer properties in moderately warm and low velocity cavity environments. We demonstrate that double-diffusive convection is the first order process controlling the melt rate and mixed layer evolution at these flow conditions, even more important than vertical shear due to a mean flow, and is responsible for the step-like temperature and salinity structure, or thermohaline staircase, observed beneath the ice. A robust feature of the multi-day simulations is a growing saline diffusive sublayer adjacent to the ice-ocean interface that drives a time-dependent melt rate. This melt rate is lower than current ice-ocean parameterisations, which consider only shear-controlled turbulent melting, would predict. Our main finding is that double-diffusive convection is an important process beneath ice shelves, yet is currently neglected in ocean-climate models.

3.1 Introduction

Ocean driven basal melting, which comprises more than half of the mass loss from Antarctica's ice shelves (Depoorter et al., 2013; Rignot et al., 2013), is thinning the Antarctic

Ice Sheet at an accelerating rate (Paolo et al., 2015; Shepherd et al., 2018). The rate of loss of grounded ice mass from West Antarctica alone has increased by 70% since 2002 (Paolo et al., 2015). Consequently, the Antarctic contribution to global sea level is accelerating, presenting a major threat to coastal regions (Cazenave and Llovel, 2010). Melting of ice shelves is also contributing a freshwater flux to the ocean which has a major impact on the production of Antarctic Bottom Water which supplies the lower limb of the global thermohaline circulation (De Lavergne et al., 2014). Understanding the fine-scale processes by which ocean and ice shelves interact, and how they depend on surrounding water properties, is essential for accurately predicting the response of the Antarctic Ice Sheet to a changing climate.

Where the ocean meets the ice shelf a boundary layer forms which regulates heat and salt exchanges between the far-field ocean and the ice, and is crucial in determining the rate at which the ice shelf melts. Predicting basal melt rates therefore requires knowledge not only of the ocean properties within the ice shelf cavity but also the processes controlling transport of heat and salt across the ice-ocean boundary layer (Dinniman et al., 2016). Basal melt projections of Antarctic ice shelves rely exclusively on numerical studies using large-scale Reynolds-Averaged Navier Stokes (RANS) models (Gwyther et al., 2016; Galton-Fenzi et al., 2012). However, the difficulty in accessing the sub-ice shelf environment to observe fine-scale boundary layer processes means that there are few observational constraints on how basal melting should be represented in these models.

RANS models of ice shelf cavities resolve flow at horizontal scales of several hundred meters and vertical scales of meters at best. These scales are too coarse to capture ice-ocean boundary layer processes, which must instead be represented using parameterisations. These parameterisations typically assume that melt is controlled by the shear (velocity gradient) induced by large-scale currents or buoyant plumes (McPhee et al., 1987; Jenkins, 1991; Holland and Jenkins, 1999) and set the melt rate as proportional to the plume or current velocity (Jenkins et al., 2010b). This common approach has not been validated beneath an ice shelf, nor can it be ubiquitously applicable; a counter example being a run without any mean flow in which melting still takes place (Gwyther et al., 2016; Keitzl et al., 2016b). Recent laboratory (McConnochie and Kerr, 2016b), turbulence resolving numerical (Gayen et al., 2016; Mondal et al., 2019) and theoretical (Wells and Worster, 2008; Kerr and McConnochie, 2015) studies have focused on the melting of sloping or vertical ice, for which meltwater drives a buoyant plume along the ice, finding

that the melt rate is controlled by the elevation of ambient temperature above the *in situ* freezing temperature and is independent of the plume velocity, providing that the velocity is sufficiently low (Wells and Worster, 2008; McConnochie and Kerr, 2017b).

Under certain ocean conditions, the differing diffusivities of heat and salt give rise to a type of convection known as double-diffusive convection (DDC) (Turner, 1974; Radko, 2013). Melting of ice shelves releases cold, fresh water above warm, salty water which can drive a type of DDC known as diffusive convection (DC), so-named to distinguish it from salt fingering (SF) -type DDC in which salinity is the destabilising component (Kelley et al., 2003). DC can form "diffusive staircases" composed of well-mixed layers separated by sharp interfaces. Diffusive staircases have primarily been observed in polar regions such as the Arctic Ocean (Timmermans et al., 2008), the Weddell Sea in Antarctica (Robertson et al., 1995) and beneath George VI Ice Shelf in Antarctica (Kimura et al., 2015). Recent observations from the grounding line of the Ross Ice Shelf are also consistent with DC (Begeman et al., 2018), where well-mixed layers in temperature and salinity were observed over the 10 m thick water column. Both ice shelf sites recorded melt rates that were much lower than common ice-ocean parameterisations—which assume turbulent, unstratified flow–would predict given the observed ocean conditions. DC has been investigated in small-scale experimental (Martin and Kauffman, 1977) and modelling (Keitzl et al., 2016b) studies of ocean-driven melting of horizontal ice. However, the role of DC remains unclear in the presence of competing processes such as turbulence and mixing due to ocean currents beneath the ice. Importantly, RANS ocean models do not capture the effect of DC on basal melting, leading to uncertainties in basal melting projections. Convection-resolving numerical simulations are urgently needed to quantify the effect of DC in ice-ocean interactions and develop parameterisations for use in RANS models.

High resolution modelling techniques such as direct numerical simulation (DNS) and large-eddy simulation (LES) are being recognised for their capabilities in resolving and quantifying ice-ocean boundary layer processes. For example, a recent DNS study demonstrated that DC can drive turbulent fluxes of heat and salt beneath the ice (Keitzl et al., 2016b). LES has been used to study the effect of current shear and ocean temperature on basal melting, demonstrating that stratification can inhibit the transport of heat and salt across the ice shelf-ocean boundary layer under warm and/or low-shear conditions (Vreugdenhil and Taylor, 2019). However, no studies to date have investigated the feedback between mixed layer dynamics and melting for a stratified, geostrophic boundary

layer, resolving both the near-ice and mixed layer processes.

Here we investigate the processes controlling ice shelf basal melting by modelling the turbulent geostrophic boundary layer beneath an ice shelf. Using LES, we perform experiments that demonstrate the dominant role of DC in ice shelf-ocean interactions at some observed Antarctic conditions. The melting and boundary layer structure in our numerical model agrees with field observations of the water column and melting beneath the Ross Ice Shelf (Begeman et al., 2018), and allow us to explain the mechanism connecting the ocean state to the basal melt rate.

3.2 Methods

To examine the relative importance of current shear and DC in determining flow structure, turbulent transport and melting beneath an ice shelf, we perform a series of simulations of the ice shelf-ocean boundary layer, varying far-field flow speed (U_0=0.0–2.0 cm s^{-1}) and temperature ($T_0 = -1.9, -2.1$ °C). The model domain consists of a planar, horizontal ice-ocean interface, at which a dynamic melt condition is imposed, over a polar ocean. A schematic of the model domain is shown in Fig. 3.1. The water column is stratified in temperature (T) and salinity (S), with cold, fresh water overlying warmer, saltier water and a stable density stratification. This configuration is consistent with available observations from beneath ice shelves, where the addition of meltwater cools and freshens the ocean nearest the ice. Model runs are initialised with linear temperature ($T_{bg} = T_0 - 9.5 \times 10^{-4} z$ °C) and salinity ($S_{bg} = S_0 - 4.0 \times 10^{-4} z$ g kg^{-1}) profiles. The flow velocities in x, y and z directions are u, v and w respectively. The Coriolis parameter $f = -1.37 \times 10^{-3}$ s^{-1} is constant within the domain. In the interior of the domain, the flow is in geostrophic balance, and an Ekman boundary layer forms beneath the ice.

3.2.1 Governing equations

The simulations solve the incompressible, non-hydrostatic Navier-Stokes momentum equation under the Boussinesq approximation along with the conservation of mass, heat and salt, and a linear equation of state. In dimensional form, these equations are:

$$\nabla \cdot \mathbf{u} = 0 \tag{3.1}$$

$$\frac{D\mathbf{u}}{Dt} = -\frac{1}{\rho_0}\nabla p_* + f\mathbf{k} \times \mathbf{u} + \nu\nabla^2\mathbf{u} - \frac{\rho_*}{\rho_0} g\mathbf{k} - \nabla \cdot \boldsymbol{\tau} \tag{3.2}$$

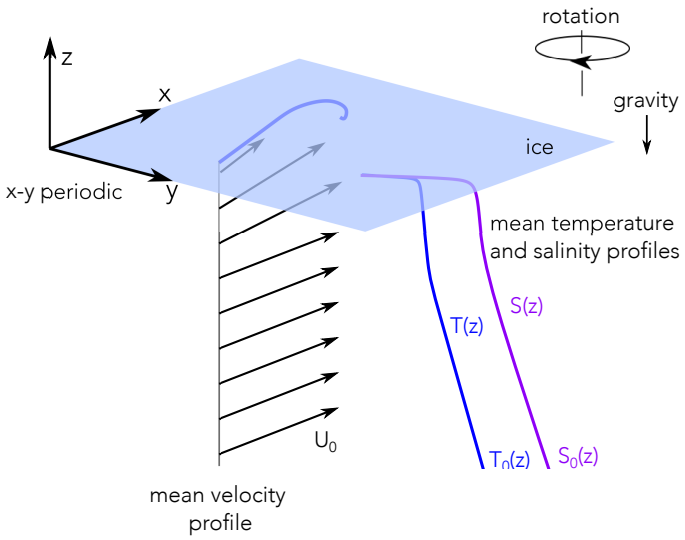

Figure 3.1: Schematic of the model domain, which consists of a horizontal ice-ocean interface with cold, salty ocean below. In the interior of the domain the ocean is in geostrophic balance and has velocity $(u, v) = (U_0, 0)$. Near the ice an Ekman boundary layer forms.

$$\frac{DT_*}{Dt} = \kappa_T \nabla^2 T_* - \nabla \cdot \boldsymbol{\lambda}^T - w \frac{dT_{bg}}{dz} \tag{3.3}$$

$$\frac{DS_*}{Dt} = \kappa_S \nabla^2 S_* - \nabla \cdot \boldsymbol{\lambda}^S - w \frac{dS_{bg}}{dz} \tag{3.4}$$

$$\rho_* = \rho_0(\beta S_* - \alpha T_*) \tag{3.5}$$

Here $\mathbf{u} = (u, v, w)$ is the flow velocity, p_* and T_*, S_* and ρ_* are the deviations from background hydrostatic pressure p_{bg}, background temperature T_{bg}, salinity S_{bg} and density ρ_{bg} profiles respectively (e.g. $S^* = S - S_{bg}$). The cold, saline water has molecular viscosity $\nu = 2 \times 10^{-6}$ m^2 s^{-1}, thermal diffusivity $\kappa_T = 1.4 \times 10^{-7}$ m^2 s^{-1}, salt diffusivity $\kappa_S = 1.3 \times 10^{-9}$ m^2 s^{-1}, thermal expansion coefficient $\alpha = 3.8 \times 10^{-5}$ °C^{-1} and haline contraction coefficient $\beta = 7.8 \times 10^{-4}$ kg g^{-1}, where these values are chosen to be appropriate for the polar ocean. The quantities $\boldsymbol{\tau}$, $\boldsymbol{\lambda}^T$ and $\boldsymbol{\lambda}^S$ are the subgrid-scale stress tensor and temperature and salinity flux vectors respectively. The subgrid-scale stress tensor is represented with a dynamic eddy viscosity model and the subgrid salinity/temperature fluxes with a dynamic eddy diffusivity model. The expressions for the subgrid-scale models are as follows:

$$\tau_{ij} = -2\nu_T \overline{M_{ij}}, \qquad \nu_T = C\overline{\Delta}^2 |\overline{\mathbf{M}}| \tag{3.6}$$

$$\lambda_j^T = -K_T \frac{\partial \overline{T}}{\partial x_j}, \qquad K_T = C^T \overline{\Delta}^2 |\overline{\mathbf{M}}| \tag{3.7}$$

$$\lambda_j^S = -K_S \frac{\partial \overline{S}}{\partial x_j}, \qquad K_S = C^S \overline{\Delta}^2 |\overline{\mathbf{M}}| \tag{3.8}$$

where M_{ij} is the strain tensor and Δ is the filter width. Smagorinsky coefficients C, C^T and C^S are evaluated through a dynamic procedure introduced by Germano et al. (1991).

3.2.2 Numerical method

The simulations use a mixed spectral/finite difference algorithm (see Bewely, 2008, for details). Spanwise derivatives are treated with a pseudo-spectral method, and the wall normal spatial derivatives are computed with second order finite differences. A third-order Runge-Kutta method is used for time stepping, and viscous terms are treated implicitly with the Crank-Nicholson method. Variable time stepping with a fixed CFL number of 0.9 is used, with typical time steps on the order of 1 s for $U_0 = 0.014$ m s^{-1} runs. Periodicity is imposed in the horizontal x and y directions. The upper (ice-water) and lower boundaries are subject to no-penetration conditions, and are no-slip and free-slip respectively. At the upper boundary, temperature and salinity are given by the melting boundary condition, while at the lower boundary they are relaxed back to initial profiles in a sponge region, maintaining an "open" boundary. Within the sponge layer, all fluctuations of velocity, salinity and temperature are suppressed. Detailed implementation of the sponge layer can be found in Gayen et al. (2010).

The melt rate m is calculated following Gayen et al. (2016). Oceanic heat and salt fluxes to the interface are balanced by the latent heat and brine fluxes due to melting, yielding the balances:

$$\rho_i L_f m = -\rho c_p \kappa_T \left.\frac{\partial T}{\partial z}\right|_b \tag{3.9}$$

$$\rho_i S_b m = -\rho \kappa_S \left.\frac{\partial S}{\partial z}\right|_b, \tag{3.10}$$

where $(\partial T/\partial z)_b$ (°C m^{-1}) and $(\partial S/\partial z)_b$ (g kg^{-1} m^{-1}) are the temperature and salinity gradients at the interface, $c_p = 4.18 \times 10^3$ (J kg^{-1} K^{-1}) is the heat capacity of seawater, $L_f = 3.35 \times 10^5$ (J kg^{-1}) is the latent heat of melting, and $\rho = 1030$ kg m^{-3} and $\rho_i = 917$ kg m^{-3} are the density of water and ice respectively. The relationship $T_b = aS_b + b$ is used to relate the freezing temperature T_b to the interface salinity S_b, where $a = -0.057$

°C kg g^{-1} is the liquidus slope and $b = -0.311$ °C accounts for freezing point depression due to a pressure of 500 dbar. The ice-ocean interface is fixed in space and remains planar, and there is an infinite supply of ice to be melted.

A geostrophic balance of $1/\rho_0(\partial p/\partial y) = -fU_0$ holds in the interior of the flow, and forms an Ekman boundary layer near the ice. As the model domain is periodic in both horizontal directions, the mean vertical motion is constrained to zero. Therefore, the features of oceanic boundary layers owing to Ekman pumping/suction driven by large-scale horizontal gradients in the ambient flow are not present in these simulations.

3.2.3 Domain and initialisation

The domain size is based upon the planetary scale $\delta_f = u_0^*/f$ where f (s^{-1}) is the Coriolis frequency and u_0^* (m s^{-1}) is the friction velocity, estimated *a priori* using the drag law relationship $u_0^* = C_d^{1/2}U_0$ taking $C_d = 0.0025$. The domain size $LX \times LY \times LZ$ is $LX, LY, LZ = 2\delta, 2\delta, 3\delta$ at a minimum. For example, for $U_0 = 1.4$ cm s^{-1} the rotational boundary layer scale is $\delta = 5$ m and the domain size is $10 \times 10 \times 25$ m. Domain sizes for all cases are outlined in Table 3.1. The LES is performed using a grid that is uniform in both the x and y directions and stretched in the z direction to achieve higher resolution near the boundary.

Table 3.1: Domain and grid size for the simulations performed. Dimensions of domain (LX, LY, LZ); number of grid points (NX, NY, NZ); grid spacing in wall units $(\Delta X^+, \Delta Y^+, \Delta Z^+)$.

run	LX, LY (m)	LZ (m)	NX, NY	NZ (m)	$\Delta X^+, \Delta Y^+$	ΔZ^+_{min}
1	5	25	64	641	$\sim$	$\sim$
2	5	25	64	641	14	0.16
3,3*	10	25	128	641	27	0.32
4	14	25	256	641	27	0.5

The grid resolution is expressed in wall units as $\Delta X^+ = \Delta X/\delta_\nu$, with ΔY^+ and ΔZ^+ equivalently defined, where δ_ν is the viscous lengthscale $\delta_\nu = \nu/u_0^*$. The resolution for each simulation, which is based on the results of Salon et al. (2007), is found in Table 3.1. The horizontal resolution $\Delta X^+ = \Delta Y^+ = 27$ was found to be sufficient due to convergence of the friction velocity and interfacial heat flux (Appendix A.2). Crucially, stretching of the model grid in the vertical direction gives sufficiently high (mm-scale) resolution to capture the near-ice diffusive sublayers, which are thin due to the realistic

κ_T and κ_S. Furthermore, high resolution is also needed over the mixed layer in order to capture the steep gradients in temperature and salinity associated with DC layers. The grid cell vertical-to-horizontal aspect ratio at the edge of the viscous sublayer was not found to influence the solution significantly over the range 1/30–1/7, and is between 1/20 and 1/26 for all experiments (Appendix A.2). Finally, at quasi-steady state (when the time rate of change of Turbulence Kinetic Energy goes to zero), the remaining terms in the TKE budget are integrated vertically and compared, to ensure closure (Appendix A.1).

Free stream velocity (U_0) and initial temperature (T_0) are varied between runs, where each T_0 has a corresponding initial thermal driving $T_0^* = T_0 - T_f(S_0)$, where $T_f(S_0)$ is the freezing temperature at salinity S_0. We investigate thermal and current forcing encompassing $U_0 = 0.0,\ 0.7,\ 1.4$ and 2.0 cm s^{-1} and $T^* = 0.175$ and 0.375 °C. For each run, a neutral (unstratified) spin-up run is performed to obtain the velocity field of a steady-state turbulent Ekman boundary layer. At model time $t = 0$ h, the initial temperature and salinity profiles are applied, after which time the temperature, salinity and velocity fields co-evolve. The simulations are run for a minimum of 100 h.

3.3 Results

Beneath the ice, a boundary layer develops which consists of a cm-scale laminar sublayer beneath the ice and a turbulent region below. This turbulence homogenizes the temperature and salinity to form a mixed layer. The mixed layer properties are important in determining the melt rate, as the mixed layer may isolate the ice from warmer far-field temperatures. In run 3, with far-field current speed U_0=1.4 cm s^{-1}, a complex boundary layer structure and mixed layer are present beneath the ice (Fig. 3.2). The effect of rotation is visible in the generation of a cross stream (v) component of velocity near the surface. The temperature field shows a layer of relatively cold and actively mixing water just beneath the ice. A thermocline is present ∼2.5 m from the ice, separating this region from the warmer and thermally stratified ocean below. The mixed layer is also visible in the vertical velocity field, where it is associated with three-dimensional small-scale structures ("eddies"). These small-scale turbulent structures influence the spatial pattern of melting, as shown in the simulated melt rate at the ice-ocean interface, and transfer energy into the stratified interior by internal gravity waves. The impingement of turbulent eddies on the strong density gradient (pycnocline) beneath the mixed layer

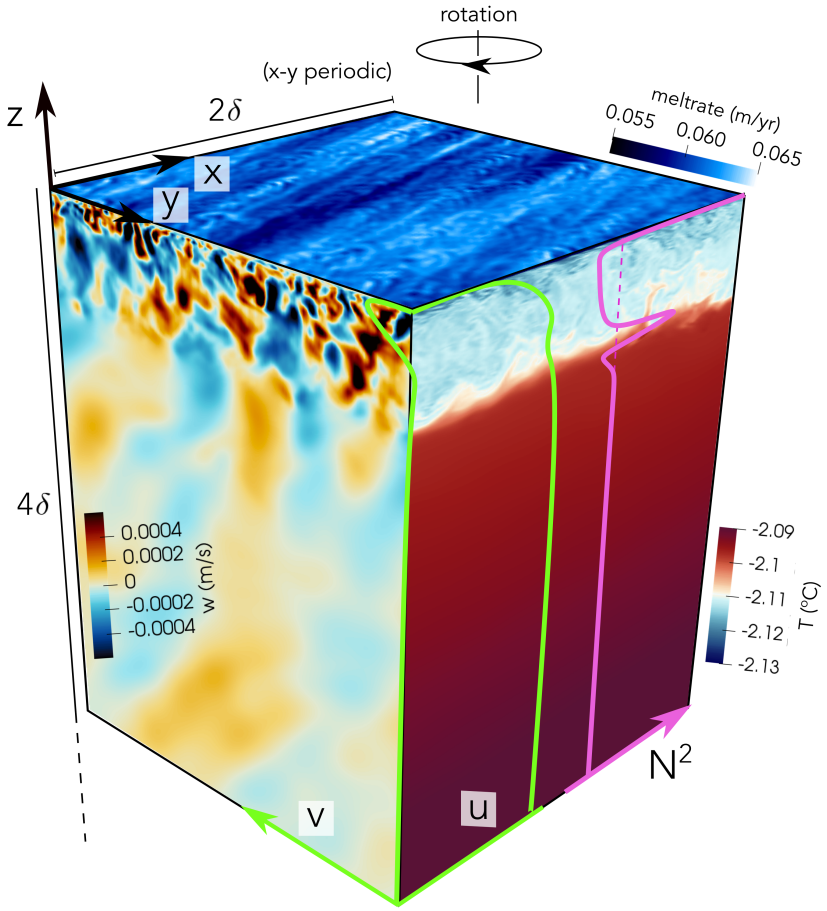

Figure 3.2: Overview of the model domain with flow and melt rate solutions for run 3. The upper $x-y$ surface shows the instantaneous melt rate m, while vertical $y-z$ and $x-z$ planes show the vertical velocity w and temperature T fields respectively. Overlaid are the horizontal velocity profiles (u, v: green solid lines) and buoyancy frequency squared at $t = 0$ h (N_0^2: pink dashed line) and $t = 30$ h (N^2: pink solid line) where $N = (-g/\rho_0(\partial\rho/\partial z))^{1/2}$ is the buoyancy frequency. Unless otherwise stated, all planes and profiles are from $t = 30$ h.

Table 3.2: Free stream velocity (U_0) , reference temperature (T_0), friction velocity ($u^* = (\tau_w/\rho_0)^{1/2}$, where τ_w is the shear stress at the ice-ocean interface), thermal driving ($T^* \equiv T_{ML} - T_f(S_{ML}, p_b)$, the temperature difference between the mixed layer and the freezing temperature at mixed layer salinity and interface pressure), temperature difference between the mixed layer and interface ($\Delta T = T_{ML} - T_b$) and melt rate (m). Overbar denotes quantities that are averaged over 50–100 h. #Observations reported in Begeman et al. (2018), from the period 05 Jan 2015–20 Jan 2015.

run	U_0 (cm s^{-1})	T_0 (°C)	$\overline{u^*}$ (cm s^{-1})	$\overline{T^*}$ (°C)	$\overline{\Delta T}$ (°C)	$\overline{m}$ (m yr $^{-1}$)
1	0.0	-2.1	$\sim$	0.163	0.072	0.042
2	0.7	-2.1	0.033	0.163	0.070	0.044
3	1.4	-2.1	0.050	0.156	0.061	0.045
3*	1.4	-1.9	0.049	0.352	0.147	0.103
4	2.0	-2.1	0.061	0.130	0.048	0.037
Obs#	1.3–1.5	-2.3 (±0.01)	$\sim$	$\sim$	0.1 (±0.01)	0.053 (±0.023)

excites these internal gravity waves, visible as the inclined, large wavelength, periodic fluctuations in the vertical velocity field. These internal waves are analogous to those generated by benthic boundary layers in stratified environments (Taylor and Sarkar, 2007; Gayen et al., 2010).

3.3.1 Diffusive convection beneath a melting ice shelf

The proposed mechanism for diffusive convection beneath a melting ice shelf is described here with the aid of Fig. 3.4. Melting cools and freshens the seawater beneath an ice shelf. For a horizontal ice shelf base, cooling will tend to destabilise the water column by producing top-heavy stratification, while the freshening will tend to stabilise the water column. Close to the ice-ocean interface, the freshening overwhelms the cooling and the water is stably stratified. However, the differential diffusion of heat and salt (the ratio of their diffusivities is $\kappa_T/\kappa_S = 110$) allows the thermal diffusive boundary layer to grow more quickly than its saline counterpart, creating an unstable density boundary layer that results in convective overturning (Martin and Kauffman, 1977). This mechanism is equivalent to the "diffusive interface" between two well-mixed layers in a diffusive staircase, which consists of a stable diffusive sublayer (sometimes called a "core") with convective boundary layers either side (Linden and Shirtcliffe, 1978; Worster, 2004; Carpenter et al., 2012).

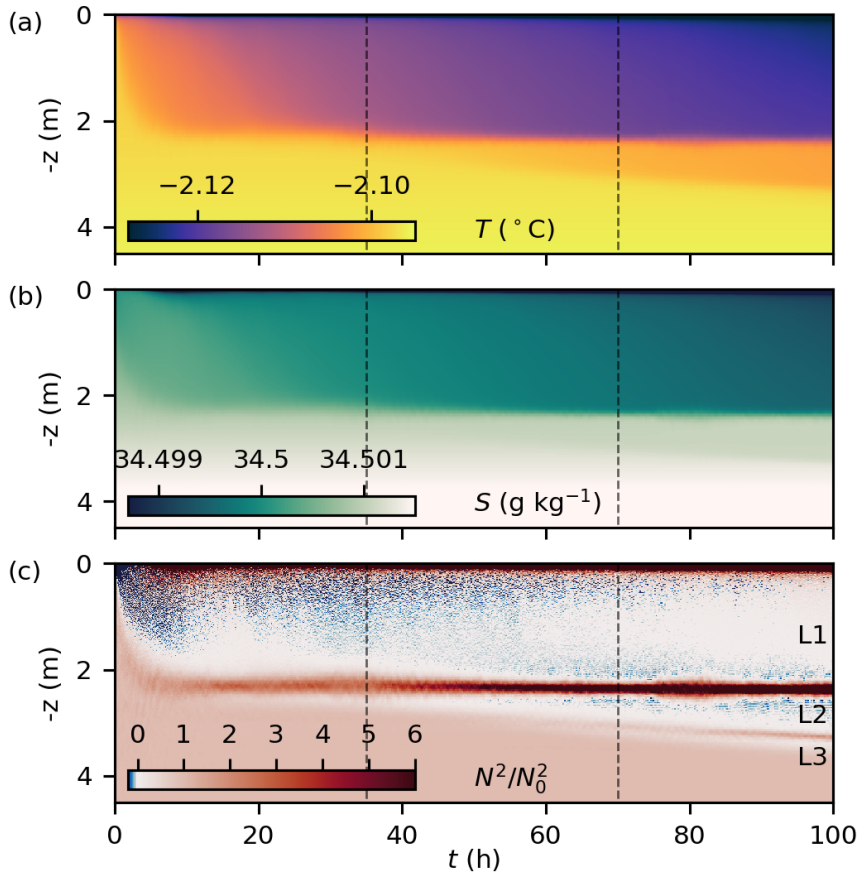

Figure 3.3: Temporal evolution of the water column for run 3. (a) Plane averaged temperature; (b) salinity; and (c) normalised buoyancy frequency N^2/N_0^2 over the upper water column through time. The mixed layers that emerge over the course of the experiment are annotated as L1, L2 and L3.

In this section we demonstrate the role of DC in basal melting and mixing beneath an ice shelf. We present qualitative and quantitative evidence for DC based on the thermohaline structure beneath the ice, density ratio and buoyancy flux.

Thermohaline structure

A mixed layer establishes rapidly at the beginning of the experiment (Fig. 3.3). The stratification of the water column is characterised by the normalised buoyancy frequency squared N^2/N_0^2, where $N = (-g/\rho_0(\partial\rho/\partial z))^{1/2} \sim [g/\rho_0(\alpha(\partial T/\partial z) - \beta(\partial S/\partial z))]^{1/2}$ (s^{-1}) is the buoyancy frequency, ρ_0 (kg m^{-3}) is the reference density, g (m s^{-2}) is the gravi-

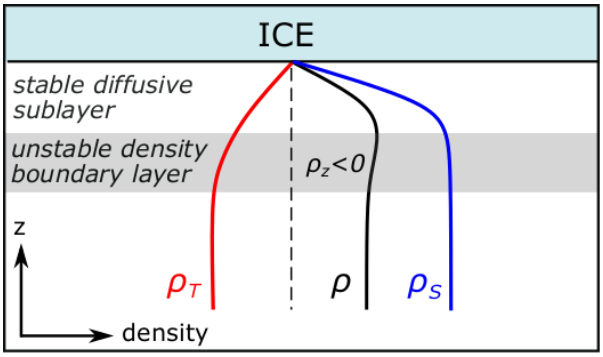

Figure 3.4: Schematic of the proposed mechanism for DC beneath a melting ice shelf, where ρ_T and ρ_S are density contributions from temperature and salinity respectively. The thermal diffusive boundary layer is thicker than its saline counterpart, resulting in a region with a negative density gradient (grey shading) which will overturn.

tational acceleration, and $N_0 = 1.6 \times 10^{-3}$ (s^{-1}) is the far-field stratification. A strongly stratified region ($N^2/N_0^2 \gg 1$) is present adjacent to the ice due to freshening associated with melting. Within this region stratification suppresses turbulence, and heat and salt are transported by molecular diffusion alone. Beneath the diffusive region, the mixed layer is identified by N^2/N_0^2 values which fluctuate around zero (and are frequently negative), indicating instability and convection. The mixed layer is separated from the stratified far-field by a pycnocline, which deepens rapidly during the first ∼10 h of the experiment, after which time the depth remains unchanged. Beneath the primary mixed layer (L1), a second mixed layer (L2) is evident in the temperature, salinity and buoyancy frequency. This layer begins to emerge at $t \sim 15$ h after which time it gradually deepens and shows signs of convection for t 50 h. From t 60 h signs of a third layer (L3) appear (Fig. 3.3c). This "diffusive staircase" structure, with well-mixed layers separated by steep gradients, is one of the hallmarks of DC (Radko, 2013). The layer-by-layer way in which the diffusive staircase forms is qualitatively similar to what is observed when a stable salinity gradient is heated from below (Turner, 1968; Fernando, 1987).

A similar diffusive staircase structure is observed for runs 1, 2, 3* and 3, supporting the idea that DC is responsible for mixing beneath the ice. Comparing the T and S profiles between experiments shows 2–3 well-mixed layers separated by steep gradients in temperature and salinity for runs 1, 2, 3* and 3 (Fig. 3.5). While staircases are not exclusively formed by double-diffusive effects—layering effects have also been observed in one-component stratified flows under weak mixing (Ruddick et al., 1989; Holford and

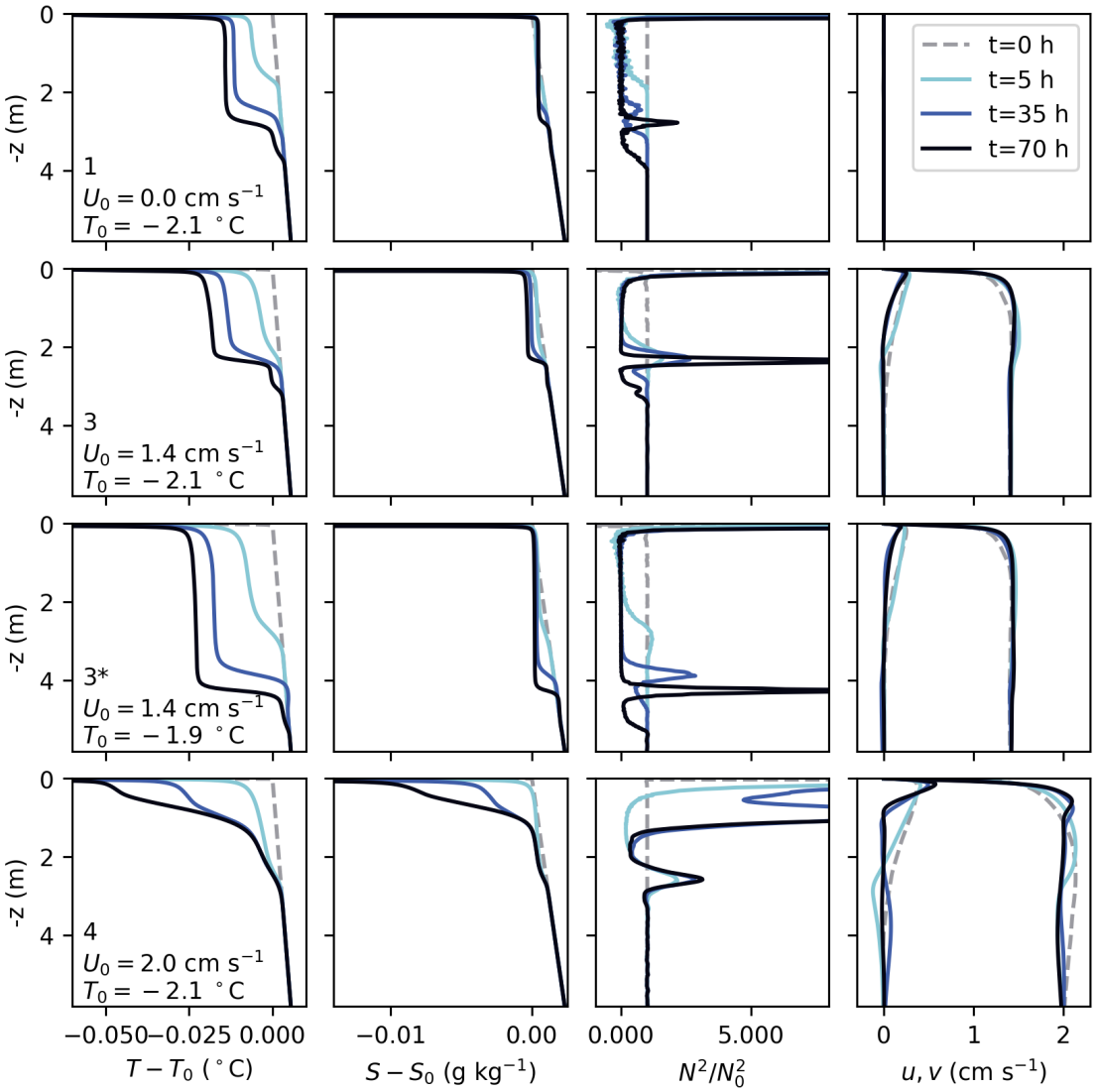

Figure 3.5: Profiles of ocean properties through time. Columns from L–R: temperature T; salinity S; stratification expressed as normalised buoyancy frequency squared N^2/N_0^2; Stream-wise u and cross-stream v velocity. Rows are labelled by experiment. Temperature, salinity and stratification for run 2 (not shown) are extremely similar to run 1.

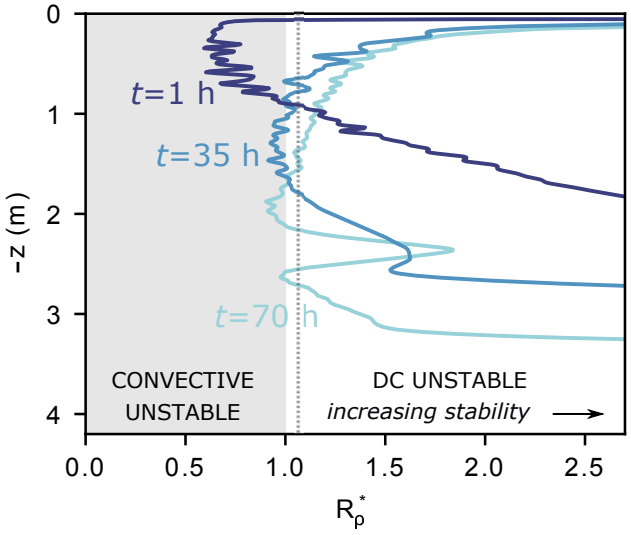

Figure 3.6: Density ratio R_ρ^* as a function of depth for run 3 at $t = 1$ h (dark blue), $t = 35$ h (medium blue) and $t = 70$ h (light blue). Dashed grey line gives the linear stability criterion $R_\rho^* = 1.07$. The initial temperature and salinity conditions give $R_\rho^* = 8.6$.

Linden, 1999) or as a "secondary" interface beneath a mixed layer formed by surface shear stress (Manucharyan and Caulfield, 2015)—there is strong evidence for the role of DC in the present experiments. Our experiments show the same layered structure in both the absence (run 1) and presence (runs 2, 3 and 3*) of vertical shear due to an ambient current, indicating that shear is not responsible for the observed thermohaline structure. The depth of a mixed layer formed by a frictional boundary layer is expected to increase monotonically with increasing free steam velocity (SI §3.5.1). However, we observe no systematic change to mixed layer depth with increasing shear for free stream currents up to 2.0 cm s^{-1}. Instead, the depth of the primary mixed layer depends on ocean temperature. For the same far-field current speed, run 3* with warmer ocean temperatures ($T_0 = -1.9$ °C) has a mixed layer that is nearly twice as deep as run 3 ($T_0 = -2.1$ °C).

For our highest velocity run (4) with $U_0 = 2.0$ cm s^{-1}, we do not observe a series of well-mixed layers. In the following section we will show that shear-generated turbulence has a dominant role in vertical mixing for this run.

Density ratio and buoyancy flux

The density ratio (R_ρ^*), a parameter that characterises T and S stratification as stable, unstable to double diffusion (SF or DC mechanism) or convectively unstable, is given by:

$$R_\rho^* = \frac{\beta \frac{\partial S}{\partial z}}{\alpha \frac{\partial T}{\partial z}}. \tag{3.11}$$

In the present configuration with cold, fresh water overlying warm, salty water the density ratio is positive, with $0 < R_\rho^* < 1$ corresponding to a gravitationally unstable density gradient and R_ρ^* 1 corresponding to T and S gradients that may be DC unstable. Linear stability analysis gives a critical density ratio ($R_{\rho\text{crit}}^*$) below which DC should spontaneously occur, where $R_{\rho\text{crit}}^*$ depends on the Prandtl number (Pr) and the ratio of thermal to saline diffusivity as $R_{\rho\text{crit}}^* = (Pr + 1)/(Pr + \kappa_S/\kappa_T)$ (Radko, 2013). Based on our model parameters $R_{\rho\text{crit}}^* = 1.07$. The initial T and S gradients provide a much larger density ratio ($R_\rho^* = 8.6$), demonstrating that boundary fluxes due to melting are needed for DC to occur at these conditions. Fig. 3.6 shows R_ρ^* for run 3 at three time intervals over the course of the simulation. In all instances the density ratio is extremely high ($R_\rho^* \sim 100$) at the interface, indicating the dominance of salinity stratification in the near-ice region. Beneath this stable region the DC instability criterion ($R_\rho^* < 1.07$) is met. Furthermore, R_ρ^* enters the convectively unstable parameter space, consistent with the mechanism presented in Fig. 3.4 in which a stable region is bounded from below by an unstable density boundary layer. Interestingly, the point at which R_ρ^* meets the linear DC stability criterion moves deeper in the water column over the course of the simulation. At $t = 70$ h the instability criterion is no longer met in the upper part of the mixed layer, however, it is met either side of the pycnocline separating L1 and L2. We will see in the following section that this is indicative that DC is no longer active at the ice-ocean interface, but persists at the interface between L1 and L2. In experimental and observational settings the density ratio is often evaluated using the difference in $T - S$ properties between two consecutive layers. Evaluated in this manner, the density ratio between L1 and L2 at $t = 70$ h is 1.6.

The presence and strength of DDC can be better quantified using the plane-averaged buoyancy flux (buoyancy production) $B = g\alpha\langle w'T'\rangle - g\beta\langle w'S'\rangle$. The buoyancy flux associated with DDC is positive, corresponding to buoyancy as a source of turbulent eddies. Negative B corresponds to buoyancy as a sink of turbulent kinetic energy (TKE), typical of a stratified flow in which mean shear is the primary mechanism for generat-

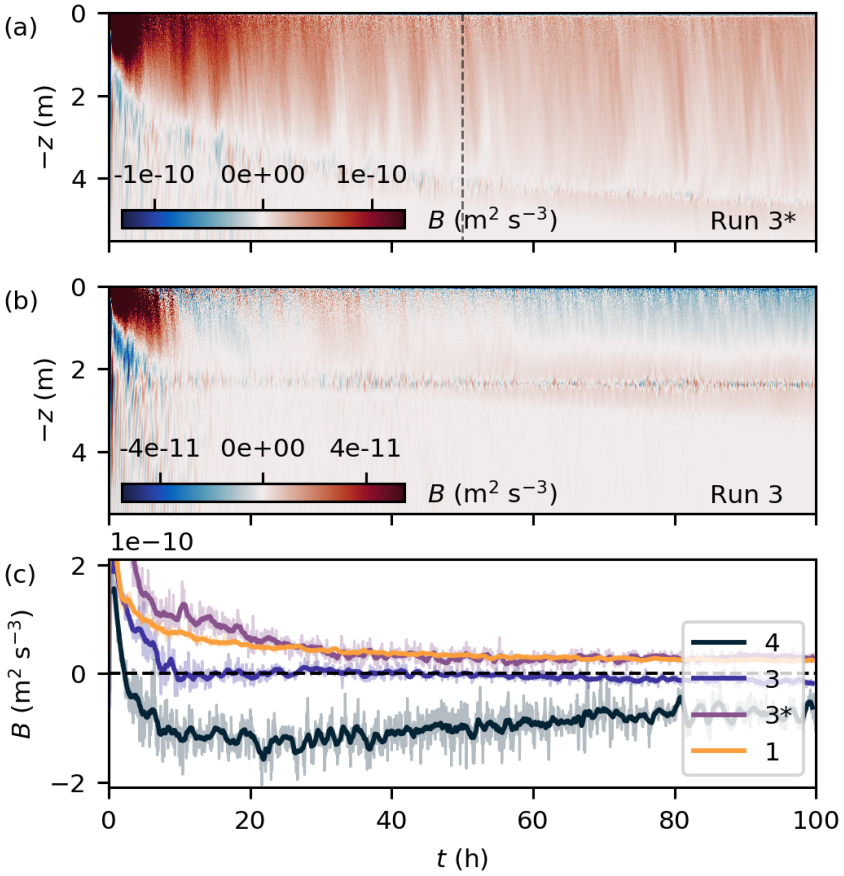

Figure 3.7: Plane-averaged buoyancy flux B as a function of depth and time for (a) run 3* ($U_0 = 1.4$ cm s^{-1}, $T_0^* = 0.375$ °C) and (b) run 3 ($U_0 = 1.4$ cm s^{-1}, $T_0^* = 0.175$ °C). (c) time-series of B at a depth of z=-0.2 m.

ing turbulent eddies (for a full explanation and breakdown of the TKE budget see SI Appendix C). In studies of flows subject to both DDC and shear instability, the sign of B determines which mixing process is dominant Wells and Griffiths (2003); Smyth and Kimura (2011). Buoyancy flux is plotted over depth and time in Fig. 3.7a. For run 3*, B is positive, demonstrating that DC is active beneath the melting ice. Initially B is large, but decreases in strength over the course of the simulation. For run 3, which is subject to the same current forcing ($U_0 = 1.4$ cm s^{-1}) but lower thermal forcing than run 3*, the buoyancy flux is initially positive but changes sign during the simulation (Fig. 3.7b). The initial growth of the mixed layer coincides with a period of positive buoyancy flux, however B becomes persistently negative after $t = 50$ h, indicating a transition to shear-dominated mixing. Notably, in run 3 the pycnocline at the base of L1 is still associated with a positive buoyancy flux. Despite shear-generated turbulence dominating mixing near the ice-ocean interface, DC is still active in the layers below.

The effect of varying U_0 and T_0 on the emergence and persistence of DC is highlighted in Fig. 3.7 which compares B at a depth of $z = -0.2$ m, outside the diffusive sublayer. For runs 1, 2 and 3*, B is positive for the duration of the simulation. For runs 3 and 4, B changes sign over the 100 h simulation period indicating a transition from DC-dominated to shear-dominated mixing. Thus, at fixed ocean temperature, increasing the free stream velocity results in a more rapid transition from DC- to shear-dominated mixing. At fixed free stream velocity, increasing ocean temperature causes DC to dominate mixing for a longer period.

The relative contributions of T and S to buoyancy production B are further broken down as a function of depth for run 3* in Fig. 3.8. The diffusive contribution $B_{diff} = g(-\alpha\kappa_T(\partial T/\partial z)+\beta\kappa_S(\partial S/\partial z))$ is also shown. Fig. 3.8 clearly illustrates the presence of a diffusive sublayer, within which molecular diffusion dominates transport and a turbulent mixed layer below. Due to the configuration of the problem (cold, fresh water over warm, salty water), the temperature contribution to buoyancy is always destabilising, while the salinity contribution is always stabilising. In the diffusive sublayer, the effect of salinity dominates and the buoyancy flux is stabilising overall ($B_{diff} < 0$), while in the mixed layer the thermal contribution is larger and the buoyancy flux is positive ($B > 0$). The diffusive and turbulent buoyancy flux contributions from heat are close in magnitude, indicating that the molecular diffusion of heat at the interface is in approximate balance with turbulent heat transport in the mixed layer. However, this is not true for the salt flux, which is much higher in the diffusive sublayer than the mixed layer. This imbalance

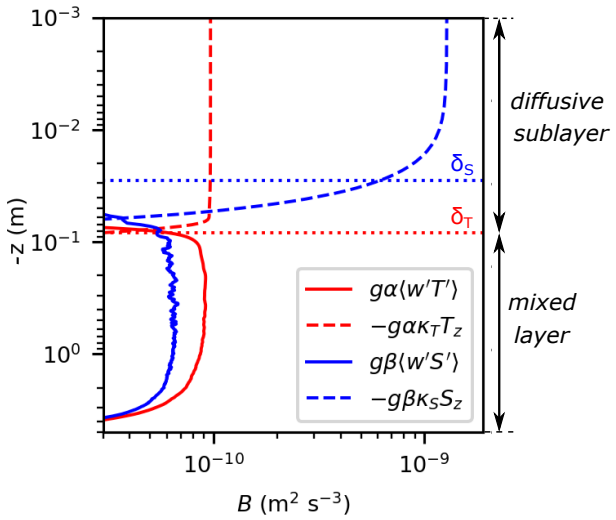

Figure 3.8: The contributions of heat and salt to the buoyancy flux at $t = 50$ h for run 3*. Both diffusive and turbulent contributions are plotted. Horizontal dotted lines show the thermal and saline diffusive sublayer scales given in Eq. 3.12.

indicates the accumulation of salt at the edge of the diffusive sublayer, allowing it to grow in time (Worster, 2004), as has been observed in DNS of melting in quiescent conditions (Keitzl et al., 2016b). This result has important implications for observational studies of the ice-ocean boundary layer, as the assumption of a balance between turbulent fluxes in the mixed layer and diffusive fluxes at the interface is commonly made (Sirevaag, 2009). Here we observe that the diffusive and turbulent salt fluxes differ by an order of magnitude. Consequently the turbulent salt flux cannot be used as a proxy for the interfacial salt flux that regulates melting.

3.3.2 Friction velocity and drag coefficient

Parameterisations of ice-ocean interactions typically depend on the friction velocity u^* (Jenkins, 1991; Holland and Jenkins, 1999; McPhee, 2008). However, u^* is not resolved in RANS models and is instead estimated as a function of the free stream velocity U_0 and drag coefficient C_d. There have been few opportunities to constrain C_d beneath an ice shelf, although it is expected to vary with the morphology and "roughness" of the ice base (Gwyther et al., 2015) as well as the stratification (Mellor et al., 1986). We find that the near-ice stratification created by meltwater acts to decrease drag at the ice-ocean

interface. In our experiments, u^* increases with the strength of the far-field current (Table 1). Experiments with a far-field current (2, 3, 3*, 4) are initialised with a fully turbulent, neutral (unstratified) Ekman boundary layer. These spin-up experiments have steady u^* with drag coefficients in the range $C_d = 0.0022$–0.0034, where the drag coefficient is defined by $u^* = C_d^{1/2} U_0$. At $t = 0$ h, the far-field stratification and melting boundary condition are applied. In response, both the friction velocity and drag coefficient decrease, an effect that is seen across all experiments. Averaged over the period 50–100 h the new drag coefficients are in the range $C_d = 0.0009$–0.0023. This behaviour is consistent with previous LES modelling results, which show a marked decrease in the drag coefficient as thermal driving increases, for fixed friction velocity (Vreugdenhil and Taylor, 2019). This result indicates that applying a drag coefficient appropriate for a neutral (unstratified) boundary layer will tend to overestimate u^* in areas where melting creates strong near-ice stratification, such as the DC regime described here.

3.3.3 Melting

Here we investigate the effect of ocean temperature and current shear on the melt rate (m) and discuss the temporal evolution of melting. Two key results emerge from Fig. 3.9a, which shows the melt rate as a function of time. Firstly, experiments with the same thermal driving (e.g. 1, 2, 3 and 4 with $T_0^* = 0.175$ °C) have extremely similar melt rates; there is no clear influence from increasing friction velocity. Secondly, m does not reach a steady value over the simulation period. We will show that the inherent time-dependence of m can be understood as a consequence of the continuously growing saline diffusive sublayer.

Controls on melting

Melting is proportional to the diffusive heat and salt fluxes at the ice-ocean interface $m \sim (\partial T/\partial z)_b \sim (\partial S/\partial z)_b$ (Eqs. 3.9 & 3.10). For a given temperature or salinity difference between the interface and mixed layer, the interfacial fluxes will be inversely proportional to the diffusive sublayer thickness, assuming linear T and S profiles across the diffusive sublayer. Making this assumption, we define diffusive sublayer scales, analogous to the "gradient thickness" defined in Gade (1993), for temperature (δ_T) and salinity (δ_S) as:

$$\delta_T \equiv \frac{T_{ML} - T_b}{\frac{\partial T}{\partial z}_b}, \qquad \delta_S \equiv \frac{S_{ML} - S_b}{\frac{\partial S}{\partial z}_b} \tag{3.12}$$

where the subscripts b and ML denote the interface and mixed layer values respectively. Fig. 3.8 shows that δ_T and δ_S accurately represent the thickness of the diffusive sublayer for heat and salt respectively, although the assumption of a linear gradient is less robust for salt than heat. Nevertheless, δ_T and δ_S can be used to measure the diffusive sublayer thickness for each scalar.

For all experiments, δ_T and δ_S are observed to increase with time proportional to $t^{1/2}$ (Fig. 3.9b). The salinity diffusive sublayer thickness, δ_S, is well approximated by salinity diffusion lengthscale $h_S = (4\kappa_S t)^{1/2}$ (Martin and Kauffman, 1977). However, δ_T is much smaller than the analogous scale in temperature $h_T = (4\kappa_T t)^{1/2}$. This is because δ_T is limited by the convective overturning of the density boundary layer (Fig. 3.4). The observation that δ_S grows with the salinity diffusion scale h_S is significant because it indicates that salt is not being removed or "scoured" by the convective overturns associated with the unstable density boundary layer. This behaviour is analogous to the high density ratio ($R_\rho^* > (\kappa_S/\kappa_T)^{-1/2} \sim 10$) run for the diffusive interface between two DC layers (Newell, 1984; Worster, 2004), across which heat and salt fluxes are inherently time-dependent.

While the dependence is weak, increasing friction velocity does affect the melt rate by decreasing the thermal diffusive sublayer thickness. This mechanism is demonstrated by the near-ice temperature profiles for runs 1 and 3 (Fig. 3.9c). In run 1, with no mean flow, the thermal diffusive sublayer thickness is solely set by DC. In run 3, with $U_0 = 1.4$ cm s^{-1}, the addition of shear generated turbulence acts to thin the thermal diffusive sublayer relative to run 1 (Fig. 3.9c). However, the effect of shear on δ_T, and correspondingly on m, is relatively minor over the range of conditions simulated here (Table 3.2). Fig. 3.9d shows the diffusive sublayer thickness ratio δ_T/δ_S as a function of friction velocity for all experiments. Although the diffusive boundary layer thickness does not reach steady state, the ratio δ_T/δ_S varies extremely slowly over the interval $100 < t < 200$ h (run 1 only). At $t = 100$ h, δ_T/δ_S ranges from 2.5 (run 4) to 3.2 (run 1), and decreases with increasing u^*. These values of the boundary thickness ratio are consistent with previous experimental, numerical and field estimates of 2.3 (Gade, 1993), 1.9 (Keitzl et al., 2016b) and 3.3 (Sirevaag, 2009, reported $\delta_T/\delta_S \sim Le/33$, which is equal to $\delta_T/\delta_S \sim 3.3$ at the Lewis number $Le = 110$ of our experiments).

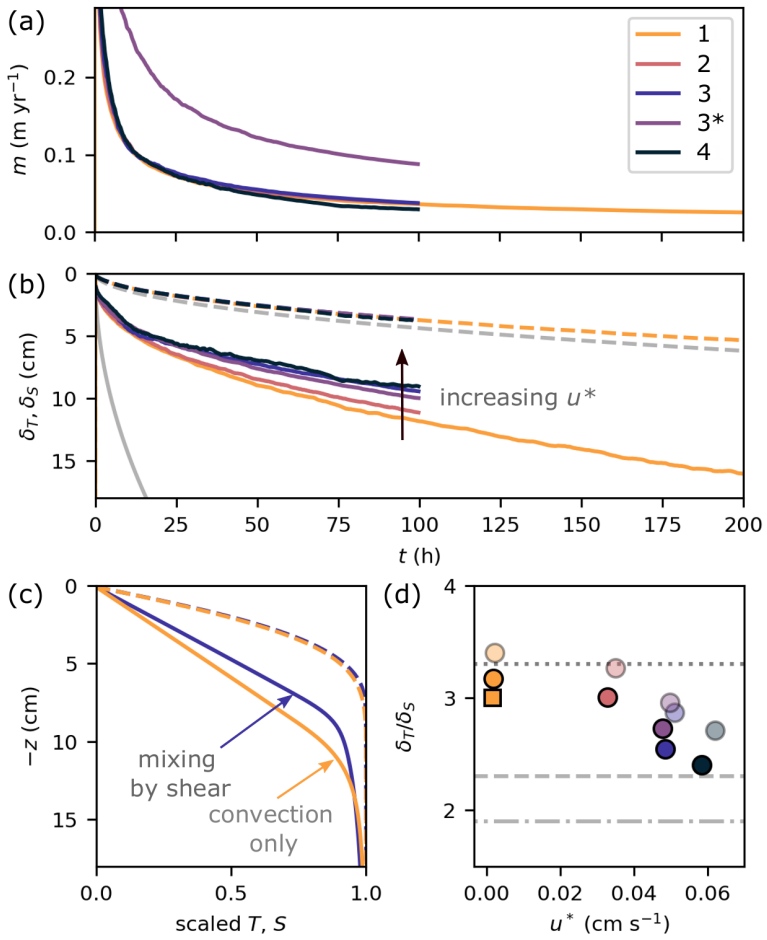

Figure 3.9: Melting and diffusion at the ice-ocean interface. (a) Temporal evolution of melt rate m and (b) scalar diffusive sublayer thicknesses δ_T (solid lines) and δ_S (dashed lines) for all experiments. Also plotted are temperature diffusion lengthscale $h_T = (4\kappa_T t)^{1/2}$ (solid grey line) and salinity diffusion lengthscale $h_S = (4\kappa_S t)^{1/2}$ (dashed grey line). (c) Profiles of near-ice temperature and salinity, scaled as $(T - T_b)/(T_{ML} - T_b)$ and $(S - S_b)/(S_{ML} - S_b)$ for experiments 1 and 3 at $t = 100$ h. In run 1 turbulence is generated by convection only whereas in run 3, shear generated turbulence is also present, resulting in a thinner thermal diffusive sublayer. (d) Diffusive sublayer thickness ratio as a function of friction velocity at $t = 50$ h (pale circles), $t = 100$ h (bold circles) and $t = 200$ h (square, run 1 only). Lines show previous estimates of δ_T/δ_S from Gade (1993) (dashed), Keitzl et al. (2016b) (dot-dashed) and Sirevaag (2009) (dotted).

Comparison with observations

Our simulated melt rates are consistent with melt rates observed beneath the Ross Ice Shelf at similar conditions. Fig. 3.10 situates our results in terms of friction velocity

u^* and thermal driving $T^* \equiv T_{ML} - T_f(S_{ML}, p_b)$, where $T_f(S_{ML}, p_b)$ is the freezing temperature at mixed layer salinity and interface pressure p_b. Note that while cases 1, 2, 3 and 4 were all initialised with the same temperature profile, they have evolved to have different T^* over the course of the experiment. Averaged over 50–100 h, the simulated melt rates depend strongly on T^*, but have only a weak dependence on u^* (Fig. 3.10). Fig. 3.10 plots simulated melt rates alongside data from beneath the Ross Ice Shelf, showing that the two are consistent at similar conditions. The thermohaline structure in our simulations is also consistent with observations beneath the RIS, which show a series of well mixed layers separated by strong gradients in T and S (Begeman et al., 2018). Limitations of the RIS data, such as contamination of the upper water column properties by the borehole opening and possible instrument noise, precluded the authors from convincingly attributing the water column structure to DC (Begeman et al., 2018). However, we suggest that the DC mixing observed in our simulations –at conditions that closely mirror those of the RIS– indicates that DC is likely contributing to mixing beneath the RIS some of the time.

While the simulated melt rates are consistent with the observed melt rate beneath the RIS, they are nearly an order of magnitude lower than melt rates predicted by the commonly used, current-velocity dependent three-equation parameterisation (Jenkins et al., 2010b) (Fig. 3.10, inset). For example, for run 3 the simulated melt rate averaged over 50–100 h is 0.045 m yr^{-1}, while the three-equation parameterisation predicts a melt rate of 0.38 m yr^{-1} at the same conditions. An important limitation of these comparisons is that time-dependent melt rates were observed in our simulations, and consequently the average melt rate values reported here are subject to the choice of averaging period. For example, were we to consider the time interval 5–15 h, the simulated melt rate for run 3 is 0.12 m yr^{-1}, while the three equation parameterisation predicts 0.47 m yr^{-1}. We do not consider the rapid transitional period t 5 h, as the diffusive sublayer is still being established at this time.

3.4 Discussion

The primary objective of this work was to investigate the role that DC plays in the basal melting of ice shelves by performing simulations of the ice-shelf ocean boundary layer using high resolution LES. These simulations were targeted at relatively warm, quiescent environments where existing parameterisations are known to perform poorly. We have

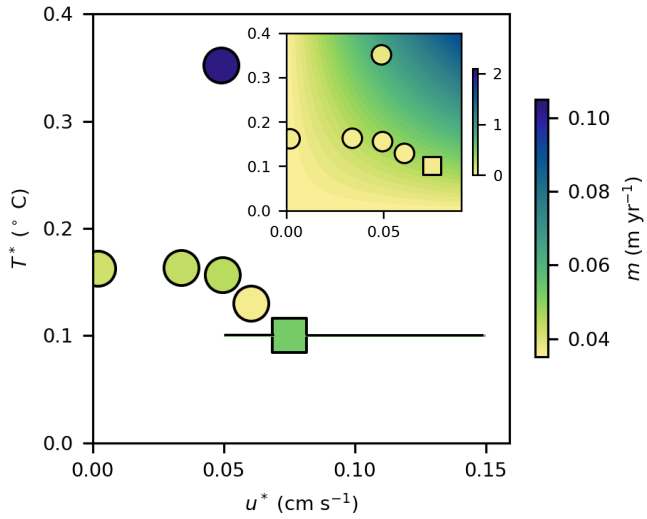

Figure 3.10: Melt rate m as a function of thermal driving T^* and friction velocity u^* from this study (circles), where all quantities are averaged over $50 < t < 100$ h, and from field data collected beneath the Ross Ice Shelf (Begeman et al., 2018) (square). Inset: as for main figure with melt rate (colour) predicted by the three-equation parameterisation with parameters recommended in Jenkins et al. (2010b) (See S1 §3.5.2 for details). Note different scale. For the field observation, u^* is calculated from the free stream velocity as $u^* = C_d^{1/2} U_0$ for $C_d = 0.0025$. Error bars show the range of u^* values obtained from choosing $C_d = 0.01$–0.001.

demonstrated that, at sufficiently warm ($T^* \geq 0.15$ °C) and low velocity ($U_0 \leq$2.0 cm s^{-1}) conditions, the fluxes associated with melting ice can drive DC beneath an ice shelf. In all simulations, positive turbulent buoyancy fluxes (indicative of DC) were observed from the onset of the simulation. In some cases, however, a transition from DC-dominated to shear-dominated mixing was observed over time. Where DC persisted for a sufficiently long period, a diffusive staircase formed beneath the ice. Despite this observed transition from DC-dominated to shear-dominated mixing, melt rates were similar across the experiments. For $T^* \geq 0.15$ °C and $U_0 \leq 2.0$ cm s^{-1} we found that melting was primarily controlled by ocean temperature and depends only weakly on vertical shear due to a far-field current. At simulated conditions the thermal and saline diffusive sublayers adjacent to the ice were not controlled by current shear, and instead grew in time. The growth of these sublayers was shown to be the rate-limiting process controlling the melt rate, driving time-dependent heat and salt fluxes to the ice, and consequently a time-dependent melt rate. This result is counter to the assumption of steady-state melting

common to typical ice-ocean parameterisations Jenkins et al. (2010b); McPhee et al. (1987); Jenkins (1991); Holland and Jenkins (1999). Importantly, the transition from DC to shear-dominated mixing did not correspond to a transition to shear-controlled melting. Despite dominating turbulent fluxes within the mixed layer, current shear was not sufficiently strong control the thickness of the diffusive sublayer and drive steady, friction velocity-dependent melting.

The tendency for the system to transition from DC-dominated to shear-dominated mixing can be understood in terms of competing shear and DC processes. Under low or weak stratification, shear-generated turbulence is expected to mix heat and salt equally (i.e. the eddy diffusivities of heat and salt are equal). This tendency is at odds with DC, which relies on unequal diffusion of heat and salt. For this reason, DC is not expected to coexist with strong turbulence (Radko, 2013). For example, in the arctic, diffusive staircases are much less common near boundaries where turbulence dissipation is higher (Shibley et al., 2017). The strength of the interfacial heat flux that drives convection beneath the ice in our simulations decreases over time. Consequently, convection weakens over time, while turbulence production from current shear remains steady. Thus, in the presence of a mean flow or elevated turbulence from other sources, it is expected that shear will eventually overtake DC and become the dominant mixing process. The duration of time for which DC persists will depend on the relative strength of the thermal driving and current shear.

Our findings have important implications for how basal melting of ice shelves is modelled at conditions favorable to DC. Two of our key results, 1) that the melt rate is unsteady in time and 2) the melt rate is largely independent of current speed, contradict assumptions in commonly used ice-ocean parameterisations, which set melt rate as a function of current speed and assume a balance between mixed layer and interfacial fluxes. Furthermore, we have demonstrated that DC has a unique influence on the water column structure, setting the mixed layer depth and properties and driving vertical fluxes of heat and salt in a different manner to shear-driven mixing. Consequently, DC may influence the properties and evolution of watermasses beneath ice shelves and have a non-local influence on cavity circulation and melting. Our results suggest that a new parameterisation is required for the DC regime if we wish to accurately model melt rates in warm and relatively quiescent environments.

A constraint on the conclusions drawn in this study is that a steady melt rate is not achieved over the multi-day simulations. The time-dependent melt rate is well explained

by the continuously growing diffusive sublayer adjacent to the ice, itself governed by salt diffusion to the ice-ocean interface. However, in a real system, processes such as variable current speeds, enhanced mixing due to interfacial roughness and non-local sources of turbulence such as a breaking internal waves may act to limit the growth of, or intermittently destroy, the highly stable diffusive sublayer. In the case of intermittent turbulent events, the frequency with which the diffusive sublayer and thermohaline staircase are disturbed will influence the melt rate, which will differ from the values presented in Table 3.2. It is therefore important that future studies of the ISOBL in the DC regime consider a wide range of ocean processes and how they interact with the highly stable diffusive sublayer observed in the present simulations.

Our experiments provide strong evidence that DC is capable of dominating shear-controlled turbulent melting and creating a thermohaline staircase structure beneath an ice shelf, consistent with what is observed at the grounding line of the Ross Ice Shelf. The moderately warm and low current speed conditions investigated in this study comprise one of only four "subsets" of conditions that have been observed beneath Antarctic ice shelves: i) warm and low velocity; ii) warm and high velocity; iii) cold and low velocity; iv) cold and high velocity. Melting is expected to behave differently at different conditions. For example, beneath the Filchner Ronne and Larsen C ice shelves, thermal driving is lower ($\sim$0.05 °C) and fast tidal currents (0–20 cm s^{-1}) are present. At these cold, high velocity conditions the freshwater released by melting does not significantly influence the turbulent environment and existing melt rate parameterizations perform well (Jenkins et al., 2010b; Davis and Nicholls, 2019), provided the drag coefficient is known. However, at warmer or more quiescent conditions, existing parameterizations perform poorly (Kimura et al., 2015; Begeman et al., 2018; Vreugdenhil and Taylor, 2019).

Our simulations target moderately warm, low current conditions in order to examine melting in DC only and "mixed" regimes, where both shear and DC influence the turbulent transport, melting and boundary layer structures. We suggest that at warmer temperatures (e.g. rapidly melting "warm water" ice shelves, which are typically characterised by temperatures O(1) °C above the local freezing temperature; Stanton et al., 2013) DC will become even more important. A fully shear-controlled melting regime was not achieved in our numerical experiments, which were conducted at the highest current speeds possible, whilst still resolving both the diffusive sublayer and mixed layer dynamics. Further work at higher current speeds is required to investigate the transition to shear controlled melting. Other features such as a rough ice surface and unsteady

forcing (e.g. time-varying flows and internal wave activity) also warrant investigation using turbulence resolving simulations, where they may shed some light on the long-term behaviour of the transient melting dynamics demonstrated in our simulations, and offer an avenue to parameterise melting in the DC regime.

3.5 Supplementary information for chapter 3

3.5.1 Shear mixed layer depth scaling

In the presence of a far-field current, boundary layer turbulence is produced by both shear and convective instability, however shear driven turbulence is more pronounced near the interface (Fig. 3.11). At low velocity (runs 2, 3 and 3*) the evolution of the mixed layer is very similar between runs. For these runs, the mixed layer depth increases with the strength of the thermal driving, indicating DC is enhanced by increased ocean temperatures. Run 4 evolves in a similar manner to runs 1–3* for the first ∼10 h of the experiment, with a 2.5 m deep mixed layer forming beneath the ice. However, later in time a second pycnocline emerges at a depth of ∼ 0.8 with a mixed layer above it. This additional mixed layer is formed by shear-generated turbulence. DC is no longer contributing to near-wall turbulent mixing of the water column. Boundary layer shear is characterised by friction velocity $u^* = (\tau_w/\rho_0)^{1/2}$, a function of the shear stress at the wall τ_w. The depth of a stable planetary boundary layer can be estimated as $\delta_{SBL} = 0.5(\eta u^*/f)$, where stability parameter $\eta \leq 1$ takes into account the effect of a stabilising buoyancy flux (in this run due to the freshening effect from melting), which reduces the boundary layer depth (McPhee, 1981). Based on this scaling, we would expect the mixed layer depths to increase with u^* and decrease with higher melt rates. For run 4 the stability parameter $\eta = 0.7$, yielding a stable boundary layer depth $\delta_{SBL} = 1.5$ m, which is in rough agreement with the pycnocline depth of ∼0.8 m. The presence of this layer demonstrates the increased importance of shear generated turbulence in mixing as the velocity is increased to U_0=2.0 cm s^{-1}.

3.5.2 Comparison between simulated melt rates and a common ice-ocean parameterisation

Here, simulated melt rates are quantitatively compared with the three-equation parameterisation from (Jenkins et al., 2010b). In this parameterisation, oceanic heat and salt fluxes are represented in terms of the temperature and salinity difference between the mixed layer and the interface. The surface and sublayer dynamics are encapsulated by the product of friction velocity u^* and heat and salt transfer coefficients Γ_T and Γ_S, resulting in:

$$\rho_i L_f m_{pred} = -\rho c_p \Gamma_T u^* (T_{ML} - T_b) \tag{3.13}$$

Table 3.3: Comparison between simulated melt rate (m) and melt rate as predicted by the three-equation parameterisation (m_{pred}).

run	T_{ML} (°C)	u^* (cm s^{-1})	m (m yr^{-1})	m_{pred} (m yr^{-1})	m/m_{pred}
1	-2.115	0.0	0.042	0.0	∞
2	-2.114	0.0339	0.044	0.27	6.1
3	-2.121	0.0495	0.045	0.38	8.4
3*	-1.926	0.0489	0.103	0.84	8.2
4	-2.147	0.0605	0.037	0.38	10.3

$$\rho_i S_b m_{pred} = -\rho \Gamma_S u^* (S_{ML} - S_b) \tag{3.14}$$

where $c_p = 4.18 \times 10^3$ (J kg^{-1} K^{-1}) is the heat capacity of seawater, $L_f = 3.35 \times 10^5$ (J kg^{-1}) is the latent heat of melting, $\kappa_T = 1.4 \times 10^7$ (m^2 s^{-1}) and $\kappa_S = 1.3 \times 10^9$ (m^2 s^{-1}) are the molecular diffusivity of heat and salt respectively and $\rho = 1030$ (kg m^{-3}) and $\rho_i = 917$ (kg m^{-3}) are the density of water and ice respectively. These parameters are consistent with those used in the numerical model. For the transfer coefficients we use the constant, empirically determined values of $\Gamma_T = 0.011$ and $\Gamma_S = 3.1 \times 10^{-4}$ from beneath the Filchner Ronne Ice Shelf (Jenkins et al., 2010b).

We solve Eqns. 3.13, 3.14 and the liquidus relationship ($T_b = aS_b + b$ where $a = -0.057$ °C kg g^{-1} and $b = -0.311$ °C) for m_{pred} as a function of the simulation-derived T_{ML}, S_{ML} and u^* in order to compare with our simulated melt rates. Both the inputs and predicted values are found in Table 3.3. For Fig. 3.10 (inset) we solve the same set of equations over a range of T_{ML} and u^*, setting $S_{ML} = 34.5$ g kg^{-1}.

3.5.3 Turbulent kinetic energy

To better understand the processes operating in the boundary layer we consider the Turbulence Kinetic Energy (TKE) budget as follows:

$$\frac{\partial k}{\partial t} = P - \epsilon + B - \text{transport of TKE} \tag{3.15}$$

where $\partial k/\partial t$ is the time rate of change of TKE (m^2 s^{-3} or equivalently W kg^{-1}), P is the shear production, ϵ is the dissipation rate and B is the buoyancy flux. Dissipation rate ϵ is positive definite and therefore a sink of TKE, while shear production P is typically positive and buoyancy flux B may take either sign, where positive B corresponds to a transformation of potential to kinetic energy. These terms are further described in Gayen

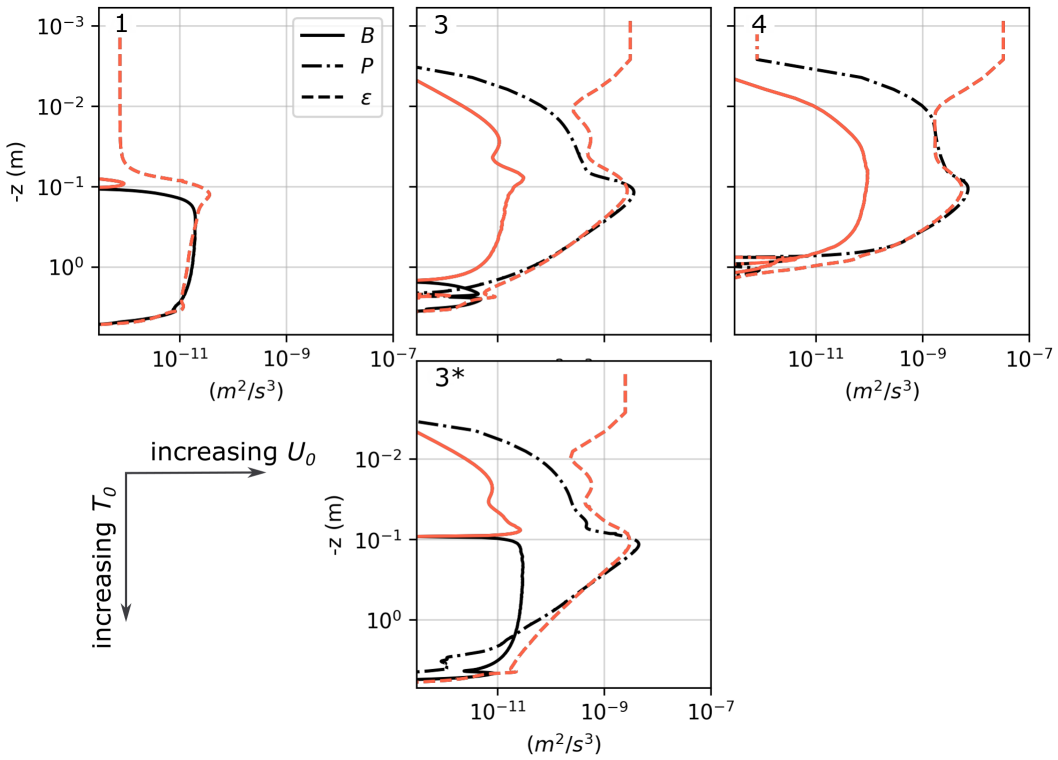

Figure 3.11: Plane-integrated buoyancy production B, shear production P, and dissipation ϵ at $t = 50$ h. Positive (negative) values for each term are shown in black (orange). Panels are labelled by run, see Table 1 for details.

et al. (2010). Fig. 3.11 shows the total (subgrid-scale + resolved) shear production, buoyancy flux and dissipation. With no far-field current, buoyancy flux is the leading source of turbulence, and dissipation near the interface is low (1, Fig. 3.11). However, in the presence of mean shear (3,3* and 4, Fig. 3.11) dissipation near the boundary increases dramatically and shear production becomes the primary source of TKE over the upper $\sim$ 1 m of the water column. Beneath this, buoyancy flux becomes positive (3 and 3*, Fig. 3.11), increases in magnitude and eventually dominates shear as the leading source of TKE, especially in the highest thermal driving run. The maximum average dissipation rate is $4{\times}10^{-9}$ ($1{\times}10^{-8}$) m^2 s^{-3} for run 3 (4) (Fig. 3.11). This result is consistent with the lower end of dissipation rate values observed beneath the Larsen C Ice Shelf (10^{-9}–10^{-6} m^2 s^{-3}), where the high values were observed for flow speeds of 0.15 m s^{-1} and greater (Davis and Nicholls, 2019). This result is also consistent with near-boundary dissipation data beneath landfast sea ice in McMurdo Sound, Antarctica (average: 3×10^{-8} m^2 s^{-3}, near surface: $1{\times}10^{-7}$ m^2 s^{-3}) (Stevens et al., 2009).

Chapter 4

Basal melting of a horizontal ice shelf driven by a steady, geostrophic current

Abstract

Ocean-driven basal melting is causing thinning of the Antarctic Ice Sheet, contributing to global sea level rise. Efforts to represent basal melting in sea level projections are undermined by poor understanding of the ice shelf-ocean boundary layer (ISOBL). This knowledge gap is addressed here using high resolution large-eddy simulations of the ISOBL forced by a steady, geostrophic flow at melting conditions. This chapter presents results for a range of free stream velocities (0.7–2.8 cm s^{-1}) and ocean temperatures (0.0025–0.05°C above the local freezing temperature). These conditions encompass a stratified regime -which occurs when boundary layer turbulence is affected by the buoyancy flux due to melting- and a well-mixed regime. In the well-mixed regime, the depth of the mixed layer can be predicted using a simple scaling law based on friction velocity, Coriolis frequency, and far-field stratification. In the stratified regime, which occurs when the Obukhov length scale (L) is the same or less than the planetary scale ($u^*/|f|$), the boundary layer depth and interfacial drag decrease as stability parameter $\mu = u^*/(fL)$ increases. Stratification tends to shoal the ISOBL, insulating the ice from warmer water below and increasing the challenge of sampling and resolving the ISOBL properties in observational and modelling studies. This chapter demonstrates that the viscous Obukhov lengthscale $L^+ = Lu^*/\nu$ determines the efficiency of heat and salt transfer to the ice-ocean interface, in agreement with the results of Vreugdenhil and Taylor (2019), where several important thresholds exist. For L^+ 2500 melting is time-dependent, while for L^+ 2500 steady melt rates are observed. In the range 2500 L^+ 25000 heat and salt transfer coefficients increase as a function of L^+, tending to a constant value for L^+ 25000. This chapter demonstrates that existing parameterisations of ice melt are

not appropriate over a large range of ocean conditions relevant to Antarctic ice shelves, and show the need to account for the effects of stratification on the mixed layer and interfacial drag.

4.1 Introduction

Understanding how the ocean drives basal melting of Antarctic ice shelves is critical for quantifying the rates of present ice mass loss and developing the capability to project future change. Despite extremely poor spatial and temporal coverage, observations from within ice shelf cavities have revealed a range of different cavity environments and melting behaviors. In cold, energetic conditions such as those observed below the Filchner-Ronne (Jenkins et al., 2010b) and Larsen C (Davis and Nicholls, 2019) ice shelves, melting is strongly controlled by current speed. At these conditions, Davis and Nicholls (2019) showed that the surface buoyancy flux due to melt water has little effect on the turbulent boundary layer beneath the ice. Observations from warmer ice shelf cavities suggest that buoyancy plays a larger role at increased ocean temperatures through driving strong circulation (Stanton et al., 2013), increasing water column stratification (Stewart, 2018) and, in some cases, resulting in diffusive convection (DC) and the formation of thermohaline staircases (Begeman et al., 2018; Kimura et al., 2015).

Recent modelling studies using large-eddy simulation (LES) and direct numerical simulation (DNS) have focused on understanding the importance of stratification (Vreugdenhil and Taylor, 2019) and diffusive convection (e.g. Keitzl et al., 2016b) beneath melting ice. Vreugdenhil and Taylor (2019) showed that stratification inhibits the turbulent transfer of heat and salt and suppresses melt rates. Keitzl et al. (2016b) and Chapter 3 of this thesis showed that melt rates in the DC regime are inherently transient due to the unchecked growth of the highly stratified diffusive sublayer adjacent to the ice. In the DC regime, melting was shown to be relatively insensitive to changes in the far-field velocity, contrary to existing parameterisations of ice-ocean interaction (e.g. McPhee et al., 1987; Jenkins, 1991; Jenkins et al., 2010b).

Ice-ocean parameterisations should represent the state of our current understanding of the ice shelf-ocean boundary layer (ISOBL). Instead, existing parameterisations match observations only under the coldest, most energetic conditions (Davis and Nicholls, 2019; Jenkins et al., 2010b; Vreugdenhil and Taylor, 2019). They are also subject to issues of implementation due to the assumption of a water column structure with a well-mixed

layer or plume adjacent to the ice. The mixed layer temperature (T), salinity (S) and friction velocity (u^*) constitute the driving parameters for the melting model and must be sampled within the mixed layer. In practice, the depth at which these properties are sampled depends on the vertical resolution of the model or an arbitrary (and constant) choice of sampling depth, resulting in an un-physical dependence of predicted melt rates on ocean model resolution or the chosen sampling depth (Gwyther et al., 2020a). Similar issues arise when the velocity $\mathbf{u}$, which is required to estimate friction velocity u^*, is taken outside of the relevant region of the boundary layer (Davis and Nicholls, 2019).

These issues highlight the need for an adequate representation of the ice-ocean boundary layer which includes melting, ISOBL structure and mixed layer properties, especially under warm conditions where stratification becomes important. This chapter addresses this need using high resolution LES of the ISOBL, forced with a steady, geostrophic current and ocean temperatures above the local freezing point. By varying the strength of ocean current and temperature forcing, the principal variables affecting the melt rate and mixing beneath the ice are identified. This chapter then classifies the results based on the dominant physics observed and develops criteria for the transition between these regimes as a function of commonly observed/resolved ocean variables.

This chapter is structured as follows. §4.2 provides detailed background on oceanic boundary layers, including those with a stabilising surface buoyancy flux, as well as currently used parameterisations of ice ocean interactions. The governing equations, numerical implementation and forcing for the numerical model are detailed in §4.3. Simulation results are then presented in §4.4, focusing first on the boundary layer and mixed layer characteristics, including the classification of boundary layer types based on the dominant observed processes, followed by analysis of the melt rates. In §4.5 the implications of the different boundary layer and melting regimes are discussed with respect to observing and modelling basal melting. Conclusions and future directions are presented in §4.6.

4.2 Background

4.2.1 The ice shelf-ocean boundary layer

The ISOBL typically refers to the frictional boundary layer that forms adjacent to the ice due to the presence of a mean flow or current in the ocean next to the (stationary) ice.

Friction acts to reduce velocity in the vicinity of the ice, creating vertical shear (velocity gradient). Due to Coriolis, the viscous stresses associated with vertical shear result in an ageostrophic (cross-stream) component of the flow and a turning of the mean flow with depth, known as an Ekman spiral. Rotation gives the Ekman layer a natural depth scale (δ_f) which depends on the Coriolis frequency (f). In an unstratified environment this scale, often called the planetary scale, is given by $\delta_f \sim u^*/|f|$. Stratification tends to limit the planetary scale.

The ISOBL can be divided into several sub-regions based on the dominant physical processes. The viscous sublayer is the region of laminar flow adjacent to the ice which is O(10^{-2} m) thick. Within the viscous sublayer, horizontal velocity scales with distance from the ice as:

$$U^+ \sim z^+ \tag{4.1}$$

where the distance z and velocity U are expressed in wall units, which are denoted by the plus superscript:

$$U^+ = \frac{U}{u^*}, \qquad z^+ = \frac{zu^*}{\nu}. \tag{4.2}$$

Here, ν is molecular viscosity and u^* is the friction velocity, a function of shear stress at the interface ($u^* = \overline{\tau_W/\rho_0}$). Adjacent to the viscous sublayer is the surface or "log" layer, which occupies approximately 20% of the total boundary layer depth. Within the surface layer, turbulence is affected by the presence of a solid boundary (in this case, the ice-ocean interface). Vertical shear is inversely proportional to the distance from the surface (z) and proportional to the strength of the turbulence. In a neutral setting (when stratification is not important) the dimensionless current shear (ϕ) is given by:

$$\phi = \frac{kz}{u^*} \quad \frac{\partial U}{\partial z} \quad = 1 \tag{4.3}$$

where $k = 0.41$ is von-Karman's constant. Integrating ϕ gives a logarithmic current profile in height:

$$U^+ = \frac{1}{k}\ln(z^+) + C \tag{4.4}$$

applying the identities in 4.2. This logarithmic scaling of velocity with depth is often called the Law of the Wall (LOW). For flow that is affected by stratification the profile is expected to depart from the LOW. Commonly, this departure is taken to be a linear function $\phi(\xi) = 1 + \beta_m\xi$ of the normalised distance from the ice $\xi = z/L$ where L is the Obukhov length:

$$L = \frac{u^{*3}}{kB}, \tag{4.5}$$

and B ($m^2\ s^{-3}$) is the surface buoyancy flux. Integrating 4.5 yields the log-linear velocity profile:

$$U^+ = \frac{1}{k}\ln(z^+) + \frac{\beta_m}{k}\xi + C \tag{4.6}$$

where constant $C \simeq 5.0$ (Bradshaw and Huang, 1995) and $\beta_m \simeq 4.7$ (Businger et al., 1971). This expression implies that stratification is affecting the mixing length, or the maximum vertical distance over which eddies can diffuse momentum (McPhee, 1994). For a positive (stabilising) buoyancy flux, the Obukhov lengthscale is an estimate of the distance from the ice where stratification effects are felt by ISOBL turbulence. This expression applies to weak stratification only. For strong stratification, it is expected that the distance to the ice will not affect the shear, and the velocity gradient will be linear (Turner, 1979).

Stratification also influences the overall boundary layer depth, where the stratification may take the form of a stratified far-field environment or through a stabilising buoyancy flux at the boundary, where both are relevant to the ISOBL. External stratification decreases the Ekman layer depth relative to the well-mixed case (Weatherly and Martin, 1978; Taylor and Sarkar, 2008a; McWilliams et al., 2009). McWilliams et al. (2009) showed that the stratified Ekman layer depth varies as a function of the stratification parameter $\gamma = N_\infty^2/f^2$. Typically in the ocean $N > |f|$ and therefore $\gamma \gg 1$. The externally stratified Ekman boundary layer depth (h_γ) is given by:

$$h_\gamma = A\frac{u^*}{|f|}\gamma^{-1/4} \tag{4.7}$$

This expression is consistent with the scaling of Weatherly and Martin (1978) for $\gamma \gg 1$. Based on the height at which the Turbulent Kinetic Energy (TKE) or turbulent mixing goes to zero, Weatherly and Martin (1978) found the constant $A = 1.3$.

A stabilising surface buoyancy flux has also been shown to limit the depth and increase the cross-stream velocity of an Ekman boundary layer (Coleman et al., 1992; Shah and Bou-Zeid, 2014). The vertical scales of turbulence are reduced by gravity under stabilising surface buoyancy forcing, and the mixed layer shoals (McPhee, 2008). Under a stabilising buoyancy flux the Ekman layer depth has been shown to depend on the stability parameter μ:

$$h_\mu = C = \frac{u^*}{f}\mu^{-1/2} \tag{4.8}$$

(e.g. Zilitinkevich, 1972; Garratt, 1982; Deusebio et al., 2014) where $\mu = u^*/(fL)$ is the ratio of the planetary scale to the Obukhov lengthscale.

4.2.2 Models of ice-ocean interaction

Thermodynamic models of ice-ocean interaction aim to determine the ice shelf melt rate (m), interface temperature (T_b) and salinity (S_b) as a function of the ocean mixed layer and ice temperatures. The interface is assumed to be at the freezing temperature, which is a weakly nonlinear function of salinity and a linear function of pressure. A linearised version is typically used, such that:

$$T_b = \lambda_1 S_b + \lambda_2 p_b + \lambda_3 \tag{4.9}$$

where λ_1 and λ_2 are the liquidus slopes in salinity and pressure and λ_3 is an offset. The melt rate of the ice is determined by balancing heat and salt fluxes at the ice-ocean interface. In the following, the subscripts i, ML and b denote ice-shelf, mixed layer and interface properties respectively. At the interface, conservation of heat allows us to balance the latent heat of melting with divergence between the oceanic and ice heat fluxes. The latent heat of melting is given by $\rho_i L_f m$, where ρ_i is the density of the ice shelf, L_f is the latent heat of freezing and m is the melt rate. The oceanic heat flux (Q_T) is given by $\rho c_p \kappa_T (\partial T/\partial z)_b$, where ρ, c_p and κ_T are the density, specific heat capacity and thermal diffusivity of the ocean and $(\partial T/\partial z)_b$ is the oceanic temperature gradient at the ice-ocean interface. In the following, the conductive heat flux into the ice is set to zero on the assumption that it is much smaller than the latent heat term, following e.g. Gayen et al. (2016); Mondal et al. (2019); Vreugdenhil and Taylor (2019). For a discussion on the influence of conductive heat flux term see Holland and Jenkins (1999). The interfacial heat balance is given by:

$$\rho_i L_f m = -\rho c_p \kappa_T \left.\frac{\partial T}{\partial z}\right|_b . \tag{4.10}$$

A similar expression can be formulated for salinity by balancing the brine flux due to melting $\rho_{ice} S_b m$ with the oceanic salt flux $Q^S_{ML} = \rho \kappa_S (\partial S/\partial z)_b$, where the ice salinity and the salt flux into the ice are taken to be zero (Oerter et al., 1992). Equating the remaining terms yields:

$$\rho_i S_b m = -\rho \kappa_S \left.\frac{\partial S}{\partial z}\right|_b . \tag{4.11}$$

The oceanic heat and salt fluxes in Eqs. 4.10 and 4.11 are not resolved in regional or circum-antarctic ocean models, and must instead be parameterised (e.g. Holland and Jenkins, 1999). The commonly used three-equation parametrisation represents these fluxes in terms of the temperature and salinity difference between the mixed layer and

the interface. The surface and sublayer dynamics are encapsulated by the product of friction velocity u^* and heat and salt transfer coefficients Γ_T and Γ_S:

$$Q_T = \rho c_p \Gamma_T u^* (T_{ML} - T_b) \tag{4.12}$$

$$Q_S = \rho \Gamma_S u^* (S_{ML} - S_b) \tag{4.13}$$

Typically the friction velocity is not known, and is instead modelled as a function of the free stream velocity U_0 and the drag coefficient C_d as $u^* = C_d^{1/2} U_0$. While a value of $C_d = 0.0025$ is often used in ocean models, C_d is not well constrained observationally beneath ice shelves (Gwyther et al., 2015). As this formulation is based on frictional boundary layer theory it predicts no melting for $U_0 = 0.0$ cm s^{-1}.

Almost all of the temperature and salinity difference between the interface and far-field occurs over the diffusive sublayer, which occupies the few O(1 cm) closest to the ice. Accordingly, Gade (1993) based a melting formulation on the fluxes within this diffusive region, defining $\delta_T \equiv (T_{ML} - T_b)/(\partial T/\partial z)_b$ and salinity $\delta_S \equiv (S_{ML} - S_b)/(\partial S/\partial z)_b$ to be the gradient thickness in temperature and salinity respectively. Terms δ_T and δ_S can be thought of as approximating the thermal and saline diffusive boundary layer depth, where the approximation will be perfect if the temperature and salinity profiles vary linearly over the diffusive sublayer. In this case the oceanic heat and salt fluxes can be expressed as:

$$Q_T = \rho c_p \kappa_T \frac{T_{ML} - T_b}{\delta_T} \tag{4.14}$$

$$Q_S = \rho \kappa_S \frac{S_{ML} - S_b}{\delta_S}. \tag{4.15}$$

The gradient thickness ratio δ_T/δ_S is related to the ratio of heat to salt transfer coefficients by the Lewis number $Le = \kappa_T/\kappa_S$ as $\Gamma_T/\Gamma_S = Le(\delta_S/\delta_T)$. To reconcile 4.12, 4.13 and 4.14, 4.15 the thermal and saline diffusive sublayers should be controlled by current shear, and thin with increasing friction velocity (e.g. Wells and Worster, 2008; McConnochie and Kerr, 2017a).

There are many conditions pertinent to the Antarctic ISOBL where shear does not control the thickness of the diffusive sublayer. In the case of a sloping ice shelf, fresh meltwater drives convection adjacent to the ice and it is convective instability, rather than shear, that controls the diffusive sublayer thickness (Kerr and McConnochie, 2015; McConnochie and Kerr, 2018; Mondal et al., 2019) and sets the melt rate. Under flat ice with relatively weak currents, double-diffusive convection occurs and melting is inherently transient (chapter 3; Martin and Kauffman, 1977; Keitzl et al., 2016a).

Table 4.1: Grid specifications for different velocity and Coriolis forcing. Free stream velocity U_0; Coriolis frequency f; domain horizontal dimension LX (= LY); domain height LZ; horizontal resolution (in wall units) ΔX^+ (=ΔY^+); vertical resolution at the ice-ocean interface ΔZ^+.

	U_0	f	LX	LZ	ΔX^+	ΔZ^+
	cm s^{-1}	$\times 10^{-3}$ s^{-1}	m	m		
G1	0.7	-1.37	3.6	6	10	0.5
G2	1.4	-1.37	7.2	7.2	20	0.9
G3	2.8	-2.74	7.2	9	20	0.9

4.3 Methods

The governing equations and numerical implementation for the simulations presented in this chapter are identical to those described in §3.2. This section provides an overview of the problem set-up and model forcing, and outlines the model domain and resolution for the present simulations. The steady flow and turbulent boundary layer beneath a horizontal ice shelf is modelled in a computational domain of height LZ and horizontal dimensions $LX = LY$. A schematic of the model domain is shown in Fig. 4.1. The flow is periodic in both horizontal directions. The upper and lower boundaries are impenetrable, assuming that the flow is statistically homogeneous in the horizontal plane. The boundary conditions at the upper and lower boundaries are no-slip and free-slip respectively. The flow velocities in x, y and z directions are u, v and w respectively.

The ambient flow, with amplitude U_0, is achieved through forcing with a constant pressure gradient in the y-direction. A geostrophic balance of $1/\rho_0(\partial p/\partial y) = -fU_0$ holds in the interior of the domain, and an Ekman boundary layer forms beneath the ice. The Coriolis parameter f is constant within the domain. A stable ambient stratification with buoyancy frequency $N_0 = 1.75 \times 10^{-3}$ s^{-1} is imposed using an initial salinity profile given by $S_{bg} = S_0 - 4.0 \times 10^{-4} z$ g kg^{-1}, where reference salinity is set to $S_0 = 34.5$ g kg^{-1} for all cases. The initial temperature profile is constant in depth, and the reference temperature T_0 is varied between runs.

The domain size and grid resolution vary between experiments. The domain size is based upon the planetary scale δ_f (the Ekman boundary layer depth is expected to be $\sim 0.7\delta_f$) which is estimated using the expression $\delta_f = u_0^*/|f|$ where f (s^{-1}) is the Coriolis frequency and u_0^* (m s^{-1}) is the friction velocity, estimated *a priori* using the

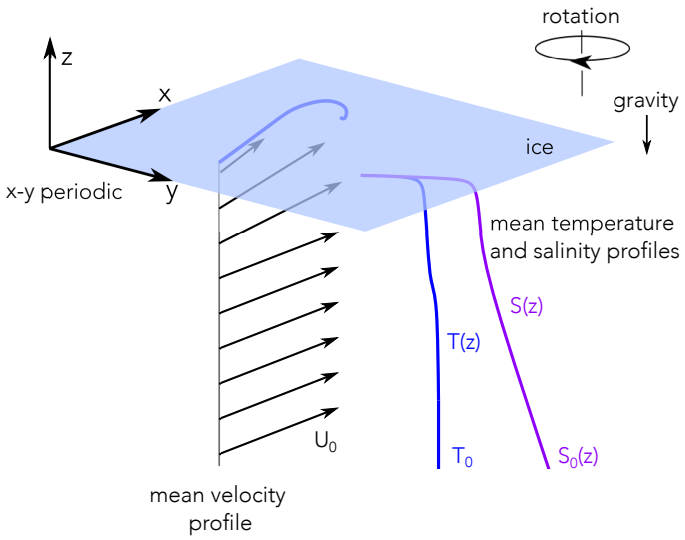

Figure 4.1: Schematic of the model domain, which consists of a horizontal ice-ocean interface with cold, salty ocean below. In the interior of the domain the ocean is in geostrophic balance and has velocity (u, v) =$(U_0, 0)$. Near the ice an Ekman boundary layer forms.

drag law relationship $u_0^* = C_d^{1/2} U_0$ taking $C_d = 0.0025$. The domain size $LX \times LY \times LZ$ is approximately $1.4\delta_f \times 1.4\delta_f \times 1.8\delta_f$. The dimensional domain sizes can be found in Table 4.1. Grid resolution is based upon the viscous lengthscale $\delta_\nu = \nu/u_0^*$ where $\nu = 2 \times 10^{-6}$ m^2 s^{-1} is the molecular viscosity. The grid resolution for each experiment is expressed in wall units as $\Delta X^+ = \Delta X/\delta_\nu$, with ΔY^+ and ΔZ^+ equivalently defined. The grid resolution is chosen to be consistent with the results of Salon et al. (2007) for resolved LES. The grid that is uniform in both the x and y directions and stretched in the z-direction to achieve higher resolution near the boundary. The horizontal resolution is typically $\Delta X^+ = 20$, with the exception of the 0.7 cm s^{-1} run, where it is $\Delta X^+ = 10$ in order to satisfy horizontal-to-vertical grid aspect ratio and vertical resolution constraints simultaneously. Extremely high resolution is required near the boundary to capture the near-ice diffusive sublayers, which are thin due to the realistic κ_T and κ_S values. The grid stretching is performed using a tanh function with resolution $\Delta Z^+ < 1$ at the wall. The aspect ratio of grid cells at the edge of the viscous sublayer (Z^+=50) has also been shown to be important, with $A = \Delta Z^+/\Delta X^+ = 1/8$ being recommended in a previous study (Vreugdenhil and Taylor, 2019). No dependence on aspect ratio was found for

$1/30 < A < 1/7$ (Appendix A.2), and most runs were performed with $A \sim 1/11$.

To ease computational constraints for the highest velocity runs, the Coriolis parameter is doubled from the physically relevant value of $f = -1.37 \times 10^{-3}$ s^{-1} to $f = -2.74 \times 10^{-3}$ s^{-1}, allowing a smaller domain to be used. Doubling f does not affect the near-ice dynamics or heat transfer (Appendix A.3), although it does affect the Ekman boundary layer and mixed layer. The influence of varying f on the ISOBL is quantified and explained in the results section.

Free stream velocity (U_0) and initial temperature (T_0) and are varied between runs, where each T_0 has a corresponding initial thermal driving $T_0^* = T_0 - T_f(S_0)$, where $T_f(S_0)$ is the freezing temperature at salinity S_0. The model is forced with $U_0 = 0.7,\ 1.4$ and 2.8 cm s^{-1} at $T^* = 0.0025,\ 0.0075$ and 0.05 °C. For each run, a neutral (unstratified) spin-up run is performed to obtain the velocity field of a steady-state turbulent Ekman boundary layer. At model time $t = 0$ h the initial temperature and salinity profiles are applied, after which time the temperature, salinity and velocity fields co-evolve. The simulations are run for 2-3 inertial periods.

4.4 Results

4.4.1 Boundary layer evolution and velocity characteristics

Flow beneath a stationary ice shelf results in vertical shear and forms a turbulent boundary layer beneath the ice. This boundary layer determines the melt rate by regulating the transfer of heat and salt from the far-field ocean to the ice. Fig. 4.2 shows the ice-ocean boundary layer and melt rate at the ice-ocean interface for run A3 (Table 4.2) with free stream velocity $U_0 = 2.8$ cm s^{-1}. Turbulence beneath the ice, visible as fluctuations in the vertical velocity field, mixes cold meltwater over the upper $\sim$ 2.5 m of the water column and supplies heat to the ice-ocean interface. The resulting melt rate is spatially heterogeneous due to the presence of elongated turbulent structures near the ice, which increase heat flux locally (Vreugdenhil and Taylor, 2019). These structures are aligned with the wall stress τ_w which, due to Coriolis, has a cross-stream component.

Fig. 4.3 shows the evolution and characteristics of this boundary layer under cold conditions over three inertial periods, where an inertial period $\Delta t = 2\pi/|f|$ (s). The difference between the initial mixed layer temperature and the *in situ* freezing temperature (a quan-

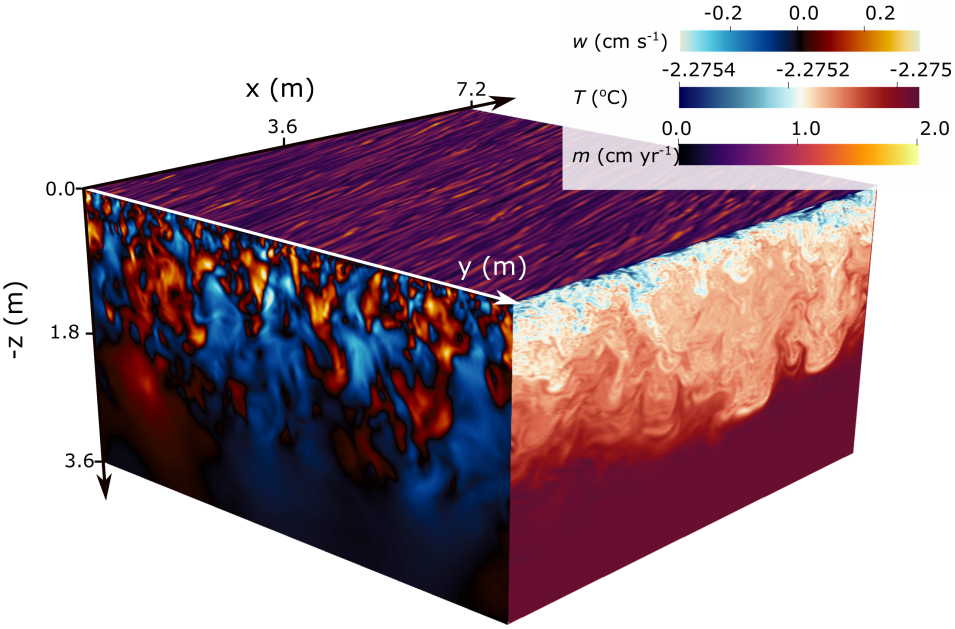

Figure 4.2: Snapshot of output for run A3 at $t = \Delta t$. Horizontal $(x - y)$ plane shows instantaneous melt rate m at the ice-ocean boundary. Vertical planes show vertical velocity w ($z - y$ plane) and temperature T ($x - z$ plane). Only the upper 3.6 m of the domain is shown.

tity known as the thermal driving, hereafter T^*) in this run is only 0.0025 °C. The steady far-field flow with magnitude $U_0 = 1.4$ cm s^{-1} exerts a shear stress on the stationary ice-ocean interface (τ_w) which is characterised by the friction velocity $u^* = (\tau_w/\rho_0)^{1/2}$. The friction velocity remains steady over the course of the simulation. Plane-averaged profiles of Turbulent Kinetic Energy (TKE, denoted by k), defined as:

$$k = \frac{1}{2}(\overline{u'u'} + \overline{v'v'} + \overline{w'w'}), \tag{4.16}$$

where u', v' and w' are deviations from the horizontal mean velocity, show active turbulence over the upper 2 m of the water column. The TKE is most intense near the ice (Fig. 4.3B). This turbulence rapidly homogenises the initial scalar profiles forming a mixed layer in temperature (Fig. 4.3C) and salinity (not shown) beneath the ice. The squared buoyancy frequency $N^2 = -g/\rho_0(\partial\rho/\partial z)$ (Fig. 4.3D) characterises the stratification of the water column. As the flow develops, a strong density gradient (pycnocline) forms at the base of the mixed layer. The pycnocline deepens gradually over the course of the experiment due to entrainment of ambient fluid into the mixed layer. The mixed

Table 4.2: Key parameters and results. Free stream velocity U_0; initial thermal driving T_0^*; friction velocity u^*; drag coefficient C_d; temperature difference between the interface and mixed layer $T_b - T_{ML}$; melt rate m; Obukhov lengthscale L; viscous Obukhov lengthscale L^+; and mixed layer classification as WM (well-mixed), STR (stratified) or DC (diffusive convective). All results are at $t = 3\Delta t$, except runs A3, B3 and C3 which are at $t = 2\Delta t$.

run	U_0 cm s^{-1}	T_0^* ° C	u^* cm s^{-1}	C_d	$T_b - T_{ML}$ ° C	m cm yr^{-1}	L m	L^+	type
A1	0.7	0.0025	0.038	0.0030	0.00080	0.097	11.17	2000	WM
A2	1.4	0.0025	0.069	0.0024	0.00083	0.264	24.42	8390	WM
A3	2.8	0.0025	0.133	0.0023	0.00101	0.674	70.56	46840	WM
B1	0.7	0.0075	0.036	0.0026	0.00258	0.260	3.78	680	WM
B2	1.4	0.0075	0.066	0.0022	0.00219	0.549	10.18	3340	WM
B3	2.8	0.0075	0.131	0.0022	0.00290	1.860	24.42	15980	WM
C1	0.7	0.05	0.034	0.0024	0.02110	1.633	0.50	80	DC
C2	1.4	0.05	0.051	0.0013	0.01723	1.779	1.47	370	STR
C3	2.8	0.05	0.121	0.0019	0.01654	7.425	4.87	2950	STR
1	0.0	0.175	$\sim$		0.07586	6.078	$\sim$	$\sim$	DC
2	0.7	0.175	0.036	0.0026	0.07511	6.229	0.17	30	DC
3	1.4	0.175	0.052	0.0014	0.06908	6.559	0.47	120	DC
3*	1.4	0.375	0.051	0.0013	0.15701	14.557	0.22	50	DC
4	2.0	0.175	0.064	0.0010	0.06115	6.167	0.90	290	STR

layer cools and freshens over time, due to the heat and salt fluxes associated with basal melting. The melt rate (Fig. 4.3A) undergoes an initial adjustment phase at the beginning of the simulation, in which the thermal and saline diffusive boundary layers form adjacent to the ice. After $\sim 1\Delta t$ the melt rate achieves a quasi-steady value, evolving gradually in response to the cooling of the mixed layer.

The ISOBL characteristics and evolution are strongly influenced by ocean temperature. Higher T^* results in an increased melt rate and higher surface buoyancy forcing, which suppresses boundary layer turbulence. Fig. 4.4 shows the evolution of the boundary layer in run C2, which has the same current forcing ($U_0 = 1.4$ cm s^{-1}) as run A2 but a much higher thermal driving ($T^* \sim 0.05$ °C). For the warmer run the melt rate is much higher, while the boundary layer turbulence is weaker. After $\sim 1\Delta t$ the TKE drops off at depth and turbulent mixing is confined to the upper $\sim$1 m of the water column. Melting, which both cools and freshens the water near the interface, constitutes a stabilising buoyancy

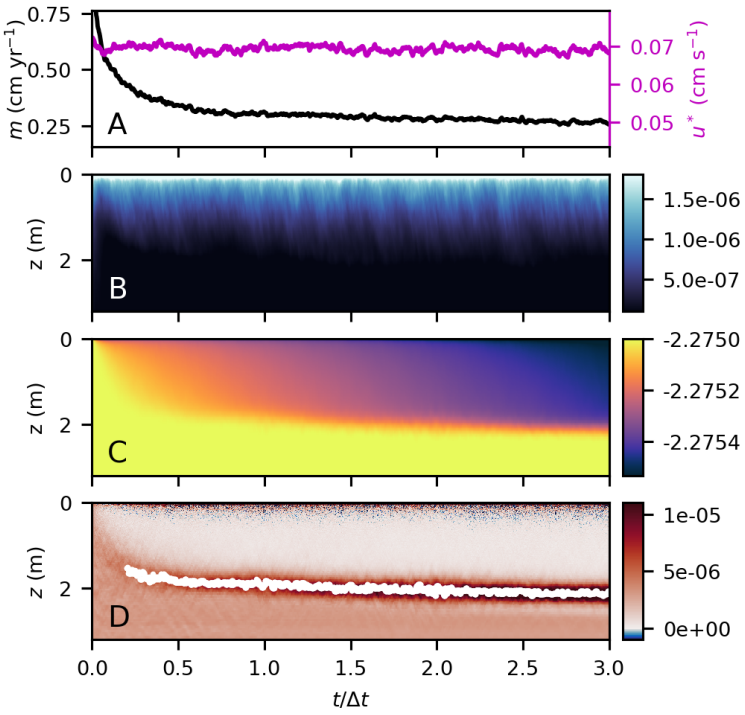

Figure 4.3: Temporal evolution of key quantities for run A2 over three inertial periods: (A) melt rate m and friction velocity u^*; (B) Turbulent Kinetic Energy k (m^2 s^{-2}); (C) temperature T (°C); and (D) squared buoyancy frequency N^2 (s^{-2}) with the base of the mixed layer (here defined by the pycnocline depth) highlighted in white.

flux which tends to stratify the water column. The increased melting, and therefore stabilising buoyancy flux, in run C2 results in turbulence suppression and a reduction of the mixing depth compared to the cooler run A2 (Fig. 4.3). The change in mixing depth causes a new pycnocline to form above the first from $\sim 2\Delta t$. The region above this pycnocline is not well-mixed, despite the active mixing occurring there, indicating that the boundary layer turbulence is insufficiently strong to mix away the buoyancy supplied by melting. Over the course of the simulation, the friction velocity decreases by $\sim 30\%$ from its original value.

At warmer conditions the boundary layer velocity profile deviates from the classic logarithmic velocity profile, with the profile appearing more "laminar" in the near-wall region. Immediately below the ice, in the viscous sublayer, the flow is laminar and the velocity scales with distance from the ice. This is shown for velocities of $U_0 = 0.7, 1.4$ and 2.8 cm s^{-1} at $T^* \sim 0.003$ and 0.05 °C in Fig. 4.5, where the velocity profiles all follow the viscous scaling for $z^+ < 5$. Away from the interface, velocity profiles are compared with

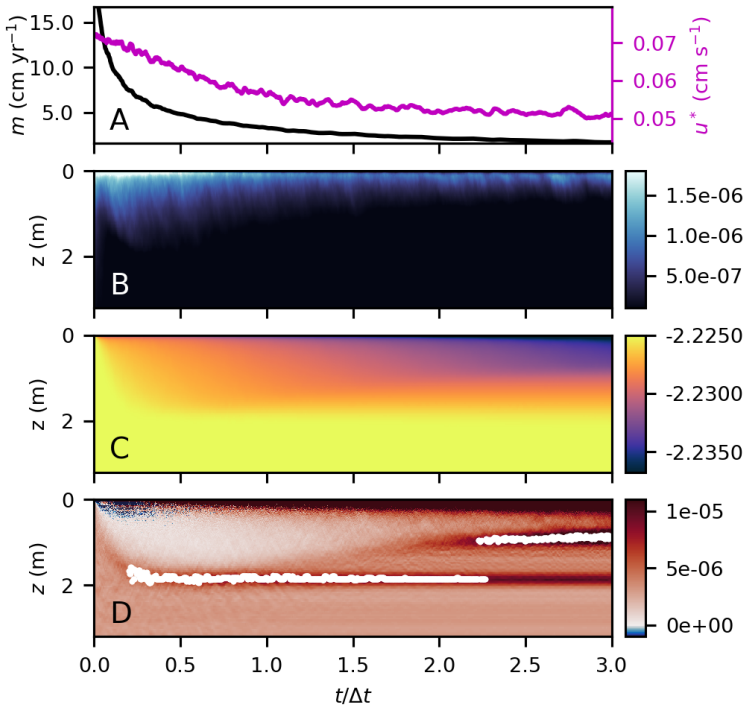

Figure 4.4: Temporal evolution of key quantities for run C2 over three inertial periods. Panels as in Fig. 4.3. The base of the mixed layer (here defined by the depth of the strongest pycnocline) is highlighted in white.

the classic log law (Eq. 4.4) and Monin-Obukhov (MO) similarity scaling (Eq. 4.6), which takes into account the effect of the surface buoyancy flux. At low thermal driving (Fig. 4.5A), with the exception of the lowest velocity run, the boundary layer profile is well explained by the MO scaling over $50 \leq z^+ \leq 500$. At these conditions, which correspond to large L, the MO-similarity scaling does not deviate much from the classic LOW scaling. At warmer temperatures, the fit between the velocity profiles and MO scaling (Eq. 4.6) is poor. While the scaling captures the tendency for the shear to be concentrated closer to the boundary it does not accurately represent the shape of the velocity profile. For runs C1 and C2, the velocity profile remains closer to the viscous scaling than the LOW scaling for $z^+ < 100$.

The behaviour of velocity profiles C1–C3 is not monotonic with increasing free stream velocity. For fixed T_0^*, stratification effects are expected to diminish with increasing u^*. However, run C2 shows the largest deviation from the classic LOW scaling suggesting that it is more "stratification-affected" than run C1. We suggest that the weaker shear in case C1 allows double-diffusive mixing to occur, and that the variation between runs C1

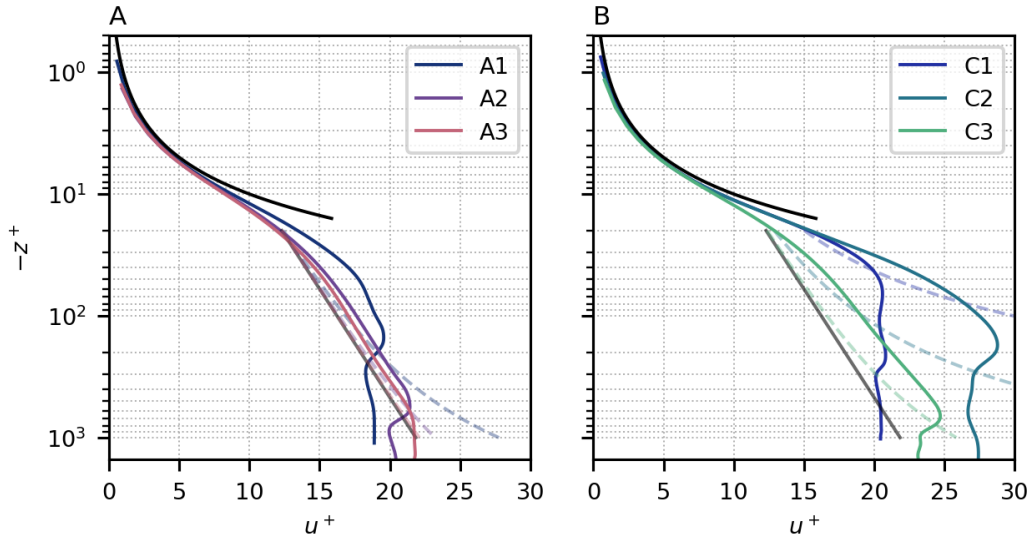

Figure 4.5: Velocity profiles in wall units for (A) experiments A1–3 and (B) experiments C1–3. Over-plotted are the viscous boundary layer scaling $u^+ = z^+$ (solid black line); logarithmic boundary layer scaling (Eq. 4.4; solid grey line) and M-O similarity scaling (Eq. 4.6; dashed lines, colours correspond to labelled experiments).

and C2 is a result of the dominance of different mixing processes. This will be discussed further in section 4.4.2.

The velocity profiles in Fig. 4.5 are scaled as $u^+ = u/u^*$, thus the far-field u^+ is related to the drag coefficient as $C_d = (1/u^+)^2$. For warm runs C2 and C3, the drag coefficients are reduced compared to their cool counterparts A2 and A3. Drag coefficients for each experiment can be found in Table 4.2. A decrease in drag due to increasing ocean temperatures in a melting scenario has been shown in both in chapter 3 and Vreugdenhil and Taylor (2019). This is also consistent with results from stabilised Ekman boundary layers, where increasing static stability decreases drag (Deusebio et al., 2014; Shah and Bou-Zeid, 2014). The surface buoyancy flux also increases cross-stream flow in the boundary layer, broadening the Ekman spiral. The horizontal velocity components (u, v) for runs A2 and C2 (at $U_0 = 1.4$ cm s^{-1}) are shown in the hodograph in Fig. 4.6A. The ageostrophic (v) component of the velocity is larger for the higher thermal driving run. The angle between the geostrophic flow and the wall shear stress has also increased and is closer to the expected angle for laminar flow of 45°. The same trend is observed, although to a lesser extent, for runs A3 and C3 (at $U_0 = 2.8$ cm s^{-1}). In terms of

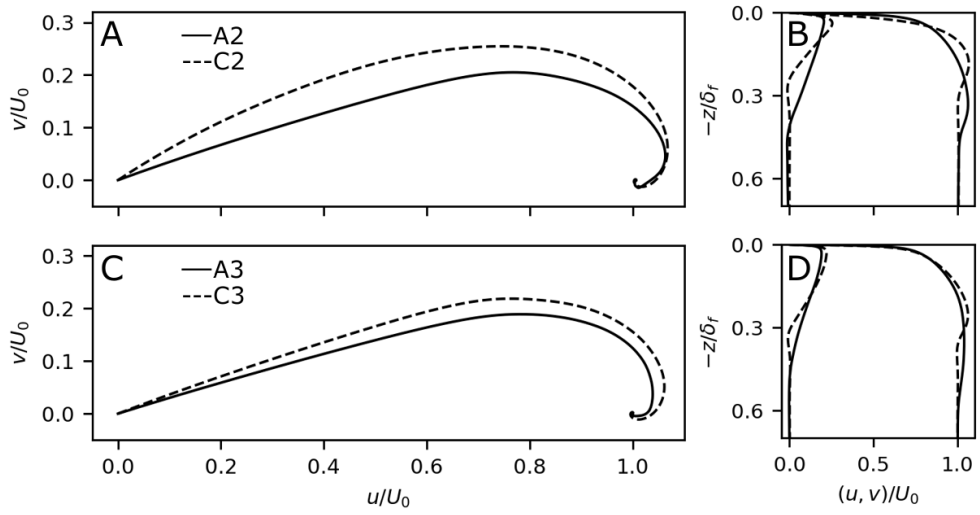

Figure 4.6: Normalised geostrophic (u) and ageostophic (v) flow for (A, B) runs A2 and C2 with $U_0 = 1.4$ cm s^{-1} and (C, D) runs A3 and C3 with $U_0 = 2.8$ cm s^{-1}. In (B) and (D) profiles are plotted as a function of z scaled by the planetary scale δ_f. Velocity components are averaged over $2\Delta t < t < 3\Delta t$ for A2,C2 and $\Delta t < t < 2\Delta t$ for A3, C3.

total transport, the enhancement of the cross stream component is offset by the overall thinning of the velocity boundary layer (Fig. 4.6B and C).

4.4.2 Mixed layer depth

Boundary layer turbulence can homogenise temperature and salinity profiles, forming a mixed layer adjacent to the ice. Depending on the dominant boundary layer processes, one of three mixed layer structures is observed. In this thesis, ISOBL "regimes" are defined based on the mixed layer structure (Fig. 4.7). These regimes are termed "well-mixed", "stratified" and "diffusive convective". In this section, simulations are categorized and existing theory is used to model the mixed layer depth for each ISOBL regime.

Well-mixed regime: effects of currents shear and stratification

At low thermal driving, the depth of the mixed layer can be predicted using a simple scaling law based on the friction velocity, Coriolis frequency and far-field stratification. Fig 4.8 shows profiles of plane-averaged buoyancy frequency (N^2) for all experiments,

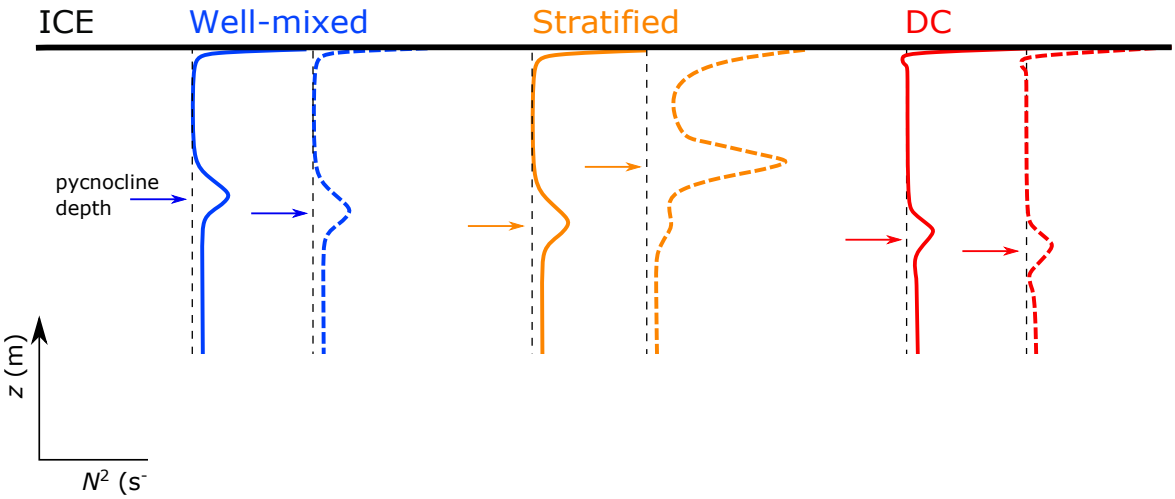

Figure 4.7: Schematic showing typical profiles of squared buoyancy frequency (N^2) for the three observed ISOBL "regimes" at $t = \Delta t$ and $t = 2\Delta t$. In each profile the pycnocline depth, which we use as a proxy for mixed layer depth, is shown with an arrow.

where depth is normalised by the planetary scale δ_f. All A- and B- experiments have a similar density structure, with a single, well-mixed layer and pycnocline beneath the ice, where we use the pycnocline depth as a proxy for the mixed layer depth (Fig. 4.7). Here, these runs are classified as "well-mixed'.

The A- and B- runs evolve in a qualitatively similar manner to what is shown in Fig. 4.3 for run A2. However, the pycnocline depths do not collapse with the scaled vertical coordinate. Rather than the f^{-1} dependence suggested by the planetary scale, the mixed layer depth scales with $f^{-1/2}$, consistent with the stratified Ekman boundary layer scale h_γ, (Eq. 4.7). See Appendix A for an extension of this result to higher f. The h_γ scaling explains the mixed layer depth well for all A- and B- experiments (Fig. 4.9) with constant $A = 1.3$, as suggested by Weatherly and Martin (1978). This result is consistent with the work of McWilliams et al. (2009) and Taylor and Sarkar (2008b) who showed that increasing external stratification thins the Ekman boundary layer and mixed layer.

Stratified regime: effects of current shear and surface buoyancy flux

At warmer ocean conditions (C- runs), the mixed layer depth and structure departs from the stratified Ekman boundary layer scaling. For runs C2 and C3, with current speeds of $U_0 = 1.4$ cm s^{-1} and $U_0 = 2.8$ cm s^{-1}, respectively, the mixing depth is observed to shoal

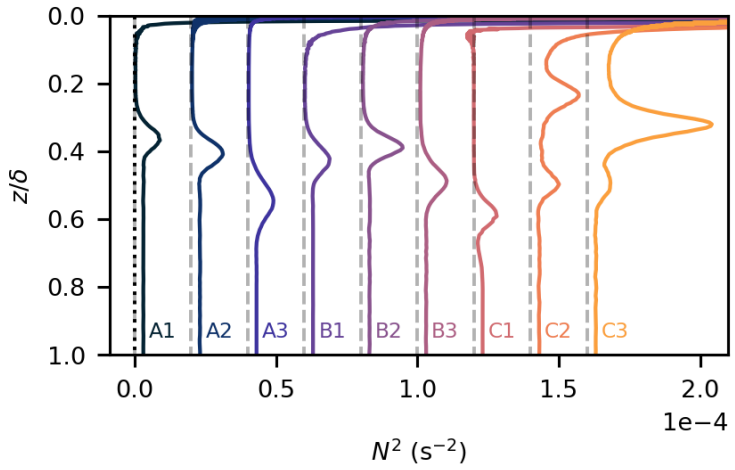

Figure 4.8: Profiles of squared buoyancy frequency (N^2) for all runs (labelled) at $t/\Delta t = 2$. Profiles are offset by $N^2 = 2 \times 10^{-5}$ s^{-2}.

over the course of the experiment and the mixed layer is observed to restratify, indicating that the boundary layer turbulence is being suppressed by the surface meltwater flux. Despite this restratification, mixing remains active, as demonstrated by the formation of a second pycnocline beneath the ice (e.g. Fig 4.4). Thus, despite the absence of a well-mixed layer, we still define a mixed layer depth based upon the depth of the strongest pycnocline beneath the ice, as shown in Fig. 4.7. Runs that exhibit this restratifing behavior are classified as "stratified".

Whether or not the ISOBL will stratify can be determined by comparing the Obukhov length L to the planetary scale δ_f, where it is the smaller scale that governs (McPhee, 2008). The Obukhov lengthscale (Eq. 4.5) gives an estimate of the depth at which turbulence will feel the effects of stratification due to surface buoyancy forcing. If the Obukhov lengthscale is much larger than the planetary scale ($\mu = u^*/(fL) \ll 1$) then the ISOBL is unlikely to be affected by the surface buoyancy forcing. However, if the two are of similar magnitude ($\mu = u^*/(fL) \sim 1$) then the boundary layer will be affected by stabilising buoyancy. Obukhov lengthscale L is compared with the planetary scale δ_f rather than the stratified Ekman scale h_γ based on the observation that the stratified boundary layer forms over the top of an initially well-mixed ($N^2 \sim 0$) region (e.g. Fig. 4.4D). Because the mixing depth shoals in time, the far-field stratification N_∞ is unlikely to be "felt" by the boundary layer turbulence. For run C2 $\mu = 2.3$ while for run C3 $\mu = 0.9$. Fig. 4.10A plots the mixed layer depth against μ. Only two of the present

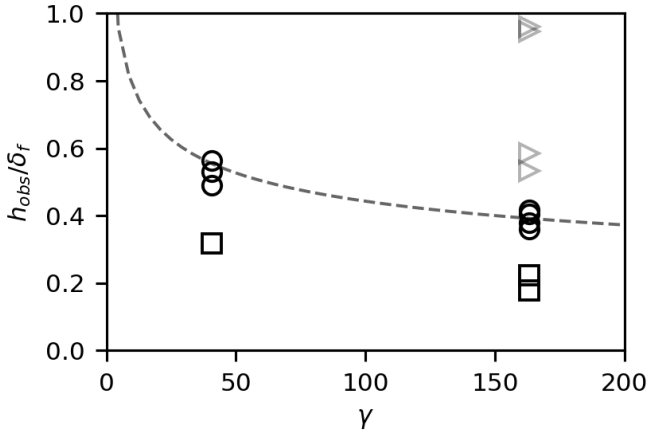

Figure 4.9: Simulated mixed layer depth h_{obs} scaled by planetary scale δ_f as a function of stratification parameter γ. Dashed line is $h_{obs}/\delta_f = 1.4\gamma^{-1/4}$. Markers show well-mixed (circle) stratified (square) and diffusive-convective (triangle) boundary layers respectively.

simulations fall within the "stratified" regime. Drawing in results from chapter 3 yield a third stratified run (Exp. 4; Table 4.2) with $\mu = 4.9$.

The scaled mixed layer depth (h_{obs}/δ_f) decreases as the stability parameter μ increases for the stratified runs. The scaling $\mu^{-1/2}$ well describes h_{obs}/δ_f, consistent with the findings of Deusebio et al. (2014) and the scaling from Zilitinkevich (1972). The expression of best fit given as $h_{obs}/\delta_f = 0.31\mu^{-1/2}$. Furthermore, the friction velocity and drag coefficient decrease as the stability parameter μ increases. The ratio u^*/U_0 scales with $\mu^{-1/5}$, consistent with the findings of Deusebio et al. (2014) (Fig. 4.10B).

Diffusive convective regime: effects of surface buoyancy flux and ambient stratification

At warm temperatures and low current speed, DC drives turbulent fluxes beneath the ice and sets the mixed layer depth. For run C1, the mixed layer is much deeper than expected from the planetary scale (Fig. 4.8). Beneath the diffusive sublayer, N^2 becomes negative over a short distance, evidence that this run is in the DC regime. Cold, fresh meltwater has a stabilising effect, resulting in strong stratification near the ice. However, heat diffuses away from the interface more rapidly than salt ($\kappa_T/\kappa_S = 110$), resulting in a gravitationally unstable region and convection some distance from the ice. As shown in

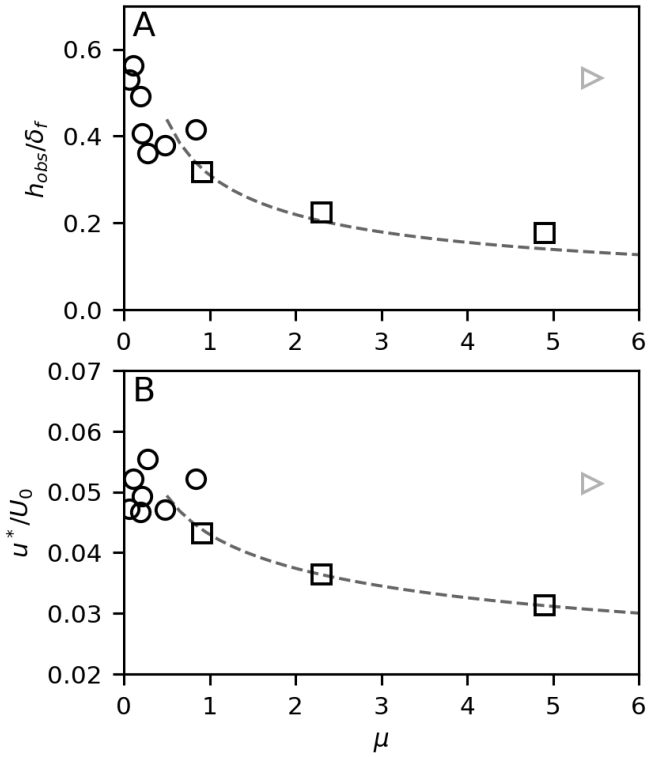

Figure 4.10: (A) Simulated mixed layer depth h_{obs} scaled by planetary scale δ_f as a function of stability parameter μ, the dashed line is $h_{obs}/\delta_f = 0.31\mu^{-1/2}$. (B) Friction velocity u^* normalised by geostrophic velocity U_0 as a function of stability parameter μ, dashed line is $u^*/U_0 = 0.043\mu^{-1/5}$. Markers as for Fig. 4.9.

chapter 3, in the DC regime the mixed layer depth depends upon the thermal driving, and the melt rate is inherently unsteady in time. Combining run C2 with results from chapter 3, mixed layer depth scaling in the DC regime can be investigated. For a dynamically similar problem, in which a stable salinity gradient was heated from below, Fernando (1987) found that the mixed layer depth is controlled by the surface buoyancy flux due to heat only (B^T) and the far-field stratification as

$$h_{DC} = C \left(\frac{B^T}{N_\infty^3} \right)^{1/2}, \tag{4.17}$$

with constant $C = 41$.

Fig. 4.11 plots h_{obs} against B^T/N_∞^3 and shows that the 1/2 power is appropriate. However, the constant $C \sim 11$ here. One key feature of the DC regime is that the melt rate, and therefore B^T, are inherently time dependent. Thus, surface buoyancy flux due to

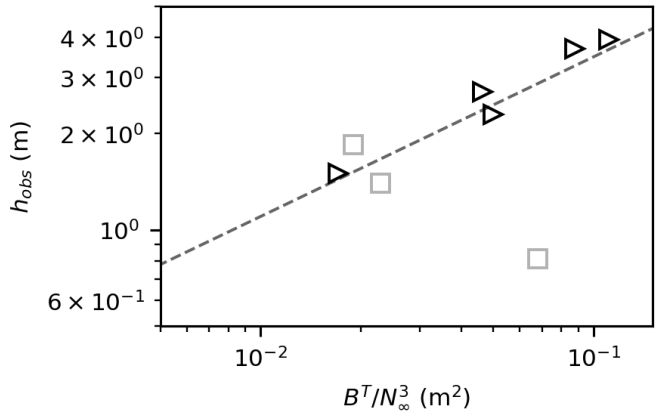

Figure 4.11: Simulated mixed layer depth h_{obs} as a function of B^T/N_∞^3, the dashed line is $h_{obs} = 11(B^T/N_\infty^3)^{1/2}$. Markers as for Fig. 4.9.

heat is taken as the mean over the first 5 h of simulation time, as the majority of the mixed layer growth occurs over that period.

4.4.3 Melting

At low thermal driving, the melt rate is a strong function of friction velocity. However, as temperature increases, the sensitivity of the melt rate to increasing friction velocity diminishes. Fig. 4.12 shows the melt rate plotted against u^* for thermal driving ranges 0.0019–0.0023, 0.006–0.007, 0.04–0.05 and 0.14–0.18 °C, where the latter results are from chapter 3. These temperature ranges account for the variation between experiments and variation in time over $1 \leq \Delta t \leq 3$. Although sets of experiments are initialised with the same far-field temperature, factors such as mixed layer depth and melt rate influence the temperature of the mixed layer as it evolves. Melt rates become increasingly insensitive to current shear as thermal driving increases (Fig. 4.12). In the temperature range 0.0019–0.0023°C, the dependence of melt rate on u^* is close to linear, and the melt rates agree well with the three-equation parameterisation (Eqs. 4.12, 4.13 and 4.9). The fit is especially good in the highest friction velocity (A3) run. As thermal driving increases, the fit between the parameterisation and the simulations worsens, especially at low friction velocity. In the thermal driving range 0.14–0.18 °C the melt rate is largely insensitive to increasing friction velocity for the simulated u^* values. These simulations show a tendency for unsteady melt rates under low friction velocity and high thermal driving

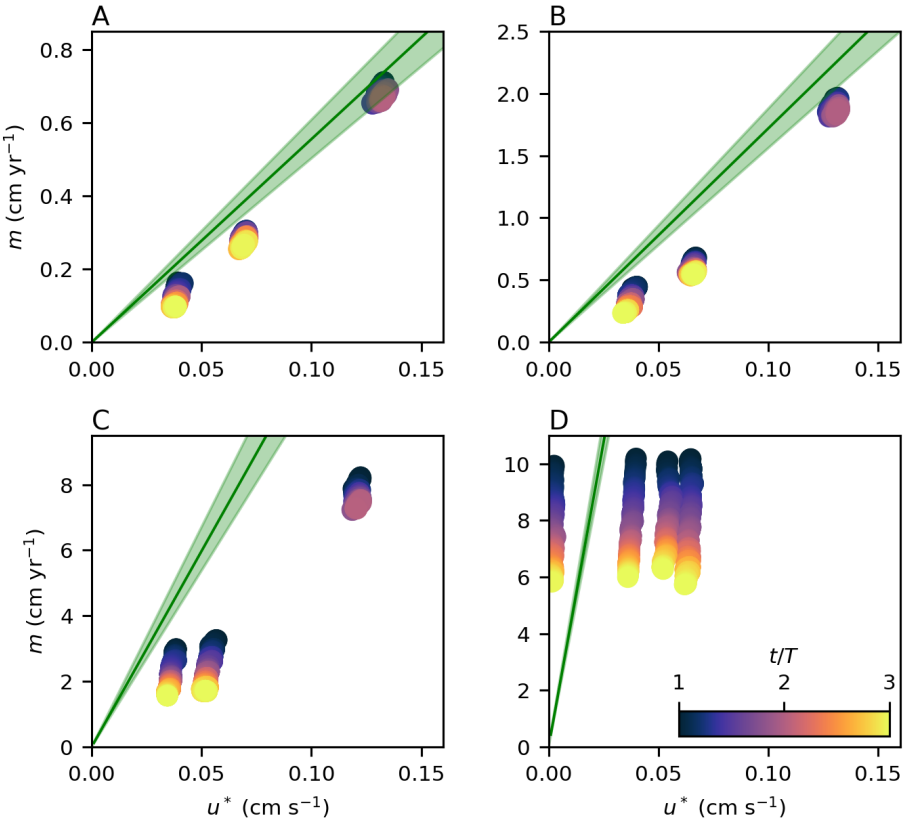

Figure 4.12: Melt rate m as a function of friction velocity u^* for (A) $0.0019 \leq T^* \leq 0.0023$, (B) $0.006 \leq T^* \leq 0.007$, (C) $0.04 \leq T^* \leq 0.05$ and (D) $0.14 \leq T^* \leq 0.18$. Markers are are coloured by time $t/\Delta t$. Green lines show the expected dependence of m on u^* from Eqs. 4.12, 4.13 and 4.9 with transfer coefficients $\Gamma_T = 0.011$ and $\Gamma_S = 3.1 \times 10^{-4}$ from Jenkins et al. (2010b).

conditions.

Unsteady melt rates indicate that shear from the mean current is not controlling the thickness of the laminar sublayer across which heat and salt must diffuse. The magnitude of the viscous Obukhov length is a good predictor of whether shear is sufficiently strong to control the thickness of the laminar sublayer. The viscous Obukhov length is defined as the ratio of the Obukhov lengthscale and the viscous lengthscale:

$$L^+ = \frac{L}{\delta_\nu}. \tag{4.18}$$

A small L^+ value indicates there is no region of the flow free from the effects of either stratification or viscosity, both of which suppress turbulence. Fig. 4.13 shows the

time evolution of the gradient thickness in temperature $\delta_T \equiv T/(\partial T/\partial z)_b$ and salinity $\delta_S \equiv S/(\partial S/\partial z)_b$, and the thermal and saline transfer coefficients Γ_T and Γ_S. Transfer coefficient Γ_T and gradient thickness δ_T are related by $\delta_T = \kappa_T/(u^*\Gamma_T)$, with an equivalent expression for salinity. In order to achieve a steady state melt rate these parameters must be constant. Of the subset of runs presented here, only run C2 does not achieve a constant diffusive sublayer width. Figs. 4.13A,B show that δ_T and δ_S, which approximate the thermal and saline diffusive sublayer thicknesses, grow continuously over the simulation period for run C2. Consequently, transfer coefficients Γ_T and Γ_S decrease in time, as does the melt rate (Fig 4.12C). However, relative to run C2, an increase in far-field velocity (run C3) or a decrease in temperature (run B2) will result in a steady state. This behaviour can be explained by L^+, which is $\sim 10^2$ for run C2 but $\sim 10^3$ for runs C3 and B2. As friction velocity increases from 1.4 cm s^{-1} (run C2) to 2.8 cm s^{-1} (run C3), δ_T and δ_S decrease, demonstrating that shear is thinning the viscous sublayer and enhancing the interfacial heat and salt fluxes. This is the mechanism by which shear determines the melt rate, and (where it applies) justifies the form of the three-equation parameterisation. Figs. 4.13C,D show that the values of Γ_T and Γ_S collapse for experiments B2 and C3 with the same L^+, despite having different thermal and current forcing. This observation provides strong support for the hypothesis that L^+ determines near-ice properties, as found in Vreugdenhil and Taylor (2019).

Fig. 4.14A shows the ratio between the predicted melt rate from the three-equation parameterisation and the simulated melt rate for each experiment. Transfer coefficients $\Gamma_T = 0.0114$ and $\Gamma_S = 3.82 \times 10^{-4}$, the maximum values found in this study, are used rather than those suggested by Jenkins et al. (2010b). These value were obtained for run C3 and consequently the ratio $m_{pred}/m_{obs} = 1$ by definition for this run. The threshold $L^+ < 2500$ separates the steady and unsteady melt rates. The ratio m_{pred}/m_{obs} is arbitrary for the unsteady melting runs, as the transfer coefficients are constantly evolving due to the temporal growth of the diffusive sublayers. For $L^+ > 2500$ the fit between the predicted and observed melt rates increases systematically with increasing L^+. Figs. 4.14B and C show the dependence of Γ_T and Γ_S on L^+ over the range $2.5 \times 10^3 < L^+ < 5 \times 10^4$. These, too, increase as a function of L^+. Both Γ_T and Γ_S appear to asymptote to constant values at high L^+, although further data at higher L^+ is required to confirm this. Vreugdenhil and Taylor (2019) performed a "passive scalar" experiment where T and S fields did not influence the flow through buoyancy. For this run, intended to determine the heat and salt transfer at infinite L^+, they found

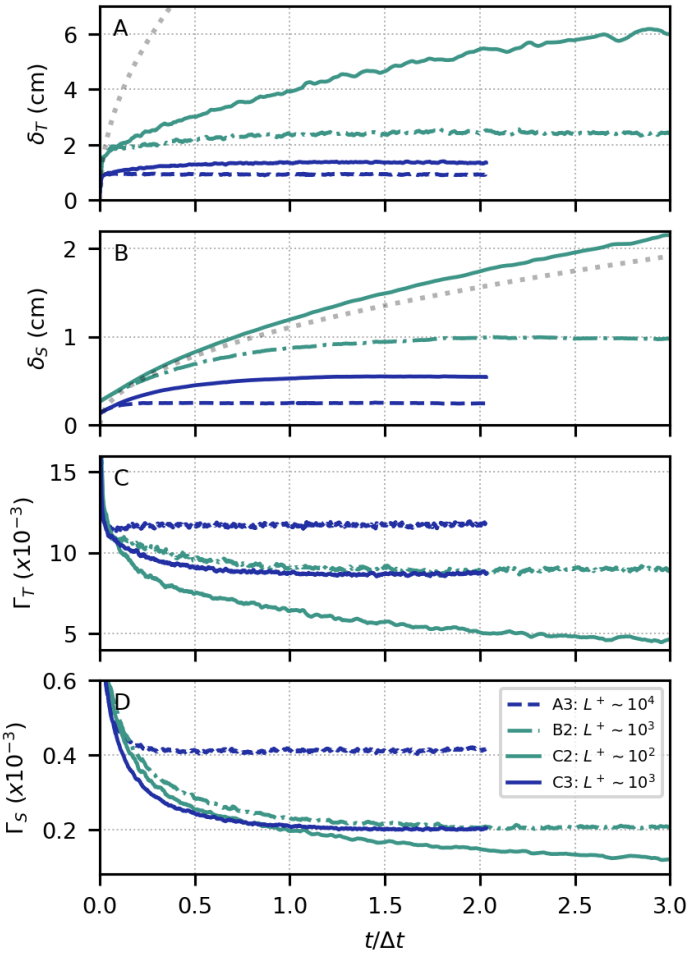

Figure 4.13: (A) Gradient thickness in temperature δ_T, (B) gradient thickness in salinity δ_S, (C) heat transfer coefficient Γ_T and (D) salt transfer coefficient Γ_S for runs A3, B3, C2 and C3. Thermal $(4\kappa_T t)^{1/2}$ and saline $(4\kappa_S t)^{1/2}$ diffusion lengthscales are over-plotted (dotted lines) on panels (A) and (B) respectively.

$\Gamma_T = 0.012$ and $\Gamma_S = 3.9 \times 10^{-3}$. In their simulations, transfer coefficients for non-passive scalar runs were observed to approach these upper limit values for $L^+ > 10^4$. Both the present results, and those of Vreugdenhil and Taylor (2019), imply that a constant transfer coefficient formulation such as that outlined in Jenkins et al. (2010b) is appropriate at cold, energetic (high L^+) conditions but not at warmer, less energetic conditions. This result will be discussed in the following section.

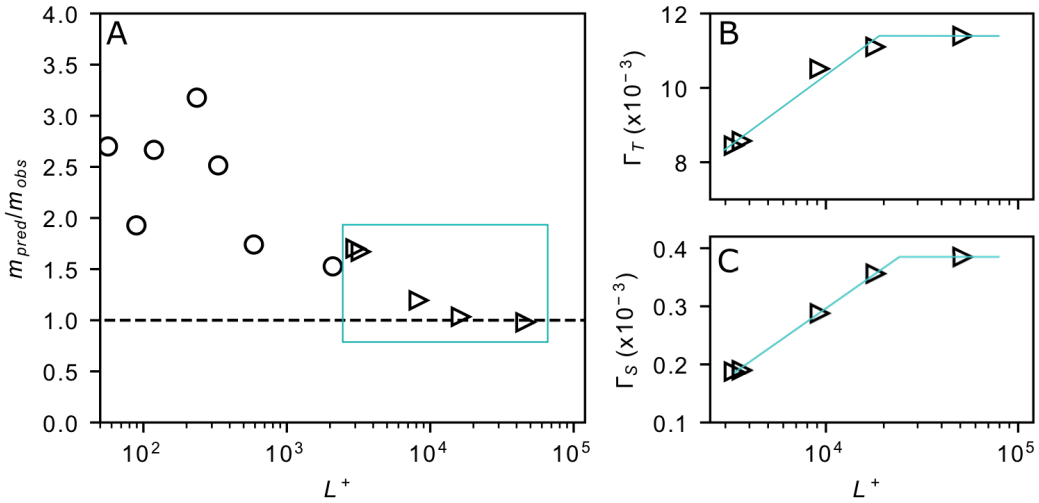

Figure 4.14: (A) Scatter plot showing ratio of simulated to parameterised melt rates as a function of the viscous Obukhov length L^+, where the predicted melt rates are obtained from the three-equation parameterisation with $\Gamma_T = 0.011$ and $\Gamma_S = 3.8 \times 10^{-4}$. Circles and triangles denote non steady-state and steady-state experiments respectively. For the steady state experiments, (B) Γ_T and (C) Γ_S are plotted as a function of L^+.

4.5 Discussion

This chapter has demonstrated the role of the viscous Obukhov lengthscale in determining the dynamics of the diffusive sublayer adjacent to the ice-ocean interface and therefore the basal melt rate. For high L^+, vertical shear due to the mean flow controls the diffusive sublayer thickness and a steady state melt rate is achieved, while for low L^+ the diffusive sublayer grows in time and melting is inherently time-dependent. The transition between steady and time-dependent melting occurs at $L^+ \sim 2500$. Over the intermediate range 2500 L^+ 25000, we have shown that buoyancy affects the efficiency with which heat and salt are transported to the ice ocean interface, leading to a decreased heat and salt transfer coefficients.

The transfer coefficients found in this study at high L^+ add to a growing body of evidence suggesting that constant values of Γ_T and Γ_S are appropriate for calculating melt rates for cold and/or energetic ice shelf cavities. The highest transfer coefficients agree extremely well with the transfer coefficients found in the modelling study of Vreugdenhil and Taylor (2019) at high L^+ (Table 4.3), as well as with observationally determined coefficients from beneath the Filchner Ronne Ice Shelf (Jenkins et al., 2010b) and sea

Table 4.3: Comparison of transfer coefficients from observational and numerical studies. Thermal Stanton number $C_d^{1/2}\Gamma_T$, drag coefficient C_d, heat transfer coefficient Γ_T, ratio of heat and salt transfer coefficients Γ_T/Γ_S, simulation Lewis number Le, gradient thickness ratio δ_T/δ_S. *Ratio assumed, not measured. #Nominal Le values used to enable comparison with modelling results.

study	$C_d^{1/2}\Gamma_T$	C_d	Γ_T	Γ_T/Γ_S	Le	δ_T/δ_S
This study	5.2×10^{-4}	0.0022	0.011	29	110	3.7
Vreugdenhil and Taylor (2019)	4.6×10^{-4}	0.0015	0.012	31	180	5.8
Davis and Nicholls (2019)	0.0011	0.0022	0.024	35*		
Jenkins et al. (2010b)	0.0011	0.0097	0.011	35*		
Sirevaag (2009)			0.013	33	110#	3.3
Sirevaag (2009)			0.013	33	180#	5.5

ice in the Arctic (Sirevaag, 2009). For example, under the Filchner Ronne Ice Shelf, Jenkins et al. (2010b) determined the product $C_d^{1/2}\Gamma_T$ from the local melt rate and *in situ* oceanographic observations, assuming a ratio of heat to salt transfer of $\Gamma_T/\Gamma_S = 35$. Drawing on results from the sea ice literature, Jenkins et al. (2010b) also suggests values for the individual parameters C_d and Γ_T. Despite the assumptions involved in separating these terms, the heat transfer coefficient Γ_T recommended by Jenkins et al. (2010b) is in close agreement with the present results, and those of Sirevaag (2009) and Vreugdenhil and Taylor (2019). Beneath the Larsen C Ice Shelf Davis and Nicholls (2019) found extremely good agreement between their observed melt rates and the three-equation parameterisation using $C_d^{1/2}\Gamma_T = 0.011$ with $\Gamma_T/\Gamma_S = 35$. Combining this with the local drag coefficient, determined from measurements of boundary layer turbulence to be $C_d = 0.0022$, they obtain a heat transfer coefficient of $\Gamma_T = 0.024$, roughly double that found in the other observational and numerical studies presented in Table 4.3. Despite this discrepancy, these collective observations and simulations support the hypothesis that the three-equation parameterisation can perform well in cold and/or high velocity (L^+ 10^4) ice shelf cavities.

The viscous Obukhov scale can also be used to understand the poor agreement between the observed velocity profiles in Fig. 4.5B (particularly run C2) and the MO velocity scaling. At low L^+, there is little separation in scale between the largest and smallest turbulent structures in the surface layer (Flores and Riley, 2011). Consequently, for $L^+ < \mathrm{O}(100)$, boundary layer turbulence may become intermittent, or collapse entirely (Flores and Riley, 2011; Deusebio et al., 2014, 2015). This phenomenon was observed for the ISOBL by Vreugdenhil and Taylor (2019) for L^+ 300. While we did not

observe this turbulence collapse in our experiments, we suggest that increasingly strong stratification effects close to this threshold (e.g. run C2 with $L^+ = 370$) reduce the applicability of the MO scaling (Eq. 4.6), which is valid for weak stratification (Turner, 1979).

A significant finding of this chapter is that buoyancy effects on the near-ice and ISOBL dynamics are governed by two different scaling parameters. The interfacial heat and salt fluxes, and therefore the melt rate, depend strongly upon the viscous Obukhov lengthscale L^+. However, in the stratified regime, boundary layer depth is observed to scale with stability parameter μ instead. The result that the near-ice conditions are best described by L^+, while the boundary layer is governed by μ, is consistent with the results of Deusebio et al. (2014) for an Ekman boundary layer under a stabilising heat flux. They found that Nusselt number (the ratio of convective to conductive heat flux) was best described by L^+, while the boundary layer depth and friction velocity scaled with μ.

This chapter has shown that in the stratified ISOBL regime the Ekman layer and mixed layer are much thinner than in the well-mixed regime. The enhanced ISOBL stratification and double pycnocline structure beneath the mixed layer also support large gradients in temperature and salinity over the upper few meters of the water column. In the context of large-scale ocean modelling, resolving a thin mixed layer is more challenging. As mixed layer properties are required to determine the ice shelf melt rate when using a parameterisation such as the three-equation parameterisation, stratified conditions may introduce errors in basal melting estimates. Stratified conditions may also present a challenge to field observations of the ISOBL. *In situ* ice shelf-ocean observations are collected in a variety of ways, such as autonomous underwater vehicles (e.g. Dutrieux et al., 2014; Gwyther et al., 2020b), profiling and the installation of moorings via boreholes drilled through the ice shelf (e.g. Davis and Nicholls, 2019; Stewart et al., 2019; Stevens et al., 2020). A key issue with these studies is identifying the presence of and sampling within the mixed layer (e.g. Stewart, 2018). Similar issues exist with sampling the velocity boundary layer in order to estimate the friction velocity (Davis and Nicholls, 2019).

Another consequence of a stratified ISOBL is a reduced drag coefficient with respect to a well-mixed ISOBL. Regional and global ocean models typically take the drag coefficient to be $C_d = 0.0025$ (Gwyther et al., 2015). While results presented in this chapter suggest that this is a reasonable approximation for the well-mixed regime (e.g. run A3 with $C_d = 0.0023$), C_d has been shown to depend on stability parameter μ in the stratified

regime. For example, for run C2 $\mu = 2.3$ and $C_d = 0.0014$. This effect is not presently accounted for in ice-ocean parameterisations, and could lead to an overestimation of the friction velocity, and therefore basal melt rate, for conditions with μ 1.

Application of results to a broader range of ice shelf cavity conditions

Here, melting and ISOBL results from this chapter are extended to a broader parameter space. Using the key results that steady melt rates are achieved for L^+ 2500 and that transfer coefficients collapse with L^+, heat and salt transfer coefficients are modelled for $L^+ > 2500$ with a logarithmic fit. The maximum transfer coefficients found in this study are used as an upper bound on Γ_T and Γ_S. The L^+-dependent transfer coefficient formulations are:

$$\Gamma_T(L^+) = \min(1.65 \times 10^{-3} \cdot \log(8.30L^+) - 8.37 \times 10^{-3}, 0.0113), \qquad L^+ > 2500 \quad (4.19)$$

$$\Gamma_S(L^+) = \min(1.01 \times 10^{-4} \cdot \log(199L^+) - 1.17 \times 10^{-3}, 3.8 \times 10^{-4}), \qquad L^+ > 2500. \quad (4.20)$$

These empirical functions are plotted over the transfer coefficient data in Figs. 4.14B and C. Using these expressions, Eqs. 4.9, 4.12 and 4.13 can be solved iteratively to obtain m and L^+.

Fig. 4.15A shows the variation of Γ_T in $T^* - u^*$ space, where thermal driving ranges from 0.001–4° C and friction velocity varies in the range 0.03–1.25 cm s^{-1}. The marker (i) shows the position of the $L^+ = 2500$ contour if Γ_T and Γ_S are taken as constant and equal to the maximum values 0.00113 and 3.8×10^{-4} respectively. Using L^+-dependent transfer coefficients (Eqs. 4.19 and 4.20) results in a shift of this contour to location (ii). A large area of parameter space, given by 2500 L^+ 25000, is subject to reduced heat transfer due to the effects of near-ice stratification. The corresponding melt rate is shown in Fig. 4.15B.

The conditions at which buoyancy is expected to modify the ISOBL are determined by solving for L and μ (Fig. 4.15C). White contours of μ show the increasing effect of buoyancy on the ISOBL, where the region μ 1 is expected to correspond to the stratified regime. This regime encompasses a large area of relevant parameter space. For example at $T^* \sim 0.2$ °C stratification effects will be important up to a friction velocity of 1 cm s^{-1}, which corresponds to a free stream velocity of 20 cm s^{-1}, assuming a drag coefficient of 0.0025.

The parameter space over which the melting and ISOBL results have been extended represents the majority of melting conditions expected in polar regions. Chapter 5 draws on these findings and discusses the relevance of the stratified ISOBL regime to observed Antarctic ice shelf conditions.

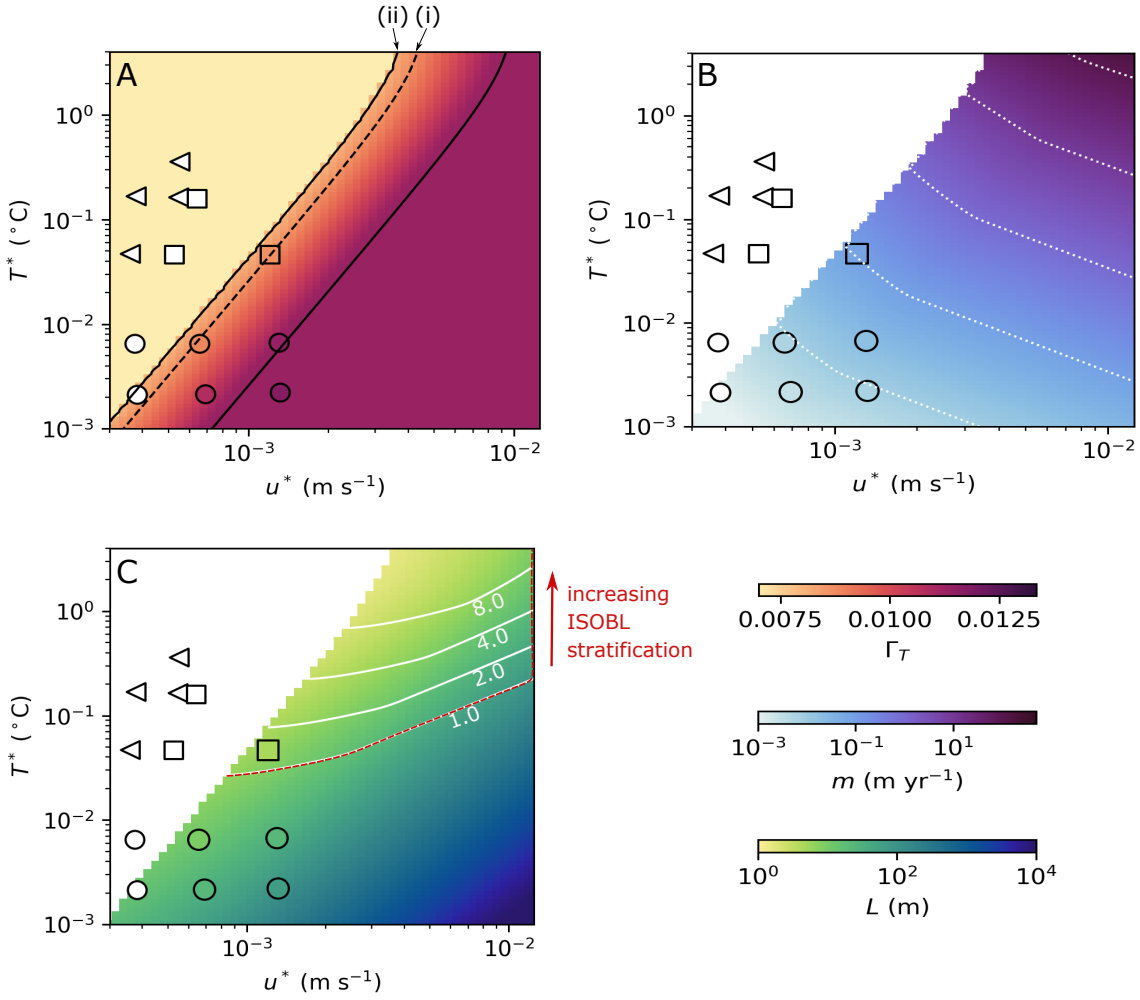

Figure 4.15: (A) Colour contour of heat transfer coefficient $\Gamma_T(L^+)$ for $L^+ > 2500$. Solid black contours show $L^+ = 2500, 25000$ dashed black contours show original $L^+ = 2500, 25000$ that would be obtained from fixed Γ_T, Γ_S. (B) Colour contour of melt rate m (C) L with contours of μ over-plotted in white. Markers denote the well-mixed (circle) stratified (square) and diffusive-convective (triangle) boundary layers respectively.

4.6 Conclusions

This chapter presents results from a suite of large-eddy simulations of the ISOBL forced by a steady, geostrophic flow at melting conditions, with free stream velocity ranging from 0.7–2.8 cm s^{-1} and thermal driving spanning 0.0025–0.05 °C. Over this range of simulated conditions three distinct ISOBL regimes were observed: well-mixed, stratified and DC. In the well-mixed regime the boundary layer was not affected by meltwater, and the depth of the mixed layer could be predicted using a simple scaling law based on the friction velocity, Coriolis frequency and far-field stratification. In the stratified regime, stabilising buoyancy due to meltwater decreases the mixed layer depth and the interfacial drag coefficient. The stratified regime occurs when the Obukhov length scale is the same or less than the planetary scale ($\mu > 1$). In this regime the boundary layer depth decreases as stability parameter μ increases, as did the interfacial drag coefficient. Finally, in the DC regime the mixed layer depth depends upon the thermal component of the surface buoyancy flux and the far-field stratification.

This chapter also highlights the role of buoyancy in determining the efficiency of heat and salt transfer to the ice-ocean interface. The effect of buoyancy on near-ice dynamics can be quantified using the viscous Obukhov lengthscale, which compares the Obukhov lengthscale and the viscous sublayer scale. For low L^+ (L^+ 2500), current shear is not sufficiently strong to control the diffusive sublayer thickness, and as a consequence melting is inherently time-dependent. For L^+ 2500 current shear controls the diffusive sublayer thickness and steady melting is achieved. However, over the intermediate range 2500 L^+ 25000 buoyancy affects the efficiency with which heat and salt are transported to the ice ocean interface, consistent with the findings of Vreugdenhil and Taylor (2019). The results presented in this chapter support the notion that buoyancy no longer affects heat and salt transfer at high L^+ (L^+ 25000).

These results have important implications for both parameterisation and observation of the ISOBL. Firstly, the L^+ dependence of heat and salt transfer coefficients is not currently accounted for in common ice-ocean parameterisations, and as a result melt rates will be over-predicted for L^+ 25000. This is especially true for $L^+ < 2500$, where time-dependent melting is observed and a steady balance between interfacial and mixed layer heat and salt fluxes cannot be assumed. Consequently, ocean models using common ice-ocean parameterisations such as that outlined in Jenkins et al. (2010b) are currently overestimating melt rates at warm and/or quiescent conditions. The meltwater released

by this additional, un-physical, basal melt will also affect the sub-ice shelf watermass properties and circulation in these models. In the stratified ISOBL regime, elevated stratification and a thin boundary layer will tend to decouple the far-field and mixed layer properties and increase the difficulty of sampling or resolving the mixed layer in observational and numerical studies respectively. Neither the effect of stratification on the ISOBL structure and depth nor its effect on interfacial drag are accounted for in melting parameterisations, where both will likely result in melting being overestimated under stratified conditions.

Chapter 5

Discussion

Chapters 3 and 4 of this thesis have demonstrated three distinct ice shelf-ocean boundary layer (ISOBL) regimes relevant to ice shelf-ocean interactions in Antarctica. These regimes are based on the dominant processes governing boundary layer turbulence and mixing and have been termed the diffusive convective (DC), stratified and well-mixed regimes. In this section, these regimes are mapped as a function of the elevation of mixed layer temperature above freezing and friction velocity due to current shear. This regime diagram extends this thesis' simulation results to a larger parameter space, and is used to contextualise available observational data from beneath Antarctic ice shelves. Finally, the Amery Ice Shelf observations of basal melting and ocean conditions presented in chapter 2 are revisited in light of the simulation results from chapters 3 and 4.

5.1 Regimes and transitions in basal melting of Antarctic ice shelves

5.1.1 Transitions in the DC regime

In the presence of turbulence generated by current shear, DC is a transient process (see §3.3.1). For runs C2, 3 and 4, a transition from DC-dominated to shear-dominated mixing was observed over the course of the simulation, where DC-dominated mixing is defined by a positive buoyancy flux ($B > 0$) within the mixed layer. For experiments that exhibited DC-mixing, the period of time (t_{DC}) for which B was positive within the mixed layer is shown in Table 5.1. Simulations for which DC persists for > 100 h are characterised by high thermal driving and low, or no, current forcing. For simulations that exhibit DC, the Obukhov lengthscale (L) is a relatively good predictor of the timescale at which a transition from DC- to shear-mixing will occur. For L =O(1 m) DC occurs at the onset of the simulation, while for L =O(0.1 m) DC persists for at least

Table 5.1: Time to transition from DC-dominated to shear-dominated mixing. Obukhov lengthscale (L); and transition time (t_{DC}). L is evaluated at $t = 10$ h.

run	L (m)	t_{DC} (h)
C2	1.47	~ 2
4	0.90	~ 2
C1	0.50	> 100
3	0.47	~ 50
3*	0.22	> 100
2	0.17	> 100
1	~ 0	> 200

100 h.

In the preceding chapter, L was discussed as the distance from the ice where shear-generated turbulence is affected by stabilising buoyancy due to meltwater. However, a hallmark of the DC regime is that the buoyancy flux changes sign between the stable interfacial sublayer and the mixed layer. Consequently, the buoyancy flux outside of the stable diffusive sublayer is destabilising in the DC runs. Thus, for the DC runs, L can be better thought of as the distance from the ice-ocean interface where turbulence production from buoyancy is larger than turbulence production from shear.

In order to classify conditions using L, a model of the (diffusive) surface buoyancy flux (B_{diff}) is needed. Given that the thermal (B^T_{diff}) and saline (B^S_{diff}) buoyancy contributions at the interface are related by the melting equations, only one component is needed. The surface buoyancy flux due to heat is given by:

$$B^T_{diff} = -g\alpha\kappa_T \left.\frac{\partial T}{\partial z}\right|_b \sim -g\alpha\kappa_T \frac{\Delta T}{\delta_T} \tag{5.1}$$

where δ_T is the thermal diffusive sublayer thickness and ΔT is the temperature difference between the interface and mixed layer. Drawing on key results from chapter 3, these variables can be modelled. Firstly, the thermal driving is approximately double the temperature difference between the interface and the mixed layer, i.e. $2\Delta T \sim T^*$ (Table 3.2). Secondly, the thermal diffusive sublayer thickness is about triple the saline diffusive sublayer thickness, i.e. $\delta_T \sim 3\delta_S$ (Fig. 3.9). Thirdly the growth of the saline diffusive sublayer can be approximated by the saline diffusive lengthscale $\sqrt{4\kappa_S t}$ (Fig. 3.9). Thus,

the surface buoyancy flux due to heat (B^T_{mod}) can be represented as:

$$B^T_{mod}(t) \sim -g\alpha\kappa_T \frac{1}{6} \frac{T^*}{\sqrt{4\kappa_S t}} \tag{5.2}$$

Despite the many assumptions in this model, B^T_{mod} is an excellent predictor of B^T for the runs 1, 2, 3* and C1 (Fig. 5.1).

Heat and salt fluxes at the ice-ocean interface are linked in melting Eqs. 3.9 and 3.10. Consequently, the ratio of the saline and thermal components of buoyancy at the ice-ocean interface is given by:

$$\frac{B^T_{diff}}{B^S_{diff}} = \frac{\beta\kappa_S \left.\frac{\partial S}{\partial z}\right|_b}{-\alpha\kappa_T \left.\frac{\partial T}{\partial z}\right|_b} = \frac{\beta S_b c_p}{-\alpha L_f} \sim -10 \tag{5.3}$$

for $S_b = 30$ g kg^{-1}. Consequently, the total interfacial buoyancy flux may be modelled as:

$$B_{mod} = B^T_{mod} + B^S_{mod} = B^T_{mod} - 10B^T_{mod} = -9B^T_{mod}, \tag{5.4}$$

and the Obukhov lengthscale, given by $L = u^{*3}/(kB)$, can be modelled as:

$$L_{mod}(t) = \frac{u^{*3}}{kB_{mod}}. \tag{5.5}$$

The modelled Obukhov lengthscale can be used to investigate the transition to DC conditions as a function of u^*, T^* and t. In Fig. 5.2, contours of $L_{mod}(t) = 0.5$ are compared with simulation results. To first order, $L_{mod}(t) = 0.5$ describes the region of $T^* - u^*$ space where DC is observed in simulations. However, some discrepancies exist with respect to the modelled vs. simulated transition timescale t_{DC}; for example, the simulation data seem to suggest that a steeper contour would better represent the transition timescale. Further work is required to understand this transition. While studies of forced convection for meteorological applications have sought expression for the critical wind speed up to which free convection determines heat transfer (e.g. Raju and Narasimha, 2003), to our knowledge no studies have considered this for diffusive convection. It is generally accepted, however, that DC does not coexist with strong, shear-generated turbulence (Radko, 2013). For example, in the arctic, diffusive staircases are much less common near boundaries where turbulence dissipation is higher (Shibley et al., 2017).

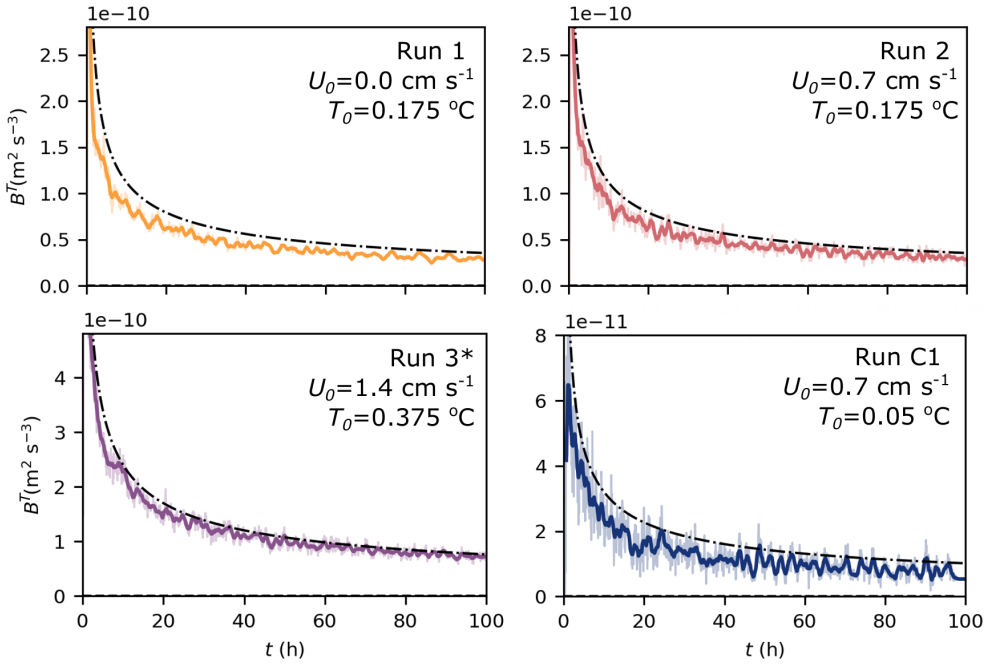

Figure 5.1: Evolution of the plane-averaged buoyancy flux due to temperature (B^T) at $z = -0.2$ m (within the mixed layer) in time for runs 1, 2, 3* and C1 compared to the modelled surface buoyancy flux due to temperature (B^T_{mod}) from Eq. 5.2.

5.1.2 Boundary layer regimes

All three ISOBL regimes summarised here—DC, stratified and well-mixed–are relevant to observed Antarctic conditions. Fig. 5.2 partitions T^*–u^* space into these respective regimes. Thermal driving and friction velocity span 0.001–4 °C and 0.03–1.25 cm s^{-1} respectively. These friction velocity values correspond to free stream velocities in the range 0.6–25 cm s^{-1}, assuming a quadratic drag relationship and a constant drag coefficient of 0.0025. The well-mixed and stratified regimes are divided by the contour $\mu = 1$, where stratified conditions are expected for $\mu \geq 1$ (see Fig. 4.15C and associated text for further details). The transition to the DC regime is based upon modelled Obukhov lengthscale (Eq. 5.5), where the expression is evaluated for $t = 1,\ 10,\ 100$ h. Contours of $L_{mod}(t) = 0.5$ are translated towards higher values of T^* and lower values of u^* over time, as the surface buoyancy flux decreases. Consequently, the area of T^*–u^* space for which DC is the dominant mixing process decreases with time, where $t = 0$ is the time when the ice first comes into contact with the water at thermal driving T^*.

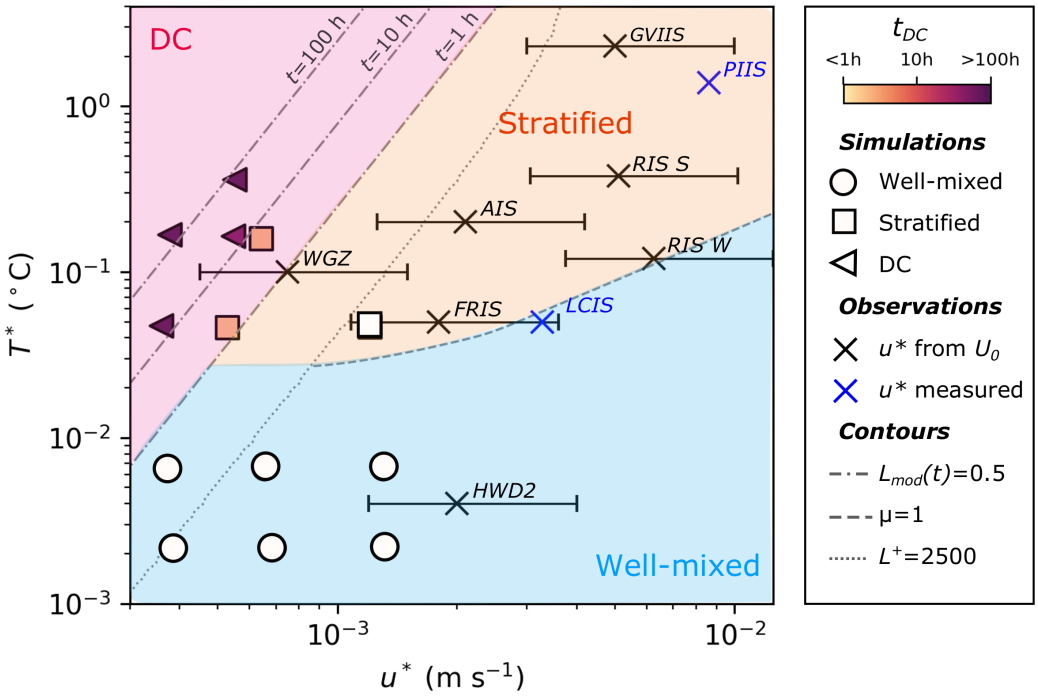

Figure 5.2: Regimes and transitions for the ISOBL. Filled markers show the positions of experiments in T^*, u^* space at $t = 10$ h. Where relevant, markers are coloured by DC transition timescale t_{DC}. Where u^* is measured directly, it is estimated from the free stream flow using $u^* = \sqrt{C_d}U$ with $C_d = 0.0025$ (mid point), $C_d = 0.001$ (lower bound) and $C_d = 0.01$ (upper bound). Observational data are described in Appendix B. Data sources are: WGZ, (Begeman et al., 2018); FRIS, (Jenkins et al., 2010b); RIS, (Stewart, 2018); GVIIS, (Kimura et al., 2015); LCIS, (Davis and Nicholls, 2019); HWD2, (Stevens et al., 2020); and PIIS (Stanton et al., 2013).

Fig. 5.2 includes a suite of observations made at different sites beneath Antarctic ice shelves at a variety of different ocean conditions. Where u^* is not measured directly the expression $u^* = C_d^{1/2}U_0$ is used, assuming a drag coefficient of 0.0025. Drag coefficients of 0.001 and 0.01 are used as lower and upper bounds on the estimate respectively. In this framework, the Larsen C Ice Shelf (LCIS) falls within the "well-mixed" regime, consistent with the observations of a turbulent, homogeneous boundary layer (Davis and Nicholls, 2019). The central Ross Ice Shelf Site (HWD2), where thermal driving is extremely low and a well-mixed ISOBL observed (Stevens et al., 2020), also falls within the well-mixed regime. The Filchner-Ronne Ice Shelf (FRIS) data are close to boundary between the well-mixed and stratified regimes. For a drag coefficient of 0.01,

as suggested by Jenkins et al. (2010b), FRIS data are also consistent with the well-mixed regime. Seasonality in thermal and current forcing near the front of the Ross Ice Shelf (RIS) result in summertime (RIS S) and wintertime (RIS W) conditions moving between the well-mixed and stratified regimes (Stewart, 2018).

Other sites are strongly affected by stratification. Pine Island Ice Shelf (PIIS) falls within the stratified regime, consistent with the observation of a strongly stratified water column to within 1 m of the ice shelf base (Stanton et al., 2013). So, too, does the Amery Ice Shelf (AIS) which will be discussed in more detail in the following section. Depending on the choice of drag coefficient, observations from the Wissard Grounding Zone (WGZ) of the Ross Ice Shelf fall within either the DC or stratified regimes. Water column observations at WGZ are suggestive of DC (Begeman et al., 2018). The only site for which observations and theory are not well reconciled is George VI Ice Shelf (GVIIS). Water column measurements show that GVIIS is prone to DC based on the observation of a diffusive staircase beneath the ice, however, the theory presented in this chapter suggests that GVIIS falls within the stratified regime. This discrepancy may indicate that present theory is incorrect or incomplete. Alternatively, it may indicate that u^* is not correctly estimated at this site. Measurements at the site show low dissipation $\epsilon \sim 4 \times 10^{-10}$ W kg^{-1} (Venables et al., 2014) and high stratification (Kimura et al., 2015). Thus, the use of the quadratic drag law may be inappropriate for estimating a turbulent velocity scale at this site. An important result from this figure is that stratification effects are very important to Antarctic ice-ocean interactions. In order to be unaffected by buoyancy, ice shelves must be either extremely cold, extremely energetic, or extremely rough—to create enhanced interfacial drag.

It is important to note that the observational data included in Fig. 5.2 come from individual sites (point measurements) beneath ice shelves and should by no means be considered representative of their entire respective ice shelf cavities. Some combination of the three ISOBL regimes, as well as regimes such as the natural convection case for sloping ice, will likely be present across each ice shelf in varying amounts.

5.1.3 Heat and salt transfer

Buoyancy effects on near-ice flow dynamics and melting are extremely relevant at observed Antarctic conditions. Fig. 5.3 plots the heat transfer coefficient $\Gamma_T(L^+)$ (Eq. 4.19), a function of the viscous Obukhov lengthscale L^+, in $T^* - u^*$ space. Fig. 5.3

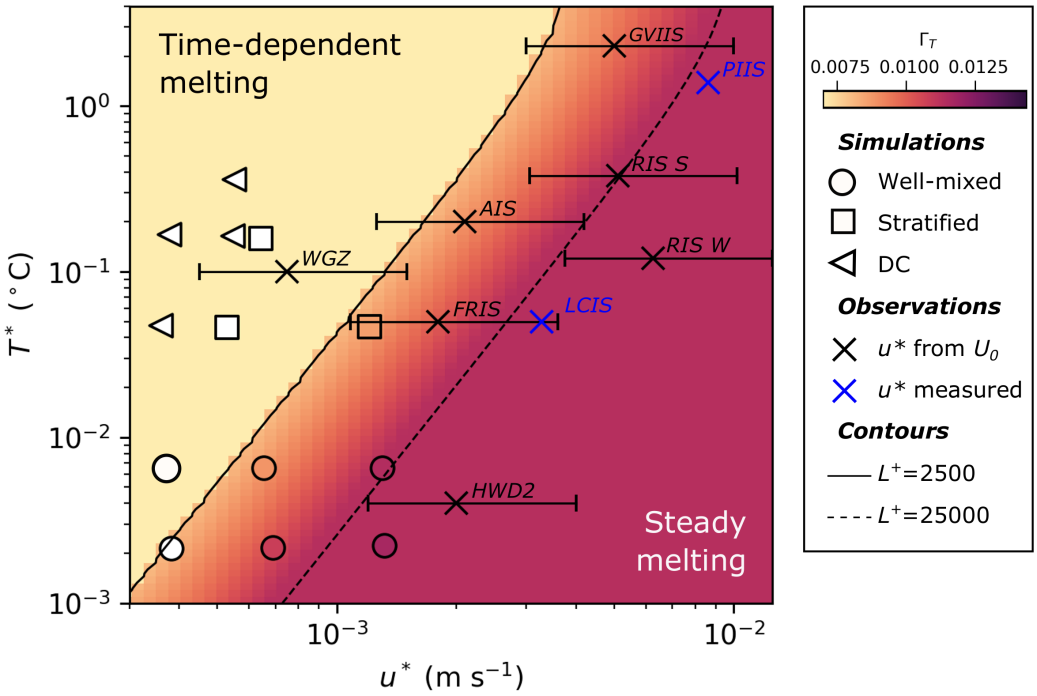

Figure 5.3: Heat transfer coefficient Γ_T (colour) as a function of friction velocity (u^*) and thermal driving (T^*). Observational data as for Fig. 5.2.

highlights the region of parameter space with inherently time-dependent melting ($L^+ \leq 2500$), as well as the area of reduced heat transfer ($2500 \leq L^+ \leq 25000$). As with Fig. 5.2, observational data is over-plotted. Fig. 5.3 demonstrates that the area of reduced transfer is extremely relevant to observed ice shelf conditions. For example, both the AIS and GVIIS sites fall within this area of reduced transfer, consistent with results from Chapter 2 and Kimura et al. (2015), respectively, which show that melting is not well predicted by Jenkins et al. (2010b) at these conditions. Seasonal variation in thermal and current forcing beneath the RIS pushes the local conditions from constant-transfer conditions in wintertime to reduced transfer conditions in summer when T^* is higher. This change in near-ice dynamics coincides with a transition from well-mixed to stratified ISOBL conditions (Fig. 5.2). Stewart (2018) showed that when conditions beneath the ice shelf were less well-mixed, the fit between the three-equation parameterisation and the observed melt rates was poorer and the dependence of melt rate on thermal driving was sub-linear. These observations are consistent with strong buoyancy effects on both melting and ISOBL dynamics.

5.1.4 Revisiting the Amery Ice Shelf

In this section, the measurements of basal melting and ocean conditions from site AM06 beneath the Amery Ice Shelf presented in chapter 2 are revisited in light of the simulation results from chapters 3 and 4. Figs. 5.2 and 5.3 showed that the ISOBL at AM06 falls within the stratified regime, and that heat and salt transfer are expected to be inhibited at AM06 conditions. Following the method outlined in §4.5, Eqs. 4.9, 4.12 and 4.13 are solved using transfer coefficient expressions 4.19 and 4.20 for the parameterised melt rate (m_{pred}), which is used to calculate L, μ and L^+ based on AM06 conditions (Table 5.2). For $C_d = 0.0016$, there is a reasonably good agreement between the observed and predicted melt rates. However, if a larger drag coefficient is used, agreement between between observations and predictions is poor.

Regardless of the choice of drag coefficient, the stability parameter μ, which ranges from 2.7–3.7 (Table 5.2), suggests that buoyancy effects will be important at AM06. At these conditions, stratification is expected to affect both the mixed layer depth and drag coefficient. With respect to the drag coefficient, Fig. 4.10B shows that for $\mu \sim 3$ the ratio of the friction and free stream velocities is $u_*/U_0 \sim 0.35$, which corresponds to a drag coefficient of 0.0012.

Based on Eq. 4.8 the mixed layer at AM06 is expected to be 2.5–7.2 m deep (Table 5.2). Given that the uppermost microcat is ∼4 m beneath the ice-ocean interface at the start of the sampling period, a value in the lower end of the range means that the instrument may be positioned outside the mixed layer some or all of the time. However, this calculation uses the time-mean flow speed. Instantaneous flow speeds at AM06 are much higher (see Fig. 2.6). For a typical tidal flow speed at AM06 of 10 cm s^{-1}, and using the same range of drag coefficients of 0.0016–0.01, the expected mixed layer depth is in the range 7.2–27 m.

Table 5.2: Key quantities for the Amery Ice Shelf. Column 1–3 are observed quantities from Table 2.4. Columns 4–9 are theoretical estimates based on the choice of drag coefficient C_d. Parameters L, μ, h_μ, L^+ and m_{pred} are calculated using melting Eqs. 4.12 and 4.13 with transfer coefficient Eqs. 4.19 and 4.20.

T^*	U	m	C_d	L	μ	h_μ	L^+	Γ_T	Γ_S	m_{pred}
°C	cm s^{-1}	m yr^{-1}	$\times 10^{-3}$	m		m		$\times 10^{-3}$	$\times 10^{-4}$	m yr^{-1}
			1.6	3.2	3.7	2.5	2600	8.1	1.6	0.55
0.2	4.0	0.46	2.5	4.1	3.6	3.1	4100	8.8	2.0	0.80
			10.0	10.9	2.7	7.2	21900	11.4	3.7	2.40

Chapter 6

Conclusions

Ocean-driven melting of ice shelves is a leading cause of mass loss from Antarctica and is crucial to ice sheet stability and global sea level. Efforts to predict the melting response of Antarctic ice shelves to ocean warming are undermined by poor understanding of the small-scale ice-ocean boundary layer processes that control melting. This thesis addresses this knowledge gap by characterising melting and ice shelf-ocean boundary layer (ISOBL) dynamics across a broad range of ocean states. Melting and ISOBL characteristics are studied using a comprehensive observational dataset from the Amery Ice Shelf and a suite of novel model simulations performed using resolved large-eddy simulation (LES). The key conclusions of this thesis, which address the objectives set out in §1.5, are as follows:

- A year-long record of basal melting and ocean observations from a mooring at site AM06 beneath the Amery Ice Shelf (AIS) indicates that melting at the mooring site is driven by Dense Shelf Water (DSW). Ocean properties and local melt rates are strongly influenced by the degree to which DSW is cooled and freshened by melting elsewhere within the AIS cavity. Consequently, the seasonal cycle of melting at AM06 is out of phase with the cavity average. The mean annual melt rate at AM06 is 0.51 m yr^{-1}, consistent with previous glaciological and modelling estimates. Melting varies seasonally, with a maximum in (Austral) autumn. The melting minimum occurs in spring and coincides with the coolest, freshest (most heavily meltwater-modified) conditions. Flow at the mooring site is characterised by an annual mean flow of 3.2 m s^{-1} oriented into the ice shelf cavity, and variability at annual, diurnal and semi-diurnal frequencies. The tidal currents have instantaneous speeds of up to $\sim$ 10 cm s^{-1}, driving flow speeds in excess of $\sim$ 15 cm s^{-1} when the background mean flow is also strong.

- Observations of ice shelf melt rate and oceanographic conditions are used to show

that common velocity-dependent ice-ocean parameterisations, which assume a turbulent, well-mixed frictional boundary layer, overestimate the melt rate at AM06 by factors of 2–4. The degree of misfit depends on the choice of drag coefficient, which is poorly constrained beneath ice shelves. The melt rate at AM06 is better predicted by a convective melting parameterisation which depends on the local ocean temperature and the slope of the ice base, although this parameterisation under-predicts melt rates by 20%.

- A new idealised model configuration of the geostrophic ISOBL has been developed with LES using the computational fluid dynamics code described in Gayen et al. (2010). The important ingredients of this model configuration are vertical grid stretching, allowing sufficient resolution at the ice-ocean boundary to resolve the diffusive fluxes responsible for melting, and a domain that is large enough to capture the planetary boundary layer. This latest point allows for the formation of a steady current in geostrophic balance in the interior of the domain—a scenario that is realistic and permits a holistic study of melting and the ISOBL, including mixed layer formation and the effects of far-field stratification.

- Using the model, the ISOBL was studied at a range of ocean temperatures and current intensities and three distinct ISOBL regimes were identified. These regimes are defined as **well-mixed**, **stratified** and diffusive-convective **DC**. The characteristics of each of the regimes are as follows:

  - **Well-mixed:** In the well-mixed regime the effects of current shear and ambient stratification are dominant. The boundary layer is not strongly affected by meltwater, and the depth of the mixed layer can be predicted using a simple scaling law based on the friction velocity, Coriolis frequency, and far-field stratification.

  - **Stratified:** In the stratified regime the effects of current shear and stabilising buoyancy due to meltwater are dominant. Relative to the well-mixed case, the stabilising buoyancy flux acts to decrease the mixed layer depth by suppressing turbulence. In the stratified regime, the mixed layer depth can be predicted as a function of friction velocity, Coriolis frequency, and surface buoyancy flux. The transition from well-mixed to stratified conditions occurs when the Obukhov lengthscale (L), which compares the relative strength of shear and buoyancy, is approximately equal to or less than the planetary

boundary layer depth scale (δ_f).

  - **Diffusive-convective:** In the DC regime the effects of surface buoyancy flux and far-field stratification are dominant. This regime relies on differential diffusion of heat and salt away from the boundary, and mixing is driven by thermal convection outside of the stable diffusive sublayer. DC forms a thermohaline staircase beneath the ice, and the depth of the primary (uppermost) mixed layer depends upon the thermal component of the surface buoyancy flux and the far-field stratification. In the DC regime melting is transient and the surface heat flux weakens over time. In the presence of shear-generated turbulence, a transition from DC-mixing to shear-mixing will occur when shear production dominates buoyancy production of turbulence at a depth of $z \sim -0.5$ m.

- Melting is controlled by near-ice ocean processes. The viscous Obukhov lengthscale (L^+) compares the Obukhov length to the viscous length scale of the interfacial sublayer. For L^+ 2500 melting is time-dependent and governed by salt diffusion via the growth of a stable diffusive sublayer. For L^+ 2500 current shear controls the interfacial sublayer thickness and melting is steady in time. At steady melting conditions, the magnitude of L^+ determines the efficiency of heat and salt transfer to the ice, in agreement with the findings of Vreugdenhil and Taylor (2019).

- The drag coefficient C_d, which relates the ambient flow speed U_0 to the friction velocity u^*, is shown to be strongly affected by stratification, as quantified by the ratio of the Obukhov lengthscale and the planetary boundary layer depth scale. Consequently, applying a constant drag coefficient to parameterise friction velocity within an ocean model simulating ice-ocean interactions will not be appropriate at stratified conditions.

Recommendations and future directions

Based on the conclusions outlined above, we make several recommendations to improve the representation of ice-ocean interactions in large-scale ocean models. We also outline several important directions for future studies of ice shelf-ocean interactions, including observational studies of the ISOBL.

- Heat and salt transfer coefficients in melting parameterisations should include a

functional dependence on the viscous Obukhov lengthscale to account for the decreased efficiency of heat and salt transfer observed for 2500 L^+ 25000. Empirical heat and salt transfer equations 4.19 & 4.20 could be used. However, one remaining challenge is parameterising the melting behaviour for L^+ 2500.

- The presence of both the stratified and DC ISOBL regimes is contrary to the assumption of a homogeneous mixed layer adjacent to the ice. Furthermore, DC influences the fluxes of heat and salt in a different manner to shear-driven turbulence. These results suggest that it is important to include the effects of stratification and DC not just in melting parameterisations, but also in the boundary layer parameterisations used in ice-ocean models. Ideally, beneath ice shelves, boundary layer and melting parameterisations should be physically consistent.

- This thesis has demonstrated three different ISOBL regimes for flow beneath flat, melting ice. However, in the presence of a basal slope, buoyant meltwater can drive a plume up-slope. Importantly, for sloping ice it is the buoyancy associated with freshening that drives convection, in contrast to the DC case where convection is driven by cooling (and relies on double diffusive effects). It is therefore important that we study the transition between the DC and natural convection regimes to understand where in Antarctica they are important. Further work is also needed to determine the transition between the natural convection and shear-dominated regimes.

- Other important aspects of Antarctic ice shelf-ocean interactions, such as time varying flows (e.g. tides), internal wave activity and the effect of a rough ice surface also require investigation using turbulence resolving simulations in future. Despite recognition in the community that tidal currents are widespread beneath Antarctic ice shelves, they are rarely included in the circum-Antarctic ocean models used to study Antarctic ice-ocean interactions. This thesis has shown that the melt rate response to variation in flow speed can be highly nonlinear. Consequently, a targeted investigation of tidally-driven melting is needed.

- Finally, further observational studies of the ISOBL are needed. These observations should include melting measurements with sufficiently high temporal resolution (e.g. hourly) to capture tidal variability, as well as observations of turbulence quantities within the ISOBL and ocean conditions. Data of this kind have been collected beneath the Filchner-Ronne Ice Shelf, however, a broad range of cavity

environments should be sampled. Based on the findings in this thesis, these observational studies should target locations affected by buoyancy (as determined by the Obukhov lengthscale) where existing parameterisations are expected to perform poorly.

Appendix A

Model details

A.1 LES closure

The LES model used in the simulations in chapter 3 and 4 is the dynamic Smagorinsky closure model (Germano et al., 1991). It is appropriate for the present ice shelf-ocean boundary layer (ISOBL) study because it carries separate diffusivities for heat and salt at each point in time and space (no turbulent Prandtl or Schmidt number approximations are made) and has been validated for stratified (Taylor and Sarkar, 2008a; Vreugdenhil and Taylor, 2018) and convective (Gayen et al., 2013) flows.

A.1.1 Subgrid-scale contributions

The Turbulence Kinetic Energy (TKE) budget is given by:

$$\frac{\partial k}{\partial t} = P - \epsilon + B - \text{transport of TKE} \tag{A.1}$$

where $\partial k/\partial t$ is the time rate of change of TKE ($\mathrm{m^2\ s^{-3}}$ or equivalently $\mathrm{W\ kg^{-1}}$), P is the shear production, ϵ is the dissipation rate and B is the buoyancy flux. Dissipation rate ϵ is positive definite and therefore a sink of TKE, while shear production P is typically positive and buoyancy flux B may take either sign, where positive B corresponds to a transformation of potential to kinetic energy. These terms are further described in Gayen et al. (2010).

Fig. A.1 shows the sources and sinks of TKE ($B,\ P,\ \epsilon$) for run 1, with no mean flow, and run 3 with a mean flow of $U_0 = 1.4$ cm $\mathrm{s^{-1}}$. In run 1 the dominant terms are buoyancy production and dissipation, where these terms are approximately balanced in depth. In the absence of a mean flow the shear production is negligible. For run 3, the primary balance is between shear production and dissipation, where these terms are two

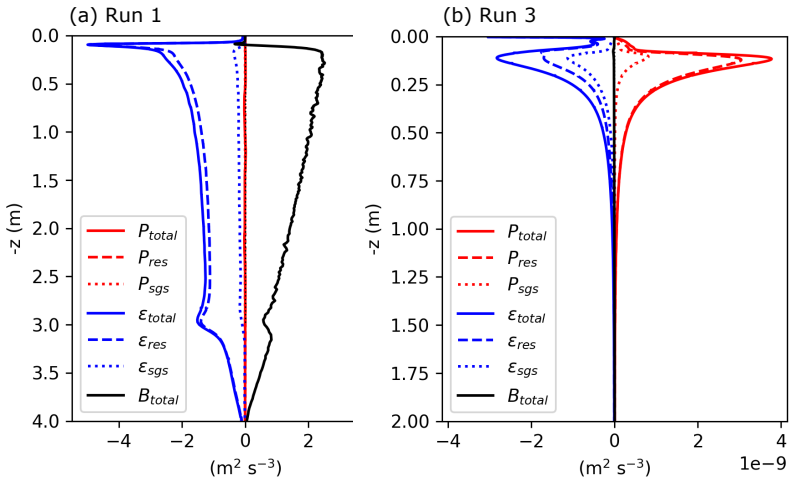

Figure A.1: Plane-integrated buoyancy production B, shear production P, and dissipation ϵ averaged over $t = 90 - 100$ h. Terms are broken down into resolved (res) and subgrid-scale (sgs) components. The largest subgrid-scale component is the subgrid-scale dissipation, which accounts for 10% of the total dissipation at $U_0 = 0.0$ cm s^{-1} and 35% of the dissipation at $U_0 = 1.4$ cm s^{-1}

orders of magnitude larger than B and/or ϵ in run 1. The terms are broken down into their resolved and subgrid-scale (SGS) components. The largest SGS component is the SGS dissipation, which accounts for 10% of the total dissipation at $U_0 = 0.0$ cm s^{-1} and 35% of the dissipation at $U_0 = 1.4$ cm s^{-1}. The SGS terms are small due to the high resolution of the simulation.

A.1.2 Closure of the TKE budget

Accurate closure of the TKE budget based on independent calculation of each of the terms is considered the most rigorous and critical text of sufficient grid resolution (Gayen et al., 2013). The experiments reach a quasi-steady state in which the time rate of change of TKE ($\partial k/\partial t$) is negligible compared to the source and sink terms. For example, for run 3 $\langle \partial k/\partial t \rangle_z \sim -1 \times 10^{-12}$ m s^{-3} and $\langle \epsilon \rangle_z = 7 \times 10^{-10}$ m s^{-3} over the period 90-100 h, where $\langle \rangle_z$ denotes depth-integration. Depth integrated, the transport of TKE is zero, leaving the balance $\langle P \rangle_z + \langle B \rangle_z - \langle \epsilon \rangle_z = 0$. We find that these terms sum to zero within 3 percent of the leading term (i.e. $(\langle P \rangle_z + \langle B \rangle_z - \langle \epsilon \rangle_z)/\langle \epsilon \rangle_z < 0.03$) for all simulations.

A.2 Grid specifications and convergence

A.2.1 Aspect ratio testing

Here we investigate the effect of the aspect ratio (A) of grid cells at the edge of the viscous sublayer (Z^+=50). Vreugdenhil and Taylor (2018) found this to be important in their study of LES of stratified plane couette flow. Vreugdenhil and Taylor (2019) recommended $A = \Delta Z^+/\Delta X^+ = 1/8$ for an ISOBL application. We investigated the effect of varying A over $1/30 < A < 1/7$, and compared the results using the Nusselt number Nu, the ratio of convective and conductive heat transfer over the ISOBL. Nu is given by:

$$Nu = \frac{Q_T d}{\Delta T \kappa_T} \tag{A.2}$$

where Q_T is the heat flux at the ice-ocean interface, ΔT is the temperature difference between the interface and location $z = -d$. Here we take $d = 0.3$ m, a nominal value within the mixed layer. Nu is only observed to vary slightly with A (Fig. A.2). Based on Fig. A.2, using $A = 1/30$ instead of $A = 1/7$ only results in a 4% decrease in Nu.

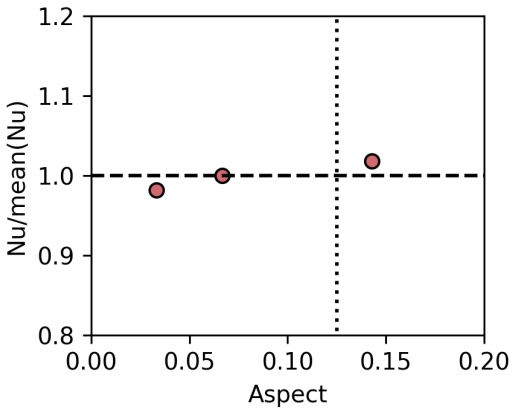

Figure A.2: Effect of varying Aspect ratio $A = \Delta Z^+/\Delta X^+$ of grid cells at Z^+=50 on Nu for supplementary runs S3–5. Thermal driving and free stream velocity are constant between runs. The vertical dotted line shows $A = 1/8$.

A.2.2 Horizontal resolution

Chapter 3 runs 1–3$*$ have horizontal resolution $\Delta X^+ = 27$, where $\Delta X^+ = \Delta X/\delta_\nu$ and $\delta_\nu = \nu/u_0^*$ is the viscous lengthscale. The recommended horizontal grid resolution for

resolved LES from Salon et al. (2007) is $\Delta X^+ = 20$. Fig. A.3 compares experiment 3, with $\Delta X^+ = 27$, to experiment S6 (Table A.1), which has $\Delta X^+ = 20$. Neither the friction velocity nor the melt rate, which is proportional to the heat flux at the ice-ocean interface, are affected by the reduced resolution.

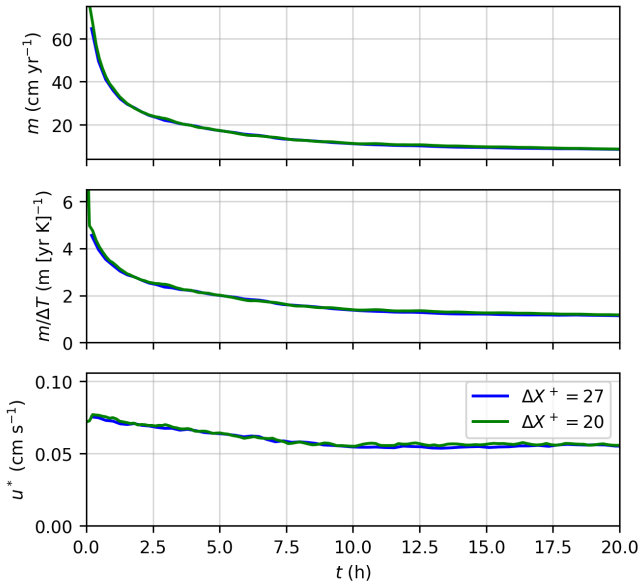

Figure A.3: Effect of horizontal resolution on (upper) melt rate; (middle) melt rate normalised by ΔT; (lower) friction velocity u^* for run 3 (main text)and supplementary run S6. Thermal driving and free stream velocity are constant between runs.

A.3 Forcing considerations: effect of varying Coriolis

In order to achieve our highest velocity ($U_0 = 2.8$ cm s^{-1}) runs we set Coriolis parameter to $f = 2f_0$ in runs A3, B3 and C3. This yields a thinner boundary layer and allows us to use a slightly smaller domain size than would be required at $f = f_0$. In order to ensure that this does not affect our results we performed two supplementary runs, S2 and S3, with Coriolis parameter set to $f = 2f_0$ and $f = 6f_0$ respectively. The grid specifications for these runs are given in Table A.1. These runs were both initialised with a thermal forcing of $T_0^* = 0.0025$ °C and a free stream velocity of $U_0 = 1.4$ cm s^{-1} allowing a direct comparison with (main text) run A2, isolating the effect of the f.

Fig. A.4 shows that the melt rate m is not affected by varying f in the range $f_0 \leq$

$f \leq 6f_0$, despite a slight increase in friction velocity u^* with increasing f. Fig. A.5 shows that the stratified Ekman boundary layer scaling from Eq. 4.7 also holds over the $f_0 \leq f \leq 6f_0$.

Based on these results we do not expect that employing $f = 2f_0$ for runs A3, B3 and C3 will influence our results relating to melting and heat transfer. Increasing f simply results in a thinner boundary and mixed layer, as described in the main text (§4.4.2).

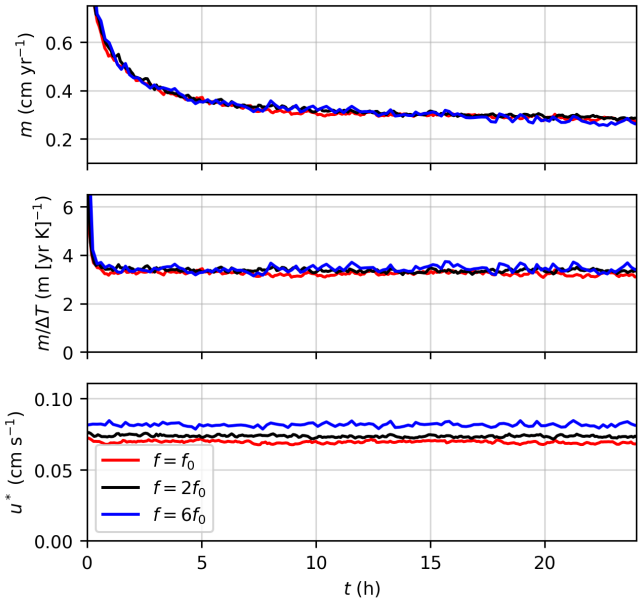

Figure A.4: Effect of Coriolis parameter f on (upper) melt rate; (middle) melt rate normalised by ΔT; (lower) friction velocity u^* for run A2 (main text) supplementary runs S1 and S2. Thermal driving and free stream velocity are consistent between runs.

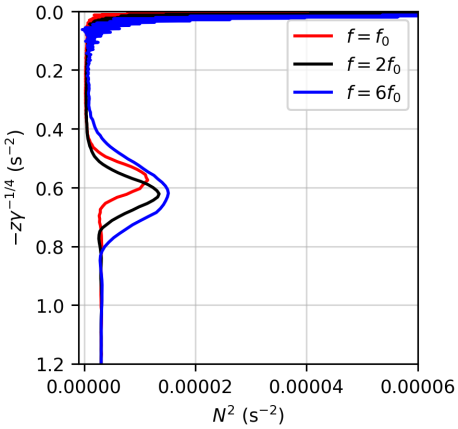

Figure A.5: Profiles of squared buoyancy frequency N^2 for runs A2, S1 and S2. The depth axis is scaled by $\gamma^{-1/4}$.

Table A.1: Grid specifications for supplementary runs varying Coriolis forcing and grid cell aspect ratio. Initial thermal driving T_0^*; Free stream velocity U_0; Coriolis frequency f; viscous lengthscale $\delta_\nu = \nu/u_0^*$; Ekman boundary layer depth δ_{f0}; domain horizontal dimension LX $(= LY)$; domain height LZ; horizontal resolution (in wall units) ΔX^+ $(=\Delta Y^+)$; vertical resolution at the ice-ocean interface ΔZ^+; Aspect ratio $(A = \Delta Z^+/\Delta X^+)$ of grid cells at the edge of the viscous sublayer (Z^+=50). $^{\#}$This run is initialised with a background temperature gradient matching that of run 3 (chapter 3).

Grid	T_0^* °C	U_0 cm s^{-1}	$\delta_{\nu 0}$ cm	f $\times 10^{-3}$ s^{-1}	δ_{f0} m	LX m	LZ m	ΔX^+	ΔZ^+	A
S1	0.0025	1.4	0.3	-2.74	1.8	7.2	7.2	20	0.9	1/11
S2	0.0025	1.4	0.3	-8.22	0.6	3.6	5.4	20	0.7	1/15
S3	0.05	1.4	0.3	-8.22	0.6	3.6	4.2	20	0.9	1/7
S4	0.05	1.4	0.3	-8.22	0.6	3.6	5.4	20	0.7	1/15
S5	0.05	1.4	0.3	-8.22	0.6	3.6	5.4	20	0.5	1/30
S6	0.175$^{\#}$	1.4	0.3	-1.37	0.6	7.2	25	20	0.6	1/19

Appendix B

Observational Data

Study	Thermal driving	Flow speed and/or friction velocity	Melting
Filchner Ronne Ice Shelf: Jenkins et al (2010)	$\boldsymbol{T^*}$**~0.05 °C** Notes: Value taken from visual inspection of Fig. 4. Value is approximate only.	$\boldsymbol{U_{mean}}$ **~3.6 cm s^{-1},** $\boldsymbol{U_{max}}$**~20 cm s^{-1}** Notes: Jenkins et al. use a tidal model to infer current speeds in 2001, based on measurements made 1996-1998, which showed that tides dominated the flow at this site. The values above are the mean and maximum from 1996-1998.	m = 0.554±0.006 m yr$^{-1.}$ The authors provide a melting estimate of m = 0.553m yr$^{-1.}$
Pine Island Ice Shelf: Stanton et al. (2013)	T^* = 1.39 °C	U_{mean} = 13 cm s^{-1} u^* = 0.86 cm s^{-1}	m = 14.2 m yr^{-1}
George VI Ice Shelf: Kimura et al. (2015)	T^* = 2.3 °C	U_{mean} = 10 cm s^{-1}	m = 1.4 m yr^{-1}
Ross Ice Shelf (WGZ): Begeman et al, (2018)	T^* = 0.1 °C	U_{mean} = 1.5 cm s^{-1}	m =0.05 m yr^{-1}
Ross Ice Shelf (front): Stewart, (2018)	Summer: T^*_{mean} = 0.38 °C Winter: T^*_{mean}=0.12 °C	Summer: U_{mean} = 10.2 cm s^{-1} Winter: U_{mean}= 12.5 cm s^{-1}	Summer: m = 2.7 m yr^{-1} Winter: m = 1.4 m yr^{-1}
Larsen C Ice Shelf: Davis et al (2019)	$\boldsymbol{T^*}$**~0.05 °C** Notes: T_{ML}~-2.06 °C from temperature profile from Fig. 2b or T_{ML}=-2.08 °C from text. S_{ML}=34.54 psu, p_i=304 db. T_f =-0.0573*S_{ML}+ 0.0832-0.000753*p_i=-2.12 °C T^*(T_{ML}=-2.06)=0.06 °C T^*(T_{ML}=-2.08)=0.04 °C	$\boldsymbol{U_{mean}}$ **~7 cm s^{-1},** $\boldsymbol{U_{max}}$**~20 cm s^{-1}** Notes: Mean flow speed at upper instrument 2.5 m from ice base from Fig. 3 of Davis et al. Site drag coefficient is C_d=0.0022	m = 0.7±1.0 m yr^{-1} The authors provide a melting estimate using Jenkins et al (2010) of m = 0.69±0.6 m yr^{-1}
Ross Ice Shelf (HWD2): Stevens et al. (2020)	T^* =0.000-0.008 °C	$\boldsymbol{U_{mean}}$ **~4 cm s^{-1}** $\boldsymbol{U_{max}}$**~10 cm s^{-1}** Notes: Flow speeds from visual inspection of Fig. 3.	

Figure B.1: Description of the observational data used in chapters 2 and 5 of this thesis. Bold values indicate that the value was not explicitly provided in the original study, and was instead inferred from data plotted or discussed. Values in bold should be considered approximate only.

REFERENCES

Adusumilli, S., Fricker, H. A., Siegfried, M. R., Padman, L., Paolo, F. S., and Ligtenberg, S. R. M. (2018). Variable Basal Melt Rates of Antarctic Peninsula Ice Shelves, 1994–2016. *Geophysical Research Letters*, 45(9):4086–4095.

Allison, I. (2003). The AMISOR project: ice shelf dynamics and ice-ocean interaction of the Amery Ice Shelf. *FRISP Report*, 14:1–9.

Andersen, M., Stenseng, L., Skourup, H., Colgan, W., Khan, S. A., Kristensen, S. S., Andersen, S., Box, J., Ahlstrøm, A., Fettweis, X., and others (2015). Basin-scale partitioning of Greenland ice sheet mass balance components (2007–2011). *Earth and Planetary Science Letters*, 409:89–95.

Arzeno, I. B., Beardsley, R. C., Limeburner, R., Owens, B., Padman, L., Springer, S. R., Stewart, C. L., and Williams, M. J. (2014). Ocean variability contributing to basal melt rate near the ice front of Ross Ice Shelf, Antarctica. *Journal of Geophysical Research: Oceans*, 119(7):4214–4233.

Bamber, J. L., Westaway, R. M., Marzeion, B., and Wouters, B. (2018). The land ice contribution to sea level during the satellite era. *Environmental Research Letters*, 13(6):063008.

Begeman, C. B., Tulaczyk, S. M., Marsh, O. J., Mikucki, J. A., Stanton, T. P., Hodson, T. O., Siegfried, M. R., Powell, R. D., Christianson, K., and King, M. A. (2018). Ocean Stratification and Low Melt Rates at the Ross Ice Shelf Grounding Zone. *Journal of Geophysical Research: Oceans*, 123(10):7438–7452.

Bewely, T. (2008). *Numerical Renaissance: Simulation, Optimization and Control*. Renaissance Press.

Bradshaw, P. and Huang, G. P. (1995). The law of the wall in turbulent flow. *Proceedings of the Royal Society of London. Series A: Mathematical and Physical Sciences*, 451(1941):165–188.

Businger, J. A., Wyngaard, J. C., Izumi, Y., and Bradley, E. F. (1971). Flux-profile relationships in the atmospheric surface layer. *Journal of the atmospheric Sciences*, 28(2):181–189.

Carpenter, J., Sommer, T., and Wüest, A. (2012). Stability of a double-diffusive interface in the diffusive convection regime. *Journal of physical oceanography*, 42(5):840–854.

Cazenave, A. and Llovel, W. (2010). Contemporary sea level rise. *Annual review of marine science*, 2:145–173.

Coleman, G., Ferziger, J., and Spalart, P. (1992). Direct simulation of the stably stratified turbulent Ekman layer. *Journal of Fluid Mechanics*, 244:677–712.

REFERENCES

Cook, A. J., Holland, P. R., Meredith, M. P., Murray, T., Luckman, A., and Vaughan, D. G. (2016). Ocean forcing of glacier retreat in the western Antarctic Peninsula. *Science*, 353(6296):283–286.

Craven, M., Allison, I., Brand, R., Elcheikh, A., Hunter, J., Hemer, M., and Donoghue, S. (2004). Initial borehole results from the Amery Ice Shelf hot-water drilling project. *Annals of Glaciology*, 39:531–539.

Craven, M., Allison, I., Fricker, H. A., and Warner, A. R. (2009). Properties of a marine ice layer under the Amery Ice Shelf, East Antarctica. *Journal of Glaciology*, 55(192):717–728.

Craven, M., Warner, R. C., Vogel, S. W., and Allison, I. (2014). Platelet ice attachment to instrument strings beneath the Amery Ice Shelf , East Antarctica. 60(220):383–393.

Dansereau, V., Heimbach, P., and Losch, M. (2014). Simulation of subice shelf melt rates in a general circulation model: Velocity-dependent transfer and the role of friction. *Journal of Geophysical Research: Oceans*, 119(3):1765–1790.

Davis, P. E. and Nicholls, K. W. (2019). Turbulence Observations beneath Larsen C Ice Shelf, Antarctica. *Journal of Geophysical Research: Oceans*, 124(8):5529–5550.

De Lavergne, C., Palter, J. B., Galbraith, E. D., Bernardello, R., and Marinov, I. (2014). Cessation of deep convection in the open Southern Ocean under anthropogenic climate change. *Nature Climate Change*, 4(4):278.

Depoorter, M. A., Bamber, J. L., Griggs, J. A., Lenaerts, J. T. M., Ligtenberg, S. R. M., Broeke, M. R. V. D., and Moholdt, G. (2013). Calving fluxes and basal melt rates of Antarctic ice shelves. *Nature*, 502:89–92.

Determann, J. and Gerdes, R. (1994). Melting and freezing beneath ice shelves: implications from a three-dimensional ocean-circulation model. *Annals of Glaciology*, 20:413–419.

Deusebio, E., Brethouwer, G., Schlatter, P., and Lindborg, E. (2014). A numerical study of the unstratified and stratified Ekman layer. *Journal of Fluid Mechanics*, 755:672–704.

Deusebio, E., Caulfield, C., and Taylor, J. R. (2015). The intermittency boundary in stratified plane Couette flow. *Journal of Fluid Mechanics*, 781:298–329. Publisher: Cambridge University Press.

Dinniman, M., Asay-Davis, X., Galton-Fenzi, B., Holland, P., Jenkins, A., and Timmermann, R. (2016). Modeling ice shelf/ocean interaction in Antarctica: A review. *Oceanography*, 29(4):144–153.

Dotto, T. S., Naveira Garabato, A. C., Bacon, S., Holland, P. R., Kimura, S., Firing, Y. L., Tsamados, M., Wählin, A. K., and Jenkins, A. (2019). Wind-driven processes controlling oceanic heat delivery to the Amundsen Sea, Antarctica. *Journal of Physical Oceanography*, 49(11):2829–2849.

REFERENCES

Dowdeswell, J. A. (2006). The Greenland ice sheet and global sea-level rise. *Science*, 311(5763):963–964.

Dupont, T. K. and Alley, R. B. (2005). Assessment of the importance of ice-shelf buttressing to ice-sheet flow. *Geophysical Research Letters*, 32(4).

Dutrieux, P., Stewart, C., Jenkins, A., Nicholls, K. W., Corr, H. F., Rignot, E., and Steffen, K. (2014). Basal terraces on melting ice shelves. *Geophysical Research Letters*, 41(15):5506–5513.

Fernando, H. J. S. (1987). The formation of a layered structure when a stable salinity gradient is heated from below. *Journal of Fluid Mechanics*, 182:525–541.

Flores, O. and Riley, J. (2011). Analysis of turbulence collapse in the stably stratified surface layer using direct numerical simulation. *Boundary-Layer Meteorology*, 139(2):241–259. Publisher: Springer.

Fofonoff, N. P. and Millard, R. C. (1983). Algorithms for computation of fundamental properties of seawater. *UNESCO. Techical Papers in Marine Science*, 44.

Foster, T. D. (1983). The temperature and salinity fine structure of the ocean under the Ross Ice Shelf. *Journal of Geophysical Research: Oceans*, 88(C4):2556–2564.

Fox-Kemper, B., Adcroft, A., Böning, C. W., Chassignet, E. P., Curchitser, E., Danabasoglu, G., Eden, C., England, M. H., Gerdes, R., Greatbatch, R. J., and others (2019). Challenges and prospects in ocean circulation models. *Frontiers in Marine Science*, 6:65.

Fretwell, P., Pritchard, H. D., Vaughan, D. G., and Al., E. (2013a). Bedmap2: Improved ice bed, surface and thickness datasets for Antarctica. *Cryosphere*, 7(1):375–393.

Fretwell, P., Pritchard, H. D., Vaughan, D. G., Bamber, J. L., Barrand, N. E., Bell, R., Bianchi, C., Bingham, R., Blankenship, D. D., Casassa, G., and others (2013b). Bedmap2: improved ice bed, surface and thickness datasets for Antarctica. *The Cryosphere*, 7(1):375–393.

Fricker, H. A., Popov, S., Allison, I., and Young, N. (2001). Distribution of marine ice beneath the Amery Ice Shelf. *Geophysical Research Letters*, 28(11):2241–2244.

Fürst, J. J., Durand, G., Gillet-Chaulet, F., Tavard, L., Rankl, M., Braun, M., and Gagliardini, O. (2016). The safety band of Antarctic ice shelves. *Nature Climate Change*, 6(5):479–482.

Gade, H. G. (1979). Melting of ice in sea water: A primitive model with application to the Antarctic ice shelf and icebergs. *Journal of Physical Oceanography*, 9(1):189–198.

Gade, H. G. (1993). When ice melts in sea water: A review. *Atmosphere-Ocean*, 31(1):139–165.

Galton-Fenzi, B. K., Hunter, J. R., Coleman, R., Marsland, S. J., and Warner, R. C. (2012). Modeling the basal melting and marine ice accretion of the Amery Ice Shelf. *Journal of Geophysical Research: Oceans*, 117(9):1–19.

Gardner, A. S., Moholdt, G., Scambos, T., Fahnstock, M., Ligtenberg, S., Van Den Broeke, M., and Nilsson, J. (2018). Increased West Antarctic and unchanged East Antarctic ice discharge over the last 7 years. *Cryosphere*, 12(2):521–547.

Garratt, J. (1982). Observations in the nocturnal boundary layer. *Boundary-Layer Meteorology*, 22(1):21–48.

Gayen, B., Griffiths, R. W., and Kerr, R. C. (2016). Simulation of convection at a vertical ice face dissolving into saline water. *Journal of Fluid Mechanics*, 798:284–298.

Gayen, B., Hughes, G. O., and Griffiths, R. W. (2013). Completing the mechanical energy pathways in turbulent Rayleigh-Bénard convection. *Physical review letters*, 111(12):124301.

Gayen, B., Sarkar, S., and Taylor, J. R. (2010). Large eddy simulation of a stratified boundary layer under an oscillatory current. *Journal of Fluid Mechanics*, 643:233–266.

Germano, M., Piomelli, U., Moin, P., and Cabot, W. H. (1991). A dynamic subgrid-scale eddy viscosity model. *Physics of Fluids A: Fluid Dynamics*, 3(7):1760–1765.

Greene, C. A., Blankenship, D. D., Gwyther, D. E., Silvano, A., and van Wijk, E. (2017a). Wind causes Totten Ice Shelf melt and acceleration. *Science Advances*, 3(11).

Greene, C. A., Gwyther, D. E., and Blankenship, D. D. (2017b). Antarctic mapping tools for MATLAB. *Computers & Geosciences*, 104:151–157.

Gwyther, D. E., Cougnon, E. A., Galton-Fenzi, B. K., Roberts, J. L., Hunter, J. R., and Dinniman, M. S. (2016). Modelling the response of ice shelf basal melting to different ocean cavity environmental regimes. *Annals of Glaciology*, 57(73):131–141.

Gwyther, D. E., Galton-Fenzi, B. K., Dinniman, M. S., Roberts, J. L., and Hunter, J. R. (2015). The effect of basal friction on melting and freezing in ice shelf-ocean models. *Ocean Modelling*, 95:38–52.

Gwyther, D. E., Kusahara, K., Asay-Davis, X. S., Dinniman, M. S., and Galton-Fenzi, B. K. (2020a). Vertical processes and resolution impact ice shelf basal melting: A multi-model study. *Ocean Modelling*, 147.

Gwyther, D. E., Spain, E., King, P., Guihen, D., Williams, G. D., Evans, E., Cook, S., Richter, O., Galton-Fenzi, B. K., and Coleman, R. (2020b). Cold ocean cavity and weak basal melting of the Sørsdal ice shelf revealed by surveys using autonomousplatforms. *Journal of Geophysical Research: Oceans*, page e2019JC015882.

Hattermann, T., Nøst, O. A., Lilly, J. M., and Smedsrud, L. H. (2012). Two years of oceanic observations below the Fimbul Ice Shelf, Antarctica. *Geophysical Research Letters*, 39(12).

Hellmer, H. H. and Olbers, D. (1989). A two-dimensional model for the thermohaline circulation under an ice shelf. *Antarctic Science*, 1(4):325–336.

REFERENCES

Hemer, M., Hunter, J., and Coleman, R. (2006). Barotropic tides beneath the Amery Ice Shelf. *Journal of Geophysical Research: Oceans*, 111.

Herraiz-Borreguero, L., Allison, I., Craven, M., Nicholls, K. W., and Rosenberg, M. A. (2013). Ice shelf/ocean interactions under the Amery Ice Shelf: Seasonal variability and its effect on marine ice formation. *Journal of Geophysical Research: Oceans*, 118(12):7117–7131.

Herraiz-Borreguero, L., Coleman, R., Allison, I., Rintoul, S. R., Craven, M., and Williams, G. D. (2015). Circulation of modified Circumpolar Deep Water and basal melt beneath the Amery Ice Shelf, East Antarctica. *Journal of Geophysical Research C: Oceans*, 120(4):3098–3112.

Herraiz-Borreguero, L., Church, J. A., Allison, I., Peña-Molino, B., Coleman, R., Tomczak, M., and Craven, M. (2016). Basal melt, seasonal water mass transformation, ocean current variability, and deep convection processes along the Amery Ice Shelf calving front, East Antarctica. *Journal of Geophysical Research: Oceans*, 121(7):4946–4965.

Hewitt, I. J. (2020). Subglacial Plumes. *Annual Review of Fluid Mechanics*, 52:145–169.

Heywood, K. J. and King, B. A. (2002). Water masses and baroclinic transports in the South Atlantic and Southern oceans. *Journal of Marine Research*, 60(5):639–676.

Hirano, D., Tamura, T., Kusahara, K., Ohshima, K. I., Nicholls, K. W., Ushio, S., Simizu, D., Ono, K., Fujii, M., Nogi, Y., and Aoki, S. (2020). Strong ice-ocean interaction beneath Shirase Glacier Tongue in East Antarctica. *Nature Communications*, 11(1):4221.

Holford, J. M. and Linden, P. (1999). Turbulent mixing in a stratified fluid. *Dynamics of atmospheres and oceans*, 30(2-4):173–198.

Holland, D. M. and Jenkins, A. (1999). Modeling Thermodynamic Ice–Ocean Interactions at the Base of an Ice Shelf. *Journal of Physical Oceanography*, 29(8):1787–1800.

Jackson, P. R. and Rehmann, C. R. (2014). Experiments on differential scalar mixing in turbulence in a sheared, stratified flow. *Journal of Physical Oceanography*, 44(10):2661–2680.

Jacobs, S. S. and Giulivi, C. F. (2010). Large multidecadal salinity trends near the Pacific–Antarctic continental margin. *Journal of Climate*, 23(17):4508–4524.

Jacobs, S. S., Helmer, H. H., Doake, C. S. M., Jenkins, A., and Frolich, R. M. (1992). Melting of ice shelves and the mass balance of Antarctica. *Journal of Glaciology*, 38(130):375–387.

Jacobs, S. S., Jenkins, A., Giulivi, C. F., and Dutrieux, P. (2011). Stronger ocean circulation and increased melting under Pine Island Glacier ice shelf. *Nature Geoscience*, 4(8):519–523.

Jenkins, A. (1991). A one-dimensional model of ice shelf-ocean interaction. *Journal of Geophysical Research: Oceans*, 96:20671–20677.

Jenkins, A., Dutrieux, P., Jacobs, S. S., McPhail, S. D., Perrett, J. R., Webb, A. T., and White, D. (2010a). Observations beneath Pine Island Glacier in West Antarctica and implications for its retreat. *Nature Geoscience*, 3(7):468–472.

Jenkins, A., Nicholls, K. W., and Corr, H. F. (2010b). Observation and parameterization of ablation at the base of Ronne Ice Shelf, Antarctica. *Journal of Physical Oceanography*, 40(10):2298–2312.

Jenkins, A., Shoosmith, D., Dutrieux, P., Jacobs, S., Kim, T. W., Lee, S. H., Ha, H. K., and Stammerjohn, S. (2018). West Antarctic Ice Sheet retreat in the Amundsen Sea driven by decadal oceanic variability. *Nature Geoscience*, 11(10):733–738.

Josberger, E. G. and Martin, S. (1981). A laboratory and theoretical study of the boundary layer adjacent to a vertical melting ice wall in salt water. *Journal of Fluid Mechanics*, 111(-1):439–473.

Jourdain, N. C., Mathiot, P., Merino, N., Durand, G., Sommer, J. L., Spence, P., Dutrieux, P., and Madec, G. (2017). Ocean circulation and sea-ice thinning induced by melting ice shelves in the Amundsen Sea. *Journal of Geophysical Research: Oceans*, 122(3):2550–2573.

Kader, B. and Yaglom, A. (1972). Heat and mass transfer laws for fully turbulent wall flows. *International Journal of Heat and Mass Transfer*, 15(12):2329–2351.

Kader, B. A. and Yaglom, A. M. (1990). Mean fields and fluctuation moments in unstably stratified turbulent boundary layers. *Journal of Fluid Mechanics*, 212:637–662.

Keitzl, T., Mellado, J. P., and Notz, D. (2016a). Impact of Thermally Driven Turbulence on the Bottom Melting of Ice. *Journal of Physical Oceanography*, 46(4):1171–1187.

Keitzl, T., Mellado, J. P., and Notz, D. (2016b). Reconciling estimates of the ratio of heat and salt fluxes at the ice-ocean interface. *Journal of Geophysical Research : Oceans*, 121:1063–1084.

Kelley, D., Fernando, H., Gargett, A., Tanny, J., and Özsoy, E. (2003). The diffusive regime of double-diffusive convection. *Progress in Oceanography*, 56(3-4):461–481.

Kerr, R. C. and McConnochie, C. D. (2015). Dissolution of a vertical solid surface by turbulent compositional convection. *Journal of Fluid Mechanics*, 765:211–228.

Khazendar, A., Schodlok, M. P., Fenty, I., Ligtenberg, S. R. M., Rignot, E., and van den Broeke, M. R. (2013). Observed thinning of Totten Glacier is linked to coastal polynya variability. *Nature Communications*, 4(1):1–9.

Kimura, S., Holland, P. R., Jenkins, A., and Piggott, M. (2014). The Effect of Meltwater Plumes on the Melting of a Vertical Glacier Face. *Journal of Physical Oceanography*, 44(12):3099–3117.

Kimura, S., Jenkins, A., Dutrieux, P., Forryan, A., Naveira Garabato, A. C., and Firing, Y. (2016). Ocean mixing beneath Pine Island Glacier ice shelf, West Antarctica. *Journal of Geophysical Research: Oceans*, 121(12):8496–8510.

Kimura, S., Jenkins, A., Regan, H., Holland, P. R., Assmann, K. M., Whitt, D. B., Van Wessem, M., van de Berg, W. J., Reijmer, C. H., and Dutrieux, P. (2017). Oceanographic controls on the variability of ice-shelf basal melting and circulation of glacial meltwater in the Amundsen Sea Embayment, Antarctica. *Journal of Geophysical Research: Oceans*, 122(12):10131–10155.

Kimura, S., Nicholls, K. W., and Venables, E. (2015). Estimation of Ice Shelf Melt Rate in the Presence of a Thermohaline Staircase. *Journal of Physical Oceanography*, 45(1):133–148.

King, M. D., Howat, I. M., Jeong, S., Noh, M. J., Wouters, B., Noël, B., and van den Broeke, M. R. (2018). Seasonal to decadal variability in ice discharge from the Greenland Ice Sheet. *The Cryosphere*, 12(12):3813.

Konrad, H., Gilbert, L., Cornford, S. L., Payne, A., Hogg, A., Muir, A., and Shepherd, A. (2017). Uneven onset and pace of ice-dynamical imbalance in the Amundsen Sea Embayment, West Antarctica. *Geophysical Research Letters*, 44(2):910–918.

Lewis, E. and Perkin, R. (1986). Ice pumps and their rates. *Journal of Geophysical Research: Oceans*, 91(C10):11756–11762.

Linden, P. F. and Shirtcliffe, T. G. L. (1978). The diffusive interface in double-diffusive convection. *Journal of Fluid Mechanics*, 87(3):417.

MacAyeal, D. R. (1984). Thermohaline circulation below the Ross Ice Shelf: A consequence of tidally induced vertical mixing and basal melting. *Journal of Geophysical Research: Oceans*, 89(C1):597–606.

Malyarenko, A., Wells, A. J., Langhorne, P. J., Robinson, N. J., Williams, M. J., and Nicholls, K. W. (2020). A synthesis of thermodynamic ablation at ice-ocean interfaces from theory, observations and models. *Ocean Modelling*, 154:101692.

Manucharyan, G. and Caulfield, C. (2015). Entrainment and mixed layer dynamics of a surface-stress-driven stratified fluid. *Journal of Fluid Mechanics*, 765:653–667.

Martin, S. and Kauffman, P. (1977). An experimental and theoretical study of the turbulent and laminar convection generated under a horizontal ice sheet floating on warm salty water. *Journal of Physical Oceanography*, 7(2):272–283.

McConnochie, C. and Kerr, R. (2017a). Testing a common ice-ocean parameterization with laboratory experiments. *Journal of Geophysical Research: Oceans*, 122(7):5905–5915.

McConnochie, C. D. and Kerr, R. C. (2016a). The effect of a salinity gradient on the dissolution of a vertical ice face. *Journal of Fluid Mechanics*, 791:589–607.

McConnochie, C. D. and Kerr, R. C. (2016b). The turbulent wall plume from a vertically distributed source of buoyancy. *Journal of Fluid Mechanics*, 787:237–253.

McConnochie, C. D. and Kerr, R. C. (2017b). Enhanced ablation of a vertical ice wall due to an external freshwater plume. *Journal of Fluid Mechanics*, 810:429–447.

McConnochie, C. D. and Kerr, R. C. (2018). Dissolution of a sloping solid surface by turbulent compositional convection. *Journal of Fluid Mechanics*, 846:563–577.

McDougall, T. J. and Barker, P. M. (2011). Getting started with TEOS-10 and the Gibbs Seawater (GSW) Oceanographic Toolbox. *Scor/Iapso Wg127*, page 28.

McDougall, T. J., Barker, P. M., Feistel, R., and Galton-Fenzi, B. K. (2014). Melting of Ice and Sea Ice into Seawater and Frazil Ice Formation. *Journal of Physical Oceanography*, 44(7):1751–1775.

McPhee, M. (2008). *Air-ice-ocean interaction: Turbulent ocean boundary layer exchange processes*. Springer Science & Business Media.

McPhee, M. G. (1981). An analytic similarity theory for the planetary boundary layer stabilized by surface buoyancy. *Boundary-Layer Meteorology*, 21(3):325–339.

McPhee, M. G. (1992). Turbulent heat flux in the upper ocean under sea ice. *Journal of Geophysical Research*, 97(C4):5365.

McPhee, M. G. (1994). On the turbulent mixing length in the oceanic boundary layer. *Journal of Physical Oceanography*, 24(9):2014–2031.

McPhee, M. G., Kottmeier, C., and Morison, J. H. (1999). Ocean heat flux in the central Weddell Sea during winter. *Journal of Physical Oceanography*, 29(6):1166–1179.

McPhee, M. G., Maykut, G. A., and Morison, J. H. (1987). Dynamics and thermodynamics of the ice/upper ocean system in the marginal ice zone of the Greenland Sea. *Journal of Geophysical Research*, 92(C7):7017.

McWilliams, J. C., Huckle, E., and Shchepetkin, A. F. (2009). Buoyancy effects in a stratified Ekman layer. *Journal of Physical Oceanography*, 39(10):2581–2599.

Mellor, G. L., McPhee, M. G., and Steele, M. (1986). Ice-Seawater Turbulent Boundary Layer Interaction with Melting or Freezing. *Journal of Physical Oceanography*, 16(11):1829–1846.

Meredith, M., Sommerkorn, M., Cassotta, S., Derksen, C., Ekaykin, A., Hollowed, A., Kofinas, G., Mackintosh, A., Melbourne-Thomas, J., Muelbert, M. M. C., Ottersen, G., Pritchard, H., and Schuur, E. A. G. (2019). Polar Regions. In *IPCC Special Report on the Ocean and Cryosphere in a Changing Climate*. [H.-O. Pörtner, D.C. Roberts, V. Masson-Delmotte, P. Zhai, M. Tignor, E. Poloczanska, K. Mintenbeck, A. Alegría, M. Nicolai, A. Okem, J. Petzold, B. Rama, N.M. Weyer (eds.)] In press.

Minchew, B. M., Gudmundsson, G. H., Gardner, A. S., Paolo, F. S., and Fricker, H. A. (2018). Modeling the dynamic response of outlet glaciers to observed ice-shelf thinning in the Bellingshausen Sea Sector, West Antarctica. *Journal of Glaciology*, 64(244):333–342.

Mondal, M., Gayen, B., Griffiths, R. W., and Kerr, R. C. (2019). Ablation of sloping ice faces into polar seawater. *Journal of Fluid Mechanics*, 863:545–571.

Monin, A. S. and Obukhov, A. M. (1954). Basic laws of turbulent mixing in the surface layer of the atmosphere. *Contrib. Geophys. Inst. Acad. Sci. USSR*, 151(163).

Morrison, A., Hogg, A. M., England, M., and Spence, P. (2020). Warm Circumpolar Deep Water transport toward Antarctica driven by local dense water export in canyons. *Science Advances*, 6(18):eaav2516.

Naughten, K. A., Meissner, K. J., Galton-Fenzi, B. K., England, M. H., Timmermann, R., and Hellmer, H. H. (2018a). Future projections of Antarctic ice shelf melting based on CMIP5 scenarios. *Journal of Climate*, 31(13):5243–5261.

Naughten, K. A., Meissner, K. J., Galton-Fenzi, B. K., England, M. H., Timmermann, R., Hellmer, H. H., Hattermann, T., and Debernard, J. B. (2018b). Intercomparison of Antarctic ice-shelf, ocean, and sea-ice interactions simulated by MetROMS-iceshelf and FESOM 1.4. *Geoscientific Model Development*, 11(4):1257–1292.

Newell, T. (1984). Characteristics of a double-diffusive interface at high density stability ratios. *Journal of Fluid Mechanics*, 149:385–401.

Nicholls, K. W. (2018). The study of ice shelf-ocean interaction – techniques and recent results.

Noble, T., Rohling, E., Aitken, A., Bostock, H., Chase, Z., Gomez, N., Jong, L., King, M., Mackintosh, A., McCormack, F., and others (2020). The sensitivity of the Antarctic Ice Sheet to a changing climate: Past, present and future. *Reviews of Geophysics*, 58:e2019RG000663.

Obukhov, A. (1946). Turbulence in an atmosphere with inhomogeneous temperature, Tr. *Inst. Teor. Geofis. Akad. Nauk. SSSR*, 1:95–115.

Obukhov, A. (1971). Turbulence in an atmosphere with a non-uniform temperature. *Boundary-layer meteorology*, 2(1):7–29.

Oerter, H., Kipfstuhl, J., Determann, J., Miller, H., Wagenbach, D., Minikin, A., and Graft, W. (1992). Evidence for basal marine ice in the Filchner–Ronne Ice Shelf. *Nature*, 358(6385):399–401.

Orsi, A. H. and Whitworth, T. (2005). *Hydrographic Atlas of the World Ocean Circulation Experiment (WOCE): Volume 1: Southern Ocean.* WOCE International Project Office Southampton, UK.

Paolo, F. S., Fricker, H. A., and Padman, L. (2015). Volume loss from Antarctic ice shelves is accelerating. *Science*, 348(6232):327–331.

Pawlowicz, R., Beardsley, B., and Lentz, S. (2002). Classical tidal harmonic analysis including error estimates in MATLAB using T TIDE. 28:929–937.

Pope, S. B. (2001). *Turbulent flows*. IOP Publishing.

Post, A., Galton-Fenzi, B., Riddle, M., Herraiz-Borreguero, L., O'Brien, P., Hemer, M., McMinn, A., Rasch, D., and Craven, M. (2014). Modern sedimentation, circulation and life beneath the Amery Ice Shelf, East Antarctica. *Continental Shelf Research*, 74:77–87.

Pritchard, H. D., Ligtenberg, S. R. M., Fricker, H. A., Vaughan, D. G., den Broeke, M. R., and Padman, L. (2012). Antarctic ice-sheet loss driven by basal melting of ice shelves. *Nature*, 484(7395):502–505.

Purkey, S. G. and Johnson, G. C. (2013). Antarctic Bottom Water Warming and Freshening: Contributions to Sea Level Rise, Ocean Freshwater Budgets, and Global Heat Gain. *Journal of Climate*, 26(16):6105–6122.

Radko, T. (2013). *Double diffusive convection*. Cambridge University Press.

Raju, H. V. and Narasimha, R. (2003). Limiting cross-flow velocity below which heat flux is determined by natural convection laws. *International Journal of Heat and Mass Transfer*, 46(25):4975–4978.

Reese, R., Gudmundsson, G. H., Levermann, A., and Winkelmann, R. (2018). The far reach of ice-shelf thinning in Antarctica. *Nature Climate Change*, 8(1):53–57.

Rignot, E., Jacobs, S., Mouginot, J., and Scheuchl, B. (2013). Ice Shelf Melting Around Antarctica. *Science*, 341:266–270.

Rignot, E., Mouginot, J., Scheuchl, B., van den Broeke, M., van Wessem, M. J., and Morlighem, M. (2019). Four decades of Antarctic Ice Sheet mass balance from 1979–2017. *Proceedings of the National Academy of Sciences*, 116(4):1095–1103.

Roberts, J., Galton-Fenzi, B. K., Paolo, F. S., Donnelly, C., Gwyther, D. E., Padman, L., Young, D., Warner, R., Greenbaum, J., Fricker, H. A., Payne, A. J., Cornford, S., Brocq, A. L., Ommen, T. v., Blankenship, D., and Siegert, M. J. (2018). Ocean forced variability of Totten Glacier mass loss. *Geological Society, London, Special Publications*, 461(1):175–186.

Robertson, R., Padman, L., and Levine, M. D. (1995). Fine structure, microstructure, and vertical mixing processes in the upper ocean in the western Weddell Sea. *Journal of Geophysical Research: Oceans*, 100(C9):18517–18535.

Robinson, N. J., Stevens, C. L., and McPhee, M. G. (2017). Observations of amplified roughness from crystal accretion in the sub-ice ocean boundary layer. *Geophys. Res. Lett.*, 44:1814–1822.

Robinson, N. J., Williams, M. J. M., Barrett, P. J., and Pyne, A. R. (2010). Observations of flow and ice-ocean interaction beneath the McMurdo Ice Shelf, Antarctica. *Journal of Geophysical Research: Oceans*, 115(C3).

Ruddick, B., McDougall, T., and Turner, J. (1989). The formation of layers in a uniformly stirred density gradient. *Deep Sea Research Part A. Oceanographic Research Papers*, 36(4):597–609.

Salon, S., Armenio, V., and Crise, A. (2007). A numerical investigation of the Stokes boundary layer in the turbulent regime. *Journal of Fluid Mechanics*, 570:253–296.

Shah, S. K. and Bou-Zeid, E. (2014). Direct numerical simulations of turbulent Ekman layers with increasing static stability: modifications to the bulk structure and second-order statistics. *Journal of Fluid Mechanics*, 760:494–539.

Shcherbina, A. Y., Rudnick, D. L., and Talley, L. D. (2005). Ice-draft profiling from bottom-mounted ADCP data. *Journal of Atmospheric and Oceanic Technology*, 22(8):1249–1266.

Shepherd, A., Ivins, E., Rignot, E., Smith, B., van den Broeke, M., Velicogna, I., Whitehouse, P., Briggs, K., Joughin, I., Krinner, G., and others (2018). Mass balance of the Antarctic Ice Sheet from 1992 to 2017. *Nature*, 556:219–222.

Shibley, N., Timmermans, M.-L., Carpenter, J., and Toole, J. (2017). Spatial variability of the Arctic Ocean's double-diffusive staircase. *Journal of Geophysical Research: Oceans*, 122(2):980–994.

Sirevaag, A. (2009). Turbulent exchange coefficients for the ice/ocean interface in case of rapid melting. *Geophysical Research Letters*, 36(4).

Smith, B., Fricker, H. A., Gardner, A. S., Medley, B., Nilsson, J., Paolo, F. S., Holschuh, N., Adusumilli, S., Brunt, K., Csatho, B., Harbeck, K., Markus, T., Neumann, T., Siegfried, M. R., and Zwally, H. J. (2020). Pervasive ice sheet mass loss reflects competing ocean and atmosphere processes. *Science*, 368(6496):1239–1242.

Smyth, W. and Kimura, S. (2011). Mixing in a moderately sheared salt-fingering layer. *Journal of Physical Oceanography*, 41(7):1364–1384.

Stanton, T., Shaw, W., Truffer, M., Corr, H., Peters, L., Riverman, K., Bindschadler, R., Holland, D., and Anandakrishnan, S. (2013). Channelized ice melting in the ocean boundary layer beneath Pine Island Glacier, Antarctica. *Science*, 341(6151):1236–1239.

Stern, A., Holland, D., Holland, P., Jenkins, A., and Sommeria, J. (2014). The effect of geometry on ice shelf ocean cavity ventilation: a laboratory experiment. *Experiments in fluids*, 55(5):1719–1738.

Stevens, C., Hulbe, C., Brewer, M., Stewart, C., Robinson, N., Ohneiser, C., and Jendersie, S. (2020). Ocean mixing and heat transport processes observed under the Ross Ice Shelf control its basal melting. *Proceedings of the National Academy of Sciences*, 117(29):16799–16804.

Stevens, C. L., Robinson, N. J., Williams, M. J. M., and Haskell, T. G. (2009). Observations of turbulence beneath sea ice in southern McMurdo Sound, Antarctica. *Ocean Science Discussions*, 6(2):1407–1436.

REFERENCES

Stewart, C. L. (2018). *Ice-ocean interactions beneath the north-western Ross Ice Shelf, Antarctica.* PhD Thesis, University of Cambridge.

Stewart, C. L., Christoffersen, P., Nicholls, K. W., Williams, M. J. M., and Dowdeswell, J. A. (2019). Basal melting of Ross Ice Shelf from solar heat absorption in an ice-front polynya. *Nature Geoscience*, 12(6):435–440.

Straneo, F., Heimbach, P., Sergienko, O., Hamilton, G., Catania, G., Griffies, S., Hallberg, R., Jenkins, A., Joughin, I., Motyka, R., and others (2013). Challenges to understanding the dynamic response of Greenland's marine terminating glaciers to oceanic and atmospheric forcing. *Bulletin of the American Meteorological Society*, 94(8):1131–1144.

Taylor, J. R. and Sarkar, S. (2007). Internal gravity waves generated by a turbulent bottom Ekman layer. *Journal of Fluid Mechanics*, 590:331–354.

Taylor, J. R. and Sarkar, S. (2008a). Direct and large eddy simulations of a bottom Ekman layer under an external stratification. *International Journal of Heat and Fluid Flow*, 29(3):721–732.

Taylor, J. R. and Sarkar, S. (2008b). Stratification effects in a bottom Ekman layer. *Journal of Physical oceanography*, 38(11):2535–2555.

Teledyne, R. (2006). Instruments. Acoustic Doppler Current Profiler Principles of Operation: A Practical Primer. P. Technical report, N 951-6069.

Thoma, M., Jenkins, A., Holland, D., and Jacobs, S. (2008). Modelling circumpolar deep water intrusions on the Amundsen Sea continental shelf, Antarctica. *Geophysical Research Letters*, 35(18).

Thompson, A. F. and Heywood, K. J. (2008). Frontal structure and transport in the northwestern Weddell Sea. *Deep Sea Research Part I: Oceanographic Research Papers*, 55(10):1229–1251.

Thompson, A. F., Stewart, A. L., Spence, P., and Heywood, K. J. (2018). The Antarctic Slope Current in a changing climate. *Reviews of Geophysics*, 56(4):741–770.

Timmermans, M.-L., Toole, J., Krishfield, R., and Winsor, P. (2008). Ice Tethered Profiler observations of the double-diffusive staircase in the Canada Basin thermocline. *Journal of Geophysical Research: Oceans*, 113(C1).

Turner, J. (1974). Double-diffusive phenomena. *Annual Review of Fluid Mechanics*, 6(1):37–54.

Turner, J. S. (1968). The behaviour of a stable salinity gradient heated from below. *Journal of Fluid Mechanics*, 33(1):183–200.

Turner, J. S. (1979). *Buoyancy effects in fluids.* Cambridge university press.

van de Wal, R., Oppenheimer, M., Glavovic, B. C., Hinkel, J., Cai, R., Magnan, A., DeConto, R., Isla, F., Ghosh, T., Marzeion, B., and others (2020). Sea Level Rise and Implications for Low Lying Islands, Coasts and Communities. In *IPCC Special Report on the Ocean and Cryosphere in a Changing Climate*.

Van den Broeke, M. R., Enderlin, E. M., Howat, I. M., Kuipers Munneke, P., Noël, B. P., Jan Van De Berg, W., Van Meijgaard, E., and Wouters, B. (2016). On the recent contribution of the Greenland ice sheet to sea level change. *The Cryosphere*, 10(5):1933–1946.

Venables, E., Nicholls, K., Wolk, F., Makinson, K., and Anker, P. (2014). Measuring turbulent dissipation rates beneath an Antarctic ice shelf. *Marine Technology Society Journal*, 48(5):18–24.

Vreugdenhil, C. A. and Taylor, J. R. (2018). Large-eddy simulations of stratified plane Couette flow using the anisotropic minimum-dissipation model. *Physics of Fluids*, 30(8):085104.

Vreugdenhil, C. A. and Taylor, J. R. (2019). Stratification effects in the turbulent boundary layer beneath a melting ice shelf: insights from resolved large-eddy simulations. *Journal of Physical Oceanography*, 49(7):1905–1925.

Weatherly, G. L. and Martin, P. J. (1978). On the Structure and Dynamics of the Oceanic Bottom Boundary Layer. *Journal of Physical Oceanography*, 8(4):557–570.

Weertman, J. (1974). Stability of the junction of an ice sheet and an ice shelf. *Journal of Glaciology*, 13(67):3–11.

Wells, A. J. and Worster, M. G. (2008). A geophysical-scale model of vertical natural convection boundary layers. *Journal of Fluid Mechanics*, 609:111–137.

Wells, M. G. and Griffiths, R. W. (2003). Interaction of salt finger convection with intermittent turbulence. *Journal of Geophysical Research: Oceans*, 108(C3).

Wen, J., Wang, Y., Wang, W., Jezek, K. C., Liu, H., and Allison, I. (2010). Basal melting and freezing under the Amery Ice Shelf, East Antarctica. *Journal of Glaciology*, 56(195):81–90.

Williams, G., Herraiz-Borreguero, L., Roquet, F., Tamura, T., Ohshima, K., Fukamachi, Y., Fraser, A., Gao, L., Chen, H., McMahon, C., and others (2016). The suppression of Antarctic bottom water formation by melting ice shelves in Prydz Bay. *Nature Communications*, 7(1):1–9.

Williams, M. J. M., Grosfeld, K., Warner, R. C., Gerdes, R., and Determann, J. (2001). Ocean circulation and ice-ocean interaction beneath the Amery Ice Shelf, Antarctica. *Journal of Geophysical Research: Oceans*, 106(C10):22383–22399.

Williams, M. J. M., Jenkins, A., and Determann, J. (1985). Physical Controls on Ocean Circulation Beneath Ice Shelves Revealed by Numerical Models. In *Ocean, Ice, and Atmosphere: Interactions at the Antarctic Continental Margin*, pages 285–299. American Geophysical Union.

Worster, M. G. (2004). Time-dependent fluxes across double-diffusive interfaces. *Journal of Fluid Mechanics*, 505:287–307.

Wählin, A., Yuan, X., Björk, G., and Nohr, C. (2010). Inflow of warm Circumpolar Deep Water in the central Amundsen shelf. *Journal of Physical Oceanography*, 40(6):1427–1434.

Yu, J., Liu, H., Jezek, K. C., Warner, R. C., and Wen, J. (2010). Analysis of velocity field, mass balance, and basal melt of the Lambert Glacier–Amery Ice Shelf system by incorporating Radarsat SAR interferometry and ICESat laser altimetry measurements. *Journal of Geophysical Research: Solid Earth*, 115(B11).

Zilitinkevich, S. (1972). On the determination of the height of the Ekman boundary layer. *Boundary-Layer Meteorology*, 3(2):141–145.

Zotikov, I. A., Zagorodnov, V. S., and Raikovsky, J. V. (1980). Core drilling through the Ross Ice Shelf (Antarctica) confirmed basal freezing. *Science*, 207(4438):1463–1465.